



HAL
open science

Detection on HF radio transmitters using passive geolocation techniques

Ankit Jain

► **To cite this version:**

Ankit Jain. Detection on HF radio transmitters using passive geolocation techniques. Signal and Image processing. Ecole nationale supérieure Mines-Télécom Atlantique, 2019. English. NNT : 2019IMTA0128 . tel-02133926

HAL Id: tel-02133926

<https://theses.hal.science/tel-02133926>

Submitted on 20 May 2019

HAL is a multi-disciplinary open access archive for the deposit and dissemination of scientific research documents, whether they are published or not. The documents may come from teaching and research institutions in France or abroad, or from public or private research centers.

L'archive ouverte pluridisciplinaire **HAL**, est destinée au dépôt et à la diffusion de documents scientifiques de niveau recherche, publiés ou non, émanant des établissements d'enseignement et de recherche français ou étrangers, des laboratoires publics ou privés.

THESE DE DOCTORAT DE

L'ÉCOLE NATIONALE SUPERIEURE MINES-TELECOM ATLANTIQUE
BRETAGNE PAYS DE LA LOIRE - IMT ATLANTIQUE
COMUE UNIVERSITE BRETAGNE LOIRE

ECOLE DOCTORALE N° 601
*Mathématiques et Sciences et Technologies
de l'Information et de la Communication*
Spécialité: *Télécommunications*

Par

Ankit JAIN

Detection of HF Radio Transmitters Using Passive Geolocation Techniques

Thèse présentée et soutenue à Brest, le 24 Janvier 2019

Unité de recherche : Lab-STICC

Thèse N° : 2019IMTA0128

Rapporteurs avant soutenance :

Martine Lienard Professeure, Université de Lille

Valérie Vigneras Professeure, École Nationale Supérieure de Chimie, de Biologie et de Physique (ENSCBP)

Composition du Jury :

Président : Yvon Erhel Professeur, Centre de recherches des Ecoles de Coëtquidan

Examineurs : Martine Lienard Professeure, Université de Lille
Valérie Vigneras Professeure, ENSCBP - Labo. IMS
Denis Le Jeune Associé de recherche, Dr., ENSTA Bretagne
Pascal Pagani Ingénieur de recherche (HDR)

Dir. de thèse : Michel Ney Professeur émérite, IMT Atlantique

Invité : Rolland Fleury Ingénieur d'études, IMT Atlantique

----- *To my mother and father*

----- *To Preksha*

“The infinite! No other question has ever moved so profoundly the spirit of man.”

- *David Hilbert*

Acknowledgement

I still remember the day I began my PhD research and I had a lot of questions then. I knew it would be challenging and I would have to solve a lot of complex problems. Now that I have finished, I could definitely say that it was an amazing experience; I really enjoyed and had fun while doing every bit of it.

The thesis research work was carried out at the Microwave department of IMT Atlantique in Brest. A lot of people helped me in some ways or other to unravel the different research questions and I would like to express my sincere gratitude to all of them. Firstly, I would like to thank my thesis director Professor Michel Ney for his support, time and valuable guidance throughout the course of the thesis. He made sure that I didn't panic at any stage of my PhD and helped me in writing the thesis summary in French. I would also like to express my deepest gratitude to my supervisor Mr. Pascal Pagani for his counsel, encouragement and the knowledge he gave me. This work would not have been possible without him. His availability, critical thinking and motivation were a great wealth for me throughout the thesis and have resulted in fruitful work. Thank you very much Pascal for all the time you took out of your schedule for our long and productive Skype sessions discussing about the research issues. I would also like to thank my co-supervisor Mr. Rolland Fleury for his valuable advice and encouragement. His passion for work would always be an example for me. I am also very grateful to Mr. Patrice Pajusco for his valuable suggestions related to the receiver prototypes.

I am thankful to Professor Matine Lienard and Professor Valérie Vigneras for accepting to be my thesis report reviewers and for their invaluable feedback. I also thank Professor Yvon Erhel and Dr. Denis Le Jeune for participating in the jury of the thesis.

For the experimental measurement setup in Grenoble, I was in contact with Professor Fabian Ndagijimana and Mr. Christophe de Mozas and I thank them for their help and availability. For the measurement setup in Lille, I had the opportunity to seek help from Mr. Maxime Catalfamo and Mr. Romain De Filippi and I also thank them for it.

I would like to express my sincere thanks to the Carnot Institute and the Brittany region in France to sponsor a part of this thesis. I would also like to thank Mr. Yannick Marinette from the Microwave department of IMT Atlantique for helping me in all the administrative things related to the thesis over the last 3 years. I would like to acknowledge my friends and colleagues, Rajendra Mitharwal, Abdelrahman Ijeh, Rizwan Masood, Emna Bel Kamel and Malika Tlili for the fruitful discussion and the wonderful time that we spent together. Life might have been monotone for me if you guys wouldn't have been around. Finally, I would like to thank my parents and brother who have supported and cared for me throughout my life. A special thanks to my wife Preksha, who supported and encouraged me in the best possible way.

Brest, France
January, 2019

Ankit Jain

Sommaire de la thèse

Résumé

Dans le cadre des missions militaires de renseignement, ou pour le déploiement d'un réseau de communication agile lors d'opérations humanitaires, il est important de pouvoir localiser les émetteurs à haute fréquence (HF) par l'analyse des signaux de communication. Pour des transmissions HF à des distances de quelques centaines de km, le signal radioélectrique se propage via une réflexion sur l'ionosphère, qui présente des caractéristiques très variables. La technique classique, dite "Localisation à Site Unique", possède des points durs car elle nécessite de déployer un large réseau d'antennes co-localisées et de disposer d'un modèle précis de profil ionosphérique ou d'ionosondes. L'objectif de la thèse est de développer une technique de localisation complémentaire, intitulée "*Time Difference of Arrival (TDoA)*" qui peut s'appliquer dès lors que l'on dispose de quelques récepteurs mono-antenne non co-localisés. Une étude préliminaire a montré que la localisation pouvait être établie sans connaissance explicite de la hauteur de la couche ionosphérique. Au cours de la thèse, la technique de localisation TDoA sera d'abord optimisée pour son application aux transmissions HF ionosphériques. Les autres pistes d'amélioration concernent la prise en compte de variations dans la structure de l'ionosphère et l'utilisation de signaux « balises » dont l'émetteur est identifié. Dans un second temps, on cherchera à mettre en œuvre cette technique par le développement de démonstrateurs basés sur des modules de radio logicielle, afin de définir l'approche opérationnelle la plus pertinente. Enfin, on cherchera comment les différentes méthodes existantes peuvent être combinées afin d'optimiser les performances.

Introduction

La transmission radioélectrique à longue distance dans la bande HF (de 3 à 30 MHz) permet de couvrir de vastes zones géographiques à l'aide d'infrastructures légères et mobiles. Elle est donc bien adaptée pour établir des communications lors d'opérations militaires. Un autre domaine d'application est le déploiement rapide d'un réseau de communication agile lors d'opérations humanitaires ou pour l'organisation de secours suite aux catastrophes naturelles. Pour ces deux applications, il est important de pouvoir localiser les émetteurs par l'analyse des signaux électromagnétiques de communication [40]. Cela est particulièrement important dans le cadre des missions de renseignement, afin d'obtenir des informations sur la position inconnue des émetteurs HF. Dans le cas des opérations humanitaires, cette localisation permet également de superviser le déploiement géographique des équipes de secours, sans attendre le déploiement de technologies plus complexes.

Pour des transmissions HF à des distances de plusieurs centaines de km à un millier de km, le signal radioélectrique se propage via une réflexion sur l'ionosphère. Celle-ci est une région de la haute atmosphère terrestre, dont les constituants sont ionisés sous l'influence essentiellement des radiations solaires, ce qui lui confère la particularité de réfracter les ondes radioélectriques qui s'y propagent. Les caractéristiques de cette couche atmosphérique sont très variables en fonction de l'activité solaire, de la position géographique et de l'heure locale [5]. Les performances des algorithmes classiques de localisation des émetteurs HF est largement dépendante de la connaissance des caractéristiques de l'ionosphère.

L'une des techniques de localisation disponibles, dite "Localisation à Site Unique" (LSU) [71][73], consiste à utiliser un large réseau de goniométrie à antennes multiples, ce qui permet d'obtenir la direction d'arrivée du signal. Cette technique présente cependant deux points durs. Premièrement, la LSU nécessite de déployer

un réseau d'antennes co-localisées, permettant d'obtenir des informations de direction d'arrivée en élévation et en azimut. Ce type de réseau peut comporter un grand nombre d'antennes et demande un espace de déploiement important en transmission dans la gamme HF. Par ailleurs, la LSU base ses calculs sur un modèle précis de profil ionosphérique. Les modèles statistiques de prévision ionosphérique ne permettent pas une précision suffisante et il est nécessaire de les corriger par des mesures en temps réel. A défaut, un équipement supplémentaire, l'ionosonde, doit être déployé pour mesurer les caractéristiques locales de l'ionosphère.

La problématique de la thèse consiste alors à développer des techniques de localisation passives complémentaires et à optimiser leur performance vis-à-vis de l'état de l'art. Plus particulièrement, le travail se focalisera sur le développement d'une technique de localisation alternative, intitulée "*Time Difference of Arrival*" (TDoA). Cette technique est généralement utilisée pour la localisation dans le cas de transmission en ligne directe [90], mais n'a été que très peu étudiée pour la transmission HF par rebond via le canal ionosphérique. Basée sur le temps de propagation du signal, elle peut s'appliquer dès lors que l'on dispose de quelques récepteurs mono-antenne non co-localisés. On s'affranchit ainsi de la contrainte du réseau massif d'antennes utilisé pour la goniométrie.

Un autre intérêt de cette technique est de permettre la localisation sans connaissance explicite de la hauteur de la couche ionosphérique. Nous avons étudié cette propriété de manière préliminaire par des simulations de la localisation par temps d'arrivée [78]. En supposant que les caractéristiques de l'ionosphère restent stables dans la zone de localisation, ces premiers résultats montrent que l'étude des signaux électromagnétiques permet simultanément de définir la position de l'émetteur et la hauteur de l'ionosphère. Plus de détails sur la physique de l'ionosphère, de la propagation des ondes avec rebonds ionosphériques et la méthode de géolocalisation HF sont expliquées en détails dans le Chapitre 2 de la thèse.

Le sujet proposé dans la thèse porte particulièrement sur les émetteurs de radiocommunication dans la bande HF. Afin de mettre au point la nouvelle technique de localisation proposée, les étapes scientifiques suivantes devront être effectuées :

- Faire une analyse de la technique de géolocalisation TDoA et proposer des améliorations dans le cadre de transmission ionosphérique HF.
- Effectuer une étude par simulation avec un modèle qui tient compte de la variation de la structure de l'ionosphère, de l'impact du nombre et positions des récepteurs sur la précision de la localisation d'un émetteur HF.
- Développer des démonstrateurs multiples basés sur des modules "*Software Defined Radio*" (SDR), capables de capturer des signaux radios HF de façon synchrone.
- Analyser la collecte des mesures expérimentales, afin d'identifier les différents paramètres nécessaires à une opération en temps réel d'un système de géolocalisation TDoA en HF.
- Etude de l'impact du rapport signal à bruit (SNR) du signal reçu sur la performance de la géolocalisation.

Le principe de la localisation HF est expliqué dans le paragraphe suivant. Les hypothèses et leur implication sur la précision de la géolocalisation sont détaillées dans le Chapitre 3 de la thèse.

Algorithme de la géolocalisation HF

Notre objectif est de développer un algorithme de géolocalisation HF qui ne dépend pas des propriétés de l'ionosphère. Ainsi, la complexité du problème est réduit en faisant les trois hypothèses suivantes : une transmission en un seul rebond ("*single hop*"), une couche ionosphérique uniforme avec une variation d'hauteur d'apogée négligeable et une terre plate.

Sous l'hypothèse d'un seul rebond, le signal de l'émetteur atteint le récepteur via une seule réflexion par la couche ionosphérique. La Figure 1 représente ce cas de géométrie pour une localisation HF. L'émetteur est

situé au point Tx et les récepteurs aux points Rx₁ et Rx₂. D'après le théorème de Breit et Tuve's [5], le chemin courbe entre Rx₁ et Tx représenté en rouge est de longueur égale au chemin triangulaire en noir Rx₁-I₁-Tx dans le vide. Le même principe s'applique pour l'ensemble Rx₂ et Tx.

Dû à la variation de l'indice de réfraction dans l'ionosphère, le signal se propage selon un chemin courbe. La hauteur d'apogée pour la longueur de l'ensemble est indiquée par h_a . Une hauteur équivalente h_{equ} correspondant à la hauteur de réflexion d'un chemin avec le même retard de groupe peut être définie en faisant l'hypothèse que les signaux sont réfléchis par réflexion spéculaire d'une ionosphère plate et supposée homogène. De plus, on néglige les variations de la hauteur d'apogée pour les différents chemins Rx-Tx qui ont des angles d'élévation similaires. Par conséquent, la hauteur des réflexion est supposée identique pour tous les chemins et égale à h_{equ} . Enfin, on néglige la courbature terrestre ce qui suppose une terre plate.

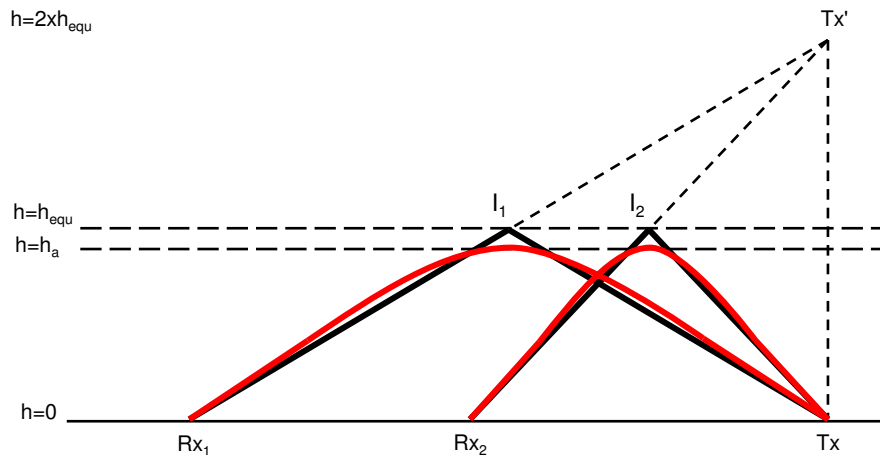


Figure 1 Illustration d'une localisation HF avec l'hypothèse d'une ionosphère homogène et plate et d'une terre plate

Par la méthode des images en électromagnétisme, la longueur du chemin entre Rx₁-Tx est égale à celle de Rx₁-I₁-Tx'. De façon similaire, la longueur du chemin de propagation entre Rx₂-Tx est égale à celle du chemin Rx₂-I₂-Tx'. La procédure de géolocalisation consiste à trouver les coordonnées de Tx' situé à une hauteur $2h_{equ}$ verticalement au-dessus de celles de l'émetteur sur la surface plate de la terre. Si les temps de propagation entre l'émetteur et les différents récepteurs sont connus, les coordonnées de Tx' peuvent être trouvées par trilatération. Quand le temps de transmission est inconnu, les coordonnées de Tx' peuvent être trouvées par multilatération en utilisant le TDoA entre les différents récepteurs.

Les procédures mentionnées ci-dessus, débouchent sur l'identification du point d'intersection entre trois sphères ou hyperboles, ce qui se traduit par la résolution d'un système d'équations quadratiques qui peut se résoudre analytiquement par linéarisation. Les développements mathématiques pour obtenir les coordonnées de Tx' sont détaillés pour les cas ToA et TDoA dans [81].

Des communications HF possibles en un rebond ont été simulées en considérant différents milieux ionosphériques homogènes. La localisation de l'émetteur HF a été trouvée en utilisant l'algorithme développé pour évaluer l'effet du nombre de récepteurs et leur position sur la précision. Des résultats sont présentés dans le paragraphe suivant. L'étude détaillée des simulations ainsi que leur analyse sont présentées dans le Chapitre 3 de la thèse.

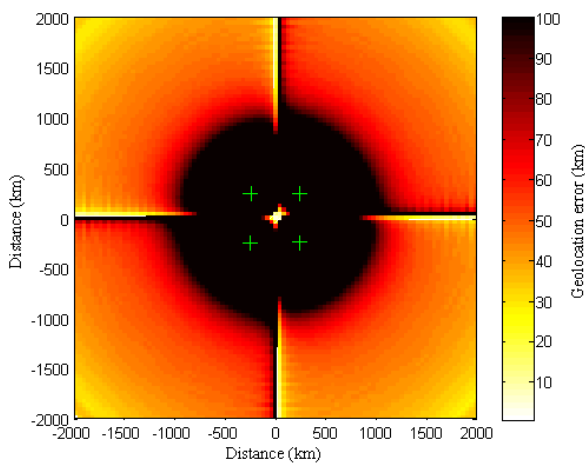
Résultats de simulation et analyse

Pour étudier l'effet du nombre de récepteur sur la précision de la géolocalisation de l'émetteur, des simulations ont été effectuées pour 4, 5, 7 et 9 récepteurs. Le modèle de l'ionosphère homogène utilisé est celui d'un profil de densité électronique correspondant à un modèle de couches QP [94]. Il est défini par les paramètres suivants : $F = 0.8$, $y_m = 100$ km, $h_m = 300$ km. Les durées de propagation sont obtenues en utilisant les expressions analytiques des chemins de groupe donnés par le modèle de couches QP. A partir

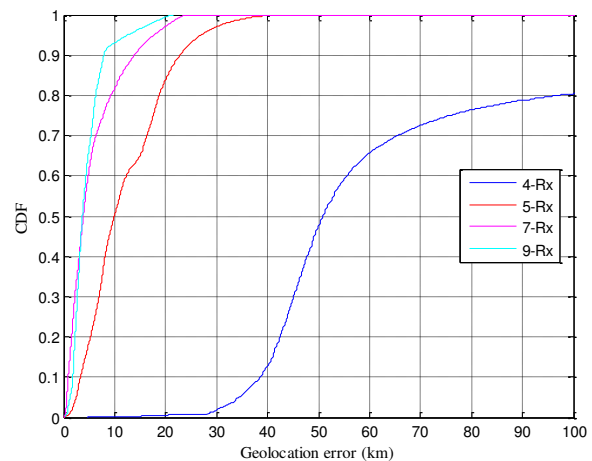
des coordonnées des récepteurs et des durées de propagation connues, celles de l'émetteur Tx sont estimée par l'algorithme TDoA en HF.

La Figure 2 (a) représente l'erreur de localisation pour un émetteur à l'intérieur d'une grille carrée de 4000 Km pour différentes configurations des récepteurs. Dans ce cas, les 4 récepteurs sont placés de façon à définir un carré. Son côté est approximativement d'une longueur de 490 km. L'artéfact observable le long des deux axes de la grille est dû à la symétrie approximative produite par la configuration des récepteurs. L'erreur de géolocalisation observée est plus large que 100 Km quand Tx est placé à des distances plus petites que 650 km de la station Rx. Cette erreur est principalement due à la variation de la hauteur équivalente. L'émetteur Tx placé à des distances entre 1100 et 2000 Km de l'origine de la grille pouvait être localisé avec des erreurs entre 25 et 50 Km. Mais lorsque Tx s'en rapproche la précision diminue.

La Figure 2 (b) montre la fonction CDF de l'erreur de géolocalisation sur les positions de Tx positions sur une grille carrée de 4000 Km mais cette fois en modifiant le nombre de récepteurs. La couche QP est définie en utilisant une hauteur d'ionisation maximum de 300 Km. Avec 4 récepteur (courbe 4-Rx) ceux-ci sont placés selon l'illustration (a) de la Figure 2. Pour la courbe 5-Rx, les 5 récepteurs sont placés selon un carré avec 4 de ceux-ci sur les sommets et le 5^e au centre de la grille. Les 4 récepteurs sont à une distance d'environ 1400 Km de l'origine respectivement à des angles d'environ 45°, 135°, 225° et 315°. Dans le cas de 7 récepteurs, (courber 7-Rx), cinq sont placés de façon similaire au cas 5-Rx mais à une distance de 1450 Km de l'origine alors que les deux derniers récepteurs sont placés dans la direction positive et négative de l'axe x de façon à ce qu'ils soient tous sur une configuration carrée. Ce cas correspond à la configuration pour laquelle les récepteurs peuvent être placés à la distance maximum de l'origine. Enfin, pour la configuration à 9 récepteurs (courbe 9-Rx), ceux-ci sont placés de façon similaire au cas 7-Rx avec les deux récepteurs additionnels placés selon la direction positive et négatives sur l'axe y de la grille. Dans cette configuration, les récepteurs peuvent être placés à des distances plus grandes de l'origine. Sur la Figure 2 (b), on peut observer qu'environ 13% des géolocalisations sont effectuées avec une erreur inférieure à 40 Km, tandis qu'elle l'est pour 100% des géolocalisations en utilisant 5 récepteurs. Il y a donc un gain substantiel dans la précision avec l'ajout d'un seul récepteur au nombre minimum de 4 requis par la procédure TDoA. De plus, il est intéressant de noter que lorsque le nombre de récepteur augmente, le gain en précision augmente mais de façon de moins en moins significative.



(a): Configuration des récepteurs : carrée



(b): Fonction CDF de l'erreur de géolocalisation pour des nombres de récepteurs différents

Figure 2 Simulations de l'erreur de géolocalisation avec l'approche TDoA et un modèle de couche QP à hauteur fixe. (a) Distribution de l'erreur avec le nombre minimum de 4 récepteurs. (b) CDF de l'erreur pour différents nombres de récepteurs

Pour démontrer la faisabilité d'un système de géolocalisation HF basé sur une procédure TDoA, des récepteurs ont été conçus et déployés sur différents sites français dans un réseau connecté. La conception du prototype des récepteurs et du réseau est expliquée dans le paragraphe qui suit. Pour plus de détails sur la

conception et la mise en œuvre des récepteurs, on se référera au Chapitre 4 de la thèse. Une première étude reliée aux propriétés des signaux capturés est aussi expliquée dans ce chapitre.

Prototypage des récepteurs et réseau associé

L'équipement de réception se compose de matériels, de scripts et de logiciels. Le diagramme fonctionnel du système récepteur est illustré sur la Figure 3. L'équipement SDR Ettus USRP N200 est connecté au PC à l'aide d'un câble Ethernet. Il se compose d'un convertisseur analogique-numérique (ADC) à échantillonnage direct capable d'échantillonner jusqu'à 100 MHz, couplé à un FPGA qui assure le sous-échantillonnage et la conversion de fréquence. Le facteur de décimation maximum qui peut être utilisé pour la réduction de la bande de fréquence étudiée est de 512, ce qui correspond à une bande d'observation minimale de 195,3125 kHz. La carte fille Ettus LFRX peut accepter des signaux de DC à 30 MHz. Le boîtier Ettus USRP N200 est capable de filtrer, et de transposer le signal en bande de base. L'antenne HF active est alimentée par un bloc d'alimentation de 12 V par un coupleur directionnel. Le kit GPSDO permet l'horodatage des échantillons avec l'heure GPS GMT et la synchronisation de l'horloge du FPGA et de l'ADC. La précision du signal est de ± 50 ns. Le kit GPSDO permet à plusieurs USRP de synchroniser leurs captures avec la même référence temporelle quelle que soit la localisation des récepteurs.

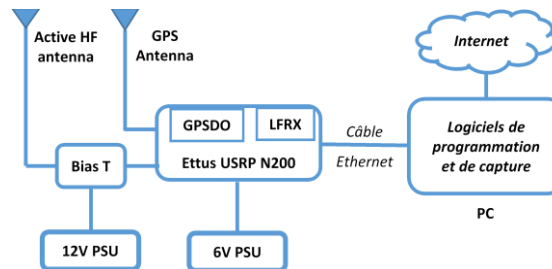


Figure 3 Diagramme fonctionnel du récepteur

La configuration matérielle est contrôlée par un ordinateur connecté par Ethernet. L'ordinateur se compose de plusieurs programmes qui sont utilisés pour planifier et capturer des données selon les besoins de l'utilisateur. Le schéma fonctionnel de la Figure 4 représente l'organisation de ces programmes. Les fichiers "Config" et "Start Stop" permettent à l'utilisateur de configurer l'heure de début et de fin pour la saisie des données, la durée de la capture, la fréquence centrale et le taux d'échantillonnage. L'ordonnancement des tâches est réalisé par un interpréteur Java. Il gère le lancement de scripts Python, qui assurent l'interface entre le matériel et le logiciel, selon le standard GNURadio. La capture génère deux fichiers : les fichiers DAT contiennent les échantillons complexes mesurés tandis que les fichiers HDR contiennent les métadonnées (base de temps, fréquence centrale, etc.). Le script de synchronisation fournit l'heure GPS à l'interpréteur de planification, ce qui permet de synchroniser régulièrement l'ordinateur avec l'horloge GPS pour s'assurer de la bonne exécution des travaux selon le calendrier programmé.

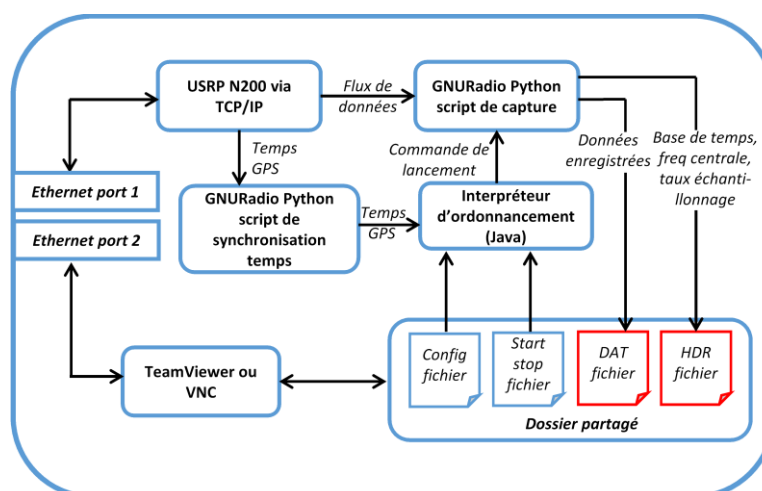


Figure 4 Diagramme des logiciels pour l'enregistrement des données

Quatre récepteurs synchronisés, contrôlables à distance et capables de faire des captures de signaux HF ont été mis en œuvre et déployés sur quatre sites différents. Ces sites sont situés à Brest (Rx₁), Bordeaux (Rx₂), Grenoble (Rx₃) et Lille (Rx₄) pour constituer un réseau TDoA distribué au niveau national. Ce réseau est contrôlé par une machine centrale positionnée à Brest. Il permet une capture synchronisée de signaux HF d'émetteurs situés partout dans le monde.

Afin d'évaluer le retard de signaux inconnus reçus par les récepteurs synchronisés du réseau, une nouvelle méthode nommée sondage inter-canal (*cross-channel sounding*) est maintenant proposée. Son principe et ses concepts sont expliqués dans le prochain paragraphe. Les équations mathématiques pour le sondage inter-canal et la validation de ses concepts au travers de mesures expérimentales sont expliquées dans le Chapitre 5 de la thèse. Des résultats expérimentaux préliminaires de géolocalisation HF sont aussi présentés dans ce chapitre.

Principe et concepts du sondage inter-canal (Cross-channel sounding)

Principe : Dans le cadre de la géolocalisation HF passive dans le domaine temporel, le temps d'émission et la forme du signal sont inconnus. Par conséquent, la durée de propagation ne peut pas être déterminée et donc la méthode ToA ne peut être utilisée. Par contre, la méthode TDoA peut être employée quand la différence de temps entre les réceptions à toutes les paires de récepteurs est connue.

Considérons le signal reçu au récepteur 1 (Rx₁) et récepteur 2 (Rx₂) comme étant respectivement $s_1(t)$ et $s_2(t)$. Ces signaux partagent la même origine qui est le signal émis $e(t)$ mais se sont propagés via différents canaux. Ces derniers sont caractérisés par les fonctions $h_1(\tau)$ and $h_2(\tau)$ respectivement pour la paire Tx-Rx₁ et Tx-Rx₂. Dans la réalité, ces signaux sont corrompus par du bruit aux récepteurs Rx₁ et Rx₂ qui affecte les performances à la détection. Ces bruits sont principalement générés par l'électronique des récepteurs et les rayonnements électromagnétiques parasites capturés par l'antenne de réception. Pour clarifier. Pour simplifier, nous ferons l'hypothèse que le sondage inter-canal s'effectue sous la condition d'un niveau SNR relativement élevé, permettant ainsi de négliger par la suite les termes dus au bruit. Par conséquent, les signaux reçus en Rx₁ et Rx₂ s'écrivent :

$$\begin{aligned} s_1(t) &= (e * h_1)(t) \\ s_2(t) &= (e * h_2)(t) \end{aligned} \quad (1)$$

La durée de propagation de chaque signal est capturée par les réponses impulsionnelles $h_1(\tau)$ and $h_2(\tau)$ sur chaque trajet. La méthode TDoA requiert l'application d'une procédure similaire à celle du sondage inter-canal classique pour retrouver cette information. Pour trouver les différences de durée de propagation des données récoltées à la réception, on peut évaluer la corrélation croisée $h_1(\tau)$ et $h_2(\tau)$. Cette procédure peut s'apparenter au sondage inter-canal qui requiert la corrélation croisée des signaux reçus $s_1(t)$ et $s_2(t)$, dénotée $R_{s_1s_2}(t)$:

$$R_{s_1s_2}(t) = (s_1 * s_2)(t) = ((e * h_1) * (e * h_2))(t) \quad (2)$$

L'équation (2) peut être simplifiée en utilisant les théorèmes de convolution et corrélation croisée :

$$R_{s_1s_2}(t) = (R_{ee} * R_{h_1h_2})(t) \quad (3)$$

où $R_{ee}(t)$ est la fonction d'autocorrélation du signal émis, $R_{h_1h_2}(t)$ est la fonction d'intercorrélation entre les réponses impulsionnelles des canaux. Cette dernière donne une estimation de la différence de temps de propagation entre les deux chemins. De l'équation (3), on peut observer que la nature du signal émis joue un rôle important en sondage inter-canal pour cette estimation. Plus précisément, l'intercorrélation entre les signaux reçus sera proche de l'intercorrélation entre les réponses impulsionnelles des canaux pourvu que l'autocorrélation des signaux transmis soit proche d'une impulsion étroite centrée à l'origine avec un large niveau de SNR.

Concepts : Plusieurs complications peuvent surgir lors de la sélection le pic d'intercorrélation qui correspond au retard entre l'arrivée de signaux à deux récepteurs synchronisés distincts, dépendant de la nature de la réponse des canaux. Supposons que ces deux canaux soient idéaux, mono-chemins et pour lesquels la propagation se produit via la couche F de l'ionosphère. La fonction d'intercorrélation des réponses impulsionnelles est représentée à la Figure 5 (a). Dans le cas d'un canal mono-chemin, le retard entre les signaux reçus peut être facilement évalué si le signal transmis possède de bonnes propriétés d'autocorrélation.

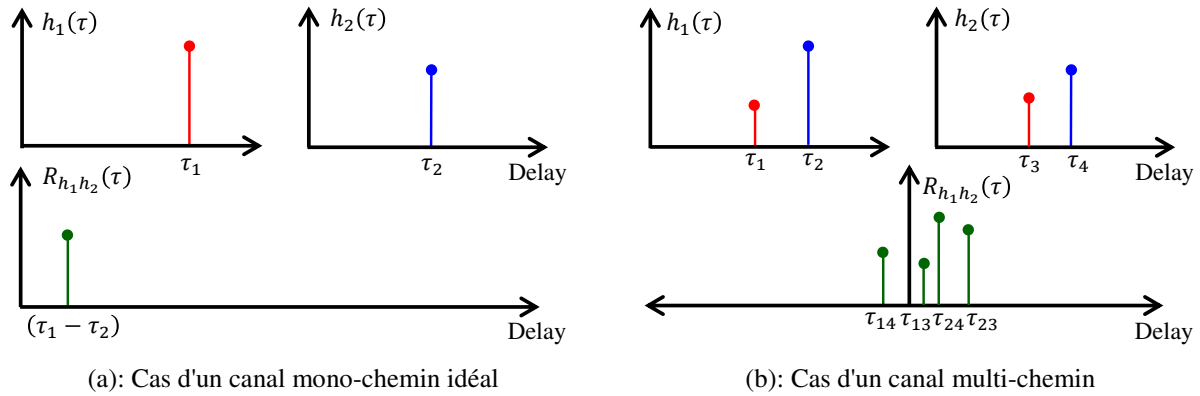


Figure 5 Fonction d'intercorrélation des réponses impulsionnelles de canaux. (a) Canal mono-chemin idéal. (b) Canal multi-chemin.

Ensuite, supposons que les deux canaux soient à chemins multiples pour lesquels la propagation se produit via la réflexion de deux couches différentes de l'ionosphère (par exemple, un de la couche E et l'autre de la couche F). La fonction d'intercorrélation pour ce cas multi-chemin est représentée à la Figure 5 (b). On remarque que dans ce cas la réponse possède plusieurs pics. Par conséquent, il devient difficile de sélectionner celui qui donnera le retard entre signaux reçus par les différents récepteurs, de façon précise. Nous suggérons de sélectionner le pic avec le niveau le plus élevé. Dans l'exemple de la Figure 5 (b), cela correspond au délai de signaux réfléchis par la couche F pour les deux chemins de propagation.

Une grande base de données de mesure a été collectée sur différentes phases, venant de différents radio-émetteurs localisés en Europe. Des détails sur la campagne de mesures et leur analyse statistique pour évaluer la performance de localisation et l'impact de différents paramètres sont donnés dans le paragraphe suivant. Les détails sur la campagne de mesures et une première analyse des données capturées peuvent être trouvés dans le Chapitre 6 de la thèse.

Campagne de mesures et analyse statistique

Un total de 22194 HF signaux radios a été capturés par intervalles de 5 secondes par les 4 récepteurs du réseau. Ils concernent 13 émetteurs HF localisés sur trois continents (Europe : 10, Asie : 2, Afrique : 1). La Figure 6 montre le placement de tous les récepteurs et des 11 émetteurs. La plupart des émetteurs sont placés à l'est du réseau de récepteurs. Plus précisément, ceux à Moosbrunn (MOS), Galbeni (GAL) and Tiganesti (TIG) sont à l'est, ceux de Cerrik (CER) et Emirler (EMR) au sud-est et celui de Nauen (NAU) au nord-est du réseau. Toutes les données ont été capturées lors de deux campagnes de mesures sur une période de 9 mois.

Maintenant, pour estimer la localisation des émetteurs des données capturées, il est nécessaire d'identifier si le signal contient des informations utiles ou du bruit. Dans le dernier cas, les données ne sont pas traitées. Pour déterminer l'utilité du signal capturé, on l'analyse selon différents critères tels que le niveau de bruit et une estimation des TDoA durant la capture. Il peut arriver que le niveau de bruit, du SNR dépendent du récepteur ou de l'émetteur, de la fréquence ou même d'une combinaison de ces paramètres. Basé sur ces résultats, nous pouvons qualifier une mesure pour un traitement à suivre ou l'exclure. Dans le dernier cas, on débouche sur une réduction des données.

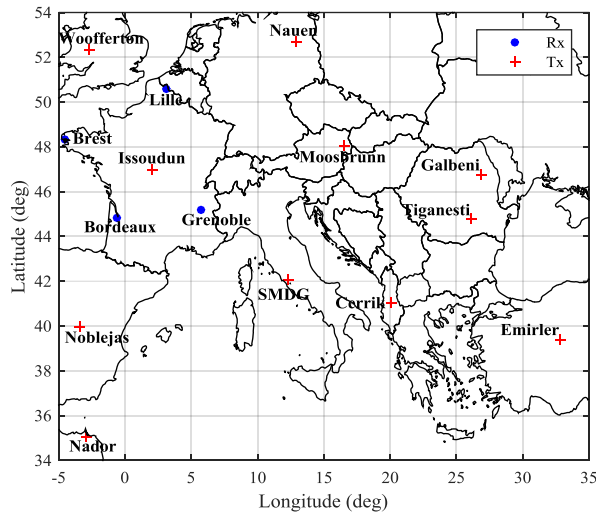


Figure 6 Situation géographique des 4 récepteurs déployés (points bleus) et des 11 émetteurs pour les campagnes de mesures (croix rouge).

En général, il a été trouvé qu'il était difficile de prendre la décision de considérer un signal pour une géolocalisation seulement sur l'analyse du bruit et du niveau de SNR. La raison est que beaucoup de signaux capturés ont des bas niveaux de SNR. De plus, la largeur bande du signal émis est inconnue ce qui rend le calcul du niveau de SNR à différents endroits difficile. Ensuite, l'analyse des TDoA basée sur un algorithme de probabilité statistique, nous a permis de voir l'évolution des TDoA dans le temps (observés sur l'ensemble des mois de mesures) et de ne considérer une valeur de TDoA comme valide seulement si elle tombe dans un certain intervalle autour de la valeur la plus probable. C'est une validation basée sur la répétition de la valeur estimée du TDoA dans le temps. Toutes les données capturées ont été traitées en utilisant l'algorithme de probabilité statistique et environ 35% des mesures a été trouvé avec une valeur consistante pouvant être considérée. Le reste des n'a pas été traité. Notons aussi que les mesures d'émetteurs placés à des distances de plus de 3500 Km étaient trop affectées par le bruit pour être considérées.

Les mesures sélectionnées étaient ensuite classées soit "valides" ou "invalides" sur la base de l'algorithme de sortie de la géolocalisation. La fonction CDF de l'erreur de géolocalisation en Km pour toutes les mesures validées de Cerrik, Nauen et Galbeni peuvent être vues respectivement dans la Figure 7 (a), (c) et (e). De façon similaire, la fonction CDF de l'erreur azimutale en degré pour toutes les mesures validées de Cerrik, Nauen et Galbeni sont illustrées respectivement dans la Figure 7 (b), (d) et (f). Les deux types d'erreur ont été calculés en prenant le récepteur de Bordeaux comme référence. Pour toutes les mesures validées de Cerrik, environ 10% des erreurs de géolocalisation est inférieure à 100 km tandis qu'environ 70% d'entre elles est inférieure à 5° en erreur azimutale. Dans le cas des mesures validées provenant de Nauen, environ 85% des erreurs de géolocalisation est inférieure à 100 Km, alors qu'environ 95% des erreurs azimutal est inférieure à 2°. Enfin, de toutes les mesures validées provenant de Galbeni, environ 7.5% donne une erreur de géolocalisation inférieure à 100 Km et environ 85% à l'erreur azimutale plus petite que 5°. Bien que la plupart des erreurs de géolocalisation soit large, l'erreur azimutale calculée pour la plupart des émetteurs est assez faible. L'erreur de géolocalisation peut être réduite de façon substantielle en augmentant le nombre de récepteurs, comme nous l'avons déjà vu plus haut.

A la fin de la thèse, le concept de résolution continue dans le temps des valeurs TDoA est expliqué et appliqué pour déterminer une surface de valeurs possibles de localisation plutôt qu'en estimer une seule. Cette surface prend la forme d'un hexagone irrégulier. Cette nouvelle approche peut résoudre les erreurs dues aux incertitudes sur les valeurs de TDoA (par exemple, l'identification difficile des différents pics due à la résolution temporelle limitée et l'erreur de quantification). L'utilisation de l'algorithme de résolution continue de valeurs, permet de déterminer les régions autour de la localisation réelle de l'émetteur. Il a été trouvé que la plupart des géolocalisations d'émetteurs estimée tombe dans la région déterminée avec l'algorithme

mentionné plus haut. On peut donc conclure que la dispersion des coordonnées GPS (autour de celles réelles de l'émetteur Tx) produit de larges erreurs de géolocalisation pour différents mesures qui sont dues au décalage aléatoire des valeurs TDoA calculées autour de la valeur réelle.

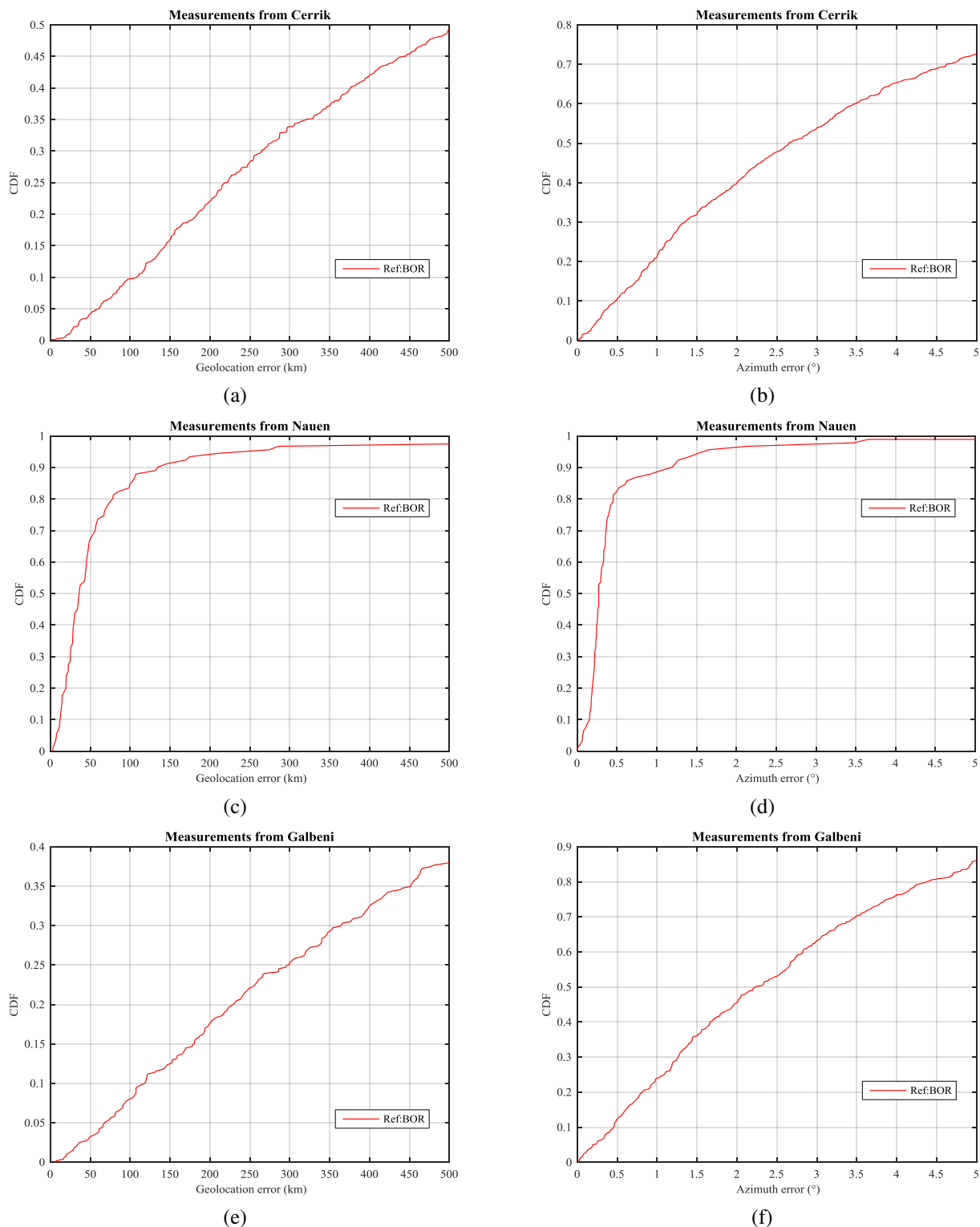


Figure 7 Fonctions CDF des erreurs de géolocalisation et azimutales pour toutes les mesures validées de différents émetteurs. Le récepteur de Bordeaux est utilisé comme référence. (a) et (b) Cerrick. (c) et (d) Nauen. (e) et (f) Galbeni.

Conclusions

Dans une première étape, l'algorithme de géolocalisation HF de méthodes dans le temps est présenté avec leur développement analytique. Concernant la géolocalisation HF passive, des résultats de simulation montrent qu'une disposition sur un carré des récepteurs donne des résultats de géolocalisation d'émetteurs avec la plus grande précision. Les simulations démontrent aussi que cette erreur est réduite de façon significative lorsque le nombre de récepteurs augmente.

Pour étudier la faisabilité d'un système réel de géolocalisation HF basé sur la méthode TDoA, le minimum de 4 récepteurs programmables et contrôlables à distance ont été mis en œuvre et déployés sur 4 différents sites en France pour former un système de réception pour la géolocalisation. Ce système est contrôlé par une station centrale située à Brest, dans les locaux d'IMT Atlantique. Par des mesures effectuées uniquement à Brest, les propriétés de corrélation des signaux ont été évaluées et il a été trouvé que des signaux d'émetteurs radios à modulation AM peuvent être utilisés pour une géolocalisation HF.

Pour estimer le temps de retard entre signaux capturés par les récepteurs synchronisés, une nouvelle méthode appelée "sondage inter-canal" est ensuite présentée. L'analyse des données capturées en juin 2017 de différents émetteurs en Europe est ensuite présentée. Des premiers résultats de mesure, il a été trouvé que sous des conditions favorables, les émetteurs HF pouvaient être localisés avec des erreurs relatives de 0,1 à 10 % par rapport à la position réelle. De plus, il a été observé que la direction azimutale des récepteurs pouvait être estimée avec une assez grande précision. Ces résultats préliminaires valident l'approche TDoA pour la géolocalisation HF d'émetteurs.

Un total de 22194 mesures de signaux émis par différents émetteurs HF situés en Europe, Asie et Afrique a été effectué. Ces données ont été traitées ensuite par un algorithme TDoA basé sur une analyse de probabilité statistique, qui permet de sélectionner les captures pouvant être utilisées pour la géolocalisation HF. De cette sélection, environ 30% des mesures validées venant des émetteurs (CER, GAL, TIG, NAU, SMDG and EMR) ont débouché sur des erreurs de localisation en dessous de 100 Km. Plus particulièrement, environ 75% des mesures validées de signaux venant de Nauen et SMDG ont conduit à des erreurs inférieures à 100 Km. On doit noter que les mesures ont été effectuées par le nombre minimum de récepteurs requis par l'approche TDoA (c'est-à-dire 4) et pourtant 80% d'entre elles validées sur tous les récepteurs ont donné des erreurs azimutales sur la direction d'émission inférieures à 5°. En général, les erreurs de géolocalisation estimées sur les données validées des différents émetteurs sont plus larges que celles prévues par les premiers résultats. Cependant, la distribution des localisations estimées remplit une région qui ressemble à une ellipse autour de la valeur réelle de l'emplacement de l'émetteur. Ces erreurs sont larges et dépendent de la configuration du réseau de récepteurs par rapport à la position de l'émetteur ainsi que de la sensibilité à la précision du temps de retard du système de géolocalisation TDoA. Elles peuvent être considérablement réduites en utilisant un nombre plus grand de récepteurs et en augmentant le temps de résolution du système de géolocalisation. Enfin, le concept de l'algorithme de résolution continue du TDoA est proposé. Il permet d'estimer une surface de localisations probables qu'une seule valeur. De cette façon, nous pouvons avoir une estimation grossière de la région qui contient l'émetteur détecté, sous la condition que l'estimation des valeurs TDoA soit assez précise.

Contents

Acknowledgement	vii
Sommaire de la thèse	ix
List of Figures	xxiii
List of Tables	xxix
List of Acronyms	xxxi
Chapter 1 Introduction	1
1.1 Context and research motivation	1
1.2 Related topics	2
1.3 Research goals	3
1.4 Thesis organization.....	3
Chapter 2 Overview of HF Radio Propagation and HF Direction Finding	5
2.1 Ionosphere	5
2.1.1 Sun and its appearance in different wavelengths.....	5
2.1.2 Formation of the ionosphere.....	7
2.1.3 Morphology of the ionosphere	8
2.1.4 Ionospheric parameters	9
2.1.4.1 Plasma and critical frequency	9
2.1.4.2 Total Electron Content (TEC).....	10
2.1.4.3 Ionogram.....	10
2.1.5 Ionospheric variations	12
2.1.5.1 Diurnal and seasonal variations	12
2.1.5.2 Geographical variations	12
2.1.5.3 Variations due solar activity	13
2.1.5.4 Sporadic E (E _s).....	14
2.2 HF radio propagation.....	15
2.2.1 Skywave propagation	16
2.2.2 Oblique propagation.....	17
2.2.3 Propagation modes	20
2.2.3.1 Ordinary and extraordinary modes.....	20
2.2.3.2 Geometric modes	20
2.2.3.3 Complex propagation modes	21
2.2.4 Factors affecting HF propagation.....	22
2.2.4.1 Multipath interference.....	22

2.2.4.2	Absorption	22
2.2.4.3	Noise	23
2.2.4.4	Fading in narrowband systems	23
2.2.5	HF communication predictions	24
2.3	HF direction finding and geolocation	24
2.3.1	HF DF techniques	25
2.3.1.1	Classical DF techniques	25
2.3.1.2	Beamforming	27
2.3.1.3	Superresolution DF	28
2.3.2	HF geolocation methods	29
2.3.2.1	Triangulation	30
2.3.2.2	Single site location (SSL)	30
2.3.2.3	Time of arrival (ToA)	31
2.3.2.4	Time difference of arrival (TDoA)	32
2.4	Conclusion	33
Chapter 3	Time-Domain HF Geolocation: Algorithm and Simulation Results	35
3.1	Ionospheric layer models	35
3.1.1	Simple models	35
3.1.1.1	Parabolic layer	35
3.1.1.2	QP layer	36
3.1.2	Composite models	40
3.2	HF geolocation algorithm	40
3.2.1	HF geolocation principle and assumptions	41
3.2.2	Mathematical approach: ToA	43
3.2.3	Mathematical approach: TDoA	44
3.2.3.1	Algorithm outputs and validation	45
3.3	Simulation results and analysis	47
3.3.1	Receiver positioning	47
3.3.1.1	ToA method	47
3.3.1.2	TDoA method	50
3.3.2	Number of receivers	53
3.3.2.1	ToA method	53
3.3.2.2	TDoA method	58
3.4	Conclusion	62
Chapter 4	HF Geolocation Receiver	63
4.1	HF receiver hardware	63
4.1.1	Software defined radio (SDR)	63
4.1.2	Receiving antenna and filter	64
4.1.3	Power supply	65

4.1.4	Computer system.....	66
4.1.5	Assembled hardware schematic and prototype.....	66
4.2	HF receiver software.....	66
4.2.1	Software development.....	67
4.2.1.1	Data acquisition parameters	67
4.2.1.2	Python scripts and Java scheduler.....	68
4.2.1.3	Remote connectivity	70
4.3	Operational TDoA receiver network.....	71
4.3.1	Site selection and description	71
4.3.2	HF broadcast transmitters.....	73
4.4	Signal processing.....	75
4.4.1	Correlation properties of the captured signal.....	76
4.4.2	Capture data length analysis.....	79
4.4.3	SNR impact on HF source geolocation accuracy	81
4.4.3.1	Received signal representation.....	81
4.4.3.2	Received signal modelling	82
4.4.3.3	Simulation results and analysis	83
4.5	Conclusion.....	85
Chapter 5	Cross-Channel Sounding Concepts and Preliminary Experimental Geolocation Results	87
5.1	Channel sounding	87
5.1.1	Channel representation.....	87
5.1.2	Principle	88
5.1.3	Frequency domain channel sounding	88
5.1.4	Time domain channel sounding	89
5.1.4.1	Correlation sounding example	90
5.2	Cross-channel sounding.....	91
5.2.1	Principle	91
5.2.2	Mathematical description	92
5.2.3	Single path channels.....	93
5.2.4	Multipath channels.....	93
5.3	TDoA estimation and identification of propagation modes	94
5.3.1	Case 1: Single path channels	95
5.3.2	Case 2: Combination of single and multipath channels.....	96
5.3.3	Case 3: Multipath channels	97
5.4	Preliminary geolocation results.....	99
5.4.1	Example: Favorable propagation conditions	100
5.4.2	Example: Moderate propagation conditions.....	101
5.4.3	Example: Geometric dilution of precision.....	101
5.4.4	Example: Effect of multipath propagation	102

5.4.5	Analysis of azimuthal vs. range error	103
5.5	Conclusion	106
Chapter 6	Large Scale Measurement Campaign: Statistical Analysis	109
6.1	Data set details	109
6.1.1	Measurement campaign 1	110
6.1.2	Measurement campaign 2	115
6.2	Measurement qualification metrics and data reduction	115
6.2.1	Noise analysis	116
6.2.2	SNR analysis	118
6.2.3	TDoA analysis using statistical likelihood algorithm	119
6.3	Data reduction statistics	122
6.4	Valid measurements statistical analysis	126
6.4.1	Geolocation in the case of sporadic E conditions	126
6.4.2	PDF of estimated reflection heights	129
6.4.3	Geolocation error vs estimated reflection height	130
6.4.4	Geolocation error vs received SNR	130
6.4.5	Estimated transmitters location in terms of GPS coordinates	131
6.4.6	Estimated geolocation and azimuth errors	132
6.5	Propagating TDoA uncertainty on geolocation output	135
6.5.1	Fixed resolution TDoA and continuous resolution TDoA	136
6.5.2	Measurement examples assuming a continuous resolution TDoA	138
6.6	Conclusion	141
	Conclusion	143
	Future work	147
	Appendix A: Minimum number of receivers required for HF geolocation using the TDoA method	149
	Appendix B: Processing of AM signal within SDR module	153
	Appendix C: Autocorrelation and cross-correlation of captured audio signal	157
	Appendix D: Study of geolocation error due to flat Earth assumption	159
	Bibliography	165
	List of Publications	173

List of Figures

Figure 1 Illustration d'une localisation HF avec l'hypothèse d'une ionosphère homogène et plate et d'une terre plate .	xi
Figure 2 Simulations de l'erreur de géolocalisation avec l'approche TDoA et un modèle de couche QP à hauteur fixe. (a) Distribution de l'erreur avec le nombre minimum de 4 récepteurs. (b) CDF de l'erreur pour différents nombres de récepteurs.....	xii
Figure 3 Diagramme fonctionnel du récepteur.....	xiii
Figure 4 Diagramme des logiciels pour l'enregistrement des données	xiii
Figure 5 Fonction d'intercorrélation des réponses impulsionnelles de canaux. (a) Canal mono-chemin idéal.....	xv
Figure 6 Situation géographique des 4 récepteurs déployés (points bleus) et des 11 émetteurs pour les campagnes de mesures (croix rouge).	xvi
Figure 7 Fonctions CDF des erreurs de géolocalisation et azimutales pour toutes les mesures validées de différents émetteurs. Le récepteur de Bordeaux est utilisé comme référence. (a) et (b) Cerrik. (c) et (d) Nauen. (e) et (f) Galbeni.	xvii
Figure 2.1 Sunspot number over the duration of last 13 years	6
Figure 2.2 Different portions of the sun (a) at different wavelengths, the sun seen (b) in white light, (c) in H_{α} light, and (d) in soft X-rays	6
Figure 2.3 Ionization distribution as a function of altitude in day and night ionosphere.....	9
Figure 2.4 Example of an ionogram captured by an ionospheric sounder.....	11
Figure 2.5 Example of diurnal variation of the E and F_2 layers	12
Figure 2.6 Geographical variations with respect to the latitude	13
Figure 2.7 Effect of sporadic E layer in the ionosphere	14
Figure 2.8 Different modes of HF propagation	15
Figure 2.9 Skywave paths for a fixed frequency wave with different elevation angles	16
Figure 2.10 Equivalent waves reflected obliquely and vertically at same real height real (B and B') and at same virtual height (A and A'), assuming the ionosphere and the earth to be flat.....	18
Figure 2.11 Transmission curves (blue color) for a distance of 2000 km at different operating frequencies superimposed on an ionogram (black color), assuming the ionosphere and the earth to be flat.....	19
Figure 2.12 Ionogram recorded in Dourbes	19
Figure 2.13 Different modes of ionospheric propagation.....	21
Figure 2.14 DF using Doppler shift of an antenna rotating around a circle	26
Figure 2.15 Beamforming using phase shifters.....	27
Figure 2.16 Array manifold for 3-antenna array	28
Figure 2.17 Schematic of triangulation principle.....	30
Figure 2.18 Geolocation using ToA method for 2D case.....	31
Figure 2.19 Geolocation using TDoA method for 2D case	32
Figure 3.1 Electron density profile of F_2 layer of the ionosphere using QP and parabolic layer models	36
Figure 3.2 HF link geometry for a QP ionospheric layer	37
Figure 3.3 Plots of ground distances at different values of F using QP layer model.....	38
Figure 3.4 Plots of group path distances at different values of F using QP layer model.....	39

Figure 3.5 Estimated median critical frequencies for E and F₂ layer of the ionosphere using all measured ionospheric parameters in March, 2016 at 2 different ionosondes in Europe, particularly at Pruhonice in Czech Republic (a) and at Chilton in England (b)..... 41

Figure 3.6 Plot of ground range versus group path for the case of flat and spherical Earth..... 42

Figure 3.7 Geometry of the HF localization principle assuming uniform single layer ionosphere 42

Figure 3.8 Location of all transmitters on the square grid..... 48

Figure 3.9 Geolocation errors and CDF's obtained using ToA method assuming a QP layer for different receiver configurations, receivers placed on a straight line in (a), at vertices of an equilateral triangle of 260-km side in (c), and at vertices of a larger equilateral triangle with 625-km side in (e) while their corresponding CDF's can be seen in (b), (d) and (f), respectively 49

Figure 3.10 Geolocation errors obtained using TDoA method assuming a QP layer for different receiver configurations, receivers configurations resembles approximately a straight line as seen in (a), isosceles triangle in (b), square in (c), rectangle in (d), circle in (e) and y-shape in (f)..... 51

Figure 3.11 Geolocation error obtained using ToA method with 4 receivers assuming a QP layer with a fixed height 54

Figure 3.12 CDF of geolocation error obtained using ToA method for different number of receivers assuming a fixed height QP layer 54

Figure 3.13 Geolocation error obtained using ToA method with 4 receivers assuming a QP layer with variable height following a gaussian distribution 55

Figure 3.14 CDF of geolocation error obtained using ToA method for different number of receivers assuming a QP layer with variable height following a gaussian distribution..... 56

Figure 3.15 Geolocation error obtained using ToA method with 4 receivers assuming a QP layer with variable height following a linear gradient across x and y direction of the square grid 56

Figure 3.16 CDF of geolocation error obtained using ToA method for different number of receivers assuming a QP layer with variable height following a linear gradient across both x and y direction of the square grid 57

Figure 3.17 Geolocation error obtained using TDoA method with 5 receivers assuming a QP layer with a fixed height 58

Figure 3.18 CDF of geolocation error obtained using TDoA method for different number of receivers assuming a QP layer with a fixed height 59

Figure 3.19 Geolocation error obtained using TDoA method with 5 receivers assuming a QP layer with variable height following a gaussian distribution 59

Figure 3.20 CDF of geolocation error obtained using TDoA method for different number of receivers assuming a QP layer with variable height following a gaussian distribution..... 60

Figure 3.21 Geolocation error obtained using TDoA method with 5 receivers assuming a QP layer with variable height following a linear gradient across both x and y direction of the square grid 60

Figure 3.22 CDF of geolocation error obtained using TDoA method for different number of receivers assuming a QP layer with variable height following a linear gradient across both x and y direction of the square grid 61

Figure 4.1 USRP N210 SDR box (left) and LFRX daughterboard (right) 64

Figure 4.2 GPSDO kit (left) and GPS antenna (right) for USRP N200/N210..... 64

Figure 4.3 Active receiving antenna 65

Figure 4.4 Coaxial low-pass filter 65

Figure 4.5 12 V DC power supply 65

Figure 4.6 Server and USRP N210 module placed within the box 66

Figure 4.7 Hardware schematic (left) and prototype (right) of the receiver setup..... 66

Figure 4.8 Software schematic for capturing signals using the receiver setup 67

Figure 4.9 24-hour cyclic reloading of the “config file”	68
Figure 4.10 Call window before the capture start time	69
Figure 4.11 Java scheduler algorithm flowchart	70
Figure 4.12 Antenna installed at the measurement location in Brest	72
Figure 4.13 Antenna installed in Bordeaux.....	72
Figure 4.14 Antenna deployed in Grenoble	72
Figure 4.15 Antenna installed at the measurement site in Lille	73
Figure 4.16 Receivers controlled via a centralized machine	73
Figure 4.17 GPS coordinates of HF receivers and transmitter sites	74
Figure 4.18 Antennas deployed in Brest prior to the actual deployment of the receiver setups in different cities	75
Figure 4.19 Representation of the captured HF radio signal at Brest from Galbeni, Romania in time domain (a) and power spectrum (b)	76
Figure 4.20 Schematic explaining the dataset on which autocorrelation and cross-correlation is evaluated.....	77
Figure 4.21 Autocorrelation of the captured speech signal in Brest.....	78
Figure 4.22 Cross-correlation of the captured speech signals in Brest represented over the full time scale in (a) and within a certain time range in (b)	79
Figure 4.23 Cross-correlation between broadcast signals captured at all receivers in Brest with a duration of 5-second, for Rx ₁ -Rx ₂ in (a), Rx ₁ -Rx ₃ in (b), Rx ₁ -Rx ₄ in (c), Rx ₂ -Rx ₃ in (d), Rx ₂ -Rx ₄ in (e) and Rx ₃ -Rx ₄ in (f)	80
Figure 4.24 Receiver and transmitter placements	82
Figure 4.25 Geolocation error as a function of SNR for different audio signals of fixed length plotted in (a) and mean geolocation error of the 20 audio signals plotted in (b).....	83
Figure 4.26 Geolocation error as a function of SNR for audio signals of varying lengths, true data plotted in (a) and data plotted after smoothing in (b)	84
Figure 4.27 Geolocation error as a function of SNR for different speech signals of fixed length plotted in (a) and mean geolocation error of all 10 speech signals plotted in (b)	84
Figure 4.28 Geolocation error as a function of SNR for speech signals of varying lengths, true data plotted in (a) and data plotted after smoothing in (b)	85
Figure 5.1 Representation of a CIR in the case of a single path ideal channel.....	88
Figure 5.2 Example of CIR measured on different HF links (Brest-Paris, Brest-Poitiers and Brest-Toulouse) using correlation sounding on 10 th March, 2015 at 10h00, frequency 8.06 MHz	90
Figure 5.3 Output of the CIRs cross-correlation for single path ideal channels.....	93
Figure 5.4 Output of the CIRs cross-correlation for multipath channels.....	94
Figure 5.5 Cross-channel sounding output for HF broadcast signals received simultaneously in Brest and Bordeaux from HF transmitter site in Nauen, Germany.....	96
Figure 5.6 Cross-channel sounding output for HF broadcast signals received simultaneously in Brest and Grenoble from HF transmitter site in Moosbrunn, Austria.....	97
Figure 5.7 Cross-channel sounding output for HF broadcast signals received simultaneously in Brest and Lille from HF transmitter site in Galbeni, Romania.....	98
Figure 5.8 HF signal captured in Grenoble from Nauen on 21 st July, 2017 at 19:19 UTC (a); TDoA estimates for HF signals captured in Brest-Grenoble (b), Bordeaux-Grenoble (c) and Lille-Grenoble (d)	100
Figure 5.9 Power spectrum of HF signal captured in Grenoble from SMDG on 18 th July at 16:12 UTC (a); TDoA estimates for HF signals captured in Brest-Grenoble (b), Bordeaux-Grenoble (c) and Lille-Grenoble (d).....	101

Figure 5.10 Geometric localization for HF transmitter situated in Moosbrunn (a) and Galbeni (b) using the TDoA method	102
Figure 5.11 TDoA estimate for HF signal captured in Bordeaux and Lille from Cerrik on 26 th July at 08:17 UTC..	103
Figure 5.12 Estimated and true geographic location of HF transmitters for different measurement examples	103
Figure 5.13 Estimated geographic locations for data captured from Moosbrunn on 27 th July, 2017	106
Figure 6.1 Actual geographic location of all receivers and 11 broadcast transmitters	109
Figure 6.2 Plots representing estimated noise floor as a function of the capture frequency for all signals received in Brest (a), Bordeaux (b), Grenoble (c), Lille (d)	117
Figure 6.3 Noise floor for all signals captured in Grenoble w.r.t different frequency bands	117
Figure 6.4 Estimated SNR for signals captured in Brest (a), Bordeaux (b), Grenoble (c) and Lille (d) from different HF transmitters assuming a signal bandwidth of 10 kHz.....	118
Figure 6.5 CDF curves for estimated SNR at different signal bandwidths of 10, 5 and 3 kHz for of all captured signals in Bordeaux from 3 different HF transmitters (CER, GAL & TIG).....	119
Figure 6.6 Plots representing the TDoA estimates between all signals received at BOR-GRE (a) and BOR-LIL (b) from Nauen along with their corresponding likelihood functions.....	120
Figure 6.7 Plots representing the TDoA estimates between all signals received at BRE-BOR (a) and BRE-LIL (b) from SMDG along with their corresponding likelihood functions.....	121
Figure 6.8 Plots representing the TDoA estimates between all signals received at BRE-BOR (a) and GRE-LIL (b) from Emirler along with their corresponding likelihood functions	122
Figure 6.9 Bar chart representing valid and invalid algorithm output for all the signals captured in different months from Cerrik in (a) and Galbeni in (b) assuming the receiver in Bordeaux as the reference.....	125
Figure 6.10 Bar chart representing algorithm validity with regards to different capture frequency bands assuming the receiver in Bordeaux as the reference	126
Figure 6.11 Skip distance computed using QP layer model at operational frequencies of the transmitter in SMDG and Nauen.....	127
Figure 6.12 Ionograms recorded in Rome (a) and Dourbes (b) on 18 th July at 16:00 UTC and 19:15:02 UTC, respectively	127
Figure 6.13 Estimated and actual geographic locations for all valid measurements from SMDG (a) and Nauen (b) in July, 2017.....	128
Figure 6.14 PDF curves representing the obtained reflection heights for all valid measurements from Emirler in (a), Cerrik in (b), Tiganesti in (c) and Galbeni in (d), considering each receiver as reference	129
Figure 6.15 Scatter plots of obtained geolocation errors as a function of estimated reflection heights for all valid measurements from Emirler in (a), Cerrik in (b), Tiganesti in (c) and Galbeni in (d), considering the receiver in Bordeaux as the reference	130
Figure 6.16 Scatter plots of the obtained geolocation errors vs the minimum SNR (least out of the signals received at 4 locations) for all valid measurements from Emirler in (a), Cerrik in (b), Tiganesti in (c) and Galbeni in (d), considering the receiver in Bordeaux as the reference	131
Figure 6.17 Estimated and actual geographic locations for all valid measurements with an estimated reflection height between 50 and 350 km from Emirler (a), Cerrik (b), Tiganesti (c) and Galbeni (d), assuming the receiver in Bordeaux as the reference	132
Figure 6.18 CDF's of geolocation errors for all valid measurements from Emirler (a), Cerrik (b), Nauen (c), SMDG (d), Tiganesti (e) and Galbeni (f), considering the receiver in Bordeaux as the reference	133
Figure 6.19 CDF's of absolute azimuth errors for all valid measurements from Emirler (a), Cerrik (b), Nauen (c), SMDG (d), Tiganesti (e) and Galbeni (f), considering the receiver in Bordeaux as the reference	134
Figure 6.20 Effect of time resolution on the estimation of TDoA.....	136
Figure 6.21 Geolocation output in terms of region computed over a certain time range.....	136

Figure 6.22 Rotated cube and its projection on a ground plane ($z = 0$) forming a hexagon 137

Figure 6.23 Diagrams of estimated regions around different transmitters ((a): Emirler, (b): Galbeni, (c): Cerrik, (d): Tiganesti) obtained from TDoA algorithm assuming a continuous resolution..... 138

Figure 6.24 Different measurement example from Galbeni and Cerrik representing the estimated region by considering a range around the estimated TDoA's in (a) and (b), respectively..... 139

Figure 6.25 Estimated geographic locations for all valid measurements with an estimated reflection height between 50 and 350 km from Galbeni (a) and Cerrik (c) superimposed on a theoretical hexagon obtained from a continuous TDoA resolution algorithm 140

Figure 6.26 Estimated geographic locations for all valid measurements with an estimated reflection height between 50 and 350 km from Galbeni (a) and Cerrik (b) superimposed on a theoretical hexagon obtained using Δt equal to 10 μs and 50 μs , respectively 140

List of Tables

Table 2.1 HF communication prediction steps.....	24
Table 2.2 Advantages and disadvantages of different classical DF techniques.....	25
Table 2.3 Range estimation using SSL method	30
Table 2.4 Comparison of different HF geolocation methods	33
Table 3.1 Geolocation accuracy evaluated using ToA method for different receiver configurations	50
Table 3.2 Percentage of a given geolocation accuracy evaluated using TDoA method for different receiver configurations	53
Table 3.3 Geolocation errors less than 50 km obtained using ToA method for different number of receivers assuming a QP layer with a fixed, gaussian distributed and linear gradient height of maximum ionization.....	57
Table 3.4 Geolocation errors less than 20 km obtained using TDoA method for different number of receivers assuming a QP layer with a fixed, gaussian distributed and linear gradient height of maximum ionization.....	61
Table 4.1 Great circle distance for different HF links.....	74
Table 4.2 Cross-correlation in terms of SNR for broadcast signals captured simultaneously by all 4 receivers in Brest with different durations.....	81
Table 5.1 Details of ionospheric conditions and the estimated theoretical TDoA for an example of single path channels	96
Table 5.2 Details of ionospheric conditions and the estimated theoretical TDoA values for an example of single and multipath channels	97
Table 5.3 Details of ionospheric conditions and the estimated theoretical TDoA for an example of multipath channels	98
Table 5.4 Summary of TDoA's obtained from measurements and simulations	99
Table 5.5 Summary of HF radio signals captured from different transmitters	99
Table 5.6 Geolocation and azimuth errors for HF radio signals captured from Galbeni, Romania on 17 th July, 2017	104
Table 5.7 Geolocation and azimuth errors for HF radio signals captured from SMDG, Italy on 18 th July, 2017	104
Table 5.8 Geolocation and azimuth errors for HF radio signals captured from Nauen, Germany on 21 st July, 2017	105
Table 5.9 Geolocation and azimuth errors for HF radio signals captured from Cerrik, Albania on 26 th July, 2017	105
Table 5.10 Geolocation and azimuth errors for HF radio signals captured from Moosbrunn, Austria on 27 th July, 2017	106
Table 6.1 GPS coordinates of HF broadcast transmitters.....	110
Table 6.2 Details of capture schedule from different HF transmitters during first phase of measurement campaign 1	111
Table 6.3 Details of capture schedule from different HF transmitters during second phase of measurement campaign 1	112
Table 6.4 Details of capture schedule from different HF transmitters during second phase of measurement campaign 1 (Continued).....	113
Table 6.5 Details of capture schedule from different HF transmitters during second phase of measurement campaign 1 (Continued).....	114
Table 6.6 Details of changed capture frequency and new capture during measurement campaign 2.....	115
Table 6.7 Shortwave broadcasting bands and the number of captures from each frequency band during both measurement campaigns	116
Table 6.8 Statistics for all measurements from Emirler based on the TDoA analysis and algorithm output	123

Table 6.9 Statistics for all measurements from Cerrik based on the TDoA analysis and algorithm output 123

Table 6.10 Statistics for all measurements from Galbeni based on the TDoA analysis and algorithm output 123

Table 6.11 Statistics for all measurements from Tiganesti based on the TDoA analysis and algorithm output 124

Table 6.12 Statistics for all measurements from Nauen based on the TDoA analysis and algorithm output 124

Table 6.13 Statistics for all measurements from SMDG based on the TDoA analysis and algorithm output 124

Table 6.14 Statistics for all measurements from Moosbrunn based on the TDoA analysis and algorithm output 125

Table 6.15 Number of qualified, rejected and unprocessed measurements 126

Table 6.16 Critical frequency of the sporadic E layer measured by the ionosonde located in Rome at 16:00 hours (UTC) [16] 128

Table 6.17 Critical frequency of the sporadic E layer measured by the ionosonde located in Dourbes at 19:15:02 (UTC) [16] 128

List of Acronyms

ADC	<i>Analog-To-Digital Converter</i>
ALF	<i>Absorption Limiting Frequency</i>
AM	<i>Amplitude Modulation</i>
AoA	<i>Angle Of Arrival</i>
CAoA	<i>Cone Angle Of Arrival</i>
CDF	<i>Cumulative Distribution Function</i>
CIC	<i>Cascaded Integrator-Comb</i>
CIF	<i>Channel Impulse Response</i>
CORDIC	<i>Coordinate Rotation Digital Computer</i>
DC	<i>Direct Current</i>
DDC	<i>Digital Down Converter</i>
DF	<i>Direction Finding</i>
DoA	<i>Direction Of Arrival</i>
DOP	<i>Dilution Of Precision</i>
EM	<i>Electromagnetic</i>
ESPRIT	<i>Estimation Of Signal Parameters via Rotational Invariance Techniques</i>
EUV	<i>Extreme Ultraviolet Light</i>
FM	<i>Frequency Modulation</i>
GALILEO	<i>Europe Global Navigation Satellite System</i>
GDOP	<i>Gemoetric Dilution Of Precision</i>
GLONASS	<i>Global Navigation Satellite System</i>
GMT	<i>Greenwich Mean Time</i>
GPS	<i>Global Positioning System</i>
GPSDO	<i>GPS Disciplined Oscillator</i>
HF	<i>High Frequency</i>
HFCC	<i>High Frequency Co-ordination Conference</i>
IEEE	<i>Institute Of Electrical And Electronics Engineers</i>
IRI	<i>International Reference Ionosphere</i>
ITU	<i>International Telecommunication Union</i>
LF	<i>Low Frequency</i>
LOP	<i>Line Of Position</i>
LORAN	<i>Long Range Navigation</i>
LOS	<i>Line-Of-Sight</i>
LPF	<i>Low Pass Filter</i>
LUF	<i>Least Usable Frequency</i>
MF	<i>Medium Frequency</i>

MIMO	<i>Multiple-Input Multiple-Output</i>
MUF	<i>Maximum Usable Frequency</i>
MUSIC	<i>Multiple Signal Classification</i>
NCO	<i>Numerically Controlled Oscillator</i>
NLOS	<i>Non-Line Of Sight</i>
NVIS	<i>Near Vertical Incidence Skywave</i>
OWF	<i>Optimum Working Frequency</i>
PCA	<i>Polar Cap Absorption</i>
PDF	<i>Probability Distribution Function</i>
POLAN	<i>Polynomial Analysis Program</i>
QP	<i>Quasi-Parabolic</i>
RF	<i>Radio Frequency</i>
SAGE	<i>Space Alternating Generalized Expectation Maximization</i>
SDR	<i>Software Defined Radio</i>
SID	<i>Sudden Ionospheric Disturbance</i>
SNR	<i>Signal-To-Noise Ratio</i>
SWF	<i>Short Wave Fadeout</i>
TD _{oA}	<i>Time Difference of Arrival</i>
TEC	<i>Total Electron Content</i>
ToA	<i>Time Of Arrival</i>
ToF	<i>Time Of Flight</i>
UHD	<i>Univeral Hardware Driver</i>
UHF	<i>Ultra-High Frequency</i>
ULA	<i>Uniform Linear Array</i>
USRP	<i>Universal Software Radio Peripheral</i>
UTC	<i>Coordinated Universal Time</i>
VLF	<i>Very Low Frequency</i>
VNA	<i>Vector Network Analyzer</i>
VOACAP	<i>Voice Of America Coverage Analysis Program</i>

Chapter 1 Introduction

This chapter explains the major objectives of the thesis. Section 1.1 explains the research motivation behind the subject of the thesis and its importance in the human society. In particular, the importance of geolocation is mentioned. In section 1.2, different topics related to the thesis are described. Specifically, the difference between active and passive geolocation is explained along with different examples. Different research activities with regards to the thesis subject were identified before the commencement of the thesis and are listed in section 1.3. Finally, the thesis outline and contributions are explained in section 1.4.

1.1 Context and research motivation

In the early 20th century, Guglielmo Marconi demonstrated that long distance wireless transmission was possible using radio signals. For the purpose of investigation, the radio signal was emitted from the transmission site located in Poldhu, Cornwall and received by an antenna of about 150 m placed in St. John's, Newfoundland. The distance of the transmission link was about 3500 km. In 1902, A. Kennelly and O. Heaviside suggested that an electronically conducting region in the atmosphere can explain the propagation of the signals at such a long distance [1]. Different experiments conducted by Edward Appleton between 1924 and 1927 led to the demonstration of existence of the ionosphere in the atmosphere. From theoretical perspective, it was later concluded that the ionized gases in the upper atmosphere are responsible for the refraction of signals in high frequency (HF) band (3-30 MHz). These refractions of the signals from the ionosphere enable long distance intercontinental communications which are not possible with other frequency bands.

With all technological advancement in the last 50 years, long-range HF communications can cover large geographical areas using lightweight, portable and cost-effective equipment. However, to achieve faster, reliable, secure and high data rate communication, there is a need of large bandwidths in modern communication systems. These are achieved by transmitting signals in higher frequency bands (i.e. UHF and other upper bands). Nevertheless, the robustness, ease of deployment and unique long-range capability of HF communications still explain the use of this technology in many applications.

The fact that long distance radio communication is possible using signals in the HF band makes it extremely viable for civil, humanitarian and military operations. Moreover, HF communication can also be used as a complement or fallback solution to satellite communication. In case of a natural disaster, HF communication systems can be rapidly deployed to convey information in the affected regions compared to other communication systems. Defense organizations all across the globe are largely interested in the HF band, with regards to the purpose of spectrum monitoring, surveillance and as back-up communication systems. These contexts might require the ability to find the location of the source of transmission, filtering valid signals from noise using advanced signal processing techniques and decoding information from the captured signals by identification of the signal type.

The subject of this thesis is to primarily study the detection of HF radio transmitters using passive geolocation methods. This detection could be particularly used in finding the location of an intruder in

military operations or even locating personnel during an emergency search and rescue operation. In addition, the detection system could be used in locating jammers and unknown sources of noise as well.

1.2 Related topics

Geolocation refers to finding the actual geographic location of an object by analyzing the received electromagnetic communication signals. Geolocation can be further classified into the following two types:

- Active geolocation
- Passive geolocation

Active geolocation: Active geolocation method consists of locating the source of the radio signal using a cooperative system i.e. source and the remote device communicates mono-directionally or bi-directionally. Radio navigation based on satellite (GPS, Galileo, GLONASS...) operates on the principle of active geolocation where the device to be localized (e.g. a cellular phone) uses a known signal transmitted by remote satellites. Similarly, ground based navigational systems (Decca, LORAN, Gee and Omega) which were operational until the last decade of the 20th century also worked on the principle of active geolocation. Another example of active localization is given by the indoor navigation systems based on fixed beacons. In the case of active geolocation, the source computes its own location with the help of the remote devices.

Passive geolocation: Passive geolocation method consists of detecting and locating an object or the source of an electromagnetic signal using a non-intrusive system i.e. without the source/object being able to detect the localization process [2]. In the case of passive geolocation, the source (i.e. target) location is estimated by processing its signal captured by multiple receivers. Passive and active radars are examples of passive geolocation. Passive radars are receivers which just listen to RF transmissions (ex. broadcast signals) and can determine the presence of a target. With multiple passive radars separated in space, one can find the location of the RF source using different localization techniques. In the case of active radars, an emitted radio signal is reflected from an object. Once the reflected signal (i.e. echo) is received by the radar system, the range at which an object is located is found by multiplying the estimated time-of-flight (ToF) with the speed of the radio signal.

Both active and passive geolocations could be achieved using different time and angular domain methods which are briefly explained in Chapter 2 (section 2.3).

Interestingly, two recent online blogs dated 28th June and 11th July, 2018 presented some experimental results of locating transmitters from different frequency bands (VLF, LF, MF and HF) using the time difference of arrival (TDoA) method based on KiwiSDR modules. The experimentation is carried using multiple public KiwiSDR modules which are located all around the world, predominantly in Europe and Asia. These KiwiSDR modules are GPS-enabled which allows synchronization among the distributed devices and also provides information about its own location. TDoA based direction finding is incorporated with all KiwiSDR modules. Thus, using public KiwiSDR modules or the web interface of KiwiSDR, one can try to estimate the source location. Transmissions from VLF, LF and MF bands could be located with higher accuracy as the signals propagate mostly through ground waves. In the case of HF band, radio propagation is mainly possible through ground wave and skywaves. In the case of ground waves, the transmitter location could be estimated but with skywaves, the task of locating the signal source is more complex and difficult to handle. Currently, the KiwiSDR receiver network is successful in estimating the transmitter location based on the TDoA computed from ground waves. More details about these KiwiSDR modules and different direction finding results can be found on the online blogs [3][4]. One must also note that this work came up during the last

phase of this thesis, confirming the current interest for passive geolocation based on a network of remote receivers. As a specific feature, however, the research in this thesis is dedicated towards the detection of HF transmitters which are located in the range of 500-4000 km from the receiver setups and at such ranges, HF radio signals arrive at the reception sites through skywaves.

1.3 Research goals

The following research questions were formulated before the start of the thesis:

- Analyzing the TDoA geolocation technique in order to propose improvements in its applications to ionospheric HF transmissions.
- Parametric simulation studies taking into account variations in the structure of the ionosphere and evaluating the impact of the number of receivers and receiver positioning on the geolocation accuracy of the HF transmitters.
- Development of multiple demonstrators based on software defined radio (SDR) modules which are capable of capturing HF radio signals synchronously.
- Analysis of the collected experimental measurements to recognize the different parameters to be considered in a real-time operational TDoA based HF geolocation system.

1.4 Thesis organization

Following the introduction of Chapter 1 which includes the motivation and objectives for the thesis, there are five more chapters.

Chapter 2 explains the current state of the art related to the thesis and the background necessary to understand the further chapters. In particular, the ionosphere, principles of HF radio propagation and various HF direction finding (DF) and HF geolocation techniques are explained in detail. The citations in this chapter serve as an extensive information center for HF radio propagation through skywaves and HF DF.

Chapter 3 presents the time-domain HF geolocation algorithm along with simulation results. This HF geolocation algorithm could be used to estimate the location of the source of radio signals that propagate through non-line-of-sight (NLOS) mode (i.e. HF propagation through skywaves). It is different from the available localization algorithms in the literature which assume that signals propagate through line-of sight (LOS) mode. Simulation results provide a better understanding of the HF geolocation accuracy with respect to the number of receivers and the positioning of the receivers.

Chapter 4 describes the design (hardware and software) of the developed HF receiver prototypes. These are designed using software defined radio (SDR) modules and deployed in different cities across France to form a nationwide HF receiver network. In addition, these prototypes are synchronized with the GPS clock and can be controlled from a remote location. The properties of HF radio signals captured using the deployed receiver network are evaluated and discussed in detail.

Chapter 5 proposes a method termed as “cross-channel sounding” which is used to evaluate the propagation duration difference of an unknown signal captured by 2 distinct synchronized receivers. Different concepts related to propagation channels are also explained in the context of the cross-channel sounding output. These concepts are validated using experimental measurements and data available from different ionosondes

located all around Europe. Initial HF geolocation results from different HF transmitters are presented and discussed.

Data are captured by the receiver network from different HF broadcasters around Europe in different measurement campaigns. Chapter 6 provides the statistical analysis of all measurements with respect to several parameters associated with the geolocation performance of the system. More specifically, investigation of measurements with regards to the received noise level, SNR level, TDoA accuracy, capture frequency, propagation conditions and geolocation errors in terms of distance are presented.

Chapter 2 Overview of HF Radio Propagation and HF Direction Finding

This chapter provides an overview of HF radio propagation and different techniques present in the literature to perform HF geolocation. Firstly, the formation of the ionosphere along with its morphology and different ionospheric variations are explained briefly in section 2.1. In section 2.2, HF radio propagation and the various factors affecting it are described. Section 2.3 explains about the different HF geolocation methods which are further classified into angular domain and time-domain methods. The principle of time of arrival (ToA) and time difference of arrival (TDoA) methods are detailed.

2.1 Ionosphere

The ionosphere is a highly stratified medium which is formed when extreme ultraviolet (EUV) light from the sun ionizes the neutral atoms present in the Earth's atmosphere, thus releasing free electrons. In the context of radio waves, the ionosphere can be seen as plasma with varying electron density which is present in the Earth's atmosphere from a height of about 50 km to around 1000 km [5]. In the context of radio transmission, the ionosphere is one of the most important layers of the Earth's atmosphere as it reflects HF radio waves and enables HF communication.

2.1.1 Sun and its appearance in different wavelengths

The sun is a star located at the centre of the solar system having a radius of about 7×10^5 km which is over 100 times that of the Earth, and a mass of 20×10^{30} kg which is over 300,000 times that of the Earth. The sun has a major impact on the ionosphere, as the ionospheric electron density is related to solar activity. In extreme cases, sudden ionospheric disturbances can disrupt HF communications. The structure of the sun and its appearances in different wavelengths are presented in Figure 2.2 [6].

The portion of the sun that is seen in white light is known as the photosphere. The photosphere is 500 km thick and has a temperature of about 6000 °C. The image of sun in white light is presented in (b) of Figure 2.2. The small dark spots seen in the figure are known as sunspots. Sunspots are temporary and may occur in groups or by themselves. Sunspots normally have a temperature of around 4000 °C and since they are cooler than the surrounding photosphere they appear dark. The number of sunspots present on the surface of the sun at any time can be used to predict the sun effect on the ionosphere. Large sunspots and sunspot groups are visible through naked eyes. The sunspot number [5] is calculated by equation 2.1:

$$R = (10g + f) \tag{2.1}$$

where R is the sunspot number, g is the number of sunspot groups, f is the number of individual spots. From equation 2.1, it is clear that a sunspot group is 10 times as important as that of an individual spot. Also, the sunspot number is a measure of magnetic field influence on the sun's surface and it almost corresponds to the ionization of the ionosphere. The sunspot number is obtained from astronomical observations and the international sunspot number data is available online [7]. Also, the real-time sunspot number and the 12-month mean running monthly sunspot number are available on the DIAS webserver [8][9]. The sunspot number varies (i.e. increases or decreases) with respect to time approximately every 11 years and it is

referred to as solar cycle. Solar maximum is the period in which there is highest solar activity during the solar cycle and the sunspot number is the highest. Solar minimum is the period of the 11-year cycle in which there is least solar activity. Figure 2.1 presents the international sunspot number for the last 13 years [7].

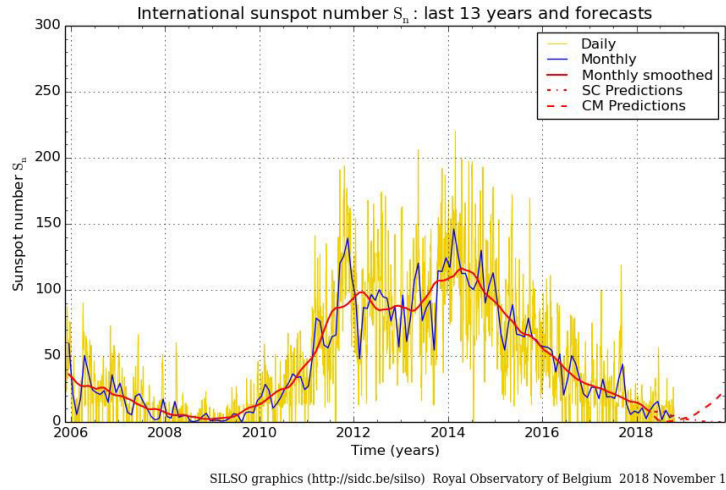
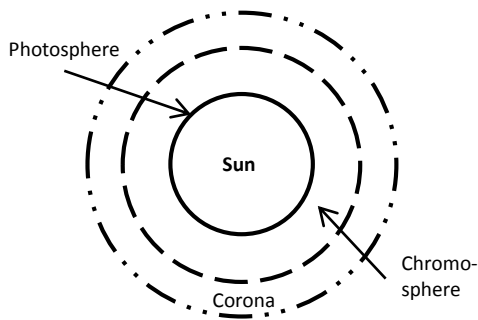
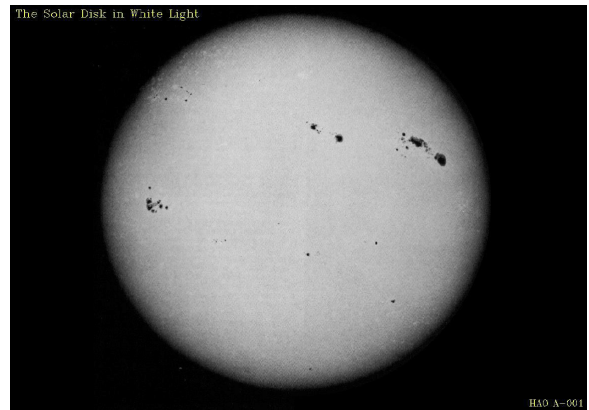


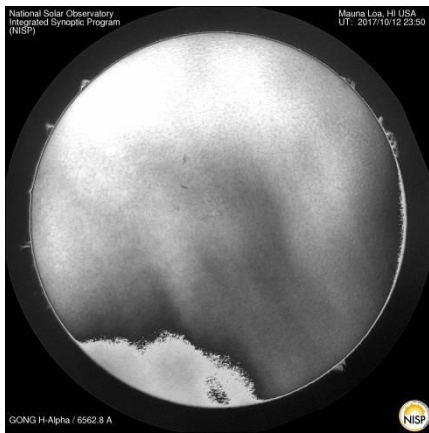
Figure 2.1 Sunspot number over the duration of last 13 years



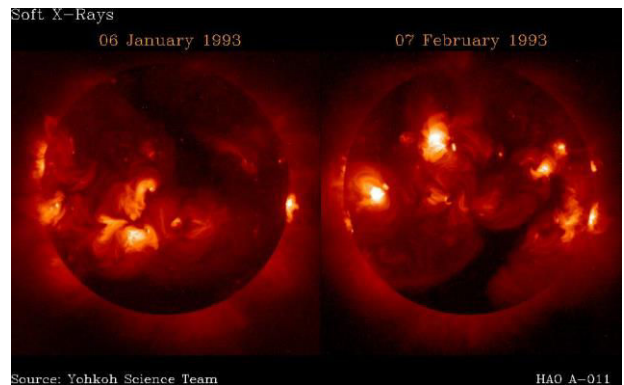
(a)



(b)



(c)



(d)

Figure 2.2 Different portions of the sun (a) at different wavelengths, the sun seen (b) in white light, (c) in H_α light, and (d) in soft X-rays

H_{α} lies in the red part of visible spectrum and has a wavelength of 656.3 nm. It corresponds to one of the spectral lines emitted by hydrogen. The portion of the sun that is seen in H_{α} is known as chromosphere. The part (c) of Figure 2.2 represents the sun in H_{α} light and the image was taken by NSO's GONG (Global Oscillation Network Group) instrument at Mauna Loa. The chromosphere is about 3000 km thick and lies directly above the photosphere as seen in (a) of Figure 2.2. Some of the important features such as plages, sunspots, prominences and filaments can be seen at the H_{α} wavelength. Plages are irregular in shape and large bright areas sometimes associated with the sunspots. Sunspots are usually present in the sun's lower atmosphere than the chromosphere and thus hidden by the overlying chromosphere. So sunspots which are seen in H_{α} are usually big spots. Plages emit huge amount of extreme ultraviolet (EUV) light which in turns leads to the formation of ionosphere and facilitate HF radio propagation. The region containing both plages and sunspots are known as active regions. Plages when observed using white light are known as faculae. A prominence is a large cloud of relatively cool gas which is suspended above the surface of the sun by magnetic fields which restrains it from falling down [10]. The cloud of gas appears bright when seen against a dark background and is known as prominence. The same cloud appears dark when seen against face of the sun as it is relatively cooler and is known as filament. Filaments are stable but sometimes it suddenly erupts and pushes solar matter into the space. When such cloud hits the surface of Earth, it can affect the earth's magnetic field and the ionosphere. Synthesized real-time images of sun in white light and H_{α} wavelength are available online [11].

The portion of the sun that is seen at EUV and X-rays wavelengths is known as corona. The corona covers the chromosphere as seen in (a) of Figure 2.2. The image of the sun as seen in the soft X-ray range is presented in (d) of Figure 2.2. The corona can be easily seen at very short wavelengths. The temperature of the corona is about 2 million °C and therefore it emits huge amounts of energy at EUV and X-ray wavelengths. At these wavelengths, the cooler photosphere does not emit energy and the corona appears brighter. Sometimes the X-ray image of sun appears to be very bright which is short lived, sudden and this resembles a solar flare. The X-ray brightness of a flaring active region is often higher than the total X-ray brightness of the rest of the sun. The very dark regions that can be seen near the south poles in (d) represent the coronal holes. The corona being relatively cool, dark areas stretch towards the equator from either side of the poles and it results in the formation of coronal holes. Coronal holes affect the ionosphere as they are sources of charged particles. Coronal holes are normally located above the solar poles but sometimes may extend down to lower latitudes.

2.1.2 Formation of the ionosphere

The ionosphere is a part of Earth's atmosphere where ions exist. EUV light is highly energetic; when a bundle of EUV light from the sun hits any neutral atom in the atmosphere, energy is transferred from the EUV light to an electron in the neutral atom. Since the electron now has energy, it separates from the atom and moves around freely. The neutral atom is positively charged now and is known as a positive ion. Thus photo-ionization is a phenomenon in which a photon (bundle of EUV light) removes an electron from a neutral atom, leaving behind a positive ion. It is the free electrons present in the ionosphere which are responsible for the refraction (i.e. bent) of HF radio waves. The positive and negative ions are bulky, approximately over 20000 times heavier than electrons and thus, cannot respond to the oscillations that are produced by radio waves.

Recombination is a phenomenon in which an electron and positive ion combine to form a neutral atom. Recombination is the reverse case of photo-ionization. In the higher regions of the ionosphere, electrons are mainly lost due to recombination. Attachment is a phenomenon in which electrons are again lost in the lower region of the ionosphere by combining to neutral atoms and thus forming negatively charged ions. Electron

density decreases by recombination and attachment process. However, the rate at which electron density decreases depends on the number of neutral molecules present at the altitude taken into consideration. As the altitude increases, the number of neutral molecules in the atmosphere decreases. Thus, recombination is less effective at higher altitudes. Recombination and attachment occur throughout the day in all the regions of the ionosphere whereas, photo-ionization occurs only when the sun is present during the day. The number of electrons present in the ionosphere is the difference between photo-ionization, recombination and attachment processes. The electron density is the greatest during the middle of the day as photoionization is also at the peak due to the sun. Electron density decreases from around sunset until the next morning when again the electron density starts increasing. As recombination is less effective at higher altitudes, the ionosphere can be used for HF communications during night also. The density of electrons in the ionosphere is the highest at some altitude because the density of neutral atmosphere decreases as the altitude increases and the intensity of EUV light from the sun increases with the altitude. Due to this opposing behavior between the neutral atmosphere and the intensity of EUV radiation from the sun, the electron density of a given ionospheric layer is a convex function of the altitude: first increasing from zero to a maximum electron density, then again decreasing down to zero. Since the atmosphere is composed of different gases present at different altitudes (such as nitrogen, oxygen etc.), the ionosphere consists of four different layers at different altitudes.

2.1.3 Morphology of the ionosphere

The ionosphere is an upper portion of earth atmosphere extending from a height of about 50 km to 1000 km above the surface of the Earth. There are free electrons in the ionosphere generated due to photo-ionization which causes the HF radio waves to be refracted (bent) from different layers of the ionosphere back to the surface of the Earth. Figure 2.3 shows a typical variation of electron density with respect to the altitudes during the day and night in the ionosphere [12]. During the day time, ionosphere consists of 4 layers which are referred as D, E, F_1 and F_2 layers in the order of increasing altitude.

The D layer is present in between 50 to 80 km above the surface of the Earth. The electron density is the lowest in the D layer of the ionosphere. It is mainly responsible for the attenuation of the HF radio waves due to the higher density of atmospheric particles. The absorption or the attenuation of the signal reduces as the frequency of the signal increases.

The E layer lies from about 80 to 150 km above the surface of the Earth. The electron density in this layer is higher than the D layer and it refracts HF radio waves. There is another layer referred to as sporadic E (E_s) layer which consists of a cloud of electrons from which it acts as a reflecting layer in the ionosphere and is formed in the E layer anytime during the day or night. E_s is a temporary layer and is explained in detail in section 2.1.5.4.

During the day time, the F region is split into F_1 and F_2 layer which lies from about 150 to 210 km and above 210 km from the Earth's surface, respectively. On the contrary, during the night time, only the F_2 layer exists in the ionosphere which is available for HF communication. During the night time, recombination is higher than photo-ionization. Thus, other layers (i.e. D, E and F_1) are depleted of free electrons and they completely disappear whereas the F_2 layer still consists of free electrons which decrease over the course of the night. The F_2 layer is sometimes referred as the F layer; it is the most important layer in the ionosphere in terms of HF radio propagation. The height ranges for F_2 layer is also the highest which allows large communication paths. The electron density is also the highest in the F_2 layer, thus allowing the reflection of the highest frequencies in the HF range.

International Reference Ionosphere (IRI) provides monthly averages of the electron density, electron temperature, ion temperature, and ion composition in the ionospheric altitude range [13].

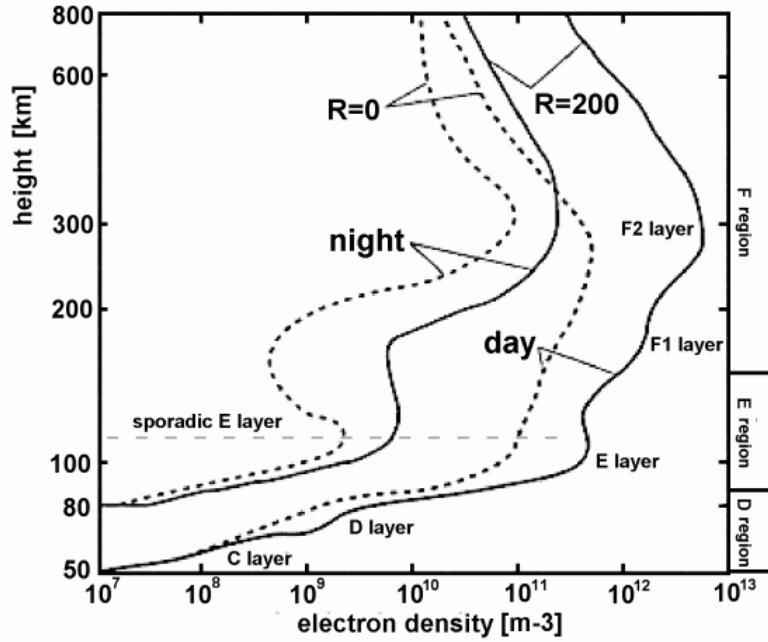


Figure 2.3 Ionization distribution as a function of altitude in day and night ionosphere

2.1.4 Ionospheric parameters

This section explains different parameters of the ionosphere, namely plasma frequency (f_N), critical frequency (f_c) and total electron content (TEC). The operation of the ionosonde used to generate an ionogram and different types of ionograms are also explained.

2.1.4.1 Plasma and critical frequency

The positive ions and the electrons present in the plasma oscillate to and fro in simple harmonic motion at an angular frequency (ω) which is given by the following equation:

$$\omega^2 = \frac{N \times e^2}{\epsilon_0 \times m} \quad 2.2$$

where N is the electron density in electrons/m³, e is the electron charge in coulombs, ϵ_0 is free space permittivity in Farad/meter and m is the mass of an electron in kg. The plasma frequency in Hz is defined as follows:

$$f_N = \frac{\omega}{2\pi} \quad 2.3$$

After substituting all the atomic constants in equation 2.2, the plasma frequency is reduced to the following:

$$f_N^2 = 80.6N \quad 2.4$$

Every layer in the ionosphere which reflects HF radio waves has a critical frequency. The critical frequency of a layer is defined as the maximum frequency which can be reflected from that layer at vertical incidence. The critical frequency of any particular layer is associated with the maximum electron density in that layer which is obtained from equation 2.4 and is approximately equal to the following equation:

$$f_c \approx 9 \times 10^{-6} \times \sqrt{N} \quad 2.5$$

The critical frequency obtained from equation 2.5 has units of MHz, provided N has units of electrons/m³. There is a critical frequency for each layer denoted by f_0E for the E layer, f_0F_1 for the F₁ layer and f_0F_2 for the F₂ layer. HF radio waves higher than the critical frequency of a specific layer will simply penetrate the layer. The critical frequency of the F₂ layer (f_0F_2) is the highest since the electron density is the greatest in this layer. As it can reflect higher frequency, it is more suitable to long distance communication.

2.1.4.2 Total Electron Content (TEC)

The number of electrons present on the path between a transmitter and receiver is known as total electron content. It is measured in terms of electrons present per square metre. The total electron content in the ionosphere depends on factors like geography (latitude and longitude), season, solar cycle, local time and geomagnetic conditions. The radio wave passes through the ionosphere and the velocity of the radio waves decreases due to electrons present in the ionosphere. Thus, the radio wave propagating through the ionosphere experiences a delay. The total delay depends on the frequency of the radio wave and the TEC between the transmitter and receiver. The ionospheric slab thickness (τ) is defined as the ratio between the total electron content (TEC) and the F₂ layer peak electron density (N_mF_2). Alternatively, τ is the depth of an idealized ionosphere which has the same electron content as the actual ionosphere but uniform electron density equal to the maximum electron density of the actual ionosphere [14]. TEC is expressed in terms of critical frequency of the F₂ layer and ionospheric slab thickness (τ) which is given by the following equation:

$$\text{TEC} = 1.24 \times 10^{-6} \times \tau \times (f_0F_2)^2 \quad 2.6$$

where TEC is measured in TEC units (1 TECU = 10¹⁶ electrons/m²), f_0F_2 is the critical frequency of the F₂ layer in MHz and the slab thickness (τ) is expressed in meters. The analysis of TEC measurements and $(f_0F_2)^2$ values demonstrates that there is high correlation between both ionospheric characteristics. In addition, correlation coefficients are normally greater than 0.8 when diurnal (median or daily) values are correlated [15].

2.1.4.3 Ionogram

In order to find the virtual height of the ionosphere, the most widely used equipment is an ionosonde. The virtual height is calculated by measuring the time difference between the vertically upward transmitted signal and the received signal, and multiplying it with the speed of light. The signal transmitted is a special signal so that it can be recognized at the receiver. An ionosonde generates an ionogram which is a plot of virtual height versus operating frequency. An ionosonde is a high-frequency radar which sends out pulses with short duration vertically into the ionosphere. If the frequency is high, the pulses are reflected from the higher layers of the ionosphere. The ionosonde captures the time difference between the transmission and reception of the pulses over a range of various frequencies. Then, knowing the speed of light, the virtual height is calculated and the ionogram is obtained. Radio waves reflected from the E layer in the ionosphere has shorter time delay as compared to the waves reflected from the F₁ and F₂ layers.

There are mainly 3 different types of ionograms namely,

- *Vertical incidence* (VI) ionograms in which the transmitting and receiving devices are situated at the same location.
- *Oblique incidence* (OI) ionograms in which the transmitting and receiving devices are separated by long distances and the signal is received by the receiving device on the ground.

- *Backscatter* (BS) ionograms in which the transmitting and receiving devices are close to each other but the signals reach the receiving device after being scattered back from surface of the Earth or from the ionosphere.

There are some sounders available for which, frequency measurements are quite accurate and use the advantages of digital techniques. The signals are basically combined using stable oscillators providing precise frequency measurements. The NOAA/HF sounder, the digisonde, the IPS-42 sounder and the chirp sounder can be used to obtain ionograms and different parameters related to the ionosphere [5].

The sounders operate in 3 different modes:

- *Ionogram* (I) mode in which there is high frequency resolution at the cost of bad time resolution.
- *Kinesonde* (K) mode in which there is high time resolution but only on a few radio frequencies.
- *Basic or intermediate* (B) mode is a combination of both modes which has adequate frequency resolution and time resolution for an ionogram.

In order to obtain the electron density profiles from the ionograms, accounting for the Earth's magnetic field, one can use the Polynomial Analysis Program (POLAN) developed in 1985 by Titheridge [5].

Figure 2.4 shows an ionogram which is a plot of range (i.e. virtual height in km) versus frequency (MHz). Due to magnetoionic splitting, we have two possible waves: ordinary and extraordinary waves which can be seen in the ionogram. The f_oF_2 and f_xF_2 represent the critical frequencies of the F_2 layers in terms of ordinary and extraordinary waves, respectively. As seen in Figure 2.4, it is clear that extraordinary wave in the F_2 layer is reflected at higher frequency than the ordinary wave in the same layer, the reason being the presence of the magnetic field. The ordinary and extraordinary wave is further explained in section 2.2.3.1.

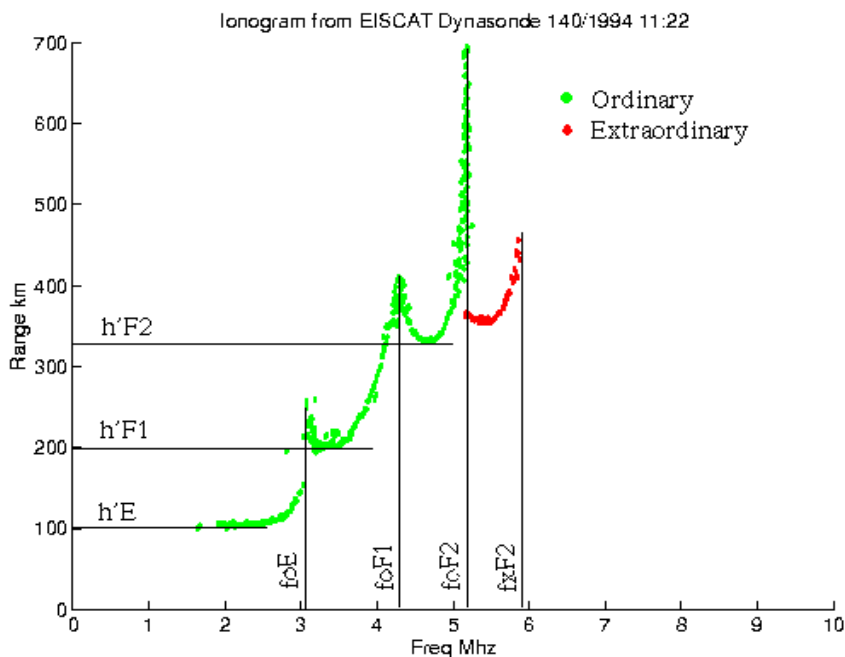


Figure 2.4 Example of an ionogram captured by an ionospheric sounder

2.1.5 Ionospheric variations

The formation of the ionosphere is largely dependent on the sun. As mentioned before, it varies largely with time of the day, season, geographic location and solar activity of the sun. HF propagation conditions can be predicted with higher accuracy if the ionospheric variations are known.

2.1.5.1 Diurnal and seasonal variations

Diurnal variations of the ionosphere mainly depend on the sun. As the sun is present during the day time, it results in higher ionization and more electrons are produced. Figure 2.5 shows the diurnal variations of the E and F₂ layers for the whole month of March 2016 at Chilton, United Kingdom. The data available for the ionosonde in Chilton [16] is downloaded and median critical frequencies are plotted over the course of different times in the day for the whole month. The critical frequency is the highest during noon for both layers. As seen in Figure 2.5, communication is only possible through the F₂ layer during the night hours as the E layer disappears due to the loss of electrons by the process of recombination and attachment. The frequency for the F₂ layer decreases gradually over the course of the night and is at minimum just before the sun rises.

As already mentioned, the ionization in the ionosphere depends on the sun; hence the critical frequencies of different layers in the ionosphere during summer should be higher than those in winter. This is the case with the E layer of the ionosphere. Also, the critical frequency of the F₂ layer at night during summer is higher than in winter. But the critical frequency of the F₂ layer at mid latitudes at noon is higher in winter than in summer season. This is known as the seasonal anomaly. A model to obtain the ionospheric characteristics using long term ionospheric data and predicted sunspot number is explained in a report by ITU [17].

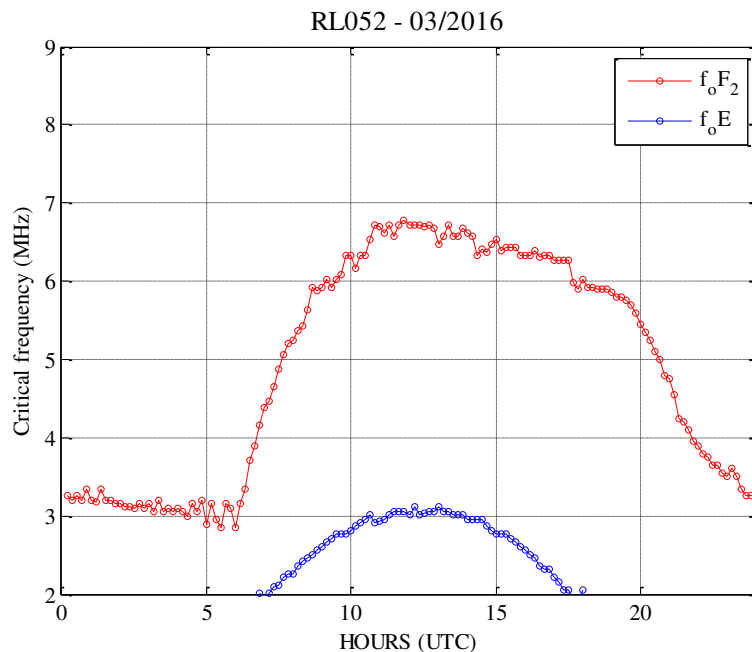


Figure 2.5 Example of diurnal variation of the E and F₂ layers

2.1.5.2 Geographical variations

Figure 2.6 shows an example of the latitude variations of the E and F₂ layer during day hemisphere (noon) and night hemisphere (midnight) between pole and equator at one particular longitude [18].

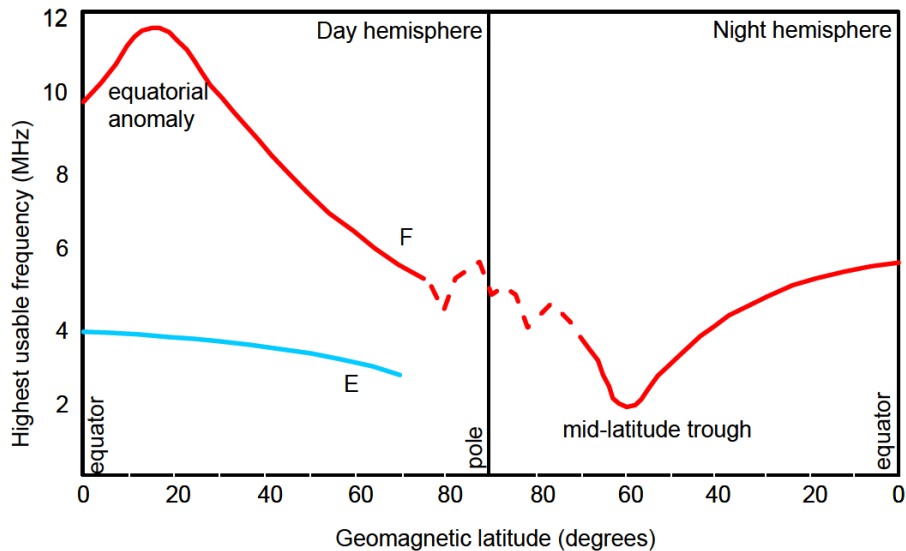


Figure 2.6 Geographical variations with respect to the latitude

As seen in Figure 2.6, frequencies supported at the equator are much higher than in other regions. The intensity of solar radiation decreases with increasing latitudes as it hits the atmosphere more obliquely as latitude increases. Thus, the critical frequencies for HF propagation decrease as latitude increases. The latitude variations are present in the F layer for the whole night due to action of upper atmospheric wind currents for the whole day. During the day hemisphere around the poles, reflection of HF radio waves is not possible using the E region. During the day hemisphere, the F₂ layer has the highest critical frequency approximately 15-20° north and south of the equator. This is known as equatorial anomaly which is the result of fountain effect caused by interaction of electric currents and magnetic field near the equator. During the night hemisphere at around 60° latitude north and south of the equator, frequencies which can be used for HF propagation has the minimum value. This is known as mid-latitude trough. The ionosphere near the poles is very dynamic since they receive input energy from the solar winds which are quite variable. The frequencies near the equatorial anomaly and mid-latitude trough changes drastically, so for communication around the equator during the day and around 60° latitude in night, one must be aware of these characteristics.

2.1.5.3 Variations due solar activity

During solar maximum, there is a large amount of active regions on the surface of the sun which results in higher levels of solar activity. Thus, we have more photo-ionization resulting in larger number of electrons which allows the use of higher frequencies. Under the same condition, the critical frequency is the highest for the F₂ layer, followed by the F₁ and the E layer. Also, radio wave attenuation is lower if higher frequencies are used. On the other hand, during solar minimum, the level of solar activity is much lower which in turn reduces the photo-ionization. Thus, only lower frequencies of the HF band are reflected by the ionosphere. Sometimes, during solar maximum large solar flares occur. They emit radiations which ionize the D layer of the ionosphere and thus contribute to an absorption increase of the HF radio waves. The absorption of radio waves is a daytime phenomenon as the D layer disappears during the night. The whole process in which the HF radio waves are absorbed after the occurrence of a solar flare is known as short wave fadeout, which affects mostly the lower frequencies. During a fadeout, higher frequencies should be used for HF radio propagation. Sometime during a solar flare, high energy protons are released from the sun which moves down the Earth's magnetic field lines, into the polar region. This again results in increased ionization in the D layer of polar region causing total absorption of the HF radio waves. This event is known as Polar Cap Absorption (PCA).

2.1.5.4 Sporadic E (E_s)

Sporadic E is a reflecting and temporary layer in the ionosphere and is highly unpredictable. It corresponds to the formation of a region made of cloud of electrons (high electron density) anytime during the day or night at heights of about 90 to 140 km. Sporadic E is very important with respect to HF propagation as it has a high electron density which is comparable to the electron density in the F_2 region. It can reflect waves at frequencies which are meant for communication using the F_2 region which might result in communication failure. Sometime, the sporadic E is highly transparent and it allows radio waves to pass through it. However, it may reflect the wave acting as a shield for the F_2 layer. The signal does not reach the F layer or the receiver, leading to communication failure. If the sporadic E layer is partially transparent, the radio waves pass through the sporadic E layer and are reflected by the F layer. But sometime, the sporadic E layer itself reflects the waves. This results in partial transmission of the signal or fading. Figure 2.7 shows how the sporadic E may interrupt the communications which was meant to occur using the F layer provided the electron density of sporadic E is high enough to reflect the wave.

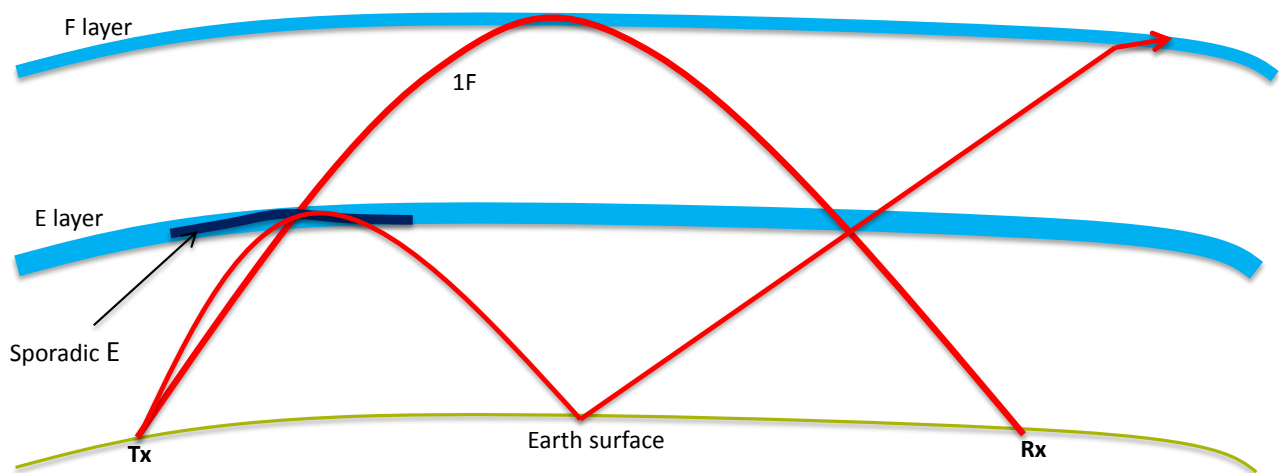


Figure 2.7 Effect of sporadic E layer in the ionosphere

As seen in Figure 2.7, the intended communication through the F layer is represented by reflection from the F layer in which the radio waves pass through the sporadic E layer that is transparent. But when the sporadic E layer is not transparent, it reflects the HF waves and the wave do not reach the intended receiver. Sporadic E in mid-latitudes and low latitudes is a daytime phenomenon and it is more dominant during the summer months. At higher latitudes it occurs mainly at night.

The ionosphere is composed of several layers of varying electron density, which are produced by the interaction of the sun's radiation with the atmospheric neutral gases. The different layers denoted by, D, E, F_1 and F_2 layers, are highly variable depending on the sun activity, the time and the location around the globe. The structure of the ionosphere can be estimated through sounding experiments using ionosondes. Well established models allow predicting the average ionospheric conditions on the basis of an estimated solar activity. Since the early times of radio transmission, the ionosphere has been used for propagating HF radio signals, mainly due to its ability to refract radio waves and therefore largely extending the communication distances. The principles of HF radio propagation are explained in section 2.2.

2.2 HF radio propagation

In HF propagation, radio waves from the HF band are transmitted and received at some distant locations using the ground waves, direct or line-of-sight (LOS) waves and skywaves as presented in Figure 2.8. The different propagation modes are described below:

Ground wave propagation: Propagation using the ground waves can be used for short distance communication and the waves travel along the ground surface. The range that can be covered using the ground waves over the land is approximately 100 km while it is about 300 km over sea. The ground range increases as the electrical conductivity and permittivity of the ground increases. The electrical conductivity and permittivity over the sea are higher than the ones of dry ground regions. Thus, one can communicate over longer distance over sea compared to using communication on the ground. Low frequencies provide communications in the range of 100-200 km. Furthermore, frequencies lower than 3 MHz are difficult to use considering the amount of man-made and atmospheric noise present during the day. The ground wave field strength can be calculated for frequencies between 10 kHz and 30 MHz as explained in the ITU report [19].

Direct or line-of-sight waves: Propagation from direct waves travels directly in line from the transmitter to the receiver (i.e. airborne station) as seen in Figure 2.8. This kind of wave may be affected by another wave which is reflected from the Earth surface, which results in interference at the receiver site.

Skywaves: Propagation using skywaves are predominantly used for long distance communication as the radio signals are reflected back to the Earth from the ionosphere. Short-range communication (50-500 km) can also be achieved using skywaves where the radio signals are transmitted upwards with higher elevation angles (typical range between 70-90°). Due to such high elevation angles at which the radio signals are transmitted, this propagation phenomenon is referred as Near Vertical Incidence Skywave (NVIS). Antenna performance and the different propagation parameters to be considered for designing an optimized NVIS telecommunication system is explained briefly in a thesis carried out at University of Twente [20].

Different phenomenon associated with skywaves is explained section 2.2.1.

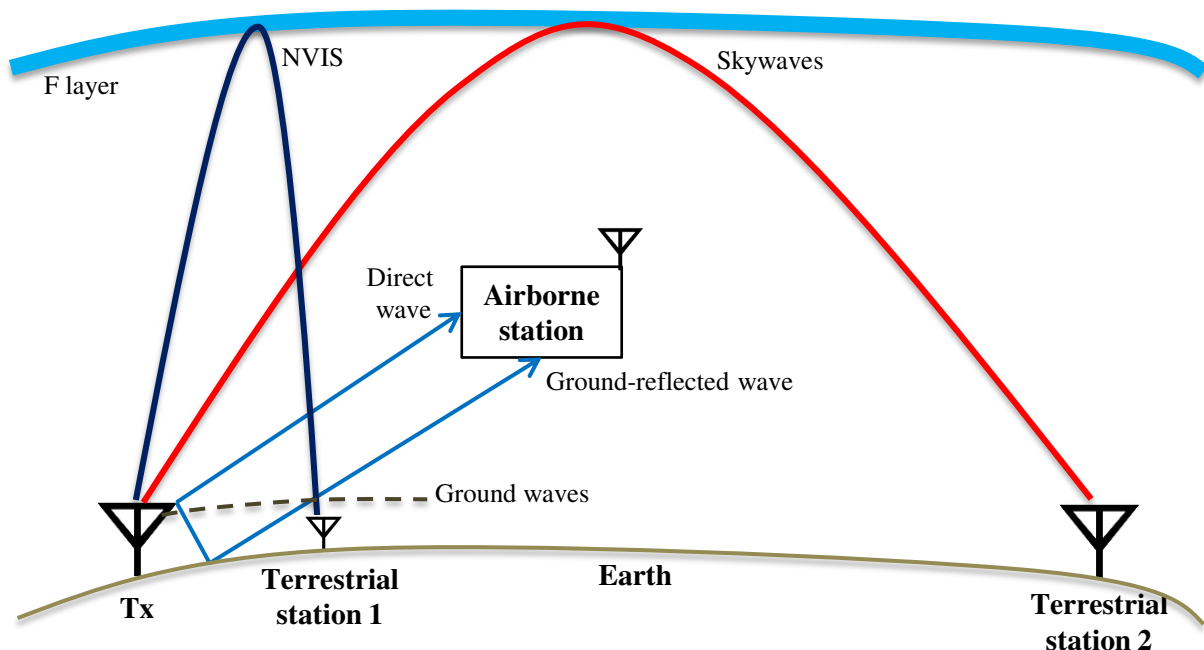


Figure 2.8 Different modes of HF propagation

2.2.1 Skywave propagation

HF radio waves transmitted from the source are reflected either by the E, F₁ or F₂ layer of the ionosphere and received by the receiver at distant locations. For propagation over long distances, the F₂ layer is the most important as explained earlier. Figure 2.9 explains the different raypaths of skywaves with a fixed frequency and different elevation angles.

As seen in Figure 2.9, the blue ray which has the lowest elevation angle is received very far away from the transmitter. The other blue ray which has a slightly greater elevation is received closer to the transmitter compared to the previous case. Thus, with the increase in elevation angle, ground range decreases until skip distance is achieved. This is represented by the yellow ray in Figure 2.9. The elevation angle increased further as compared to that of the yellow ray results in the increase of ground range. From Figure 2.9, it is also clear that a transmitter and receiver pair always have 2 raypaths for a specific frequency in all the layers of the ionosphere (i.e. 2 blue-red paths, each for a different ground range). The rays with higher elevation angles and higher reflection heights are known as high rays or Pedersen rays (red color rays) while the rays with lower elevation angles and lower reflection heights are known as low rays (blue color rays). The high rays are normally more attenuated than the low rays. The high or the low ray splits into ordinary and extraordinary waves when it hits the ionosphere because of magnetoionic splitting. The ordinary and extraordinary waves move independently through the ionosphere.

The region between the transmitter and the skip distance is known as the skip zone. Propagation between transmitter and receiver in skip zones is not possible using skywave but still possible using the ground waves at a range of about 100 km in the skip zone. The extent of the skip zone depends upon the operating frequency of the transmitter and critical frequency of the reflecting layer. Skip zones increases as the operating frequency of the transmitter increases and the range varies with the ionospheric variations. Skip zones can be used for secure communications.

Maximum Usable Frequency (MUF) is defined as the highest frequency at which skywaves can be reflected by the ionosphere when propagate obliquely. The highest frequency which can be reflected from the E layer and F layer is known as EMUF and FMUF respectively. If the transmitting frequency is greater than the FMUF, the skywaves penetrate the ionosphere and continue into space.

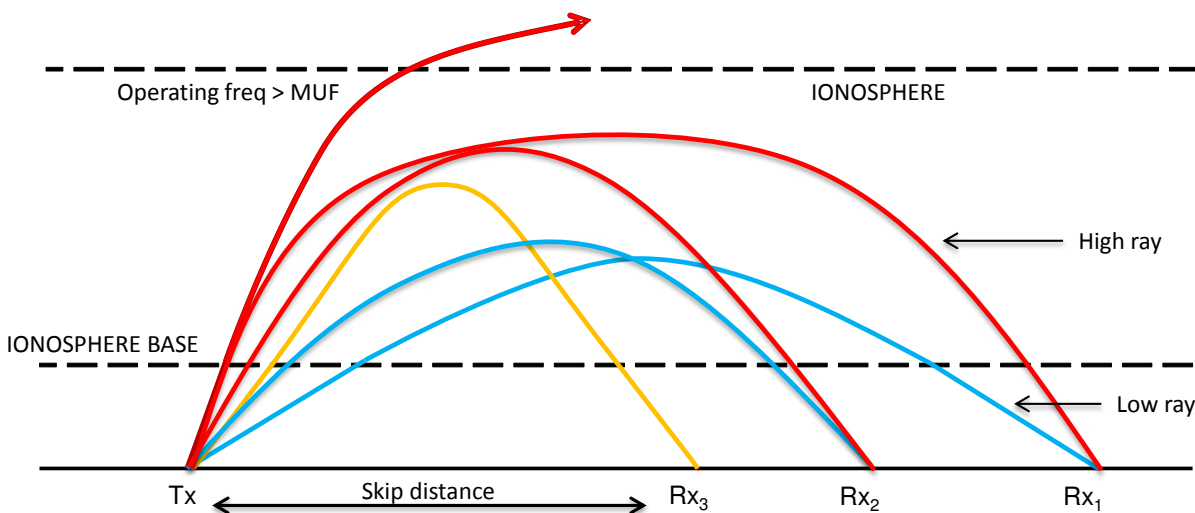


Figure 2.9 Skywave paths for a fixed frequency wave with different elevation angles

MUF depends on the critical frequency of the ionosphere at the point of reflection and the geometry of the HF link. MUF can be calculated using the secant law [10] and is given by the following equation:

$$\text{MUF} = \frac{f_c}{\cos \varphi_0} = f_c \sec \varphi_0 \quad 2.7$$

where f_c is the critical frequency of the HF link and φ_0 is the angle of incidence of the wave. In the case of vertical incidence, the MUF is equal to the critical frequency of the ionosphere. As the angle of incidence grows larger, the value for MUF is much higher than the critical frequency of the ionosphere.

Least usable frequency (LUF) can be defined w.r.t the receiver performance in terms of sensitivity. LUF can be determined by assuming the maximum tolerated channel attenuation for the system or the minimum signal-to-noise ratio (SNR) at the receiver, for a specified transmission power and specified received noise level. LUF of the HF link also depends on the efficiency of the antenna, transmitted power and the absorption the signal suffers while propagating through a specific layer in the ionosphere. Since the gain of the antenna generally decreases with frequency, a point will be reached where the signal arriving at the receiver cannot be detected above the background noise level. This corresponding frequency is known as LUF.

2.2.2 Oblique propagation

Consider two waves, one of which is reflected with normal incidence and other is reflected by oblique incidence from the same height. As seen in Figure 2.10, the ray with frequency (f_o) on the curved path “Tx-B-Rx” is reflected from point B whereas the ray with frequency (f_v) on the path “Tx'-B'-Rx” at normal incidence is reflected from same height represented by point B', along their real paths. Secant law relates the frequencies of waves reflected obliquely and vertically from the same height and is given by the following equation:

$$f_o = f_v \sec \varphi_0 \quad 2.8$$

where φ_0 is the angle of incidence at the base of the ionosphere and f_v is known as the equivalent vertical incidence frequency. Equation 2.8 also shows that the ionosphere can reflect waves at much higher frequencies with oblique propagation compared to vertical propagation. Furthermore, if straight line segments of the raypaths are extended, they meet at point A, as shown in Figure 2.10. Breit and Tuve’s theorem states that the time required by the radio wave to travel along the curved path “Tx-B-Rx” through the ionosphere is equal to the travel time along the triangular path “Tx-A-Rx” in vacuum [5]. The radio wave along the curved path is slowed down due to the varying electron density in the ionosphere whereas the radio wave along the triangular path is assumed to be travelling at the speed of light in vacuum.

Martyn’s equivalent path theorem states that if f_o and f_v are the corresponding frequencies reflected from the same real height (i.e. B and B') at oblique and vertical incidence respectively, then the virtual height of reflection of f_v is equal to the height of the equivalent triangular path for the oblique signal [5]. The ionosphere and the Earth are assumed to be flat.

For a distance (D) between Tx and Rx, a simple trigonometric calculation gives the following equation:

$$h' = \frac{D}{2\sqrt{(\sec \varphi_0)^2 - 1}} \quad 2.9$$

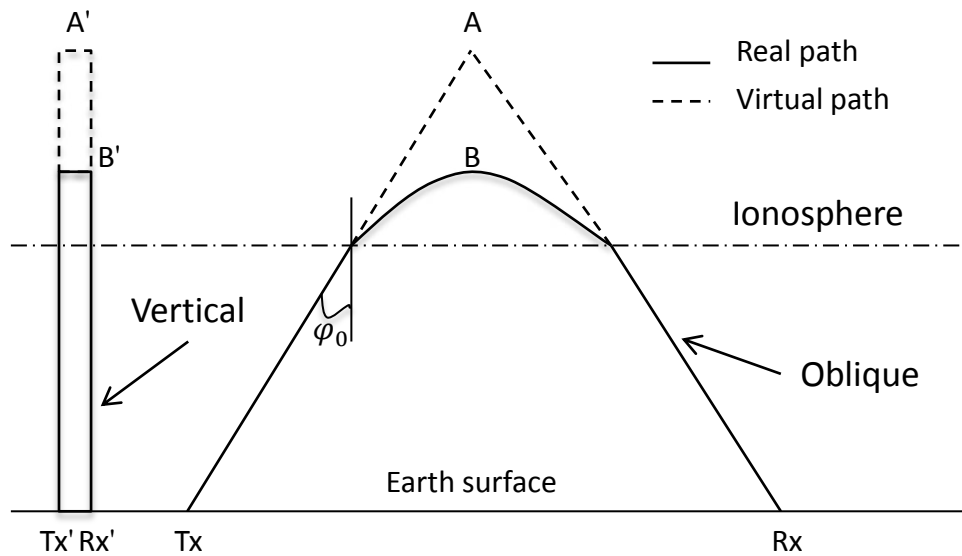


Figure 2.10 Equivalent waves reflected obliquely and vertically at same real height real (B and B') and at same virtual height (A and A'), assuming the ionosphere and the earth to be flat

By combining equations 2.8 and 2.9, the virtual height (h') can be expressed as follows:

$$h' = \frac{D}{2 \sqrt{\left(\frac{f_o}{f_v}\right)^2 - 1}} \quad 2.10$$

A transmission curve represents the relationship between h' and the operating frequency of the signal (oblique frequency) for a fixed vertical frequency (f_v) and fixed transmission distance (D). In order to obtain the oblique frequency for a given vertical frequency, one should know the virtual height as function of vertical frequency and it can be obtained from an ionogram. When a transmission curve is superimposed on an ionogram, one can obtain the virtual heights for oblique propagation at a specific distance and operating frequency. Figure 2.11 represents a set of transmission curves for a distance equal to 2000 km at different operating frequencies varying from 10 to 22 MHz which are superimposed on an ionogram recorded on 21st June, 2017 at 14:10:02 UTC in Dourbes, Belgium by a group which is a part of the Royal Meteorological Institute of Belgium (RMI) [16]. The ionogram can be seen in Figure 2.12.

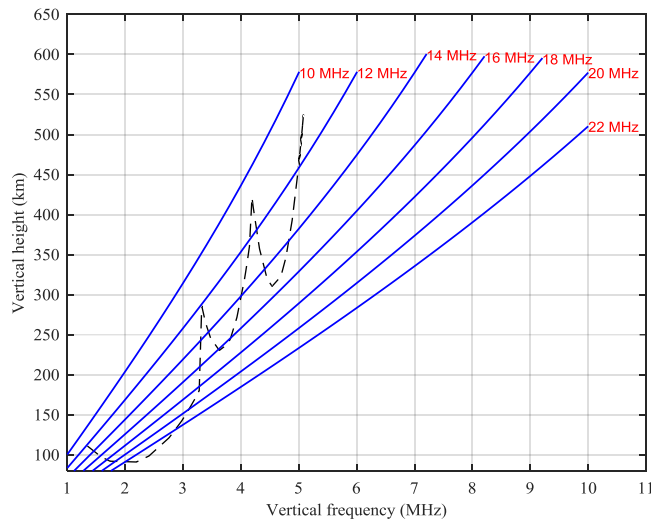


Figure 2.11 Transmission curves (blue color) for a distance of 2000 km at different operating frequencies superimposed on an ionogram (black color), assuming the ionosphere and the earth to be flat

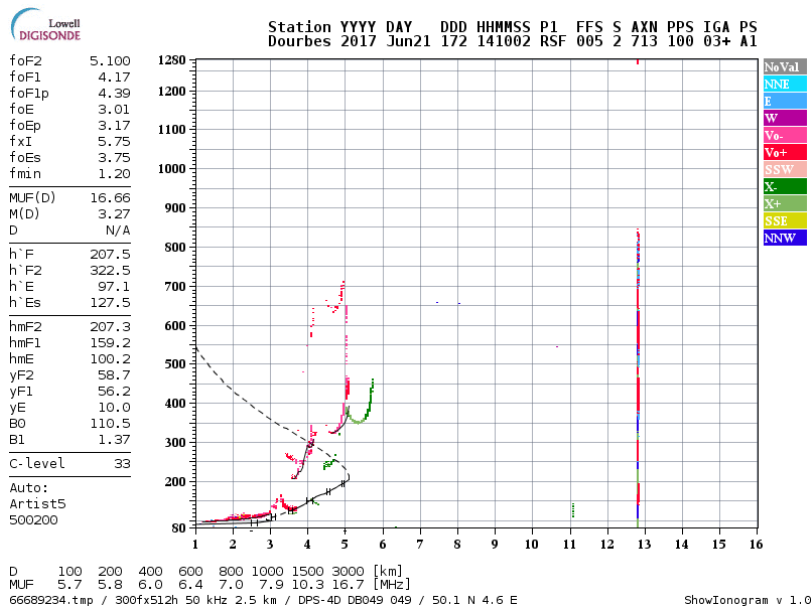


Figure 2.12 Ionogram recorded in Dourbes

In Figure 2.11, the three sections of ionogram correspond to the reflections from the E, F₁ and F₂ layers. Consider a wave frequency of 12 MHz propagating over a distance of 2000 km and it could travel using different paths, two of which could be reflected from the F₂ layer at different heights. The same transmission curve intersects the F₁ layer at one more point (i.e. more than one transmission path possible). As explained earlier, the ray corresponding to the lower virtual height is known as low ray while the ray corresponding to the higher virtual height is known as high ray or Pedersen ray. To conclude, the wave operating at 12 MHz can propagate to a ground distance of 2000 km through 3 different paths (2 paths using the F₂ layer and 1 using the F₁ layer). As the high rays are more attenuated than the low rays, it would always be better to select the frequency with the low ray for HF propagation.

Note that the above analysis assumes that the structure of the ionospheric layers remains the same at the location where the ionosphere is sounded (leading to a vertical ionogram) and at the location where the wave is actually reflected from the ionosphere. Generally, an ionosonde is available only at a few known locations, and the structure of the ionosphere may vary at the mid-point of the propagation path.

The maximum-usable-frequency factor (M factor) for the F_2 layer is defined as the ratio of the maximum usable frequency for the F_2 layer to the critical frequency of that layer. The peak altitude of maximum electron density of the F_2 layer ($h_m F_2$) can be obtained from the M factor as explained in an ITU report [21].

2.2.3 Propagation modes

HF radio waves from the transmitter can reach the receiver through several paths. A propagation mode defines the path through which the radio waves travel from the transmitter to the receiver. In general, propagation modes are further classified into 3 different categories which are as follows:

- Ordinary and extraordinary modes
- High and low rays
- Geometric propagation modes
- Complex propagation modes

The concept of high rays and low rays has been explained in detail in section 2.2.1. The other propagation modes will be detailed in the following sections.

2.2.3.1 Ordinary and extraordinary modes

Appleton proved mathematically that an electromagnetic (EM) wave entering the ionosphere is split into two different characteristic waves under the influence of the magnetic field [5]. These two characteristic waves are referred to as ordinary (o-mode) and extraordinary (x-mode) waves which travel independently through the ionosphere and are elliptically polarized. An ordinary wave is present even in the absence of magnetic field but extraordinary waves are present only in the presence of magnetic field. Also, the extraordinary waves are more attenuated compared to the ordinary waves. Both these modes can be distinguished with respect to the polarization sense (direction of rotation) of the waves. The direction of rotation of an extraordinary wave is opposite to that of an ordinary wave. The polarization diversity property could be used at the reception end by capturing signals from two different antennas placed at right angles to each other and receive the signals from the two modes separately [22]. For a HF Multiple-Input Multiple-Output (MIMO) system, the diversity in transmitted polarizations could be used to increase the capacity gain of a long-range HF link [23]-[25].

2.2.3.2 Geometric modes

The hop length is the ground distance covered by a radio wave once it is reflected by the ionosphere and returned back to earth. To cover larger ground distances, radio waves should be reflected from the F_2 layer of the ionosphere. Geometric propagation modes are classified as one hop mode, two hop mode and combination modes. In one hop mode there is one reflection from the ionosphere, in two hop modes there are two reflections from the ionosphere with a reflection from the ground in between the two reflections while in the combination modes there is reflection from both E and the F layers.

Figure 2.13 (a) represents one hop modes namely 1E, $1E_s$ and 1F with one reflection from their respective layers; Figure 2.13 (b) represents two hop modes namely 2E, $2E_s$, and 2F with two reflections from their respective layers; Figure 2.13 (c) represents the combination modes namely 1F1E, $1E_s1F$ and $F(E_s)F$. In 1F1E mode, there is a reflection from the F_2 layer and another one from the E layer. In $1E_s1F$ mode, there is a reflection from the sporadic E layer and another one from the F_2 layer. In $F(E_s)F$ mode, there are two

reflections from the F_2 layer with a reflection in between from the sporadic E layer. The higher the number of hops, the lower is its signal strength as each reflection from the ground or any layer of the ionosphere results in loss of energy. Thus 1F mode will always benefit from lower loss than other higher order modes (2F, 3F and so on). The maximum usable frequencies of lower order propagation modes are higher than those of the higher order propagation modes.

Note: In the case of multiple reflections from the same region (i.e. E or F), the reflection heights might not be equal as shown in Figure 2.13 (b) and (c).

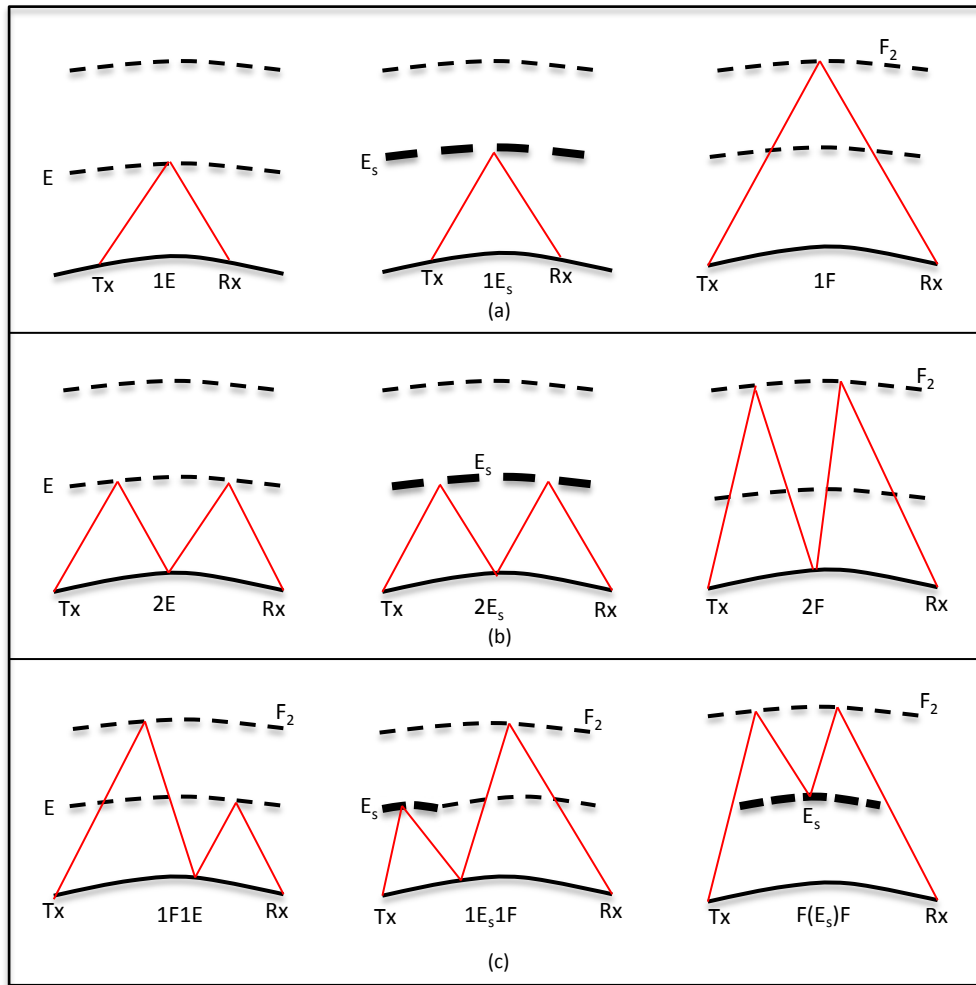


Figure 2.13 Different modes of ionospheric propagation

2.2.3.3 Complex propagation modes

There are some complex propagation modes such as chordal mode and ducted mode. They occur when the ionospheric layers tilt. In these modes, propagation of the HF radio waves in the ionosphere occurs in a guided manner. Ionospheric tilting is more likely to occur in equatorial anomaly, mid-latitude trough and near sunrise and sunset. When such modes occur, signals travel large distances with high signal strength. The signal strength is higher as there are no intermediate ground reflections and the absorption is very low. Ionospheric tilting near the equatorial anomaly results in chordal modes which travel large distances with good signal strength. Ducting in the E-F region of the ionosphere occurs when power is successively reflected from lower surface of the F layer and upper surface of the E layer. Ducting mostly occurs at equatorial ionosphere, near auroral zone and mid-latitude trough [5] [18]. Ionospheric guided propagation of the HF radio signals that does not involve ground reflection is explained in [26].

2.2.4 Factors affecting HF propagation

There are various factors such as multipath interference, absorption, fading, noise etc. which acts as disturbances in HF propagation.

2.2.4.1 Multipath interference

Signals transmitted from the source can reach to the receiver through multiple paths. When two signals with slightly different signal strength and different phase arrive at the receiver simultaneously, they interfere with each other and it is known as multipath interference. The signals have different travel time as they propagate through different paths covering slightly different distances. Multipath interference can reduce the SNR and sometime there could be loss of information. If the signals arrive at the receiver in phase, then it results in constructive interference and the signal received has higher intensity. On the other hand, if they arrive at the receiver in opposite phase, this result in destructive interference and the total received signal is attenuated to a large extent. The phase change of each path results in several signal peaks and signal fades. This phenomenon is known as **fast fading**. Spatial selectivity depends on phase differences of multiple paths.

In the case of narrowband signals, all transmitted signals undergo similar phase variations. Thus, the intensity of fading across the whole band is almost similar. This is referred to as **flat fading**. On the other hand, for wideband signals, different frequencies undergo different levels of fading. The received signal is attenuated and one observes frequency selective fading with the variation in the intensity of the total signal over the wide frequency band. The bandwidth over which the frequency components are similarly affected is known as **coherence bandwidth**. In flat fading, the coherence bandwidth of the channel is larger than the bandwidth of the signal whereas in frequency selective fading, the coherence bandwidth of the channel is smaller than the signal bandwidth. In the case of wideband signals, the presence of multiple paths is characterized by the **delay spread** in the time-domain and coherence bandwidth in the frequency domain. In HF propagation, the delay spread must be characterized, since it affects the Inter Symbol Interference (ISI). Smaller the delay spread, larger is the coherence bandwidth of the signal and lesser the ISI. Different expressions to model the HF propagations through skywaves for both narrow and wideband systems exist in the literature. The narrowband model proposed by Watterson is explained in [27] whereas the wideband model developed by Vogler and Hoffmeyer is detailed in [28]. In order to avoid multipath interference, the chosen frequency should be high (MUF) to propagate only the lowest order mode.

2.2.4.2 Absorption

Radio waves reflected from the E, F₁ and F₂ layers of the ionosphere are partially absorbed by the D layer when they pass through it on both ways. Absorption of the radio waves is the strongest where the number of neutral atoms is the highest and it is in the lower altitudes of the atmosphere. The largest absorption occurs in the D region of the ionosphere and it is relatively weak in the lower parts of the E region. Absorption occurring in the D region is known as non-deviative absorption as the ray passes without deviating through the D region. The rate at which the electrons rotate around the magnetic field lines is defined as gyro-frequency. It depends on the weight and electric charge of electrons and also the strength of the magnetic field. If the operating frequency is slightly less than gyro-frequency, absorption varies inversely with the square of frequency. Thus, higher frequencies should be used to avoid absorption. The absorption of a radio wave also depends on its polarization. Absorption of an extraordinary wave is much higher than ordinary wave, since an extraordinary wave gives energy to the free electrons and speeds them up. The electrons having more energy travel in a circle with large radius. As a result, the occurrence of collision with a neutral atom and thus losing all their energy increase. When the frequency of extraordinary wave is equal to the

gyrofrequency, all wave energy is transferred to the neutral atom and extraordinary wave is completely absorbed [10].

2.2.4.3 Noise

Radio noise arises from internal and external sources. Internal or thermal noise is basically generated in the receiving system which is normally negligible with respect to the external noise for good quality receiver. External sources of noise are atmospheric noise, manmade noise and galactic noise. Atmospheric noise is generated by thunderstorms which are capable to emit radio waves. These emitted radio waves are similar to communication radio waves and can be received by all receivers. Since, atmospheric noise cannot be eliminated, it should always be considered when estimating the signal strength at the receiver. Atmospheric noise level decreases as frequency increases and has the largest contribution at lower altitudes. Galactic noise arises from our galaxy and is not as important as the atmospheric noise. Galactic noise only affects frequencies above f_0F_2 . Manmade noise is caused by motor vehicle ignition systems, welding machines, electrical cables, power transmissions lines etc. To avoid manmade noise horizontally polarized antenna should be used, as most of the manmade noise tends to be vertically polarized. Data for external sources of noise over the radio frequency range is explained in a report by ITU [29].

2.2.4.4 Fading in narrowband systems

Fading refers to the variation of received signal intensity due to changes over the propagation paths. If it is described by its depth, it can be shallow or deep and if described by the rate at which occurs, it can be fast or slow. Sometime in deep fading, the signal level at the receiver is below the noise level, resulting in loss of information. To ensure that the signal is not lost, adequate fading margin should be maintained for which the signal level is above the noise level. There are different types of fading such as multipath fading, polarization fading, skip fading (MUF fading) and absorption fading [10].

Multipath fading normally occurs when the waves travel from the transmitter to receiver using several paths which have variations in amplitude and phase. Thus at the receiver when the rays combine, the resultant signal will fluctuate in intensity as the individual rays are in and out of phase. For instance, consider two propagation modes, both rays can interfere in such a way that they cancel out each other and no signal is detected at the receiver. Multipath fading is severe when 1F and 2F modes or 2E and 1F modes exist on the same trajectory because the ray paths will be nearly equal in length. When the difference between path lengths becomes equal to half a wavelength, the two signals would be out of phase and cancel out each other on a large extent. Polarization fading mainly occurs when there is change in polarization of the ordinary and extraordinary wave with respect to the polarization of the receiving antenna. Thus, due to polarization fading the receiving antenna receives only parts of the signals that match its polarization state. Polarization fading occurs when the total number of electrons changes along the propagation path. Skip or MUF fading normally occurs when the receiver is on the edge of the skip zone for propagation from the transmitter. Thus, the operating frequency is equal to the MUF of the HF link. However, due to variations in the ionosphere, MUF sometime falls below the operating frequency and the signal disappears. Absorption fading is due to non-uniformity in the lower ionosphere. To cancel the effects of fading, different diversity techniques can be applied in which the signal is received using two or more paths and combined in the receiver in a way that the signal strength is increased. According to [5], fast ionospheric fading can be modelled using a Rayleigh distribution while slow ionospheric fading resemble a lognormal signal distribution.

2.2.5 HF communication predictions

The ionosphere is a highly dynamic medium and changes as a function of ionospheric variations as explained in section 2.1.5. It is not possible to use the same frequency for propagation at all times for a specific ground range. It is therefore essential to use specific frequency for reflection from the ionosphere which will result in successful communication at given time of the day on a specific HF link. All ionospheric and propagation factors should be taken into account to determine different parameters essential for HF communication using skywaves. Table 2.1 explains the different step that needs to be followed to predict HF parameters to ensure successful communication [10].

Step 1	Predict the solar activity of sun during the time for which the HF predictions needs to be calculated
Step 2	Develop an ionospheric model from the predicted solar activity
Step 3	From the ionospheric model, calculate the propagation modes and the geometry of the HF link under consideration
Step 4	Calculate MUF, LUF and the field strength.

Table 2.1 HF communication prediction steps

There are some online tools available namely GRAFEX [18], VOACAP (Voice of America Coverage Analysis Program) [30], and the Point to Point software (SATIS) [31] which helps in determining the HF propagation parameters like MUF, signal strength at the receiver, possible propagation modes, elevation angle, reliability of the HF link etc. It is also possible to calculate the skywave field strength at the receiver and the transmission losses for frequencies between 2-30 MHz [32]. A propagation model suitable for prediction of all relevant HF propagation parameters that are needed to characterize the HF channel is explained in [33].

HF communication over inter-continental distances is achieved through skywaves where radio signals are reflected from the ionospheric layers. Further, propagation through skywaves occurs via different propagation modes depending on the magnetic field, elevation angles, geometry of the link and ionospheric titling. Generally in the case of geometric modes, communication range of a two-hop propagation mode is larger than that of a one-hop mode. Different parameters such as interference, noise, absorption and fading affect skywave HF propagation. By taking account of these parameters and the ionospheric variations, one can establish a long-range HF communication link using the different software's available online. Different methods of locating the source of HF radio signals are discussed in section 2.3.

2.3 HF direction finding and geolocation

Direction Finding (DF) refers to finding the direction of arrival (azimuth and elevation) of the incoming radio signals from a distinct source whereas geolocation technique refers to finding the location of the source of the radio waves. Direction finding systems generates bearing (also known as line of bearings or azimuth) which indicates the direction towards the source of signal. The bearing or the azimuth obtained from two or more spaced receivers can be combined to find the location of the source through triangulation.

Geolocation methods are classified as active or passive as explained in section 1.2. A passive radiolocation system was designed by Timothy Hall in MIT using AM signal of opportunity (SOP). He determined the relative position vector estimates between a navigation receiver at known location and a freely moving rover which acted as a base station by multilateration. From observations of the carrier phases of signals received from AM broadcast stations, he found the horizontal components of the baseline with an error of about 10 meter for baseline lengths up to about 35 kilometers [34][35]. He also showed the effect of how electrical conductors in the close proximity of the AM positioning system severely degrade its performance [36]. TDoA based navigation using SOP from the AM band (520 to 1710 kHz) shows that absolute navigation is

possible at the sub-meter level in the ideal case of high SNR, absence of multipaths and zero frequency errors [37]. Another, TDoA based navigation system using National Television Systems Committee (NTSC) broadcast signals showed that navigation is possible with typical errors ranging between 10 and 40 meters. The most significant error was due to the multipath signals [38] [39].

2.3.1 HF DF techniques

HF DF is a radio direction finder which was initially used in the Second World War. There exist different methods which can be used to find the Direction of Arrival (DoA) of the radio signals and are explained in the following sections.

2.3.1.1 Classical DF techniques

Classical DF consists of 4 different methods, namely:

- Maximum power method
- Watson-Watt
- Doppler-DF
- Interferometer

Table 2.2 illustrates different classical techniques along with its advantages, disadvantages and the parameter considered in each method to find the signal bearing (horizontal component (azimuth) of angle of arrival). Different ways to evaluate the DoA of the radio signal by deploying a large array of co-located antennas is explained in [40].

Method	Bearing calculation	Advantages	Disadvantages
Maximum Power	Maximum signal strength	Portable handheld antennas and receivers, low cost.	Accuracy decreases as distance towards source increases.
Watson-Watt	Amplitude comparison	Accuracy and sensitivity is high, fast response time.	Accuracy depends on the omni-directionality of the radiation pattern, elevation angle cannot be measured.
Doppler DF	Frequency shift measurements	Low cost, works with the source stationary or moving.	Continuous wave signal required, does not work in case horizontally polarized signals
Interferometer	Phase measurements made on number of spaced antennas	Very high accuracy, immunity to reflections and elevation angle can be measured	Large antenna arrays required to obtain phase difference.

Table 2.2 Advantages and disadvantages of different classical DF techniques

Maximum Power: This technique involves the use of a directional antenna and a receiver which is rotated until the maximum signal strength based on amplitude of the received signal is obtained. The antenna scans all locations where the source could be present and multiple lines of bearing towards the signal source are obtained. Multiple lines are then plotted and used to triangulate the location of the source. Usually when the

distance to the source is reduced to about 100 meters, precise location can be obtained using this method. Owing to its simplicity, this method is often performed manually using handheld antennas.

Watson-Watt: The method was first proposed in 1926 for direction finding in the HF band [41]. This method involves the use of 2 Adcock antenna pairs to perform amplitude comparison on the signal received from the source. The 2 Adcock antenna pairs (referred as North-South axis (N-S) and East-West axis (E-W)) are either made of monopole or the dipole antennas and are perpendicular to each other. As both antenna pairs are perpendicular, the radiation pattern has maximum sensitivity along the axis and nulls perpendicular to the axis. Thus due to the radiation pattern we have unique set of magnitude for each direction. The output signal at each antenna pair is the difference of the received signal at each antenna i.e. at every Adcock antenna pair we just have one output. These outputs are passed to the receiver where the bearing angle is calculated by the arctangent of the ratio of the N-S to E-W signals. The formulations of the bearing angle using the Watson-Watt system and the Adcock array is explained in detail in [42].

Doppler DF: This method was first proposed in 1947 along with its advantages over Watson-Watt method [43]. It uses a single antenna which is physically rotated to form a circular trajectory. It is also possible to use a rotating multi-antenna circular array with each antenna sampled in succession. The bearing angle of the received signal from the source is estimated by Doppler shift of an antenna signal at different points on the circular trajectory (see Figure 2.14 [44]). Doppler shift is a physical effect in which the observed frequency increases when the source moves towards the observer whereas it decreases when the source moves away. In DF, as we move closer to the signal, the frequency will increase and the frequency shift can help to detect if we are aiming at the correct direction.

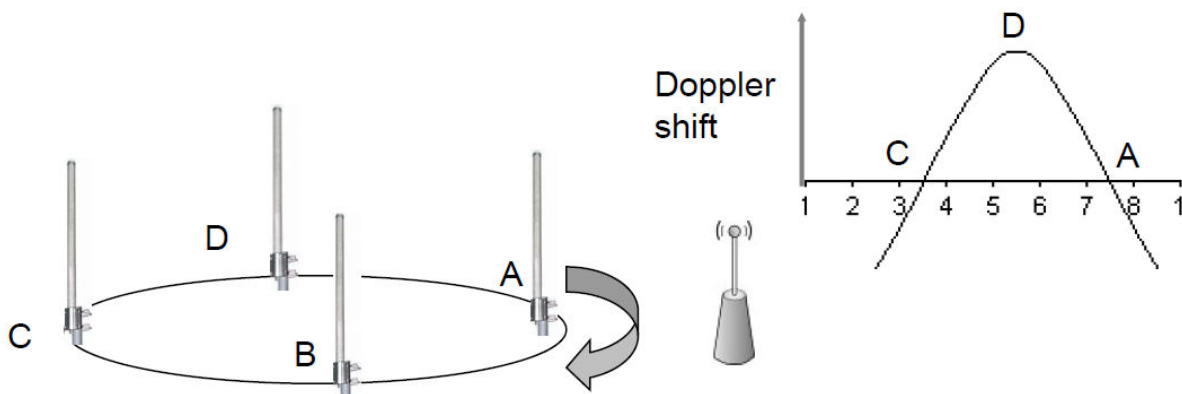


Figure 2.14 DF using Doppler shift of an antenna rotating around a circle

Consider an antenna mounted on rotating disk. As the disk rotates, the antenna moves closer and away from the transmitter. As seen in Figure 2.14, the antenna at point A and C is stationary with respect to the transmitter and so the Doppler shift is equal to 0. At position B, the antenna is moving away from the transmitter and the Doppler shift decreases while at position D; the antenna is moving towards the transmitter and the Doppler shift increases. When we make continuous frequency shift measurements along the rotating disk, we obtain a Doppler sine-wave which shows 2 zero crossings (at point A and C) since the Doppler shift is equal to zero at this location. The second 0 crossing point is the closest to the transmitter (point A as seen in Figure 2.14). The frequency of the Doppler sine wave is equal to the antenna rotation frequency. Based on the measured Doppler shift and the spatial location of the receiving antenna, the AoA is computed. The accuracy of direction finding using Doppler method mainly depends upon the linearity of the demodulator [45].

Interferometer: DF in the HF band using an interferometer was first explained around 1961 [46]. In an interferometer system, the DoA of the incoming signal is calculated from the phase measurements made on number of spaced antennas [47]. These antennas are placed in a circular pattern and one of the antennas serves as a reference channel. The phase difference of each antenna element is calculated for each reference angle (0 to 360°) with respect to the reference antenna. In correlative interferometry, the measured phase difference of the antenna is compared with reference phase difference of the antenna at each wave angle. The angle at which we obtain maximum correlation when comparing the reference and the measured phase difference yields the bearing or the azimuth angle. The accuracy of the bearing or azimuth angle can be increased if the number of antennas on the circular array is increased. An algorithm for DF based on the interferometer principle which can be used for high precision measurements in short duration of time is explained in [48].

2.3.1.2 Beamforming

Beamforming is a signal processing technique used in an array of antennas for directional transmission and reception of the signal [49]. It is achieved by combining elements in phased array such that the signals experience constructive interference at some angle while destructive interference at other angles. A receive beamformer is used to estimate the DoA of the signal in presence of noise and interference. The output of the array of antennas in the receive beamformer are combined linearly using the spatial filter coefficients (weights) such that the signals from the desired direction passes through the beamformer undistorted while the signals from other directions are blocked.

Beamforming is classified into conventional beamformer and adaptive beamformer. Conventional beamformer uses weights which are pre-calculated depending upon the location of antennas in space and wave direction while adaptive beamformer uses weights which are calculated as the function of the incoming data to optimize its performance. Adaptive beamformer have better resolution and high interference rejection capability than conventional beamformer. A survey of estimating DoA using different ways of beamforming is given in [50]. To obtain the DoA of the incident signal, the beam can be electronically steered by adjusting the delay and phase shift of the array of antennas. Figure 2.15 illustrates the principle of 2D beamforming using phase shifters [51].

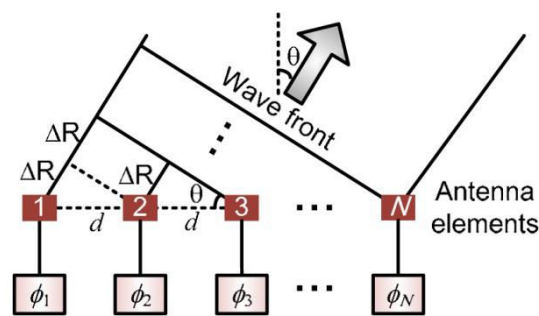


Figure 2.15 Beamforming using phase shifters

The signal at the 2D beamforming output is given by:

$$y(t) = \sum_{i=1}^N e^{j\omega \frac{(i-1)d[\sin \theta - \sin \theta_0]}{c}} s(t) \quad 2.11$$

where θ_0 is the incidence angle of the received signal, θ is the steering angle for the beamformer, d is the spacing between the antennas and c is the speed of light. The steering angle θ is a function of the phase

difference which is controlled using the phase shifters. When both angles are equal ($\theta = \theta_0$), the output at the beamformer is increased N times. Noise is not correlated, hence it is not increased and, thus, the overall SNR is increased N times. At steering angle other than θ , the complex weights cancel out each other and the output for the beamformer is neither increased nor decreased.

The beamformer explained is without any amplitude weight on the elements. Different ways of weighting the incoming signals exist [52] which are used to change the characteristics of the pattern of the equivalent steerable antenna. In order to evaluate the azimuth and elevation angle of the incoming signal, one can use the 3D beamformer which is explained briefly in [53]. HF DF using beamforming technique is explained in [54] along with experimental results.

The spatial resolution is proportional to the overall array size. When the spacing between antenna elements is large, the antenna array generates grating lobes which are unintended beams of radiation while if the spacing is less, the overall array size decreases (for a fixed number of antenna elements). Two sources very close to each other cannot be distinguished with beamforming. Thus, DoA of only single source can be found at once whereas using superresolution algorithms, DoA of multiple sources can be found as explained further.

2.3.1.3 Superresolution DF

Using superresolution methods, two signals from different sources close to each other can be resolved. They use an antenna array with multiple synchronous receivers. DF using superresolution method requires the knowledge of the array manifold.

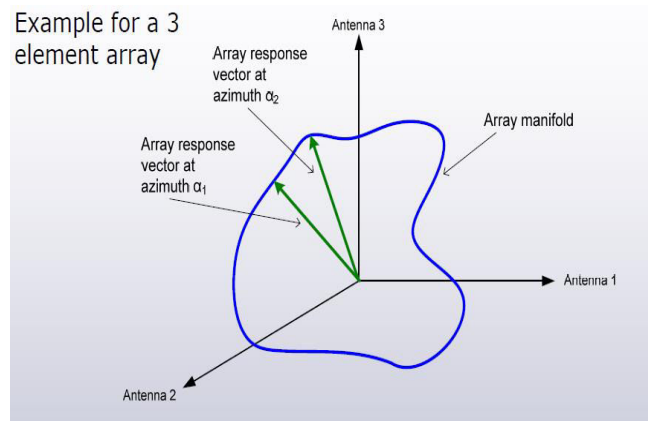


Figure 2.16 Array manifold for 3-antenna array

Figure 2.16 explains the principle an array manifold for a 3-antenna array [55]. An array response is the magnitude of output which is the function of the incident angle of the wave. An array response vector is defined by the set of relative gains and phases at the antennas for a signal which arrives at the array from a specific direction. An array manifold is the curve or the locus of all the points of the array response vector in all directions. The array manifold characterizes the antenna array, the unknown signals received at the array is compared with the array calibration function to estimate the line of bearings (azimuth). Superresolution direction finding is possible using algorithms like MUSIC [56], ESPRIT [57], Root MUSIC [58], and SAGE [59]. The following paragraphs provide some details about the MUSIC and ESPRIT algorithms.

MUSIC (Multiple signal classification): It is a high resolution DoA subspace algorithm to estimate the number of incident plane waves on the antenna array and their angle of incidence. MUSIC algorithms deals with eigen decomposition of the covariance matrix into two different subspace matrices (noise subspace and signal subspace) which are orthogonal to each other. The signal subspace is composed of the eigenvectors associated with the arriving signal while the noise subspace is composed of eigenvectors associated with

noise. Due to orthogonality condition between the noise subspace eigenvectors and array steering vector, the Euclidean distance between them is zero for each angle of arrival. This distance is placed in the denominator of the pseudospectrum (Equation 2.12) and it yields sharp peaks at the angles of arrival. Thus, the DoA of multiple incident signals can be estimated by locating the peaks in the pseudospectrum given by:

$$P_{Music}(\theta) = \frac{1}{abs [a(\theta)^H E_N E_N^H a(\theta)]} \quad 2.12$$

The term in the denominator represents the Euclidean distance, $a(\theta)$ represents the array steering vector and E_N represents the noise subspace vector [60]. The peaks in the pseudospectrum become sharper if the array size is increased and resolution capability for two signals which are closely spaced decreases if the SNR decreases [61].

ESPRIT (Estimation of signal parameters via rotational invariance techniques): The ESPRIT algorithm is more robust with respect to the array imperfections than MUSIC. The computational complexity and the storage requirements are reduced drastically compared to MUSIC algorithm where the entire parameter space is searched to find the DoA of different signals from different sources. In the ESPRIT algorithm, the reduction is achieved in computational and storage costs since the array elements are placed in identical displacement forming matched pairs which are also known as doublets. The algorithm exploits the rotational invariance of the signal subspace created by two subarrays derived from the original array with a translational invariance structure. The algorithm to estimate the direction of arrival of different signals from different sources is explained in [57].

MUSIC and ESPRIT are high resolution algorithms which provide better spatial resolution compared to beamforming and are able to detect multiple sources placed very close to each other at once. The ESPRIT algorithm can be used if the number of sensors is larger than the number of sources to be detected and if computational power is limited. MUSIC algorithm can be used if there is less sensors than sources and computation power is high. Both MUSIC and ESPRIT algorithms face problems when uncorrelated and coherent signals exist together. An efficient DoA method is explained in [62] which estimates the angle of arrival for both uncorrelated and coherent signals separately.

HF radio DF using MUSIC algorithm is experimentally validated by deploying a receiver system based on a heterogeneous circular array in [63]. There is a slight bias between the estimated azimuth and elevation angles when compared with the expected values. Results presented in [64][65] shows the performance of HF DF using the MUSIC algorithm.

2.3.2 HF geolocation methods

HF geolocation refers to finding the geographic location of the source of the radio waves emitted in the HF band. HF geolocation can be achieved using angular-domain or time-domain methods. All HF DF techniques explained in the section 2.3.1 are angular-domain methods where the DoA of the incoming radio signal is estimated. Later, using the DoA's from multiple receivers, the location of the HF source is found using the triangulation method which is explained further. HF geolocation is also possible using time of arrival (ToA) and time difference of arrival (TDoA) method. Time-domain methods uses the time information acquired from the signals received at multiple sites.

2.3.2.1 Triangulation

Triangulation is a method in which the location of the transmitter could be found by using two or more single antenna receivers or an array of antennas, placed at known locations. Figure 2.17 explains the concept of triangulation.

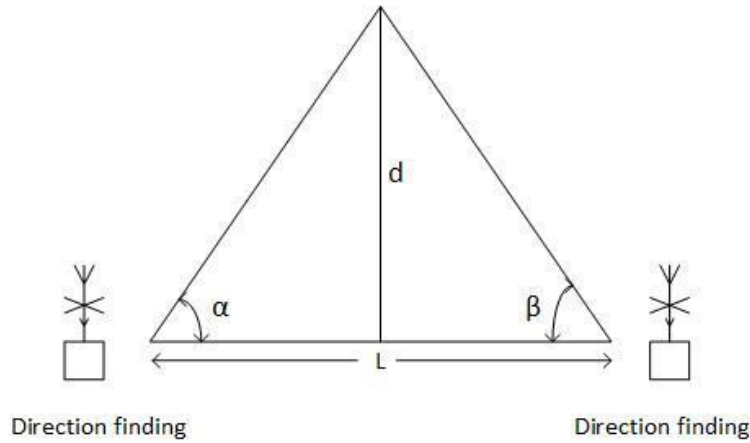


Figure 2.17 Schematic of triangulation principle

As seen in Figure 2.17, the two DF sites act as a receiver and are used to measure the DoA of a radio signal at the receiver. If the DF site consists of an array of antennas, then the DoA is computed by measuring the phase difference between the angles received at different antennas of the array. If the DF site is just a single directional antenna, then the orientation of the antenna which indicates the strongest signal gives us the direction of the transmitter. As we know the distance between the two DF site and the DoA of radio signal at both sites, a triangle could be constructed. The point where the two sides of the triangle intersects, gives us the location of the transmitter. The distance “d” as seen in Figure 2.17 is calculated as follows:

$$d = \frac{L \sin \alpha \sin \beta}{\sin(\alpha + \beta)} \quad 2.13$$

where L is the length between both DF sites, α and β are the DoA’s at both DF sites, respectively. Results presented in [66] used triangulation method to compute the source location.

2.3.2.2 Single site location (SSL)

SSL is an angular-domain method and it consists of a large antenna array at a single site. Moreover, it provides DoA in terms of the horizontal (azimuth) and vertical (elevation) component of the incoming radio signal. The azimuth and elevation angles measured at a single site are enough to find the location of the HF source [67]-[71]. The knowledge of the ionosphere along the skywave path is required. Range estimation using the SSL method is the application of the results obtained from secant law, Breit and Tuve’s theorem and Martyn’s equivalent path theorem which are explained earlier in section 2.2.2. Table 2.3 explains the different steps to calculate the range using the SSL method [10].

Step 1	Incoming signal at frequency f is observed to have an elevation angle of β_0
Step 2	Equivalent vertical frequency (f_v) is calculated using secant law
Step 3	The virtual height is obtained from a vertical incidence ionogram at f_v
Step 4	Signal is assumed to travel a triangular path with elevation angle β and the reflection occurring at altitude equal to the virtual height
Step 5	Range to the transmitter is calculated as $\{2h' \tan \beta_0\}$

Table 2.3 Range estimation using SSL method

Using the SSL method, it is possible to locate a HF transmitter located about 2000 km away from the receiving system with an error of about 10% [72][73]. The drawback of SSL method lies in deploying a large antenna array to measure the DoA components and the need of an accurate ionospheric profile to estimate the height of ionospheric reflection. Due to the variable nature of the ionosphere, this ionospheric profile needs to be measured using an ionosonde. Using a prediction model may lead to a considerable error in location estimation.

In the case of multipath HF propagation, passive HF geolocation is possible using SSL method as explained in [74]. Both paths are resolved using the MUSIC algorithm and the geolocation error is about 17% of the true range. Simulation results presented in [75] demonstrate that HF transmitter can be located with a higher accuracy by exploiting the real time ionospheric information available from the measured multiple elevation angles using a SSL setup. Another study showed that the HF source located about 1160 km away from the SSL setup could be estimated with an error of about 10 km by exploiting multipath HF propagation [70]. The transmitter location is estimated using a combination of TDoA and cone angle of arrival (CAoA) measured by a uniform linear array (ULA) along with the ionospheric information gathered by deploying an ionosonde near the receiver site. Though the obtained geolocation accuracy is very high, the requirement of setting up an ionosonde is not feasible in large scale practical applications.

2.3.2.3 Time of arrival (ToA)

The ToA method calculates the distance between transmitter and receiver using the time the signal took to travel from the transmitter to the receiver. ToA is based on trilateration principle of distance measurement, where the measured time is multiplied by the speed of light to find the distance. In the ToA method, location estimates are determined by the point of intersection of circles (2D) or spheres (3D) where centers are the positions of the known receivers and radius of the circles are the estimated distances to the transmitter. Figure 2.18 illustrates Tx geolocation using the ToA method where the intersection of the circles denotes the Tx location. In the ToA method, there must be synchronization between the transmitter and all the receivers. Moreover, a minimum of three stations are required to locate the target using the ToA method [76]. Global Positioning System (GPS) is the most widely used navigation system which operates using the ToA method [77]. Note that all signals received follow the line-of-sight (LOS) path which is not the case for HF radio transmissions through skywaves.

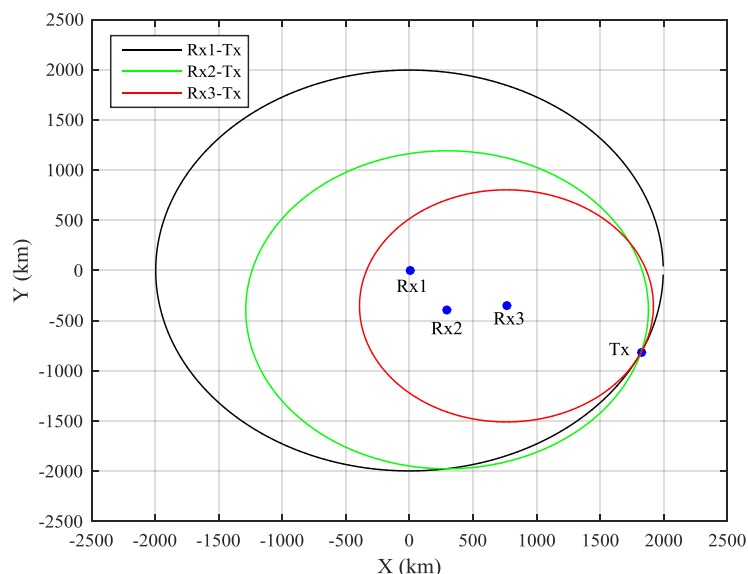


Figure 2.18 Geolocation using ToA method for 2D case

A preliminary study of HF geolocation for transmitters in the range of 1000-2000 km using time-domain method was investigated by our team. It showed that the Tx location could be estimated with an error in the order of 25 km under certain assumptions and without the explicit knowledge of the ionospheric reflection height [78]. Further in order to validate this concept and simulation results, an experimental campaign was carried out in France by deploying single antenna receivers over multiple locations. It showed that in favorable conditions, the Tx could be located with an error of 5 km using the ToA method [79].

2.3.2.4 Time difference of arrival (TDoA)

The TDoA method calculates the location using the time difference of arrival measured at pairs of transmission paths between transmitter and receivers. TDoA is based on the multilateration principle of distance measurement at receivers, where the measured time difference is multiplied by the speed of light to find the range difference. The TDoA method locates the target at intersections of hyperbolas (2D) or hyperboloids (3D) which are generated with the foci located at the known receiver locations. Figure 2.19 represents the Tx geolocation using the TDoA method where the Tx lies at the intersection of the three hyperbolas. The obtained range differences are used to plot the hyperbolas. In TDoA method, synchronization is only required on the receiver ends. TDOA systems require at least three receivers for a 2D location problem and at least four receivers to estimate the 3D coordinates [76]. The LORAN-C (long range navigation) was the most widely used system for the purpose of navigation in the 1980's which used the TDoA's between different terminals to locate the position of the transmitter via multilateration [80]. Different mathematical approaches for finding the location of the target using the TDoA method are explained in [81][82], it is assumed that the signals propagate through LOS mode.

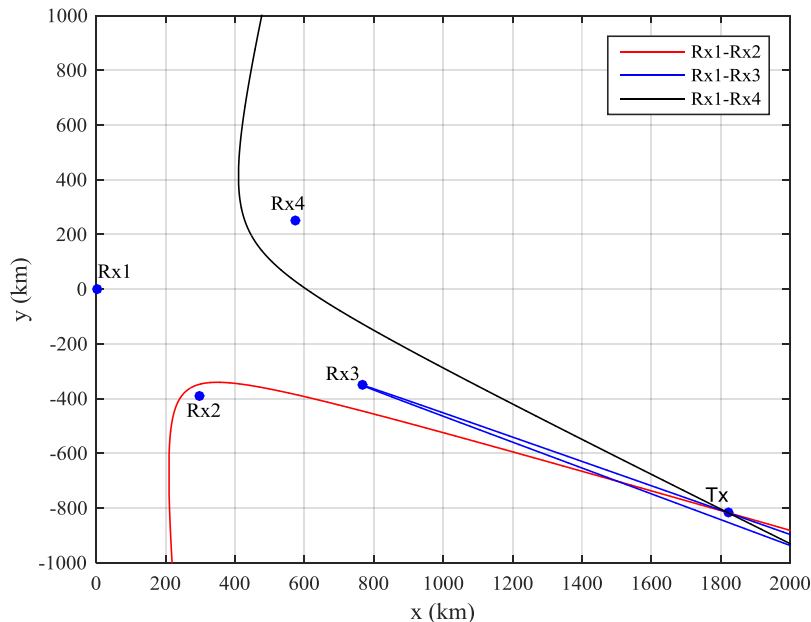


Figure 2.19 Geolocation using TDoA method for 2D case

HF radio transmissions over long distances propagate through skywaves (i.e. NLOS mode). Experiments performed in 1959 [83] showed that geolocation of VLF Tx based on TDoA method could lead to an accuracy of about 50 km for distances of about 5000 km. HF geolocation for radio signals propagation through skywaves is possible using ToA or TDoA measurements [78][79]. But due to the variability of the ionosphere, there are variations in the measured time. Experiments conducted to measure the time delay variations in HF propagation showed that the standard deviation of the mean arrival time is always greater

than 10 μs and more often it was around 25 to 50 μs [84]. Different layers in the ionosphere evolve at different times during the day and night; they are highly uncorrelated. Thus, due to the temporal variation in the formation of different layers in the ionosphere, different propagation modes can occur with equal probability at the same time. It also accounts for the variability of the measured arrival time [85][86]. The differential time delay errors introduced due to varying ionosphere can be reduced to a certain extent by using a prediction model which is explained in detail in [87]. There is a significant reduction in the positional estimate errors using a simple prediction model [88]. Another study of HF transmitter geolocation using a combination of TDoA and DoA methods [89], achieves good geolocation performance when information from multipaths are considered at different receivers. However, an antenna array is required at each receiving station and the simulation is performed assuming quite accurate TDoA measurements, which is far from realistic cases.

This thesis aims to detect HF radio transmitters using passive geolocation techniques. In the context of passive geolocation, the signal transmission time is unknown and thus the ToA method cannot be used. But, passive geolocation can be achieved using the TDoA method. A study for passive location systems using TDoA method for LOS transmissions is explained briefly in [90]. Table 2.4 provides a summary of different HF geolocation methods along with its requirements.

Geolocation Method	Number of receiver setup	Ionospheric model	Antenna design	Synchronization between Tx and Rx
SSL	1	Required	Antenna array	Not required
ToA	2 receivers – Location ambiguity 3 receivers – Location exact	Not required	Single antenna receivers	Required
TDoA	4 receivers – Location exact (3D)	Not required	Single antenna receivers	Not required. Receivers must be synchronized

Table 2.4 Comparison of different HF geolocation methods

2.4 Conclusion

First of all, this chapter explained the different phenomenon through which the ionosphere is formed. The ionosphere consists of different layers which have a varying electron density and are capable of reflecting HF radio signals. Moreover, the ionosphere is a highly dynamic medium which varies with respect to the solar activity and the geographic location.

The principles of HF radio propagation through ground waves and skywaves are explained. Using ground waves, propagation can be established over short ranges (100-300 km) whereas using skywaves, long distance HF transmission is possible wherein the radio signals are reflected back to the Earth via different propagation modes. The various parameters (noise, absorption...) which needs to be considered while setting up a long-haul HF communication link are also discussed.

Different angular and time-domain HF geolocation techniques are explained in detail along with the references to most of the work that have been carried out in this domain. Angular-domain methods estimate the position of the transmitter by measuring the DoA of the incoming signal. On the other hand, time-domain

methods estimate the transmitter position using the trilateration or multilateration principle. Time-domain HF geolocation techniques are more cost-effective than angular-domain methods.

In the context of passive HF geolocation, the TDoA method is well suited. Chapter 3 explains the time-domain HF geolocation algorithm along with its mathematical formulations. Using the HF ToA/TDoA algorithm and an ionospheric model, simulations are conducted to analyze the effect of the number of receiver and their positioning on the accuracy of HF geolocation systems.

Chapter 3 Time-Domain HF Geolocation: Algorithm and Simulation Results

Chapter 2 outlined the theory of HF radio propagation and its geolocation in detail. This chapter outlines the time-domain HF geolocation algorithm and the obtained simulation results. In section 3.1, different models to approximate the electron density profile for the different layers of the ionosphere are explained. These models are also used to evaluate the ray-path parameters of the HF link in different simulation studies. In addition, an analysis of the Quasi-Parabolic (QP) model of the ionosphere is provided and the limitations of the model are emphasized. In section 3.2, the HF geolocation algorithm based on ToA and TDoA methods are described along with its mathematical equations. Finally, from simulation results the effects on the geolocation accuracy for both ToA and TDoA method when using a larger number of receivers and changing their position are discussed in section 3.3. Part of the work presented in this chapter has been published in [91].

3.1 Ionospheric layer models

Ionospheric layer models are given by analytical expressions that are used to define the electron density profile for one or multiple layers of the ionosphere. These models can be differentiated as simple models, which represent a single layer of the ionosphere, and composite models, which represent several layers of the ionosphere. Moreover, these models are integrated as programs in computers to perform ray-tracing of radio signals propagating through the ionosphere.

3.1.1 Simple models

There are many simple models namely square-root layer, linear layer, exponential layer, sech-squared layer, Chapman layer, parabolic layer and QP layer which defines the electron density profile of an ionospheric layer [5]. The expressions used to model the electron density profile for a linear ionospheric layer are explained in [92]. The analytical expressions to model the electron density profile using the exponential layer, sech-squared layer, Chapman layer are detailed in [93] along with their performances in different conditions. More specifically, the exponential layer is more suitable for modeling the electron density profile during the daytime whereas during the night-time, the sech-squared and Chapman layer provides better results. The parabolic and QP layer models are closer to the realistic ionospheric layer and are explained further in detail.

3.1.1.1 Parabolic layer

As the name suggests, this model is defined by the equation of a parabola in electron density versus the height and is given by the following equation:

$$N = \begin{cases} N_m \left[1 - \left(\frac{r - r_m}{y_m} \right)^2 \right] & r_b < r < r_m + y_m \\ 0 & elsewhere \end{cases} \quad 3.1$$

where N is the electron density having maximum value equal to N_m , r is the radial distance from the center of the Earth (comprising the Earth radius r_0 and the height from the ground), r_m is the value of r where the electron density is equal to N_m , r_b is the value of r at the base of the layer, equal to $r_m - y_m$ and y_m is the layer semi-thickness [94].

The electron density profile calculated using the parabolic layer model for the F₂ layer is illustrated in Figure 3.1 with the following parameters: $f_c = 8$ MHz, $h_m = 300$ km, $y_m = 120$ km. As seen in the Figure 3.1, the maximum electron density is at 300 km.

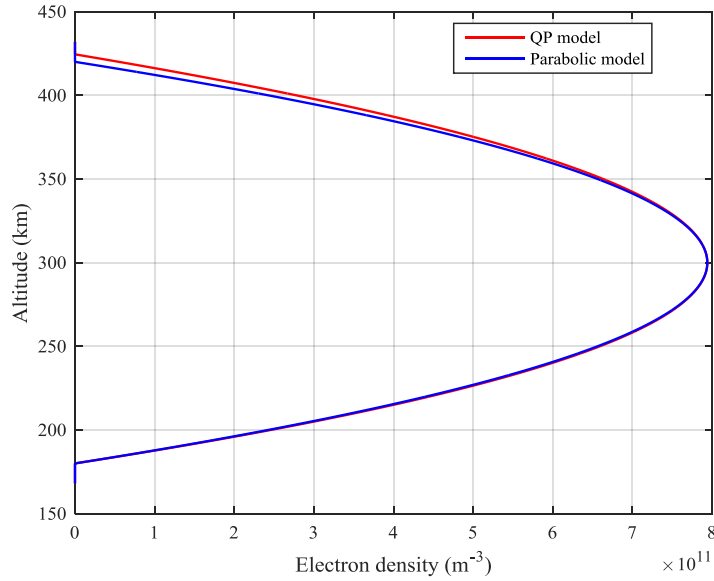


Figure 3.1 Electron density profile of F₂ layer of the ionosphere using QP and parabolic layer models

3.1.1.2 QP layer

The QP ionospheric layer model developed by Croft and Hoogasian is obtained by a slight modification of the parabolic layer model which is used to define the electron density profile of the ionosphere. The electron density profile of an ionospheric layer in the QP model [94] is defined as follows:

$$N = \begin{cases} N_m \left(1 - \left(\frac{r - r_m}{y_m} \right)^2 \left(\frac{r_b}{r} \right)^2 \right), & r_b < r < r_m \left(\frac{r_b}{r_b - y_m} \right) \\ 0, & \text{elsewhere} \end{cases} \quad 3.2$$

The difference between the QP and parabolic layer is the precise variation of the electron density between the peak and the bottom of the layer. This modification allows the QP layer model to provide analytic expressions describing the ray-path parameters of oblique propagation considering the ionospheric medium. Figure 3.2 presents the ray path geometry for a QP layer model of the ionosphere. As seen in Figure 3.2, the QP model also accounts for the curvature of the Earth.

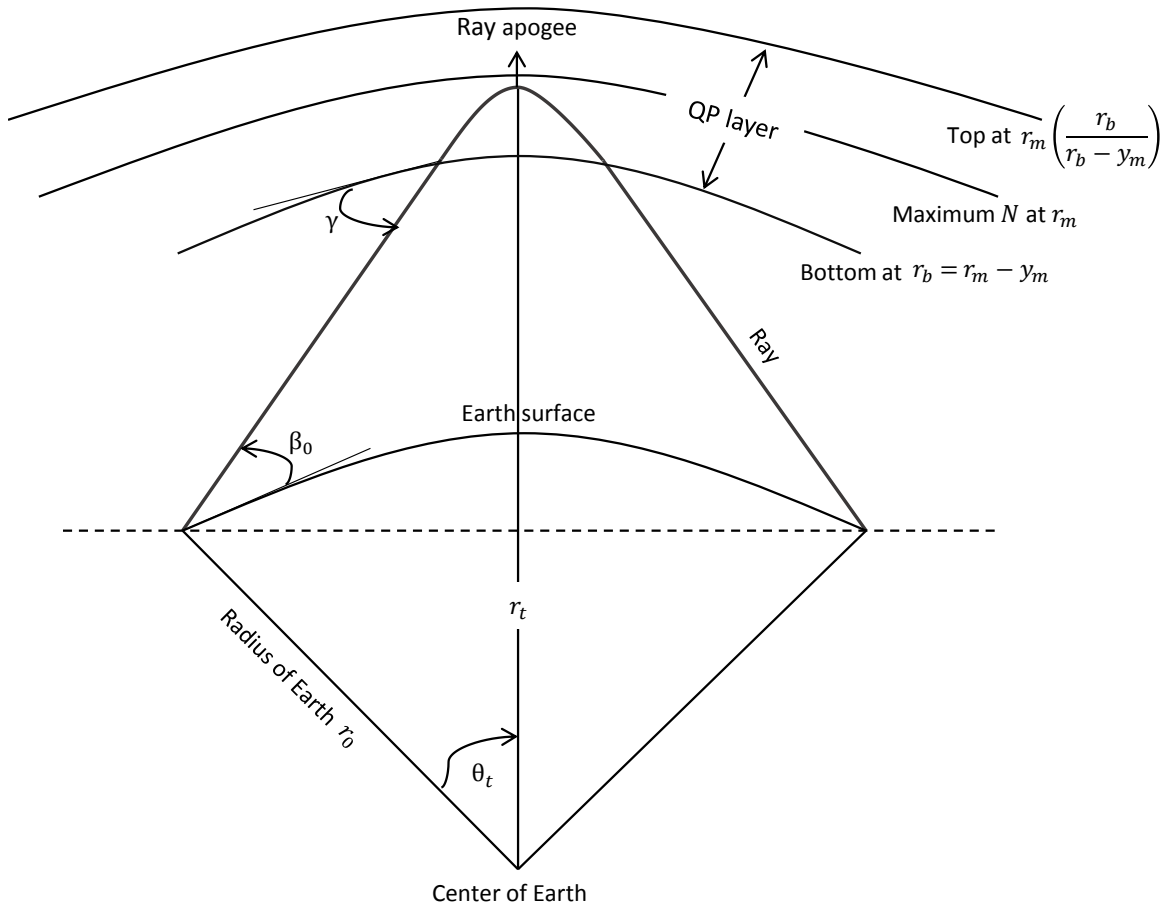


Figure 3.2 HF link geometry for a QP ionospheric layer

Using the QP model, one can obtain the ground distance (D), group path distance (P) and the phase path distance (P') between a Tx-Rx pair for a specific elevation angle β_0 and operating frequency from the Tx. The ground distance measured along the earth's surface is given by the following equation [94]:

$$D = 2r_0 \left\{ (\gamma - \beta_0) - \frac{r_0 \cos \beta_0}{2\sqrt{C}} \ln \frac{B^2 - 4AC}{4C \left(\sin \gamma + \frac{\sqrt{C}}{r_b} + \frac{B}{2\sqrt{C}} \right)^2} \right\} \quad 3.3$$

where r_0 is the radius of earth, β_0 is the elevation angle of the ray, γ is the angle of ray at the bottom of the ionosphere. The variables A, B, C and γ can be obtained by the following equations:

$$A = 1 - \frac{1}{F^2} + \left(\frac{r_b}{F y_m} \right)^2 \quad 3.4$$

$$B = -\frac{2r_m r_b^2}{F^2 y_m^2} \quad 3.5$$

$$C = \left(\frac{r_b r_m}{F y_m} \right)^2 - r_0^2 \cos^2 \beta_0 \quad 3.6$$

$$\cos \gamma = \frac{r_0}{r_b} \cos \beta_0 \quad 3.7$$

where F is the ratio of the operating frequency (f) to the critical frequency (f_c). The group path is obtained by multiplying the signal transmission time with the speed of light (c) in the QP layer model and is expressed as follows:

$$P = 2 \left\{ r_b \sin \gamma - r_0 \sin \beta_0 + \frac{1}{A} \left[-r_b \sin \gamma - \frac{B}{4\sqrt{A}} \ln \frac{B^2 - 4AC}{(2Ar_b + B + 2r_b \sqrt{A} \sin \gamma)^2} \right] \right\} \quad 3.8$$

Finally, the phase path distance is obtained by multiplying the wavefront transit time with the speed of light. It can be calculated using the following equation in the case of a QP layer model.

$$P' = 2 \left\{ -r_0 \sin \beta_0 + \frac{B}{4} \left[\frac{1}{\sqrt{A}} \ln \frac{B^2 - 4AC}{4 \left(Ar_b + \frac{B}{2} + \sqrt{A} r_b \sin \gamma \right)^2} + \frac{r_m}{\sqrt{C}} \ln \frac{B^2 - 4AC}{4C \left(\sin \gamma + \frac{\sqrt{C}}{r_b} + \frac{B}{2\sqrt{C}} \right)^2} \right] \right\} \quad 3.9$$

The QP layer model of the ionosphere is a monolayer model. It provides the ray path parameters considering reflection only from a specific layer in the ionosphere; it is one of the limitations of this model. Also the effect of magnetic field is not included while deriving the analytical expressions of the ray-path parameters.

Figure 3.3 illustrates the ground distance D against the ray elevation angle β_0 , plotted using the QP model for different values of F . The curves are obtained from the analytical expression of equation 3.3, where we fixed the following parameters: $f_c = 8$ MHz, $h_m = 300$ km, $y_m = 100$ km. These values correspond to a typical F layer of the ionosphere. One first observes that the maximum ground distance is obtained for $\beta_0 = 0^\circ$, independently from the value of F . Thus, $D(\beta_0 = 0^\circ)$ is the maximum distance at which a transmitter-receiver link could be established using one-hop propagation through a single ionospheric layer following a QP model. In this example representative of a typical F layer, the maximum ground distance for a one-hop transmission reads approximately 3200 km. Note that a ray elevation angle $\beta_0 = 0^\circ$ corresponds to a direction of departure tangential to the Earth curvature. While this situation is coherent with the QP model, where the Earth takes the theoretical shape of a sphere, it may not be realizable in practice. In a practical HF setup, the farthest one-hop link would be achieved with a departure angle pointing slightly over the horizon.

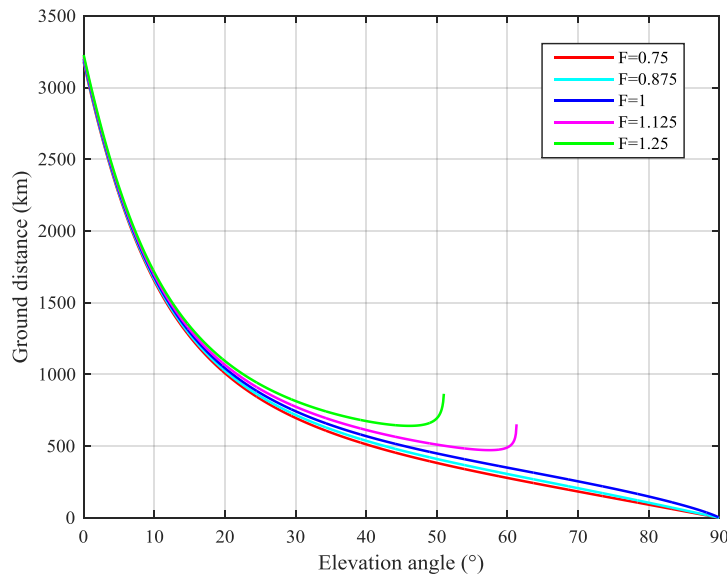


Figure 3.3 Plots of ground distances at different values of F using QP layer model

The second observation from Figure 3.3 is that the ground distance D decreases as the elevation angle β_0 increasingly departs from 0° . When the operational frequency is lower than the critical frequency, i.e. when parameter F takes values lower than 1, the ground distance D decreases down to 0 for a vertical incidence ($\beta_0 = 90^\circ$). In contrast, skip distance occurs when the critical frequency of a layer is lower than the operational frequency of the signal [95]. The skip distance can be found by calculating the minimum value of the ground distance for the curves represented by $F > 1$. As explained earlier in section 2.2.1 and seen in Figure 3.3, the ground distance starts increasing again with increasing β_0 after the skip distance is reached; it is due to high rays (or Pedersen rays) whereas, the ground distance before the skip distance is achieved is due to low rays. Skip distance is a point where both the high and the low rays of a signal coincide. Note that the concept of skip distance is only related to ground distance and not to the group path distance. Finally, one observes that for each value of F , there exist a maximum value of β_0 beyond which the HF ray is not refracted towards Earth anymore but is diverted towards higher altitudes.

Figure 3.4 represents the group path P as a function of the elevation angle β_0 , plotted using the QP layer model for different values of F . The curves are obtained from the analytical expression of equation 3:5, with the same layer parameters as used in Figure 3.3. At first, a similar behavior with respect to the elevation angle is observed for the group path distance as for the ground distance. There exists a maximum group path distance obtained at an elevation angle $\beta_0 = 0^\circ$, which is not dependant on the parameter F . In addition, the group path distance is initially decreasing while β_0 take increasing values above 0° .

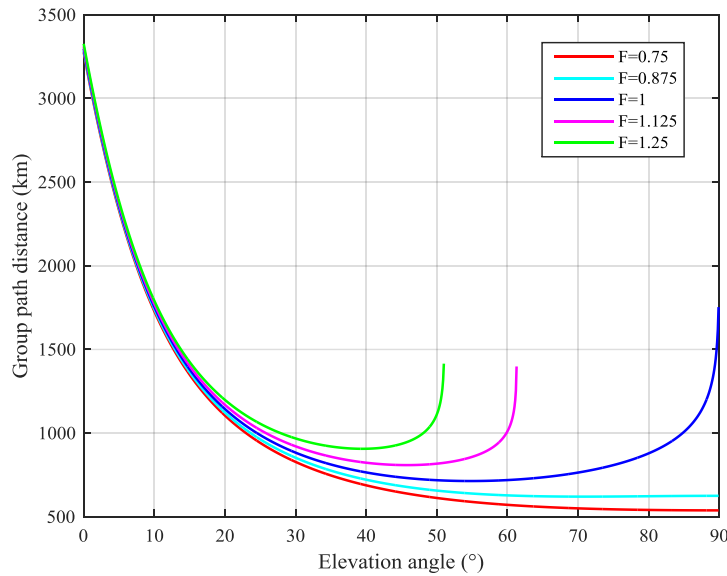


Figure 3.4 Plots of group path distances at different values of F using QP layer model

A surprising behavior is observed, however, when considering the values taken by the group path distance at higher elevation angles. Take for instance the case of vertical incidence ($\beta_0 = 90^\circ$): while this incidence does not allow one-hop transmission for values of $F > 1$, transmission is possible when the operational frequency is lower than or equal to the critical frequency ($F \leq 1$). However, the group path distance increases with increasing F , and eventually takes an infinite value for $F=1$. This can be explained by considering the refractive index and the group velocity within the ionosphere, as explained in the following paragraphs.

The QP layer model considers the refractive index of the ionospheric medium while deriving the analytical expressions for the ray path parameters. The refractive index (μ) is defined by neglecting the earth's magnetic field and the electron collisions in the QP layer model. It is expressed by the following equation:

$$\mu^2 = 1 - \left(\frac{f_N}{f}\right)^2 \quad 3.10$$

The electron density varies with the altitude in the ionosphere. For $N = N_m$, the plasma frequency is equal to the critical frequency of the ionospheric layer leading to the least refractive index at the height of maximum electron density. Thus, the refractive index varies with the altitude in an ionospheric layer. In the case of ionospheric propagation, the group velocity is given by the following equation [96]:

$$v_g = c\mu \quad 3.11$$

In addition, by substituting the value of μ from equation 3.10, equation 3.11 can be expressed as:

$$v_g = c \sqrt{1 - \left(\frac{f_N}{f}\right)^2} \quad 3.12$$

From equation 3.12, it is clear that the group path velocity will be equal to zero at the height of electron density resulting in $N = N_m$, provided both the operating and critical frequencies are the same. This condition results in infinite travel time of the radio signal. As mentioned earlier, the group path distance corresponds to group travel time multiplied with the speed of light leading to an infinite group path distance. This case is a singularity inherent to the theoretical QP model and does not occur in practical conditions in the ionosphere. Due to similar considerations on the varying group velocity, the elevation angle β_0 at which the group path distance reaches a minimum for a given value of $F > 1$ does not coincide with the elevation angle providing the minimum value of the ground distance. However, the curved shape of the graphs on Figure 3.4 still results from the existence of both low and high rays.

As another example of the simple ionospheric model, the electron density profile model that assumes a quasi-linear ionospheric layer and the analytical expressions to compute the different ray path parameters are explained in [97]. Recently, two errors in the analytical expressions were corrected and published as errata [98].

3.1.2 Composite models

These models estimate the electron density profile of two or more layers of the ionosphere at the same time. A two-parabola is the simplest composite model where one parabola represents the electron density profile of the E layer while the other parabola represents the profile for the F₂ layer and is explained in [99]. Another model representing the variation of electron density in the E, F₁ and F₂ layers of the ionosphere was proposed by Dudeney in 1978 [100]. Also, equations to obtain the different ray path parameters for a multisegment QP ionosphere are explained in detail in [101].

Based on the different models differentiated as simple and complex, the electron density profile along the propagation path can be evaluated. The QP model of the ionosphere provides analytical expressions to compute the ground range and group path for a radio signal propagating through the ionosphere by a one-hop mode. The principles of time-domain HF geolocation algorithm along with their mathematical description are explained in section 3.2.

3.2 HF geolocation algorithm

The proposed HF geolocation algorithm to find an estimate of the transmitter's geographic location without any knowledge of the ionospheric reflection height along the propagation path is explained.

3.2.1 HF geolocation principle and assumptions

In order to develop an HF geolocation algorithm that could be independent from the knowledge of the ionospheric parameters, the problem complexity is reduced by making 3 assumptions, namely the assumptions of *one-hop transmission*, of *uniform ionosphere with negligible apogee height variation* and of *flat Earth*.

For geolocation of HF transmitters in the range of 500-3000 km, one can assume a *one-hop transmission*. This assumption is practicable, since at distances between 500 and 3000 km, the one-hop mode is the most probable geometrical propagation mode. Propagation may even occur with multi-hop modes, but propagation through 1E and 1F mode will be the least attenuated; thus can be considered as the main contributions of the received signals.

The ionospheric variations at mid-latitudes are negligible when compared to the variations at poles and equator. In addition, the ionospheric variations over Europe are very low. Hence, we assume a *uniform ionosphere with negligible apogee height variation* for all the HF paths. Figure 3.5 (a) and (b) represents the calculated median monthly critical frequencies for E and F₂ layer of the ionosphere using the ionograms recorded every day with an interval of 10-15 minutes in March, 2016 at Pruhonice, Czech Republic and Chilton, United Kingdom, respectively. These recorded data from different ionosondes are available online [16]. It can be observed that the median monthly critical frequencies at different hours of a day for E and F₂ layers are approximately the same at both locations which are far away from each other. Also, results presented in [102] show that the quiet time ionospheric TEC (section 2.1.4.2) over Europe are mostly similar.

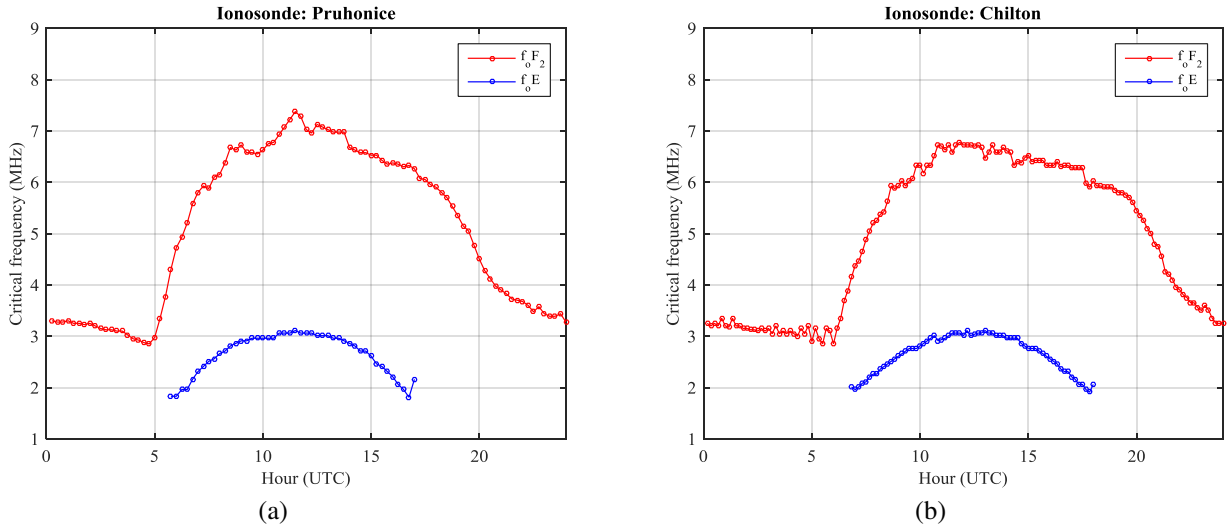


Figure 3.5 Estimated median critical frequencies for E and F₂ layer of the ionosphere using all measured ionospheric parameters in March, 2016 at 2 different ionosondes in Europe, particularly at Pruhonice in Czech Republic (a) and at Chilton in England (b)

Figure 3.6 presents the group paths for ground ranges corresponding to one-hop HF links by assuming the Earth to be flat and spherical. The group paths corresponding to their ground ranges are computed using a specular reflection model with a reflection height of 250 km. It can be observed that the difference between the group paths with flat and spherical Earth increases as the ground range increases. At ground range of about 2000 km, the group path error by assuming the Earth to be flat is around 35 km. Hence, the third assumption of *flat Earth* will result in error if the transmitter is located far away from the receiver network. A detailed study on the geolocation error due to the assumption of flat Earth is explained in Appendix D.

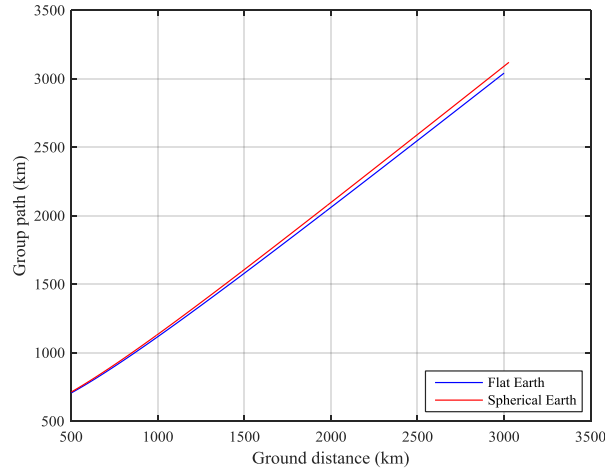


Figure 3.6 Plot of ground range versus group path for the case of flat and spherical Earth

Under the assumption of one-hop transmission, the signal reaches the destination via a single reflection from the ionospheric layer. Figure 3.7 represents HF geolocation geometry considering a uniform and single layer ionosphere. The transmitter is located at point Tx and the receivers are located at point Rx₁ and Rx₂. As per the Breit and Tuve's theorem which is explained earlier, the group path between Rx₁ and Tx represented by the red curved path is equal to the black triangular path Rx₁-I₁-Tx in vacuum and the same applies for Rx₂ and Tx.

Due to the varying refractive index in the ionosphere, the signals propagate along a curved path. The apogee height for the group path length is indicated by h_a . An equivalent height h_{equ} corresponding to the reflection height of a path with same group delay can be defined assuming the signals are reflected via specular reflection from a flat ionosphere. The ionosphere is assumed to be uniform; in addition we neglect the variation of the apogee height for different Rx-Tx links with similar elevation angles. Thus, the reflection height is assumed to be identical for all the considered paths and equal to h_{equ} . The Earth is considered to be flat by neglecting its curvature. The effect of the Earth's magnetic field is also ignored. Results presented in [103] showed that the geolocation errors calculated using the angle of arrival (AoA) method by neglecting the earth's magnetic field are generally smaller at mid-latitudes which is the region of interest for our study.

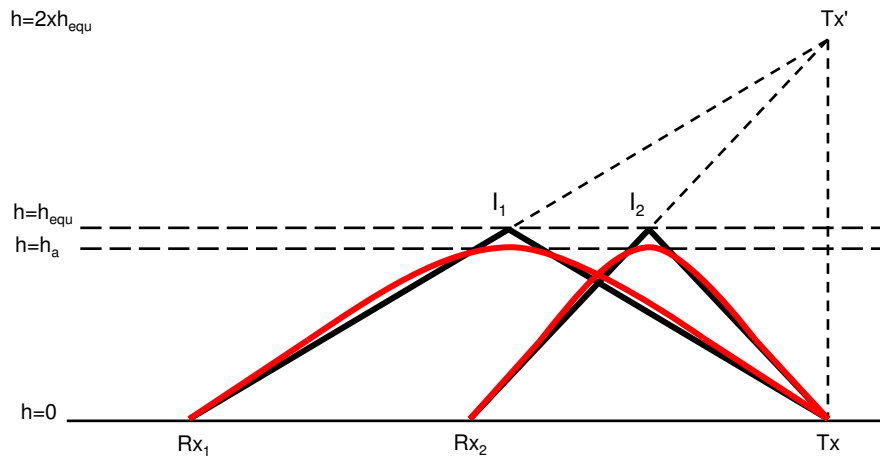


Figure 3.7 Geometry of the HF localization principle assuming uniform single layer ionosphere

Due to electromagnetic image theory, the length of propagation path between Rx₁-Tx is equal to Rx₁-I₁-Tx'; similarly the propagation path between Rx₂-Tx is equal to Rx₂-I₂-Tx'. The geolocation process consists in

finding the coordinates of Tx' situated at a height of $2h_{equ}$ vertically above the location of the transmitter on the flat earth surface. If the propagation time between the transmitter and different receivers are known, the coordinates of Tx' can be found by trilateration. When the transmission time is unknown, the coordinates of Tx' can be found by multilateration using time TDoA between different receivers.

The geometrical problem of identifying the intersection of three spheres or three hyperboles requires solving systems of quadratic equations which need linearization to be solved analytically. A mathematical approach to obtain the location of Tx' is explained further for the ToA and TDoA case, which is based on the developments in [81].

3.2.2 Mathematical approach: ToA

Let the receivers (Rx_i) be located at position $\mathbf{P}_i = (x_i, y_i, z_i)$ where $i = 1, 2, 3 \dots n$; the transmitter on the flat earth surface is located at position $\mathbf{P}_0 = (x_0, y_0, z_0)$. The coordinates of point Tx' which is located $2h_{equ}$ vertically above the location of the transmitter on the flat Earth surface are represented by position $\mathbf{P}_0' = (x_0, y_0, z_0')$ where z_0' is given by the following equation:

$$z_0' = z_0 + 2h_{equ} \quad 3.13$$

The length of propagation path (group path) between a transmitter and a specific receiver via a single reflection from the ionosphere (one hop) can be evaluated as follows:

$$P_i = c(t_i - t_0) = \|\mathbf{P}_0' - \mathbf{P}_i\| \quad 3.14$$

where t_i is the signal arrival time at the i^{th} receiver, t_0 is the signal transmit time, c is the speed of light, P_i is the propagation path length between the transmitter and the i^{th} receiver; $\|\ \|$ represents the norm.

Using three receivers, a system of three quadratic equations with three unknowns are obtained. In order to linearize this problem, squaring equation 3.14 results in the following:

$$P_i^2 = \|\mathbf{P}_0' - \mathbf{P}_i\|^2 = c^2(t_i - t_0)^2 \quad 3.15$$

Using equation 3.14, the group path lengths from a transmitter to different receivers can be evaluated. Computing the difference between equation 3.15 at $i = 1$ (Rx₁) and equation 3.15 at $i = 2$ (Rx₂), one obtains the following equation:

$$P_2^2 - P_1^2 = \|\mathbf{P}_0' - \mathbf{P}_2\|^2 - \|\mathbf{P}_0' - \mathbf{P}_1\|^2 = c^2 [(t_2 - t_0)^2 - (t_1 - t_0)^2] \quad 3.16$$

After further simplification, equation 3.16 can be written as follows:

$$2(\mathbf{P}_2 - \mathbf{P}_1)^T \mathbf{P}_0' = (\|\mathbf{P}_2\|^2 - \|\mathbf{P}_1\|^2) - c^2 [(t_2 - t_0)^2 - (t_1 - t_0)^2] \quad 3.17$$

where T represents the transpose operator.

Similarly by evaluating the difference between receiver pairs 2-3 and 1-3; one obtains two more equations which are similar to equation 3.17. Hence we obtain a system of three linear equations with three unknowns of the following form:

$$\begin{cases} a_{11}x_0 + a_{12}y_0 + a_{13}z_0' = b_1 \\ a_{21}x_0 + a_{22}y_0 + a_{23}z_0' = b_2 \\ a_{31}x_0 + a_{32}y_0 + a_{33}z_0' = b_3 \end{cases} \quad 3.18$$

The constants of first row of equation 3.18 are obtained by comparing it with equation 3.17, which is as follows:

$$\begin{aligned} a_{11} &= 2(x_2 - x_1); a_{12} = 2(y_2 - y_1); a_{13} = 2(z_2 - z_1) \\ b_1 &= x_2^2 - x_1^2 + y_2^2 - y_1^2 + z_2^2 - z_1^2 - c^2 [(t_2 - t_0)^2 - (t_1 - t_0)^2] \end{aligned} \quad 3.19$$

Likewise the constants of other two rows of equation 3.18 can be obtained from other two equations computed considering different receiver pairs as explained earlier.

The system of equation 3.18 is of rank 2 where the 3rd equation can be obtained as a linear combination of the 1st and 2nd equation, respectively. However, the number of unknowns can be reduced by assuming that all receivers are situated on the flat Earth surface. So one can consider $z_1 = z_2 = z_3 = z_0$; this results in $a_{13} = a_{23} = a_{33} = 0$ and the system to solve is reduced to:

$$\begin{cases} a_{11}x_0 + a_{12}y_0 = b_1 \\ a_{21}x_0 + a_{22}y_0 = b_2 \end{cases} \quad 3.20$$

The transmitter coordinates (x_0, y_0) can be obtained by solving equation 3.20. The value of z_0' can be obtained by substituting (x_0, y_0) in equation 3.15. Finally, the equivalent height h_{equ} can be obtained by resolving equation 3.15.

Note: Equation 3.20 can be realized in the following form:

$$(x_0, y_0)^T = \mathbf{A}^{-1}\mathbf{B} \quad 3.21$$

where $\mathbf{A} = \begin{bmatrix} a_{11} & a_{12} \\ a_{21} & a_{22} \end{bmatrix}$ and $\mathbf{B} = \begin{bmatrix} b_1 \\ b_2 \end{bmatrix}$.

In the case of N receivers where $N > 3$, \mathbf{A} is a $(N - 1) \times 2$ matrix, \mathbf{B} is a vector of $N - 1$ elements, and the system is solved using the pseudo inverse \mathbf{A}^+ of matrix \mathbf{A} :

$$(x_0, y_0)^T = \mathbf{A}^+\mathbf{B} \quad 3.22$$

The pseudo inverse can be calculated using the following equation:

$$\mathbf{A}^+ = [\mathbf{A}^H\mathbf{A}]^{-1}\mathbf{A}^H \quad 3.23$$

where \mathbf{A}^H is the conjugate transpose (also known as Hermitian transpose) of matrix \mathbf{A} .

It is interesting to observe that adding more receivers leads in an increase in the algorithm accuracy. Indeed, using the pseudo-inverse operator leads to a solution that is optimum in the least square sense, thus averaging out possible errors linked with a particular receiver.

3.2.3 Mathematical approach: TDoA

In the case of TDoA, the transmission time t_0 is unknown. Equation 3.17 can be written in the following form:

$$\frac{-2(\mathbf{P}_2 - \mathbf{P}_1)^T\mathbf{P}_0'}{t_2 - t_1} + 2c^2t_0 = (t_1 + t_2)c^2 - \frac{(\|\mathbf{P}_2\|^2 - \|\mathbf{P}_1\|^2)}{t_2 - t_1} \quad 3.24$$

As all the receivers are situated on the earth surface, one can consider $z_1 = z_2 = z_3 = z_0$. After simplification, the equation 3.24 can be expressed as follows:

$$\frac{-2(\mathbf{P}_{2(x,y)} - \mathbf{P}_{1(x,y)})^\top \mathbf{P}_{0(x,y)'}}{t_2 - t_1} + 2c^2 t_0 = (t_1 + t_2)c^2 - \frac{(\|\mathbf{P}_{2(x,y)}\|^2 - \|\mathbf{P}_{1(x,y)}\|^2)}{t_2 - t_1} \quad 3.25$$

Furthermore, in the case of TDoA, time delays between different receivers are calculated with regards to a reference receiver. So with 3 receivers, one can obtain two linear equations with 3 unknowns (the x and y coordinates of point \mathbf{P}_0' , and the transmit time t_0). Thus, to obtain the 3 unknowns, a 4th receiver is used. Then, by considering the reference receiver as Rx_1 , the above equation can be generalized as follows for the three receiver pairs (1-2, 1-3 and 1-4):

$$\frac{-2(\mathbf{P}_{i(x,y)} - \mathbf{P}_{1(x,y)})^\top \mathbf{P}_{0(x,y)'}}{t_i - t_1} + 2c^2(t_0 - t_1) = (t_i - t_1)c^2 - \frac{(\|\mathbf{P}_{i(x,y)}\|^2 - \|\mathbf{P}_{1(x,y)}\|^2)}{t_i - t_1} \quad 3.26$$

As a result, a linear system of three independent equations with three unknowns is obtained with 4 receivers:

$$\begin{cases} a_{11}x_0 + a_{12}y_0 + a_{13}\Delta = b_1 \\ a_{21}x_0 + a_{22}y_0 + a_{23}\Delta = b_2 \\ a_{31}x_0 + a_{32}y_0 + a_{33}\Delta = b_3 \end{cases} \quad 3.27$$

where $\Delta = (t_0 - t_1)$. Constants of 1st row of equation 3.27 for receiver pair 1-2 are obtained from equation 3.26 and are given by:

$$\begin{aligned} a_{11} &= \frac{-2(x_2 - x_1)}{t_2 - t_1}; \quad a_{12} = \frac{-2(y_2 - y_1)}{t_2 - t_1}; \quad a_{13} = 2c^2 \\ b_1 &= c^2(t_2 - t_1) - \frac{(x_2^2 - x_1^2)}{t_2 - t_1} - \frac{(y_2^2 - y_1^2)}{t_2 - t_1} \end{aligned} \quad 3.28$$

From equation 3.26 and the above expressions, it can be seen that the geolocation algorithm based on TDoA is dependent on the reference receiver (as most of the constants of equation 3.27 will vary with the value of t_1 as Rx_1 is considered the reference receiver). From receiver pairs 1-3 and 1-4, constants of the other rows of equations 3.27 can be found in a similar manner.

3.2.3.1 Algorithm outputs and validation

The transmitter coordinates (x_0, y_0) and Δ can be obtained by doing a simple matrix inversion operation as follows:

$$(x_0, y_0, \Delta)^\top = \mathbf{A}^{-1}\mathbf{B} \quad 3.29$$

$$\text{where } \mathbf{A} = \begin{bmatrix} a_{11} & a_{12} & a_{13} \\ a_{21} & a_{22} & a_{23} \\ a_{31} & a_{32} & a_{33} \end{bmatrix} \text{ and } \mathbf{B} = \begin{bmatrix} b_1 \\ b_2 \\ b_3 \end{bmatrix}.$$

As for the ToA algorithm, in the case of N receivers where $N > 4$, \mathbf{A} is a $(N - 1) \times 3$ matrix, \mathbf{B} is a vector of $N - 1$ elements, and the system is solved using the pseudo inverse \mathbf{A}^+ of matrix \mathbf{A} :

$$(x_0, y_0, \Delta)^\top = \mathbf{A}^+\mathbf{B} \quad 3.30$$

As in the ToA procedure, using the pseudo-inverse computation for a large number of receivers allows a better algorithm output accuracy. The paragraphs below discuss the possible outputs of the algorithm and their interpretation.

Time causality: The parameter $\Delta = (t_0 - t_1)$ obtained has to be negative as $t_1 > t_0$ in any time reference frame. If Δ is not negative, it means that the algorithm output is not causal and the measured TDoA's are erroneous. This could be a cause of rejection of the geolocation result. Further, if the geolocation algorithm leads to causal output (i.e. where $\Delta = (t_0 - t_1)$ is negative), one can compute the propagation durations of the signals at each receiver. Propagation durations the signals took to travel from the transmitter to the different receivers correspond to the values $t_1 - t_0$, $t_2 - t_0$, $t_3 - t_0$ and $t_4 - t_0$. They can be evaluated from the TDoA's and the algorithm output as follows:

$$t_1 - t_0 = -\Delta \quad 3.31$$

$$t_2 - t_0 = -\Delta + (t_2 - t_1) \quad 3.32$$

$$t_3 - t_0 = -\Delta + (t_3 - t_1) \quad 3.33$$

$$t_4 - t_0 = -\Delta + (t_4 - t_1) \quad 3.34$$

If the four propagation durations are all greater than zero, the algorithm output is causal. If one of these values is negative, then the algorithm output is not causal and the measured TDoA's are erroneous. Again, this could be a cause of rejection of the geolocation result.

Distance physicality: If all obtained propagation durations are causal (i.e. greater than 0), then the group paths for the different HF links between the Tx and different receivers can be computed. The obtained propagation durations are multiplied with the speed of light to obtain different group paths for the different HF links. As the receiver locations are known and from the estimated Tx coordinates (i.e. x_0, y_0), ground distances can be calculated.

In the case of HF radio signals propagating using skywaves through the ionosphere, the group path distance is always greater than the corresponding ground distance. The calculated group paths and the corresponding ground distances are compared to determine whether the geolocation result is acceptable or not. If all group paths are not greater than the corresponding ground distances, the geolocation result is rejected as the obtained distances are not physical in realistic scenarios.

Geolocation validity: If the algorithm output is fully causal (i.e. transmission time is earlier than any of the reception times) and the algorithm output is physical (i.e. all the obtained group paths are greater than the corresponding ground distances), then the geolocation algorithm output is said to be valid. For all other cases, the geolocation algorithm output is said to be invalid.

Ionospheric reflection height: If the geolocation output is valid, one can compute the ionospheric reflection height of the radio signals. Equation 3.15 can be used to evaluate the ionospheric reflection height, assuming a flat earth surface, and is given by the following equation:

$$h_{equ} = \frac{1}{2} \sqrt{c^2(t_i - t_0)^2 - ((x_i - x_0)^2 + (y_i - y_0)^2)} \quad 3.35$$

From the estimated ionospheric reflection height, one can identify the layer from which the reflection occurs. If the obtained height is between 60 and 120 km, it can be said that the reflection occurs via the E layer of the ionosphere. Alternately, if the obtained height is between 150 and 350 km, the reflection occurs via the F layer of the ionosphere. In case the reflection height is computed for an invalid geolocation case, it will result in a complex height which again is due to the erroneous measured TDoA's.

The HF geolocation algorithm provides an estimate of the transmitter location independent from the knowledge of the ionospheric profile along the propagation path. Based on the algorithm outputs, the geolocation can be classified as valid and invalid. Using the analytical expressions of the QP layer model explained in section 3.1.1.2 and the HF geolocation algorithm, simulations are done to evaluate the geolocation performance with respect of different parameters and presented in section 3.3.

3.3 Simulation results and analysis

This section presents the simulation results and their analysis in detail. The simulations are conducted using the HF geolocation algorithm and the QP layer model of the ionosphere explained in sections 3.2 and 3.1.1.2, respectively. The QP layer model is used to compute the ray path parameters. The effect of the receiver location and the number of receivers on the geolocation accuracy for both ToA and TDoA methods are discussed.

3.3.1 Receiver positioning

In the case of LOS propagation, the receiver placements relative to the source location have an impact on the localization accuracy when estimated using the ToA and TDoA methods [104]. The effect of different receiver location configurations for HF source geolocation using different time-domain methods are explained in the following section. It must be noted that the HF radio signals arrive at the receivers through NLOS mode (i.e. propagation using skywaves).

3.3.1.1 ToA method

Simulations are done to evaluate the effect of different receiver placement configurations on the HF source geolocation accuracy. Figure 3.8 shows the locations of all 10000 transmitters on a square grid of side 4000 km. Figure 3.9 represents the geolocation errors and their corresponding cumulative distributive functions (CDF's) in locating these transmitters for different receiver configurations. The minimum number of receivers (i.e. three) required by the ToA method are used to locate the transmitter and their position are marked by “+” green symbols in (a), (c) and (e) of Figure 3.9. It is considered that the electron density profile in the ionosphere follows a QP layer model and the radio signals arrive at the receivers through one-hop propagation mode. The group path distances between the different receivers and all transmitters on the square grid are calculated using the analytical expression of the QP layer model. More precisely, for each considered Tx-Rx link, the elevation angle β_0 is first deduced from the ground distance D using equation 3.3, and the group path distance P is then computed from the elevation angle β_0 using equation 3.8. The propagation durations for the different HF links on the grid are found by dividing the obtained group path distances with the speed of light.

The values used to define the QP layer model in all the simulations for receiver positioning study are: $F = 0.8$, $r_m = 300$ km, and $y_m = 100$ km, which represents a transmission at a frequency below the ionospheric critical frequency in a typical F layer. The height of maximum ionization r_m and the layer semi-thickness y_m are assumed to be fixed, thus leading to a uniform ionosphere. The HF transmitter coordinates can be found at the intersection of spheres using the ToA geolocation algorithm explained in section 3.2.2. Finally, the geolocation error is evaluated by computing the difference between the true location and the estimated location. All the geolocation errors greater than 100 km are represented by the black color.

Note that the proposed geolocation algorithm is exact in the sense that it exactly retrieves the Tx location provided the simulated Tx-Rx links meets the underlying assumptions of *one-hop transmission*, of *uniform ionosphere with negligible apogee height variation* and of *flat Earth*. In other words, if one used a simplistic

model of the ionosphere represented by a mere specular reflection at a fixed height, the geolocation error would be zero for any simulated Tx-Rx link. The QP model as used in the following study is a more realistic model of the ionosphere that departs from the ideal conditions assumed by the algorithm. More precisely, the QP model still considers a one-hop transmission and a uniform ionosphere over the grid of possible transmitter locations. However, the QP model renders different ray apogee heights for transmission paths with different elevation angles, and accounts for the Earth curvature. Thus, the geolocation error observed in the simulations below can be interpreted as the direct effects of infringing the assumptions of *negligible apogee height variation* and *flat Earth*.

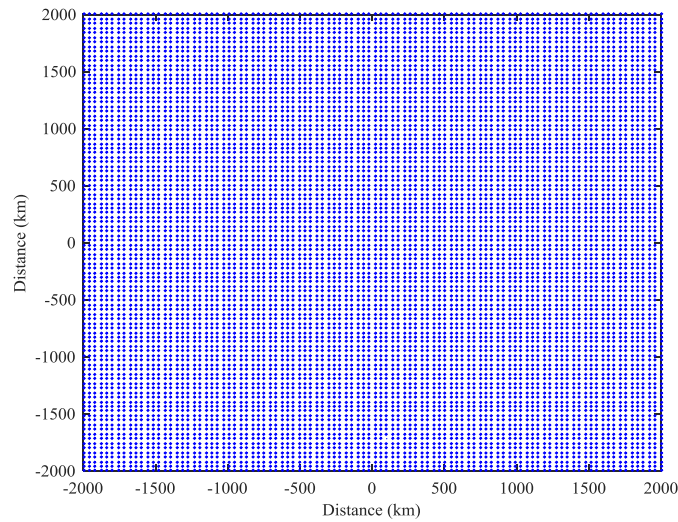
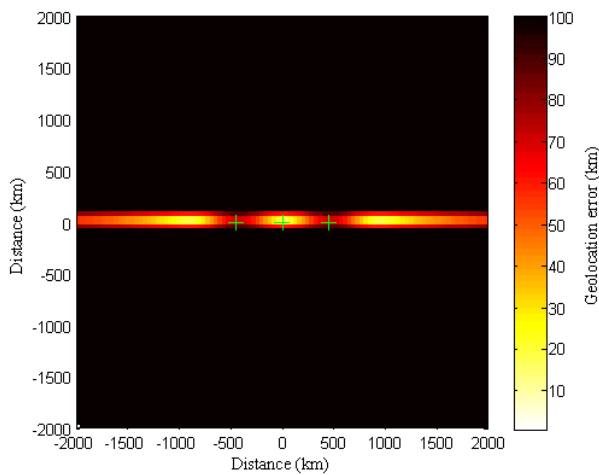
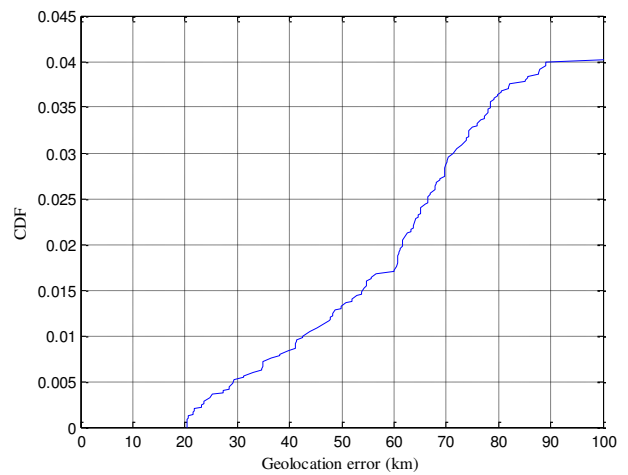


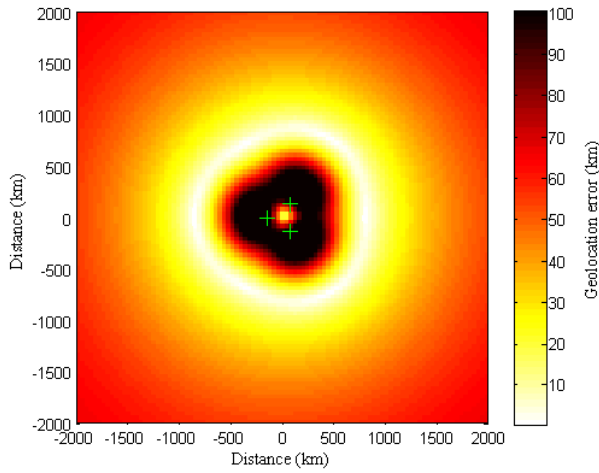
Figure 3.8 Location of all transmitters on the square grid



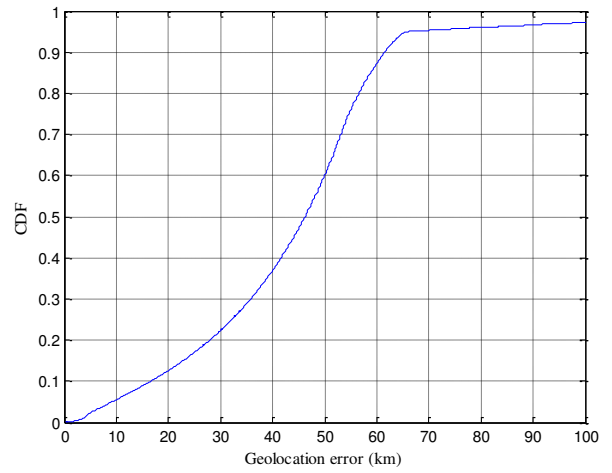
(a): Straight line



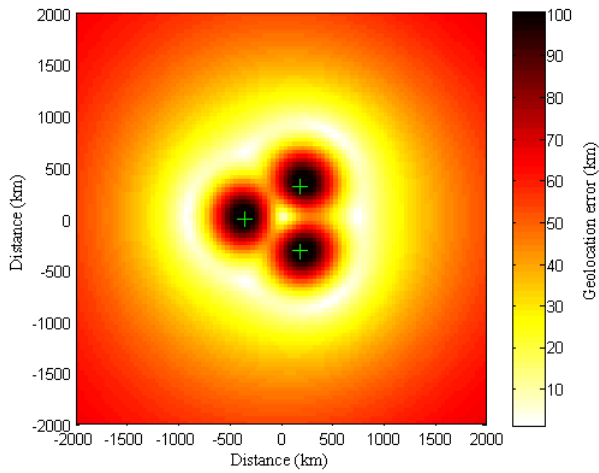
(b): Geolocation error CDF plot for (a)



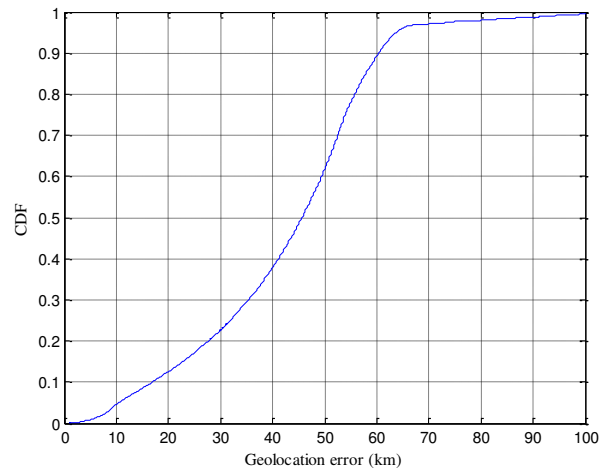
(c): Smaller equilateral triangle



(d): Geolocation error CDF plot for (c)



(e): Larger equilateral triangle



(f): Geolocation error CDF plot for (e)

Figure 3.9 Geolocation errors and CDF's obtained using ToA method assuming a QP layer for different receiver configurations, receivers placed on a straight line in (a), at vertices of an equilateral triangle of 260-km side in (c), and at vertices of a larger equilateral triangle with 625-km side in (e) while their corresponding CDF's can be seen in (b), (d) and (f), respectively

Case 1: The three receivers are placed in a straight line equidistant from each other as seen in (a) of Figure 3.9. The distance between all neighboring receivers are 450 km. This is the maximum distance at which the receivers can be placed further apart from each other for this square grid of 4000 km. Any further increase in the distance among the receivers leads to a condition where one of the receivers is beyond the radio horizon for one or more Tx's placed on the square grid. Thus the signal will be received only by 2 receivers and the algorithm will not be able to estimate the Tx coordinates. In Figure 3.9 (a), it can be observed that the geolocation error is very large across the whole grid except along the horizontal axis of the square grid. One of the reasons for the higher geolocation error is the large variation of the equivalent height between the transmitter and different receivers when they are placed in a straight line. Another reason for the higher geolocation error is geometric dilution of precision (GDOP). It affects the localization accuracy w.r.t the receiver-transmitter geometry, for localization based on ToA and TDoA methods [104].

Case 2: The three receivers are placed in a manner that it forms an equilateral triangle as seen in (c) of Figure 3.9. The length of each side of the equilateral triangle is about 260 km. This receiver configuration can also be interpreted as three receivers placed uniformly along the circumference of a circle with radius of 150 km. As seen in (c) of Figure 3.9, one can observe very large geolocation error for Tx located at distances less than 500 km from a receiver. Again, the reason for higher geolocation errors is the large variation of the

equivalent height between the transmitter and different receivers when they are placed close to each other. Also, at such short distances, the assumption of one-hop propagation in a QP layer ionosphere does not seem to be valid. However, for Tx in the range of 650-1250 km from the center of the grid, the observed geolocation error is very small (i.e. less than 30 km). Finally, as the Tx station moves away from the origin of the square grid, the geolocation error increases up to about 50 km when the Tx station is located 2000 km away from the origin.

Case 3: Again, the three receivers are placed in a manner that it would form an equilateral triangle as seen in (e) of Figure 3.9 but the length of each side of the equilateral triangle is about 625 km. Moreover, this receiver configuration can be interpreted as three receivers uniformly placed along the circumference of a circle with radius of 360 km. In this case, the length of each side is increased to see if the geolocation error changes for Tx which are very close around the center of the grid. Moreover, this is the maximum distance at which the receivers can be placed apart from each other for this configuration of receiver placement. As seen in (e) of Figure 3.9, one can see that the geolocation error is reduced to some extent around the origin of the grid. Errors when Tx is very close to the receiver locations are still higher due to large variations in equivalent height difference. The geolocation errors for Tx's in the range of 600-2000 km from the origin are similar to the pervious case.

Table 3.1 provides the summary of geolocation errors obtained for all transmitters on the square grid using the ToA method for different receiver configurations. It is also clear that the receivers must not be placed in a straight line as it is largely affected by GDOP. An equilateral triangle with maximum possible lengths between the receivers implied that the receivers fall within the radio horizon of the Tx, results in better geolocation accuracy.

Receiver configuration	Geolocation error ≤ 90 km
Straight line	4%
Equilateral triangle (side length: ≈ 260 km)	96%
Equilateral triangle (side length: ≈ 625 km)	99%

Table 3.1 Geolocation accuracy evaluated using ToA method for different receiver configurations

3.3.1.2 TDoA method

An optimal receiver distribution for locating the Tx using 4 station TDoA system is explained in [105] by presenting the positioning errors and GDOP maps across a square grid for 8 different receiver configurations, assuming that signals arrive through LOS mode. This study showed that the receivers placed to resemble a Y-shape have the largest coverage and the localization accuracy is high as well. In order to study the effect of different receiver configurations on geolocation accuracy for HF radio signals propagating through the ionosphere (skywave mode, i.e. NLOS case), simulations were done to evaluate the geolocation accuracy using the TDoA method.

Figure 3.10 represents the geolocation error in estimating the location of the transmitters on a square grid with a length of 4000 km for different receiver configurations. The location is estimated using the minimum number of required receivers (i.e. 4) by the TDoA method. Using the QP layer model, the propagation durations are evaluated as explained in the previous section. The TDoA's are calculated from the obtained propagation durations. The HF transmitter coordinates can be found by the intersection of three hyperboloids using the TDoA geolocation algorithm explained in section 3.2.3. The geolocation algorithm based on TDoA is dependent on the reference receiver. Thus, the Tx coordinates are calculated considering each receiver as the reference receiver. The final location is obtained by computing the mean of the Tx coordinates obtained from each reference receiver. Finally, the plotted geolocation errors are the difference between the true

locations and the estimated final locations. All geolocation errors greater than 100 km are represented by black color.

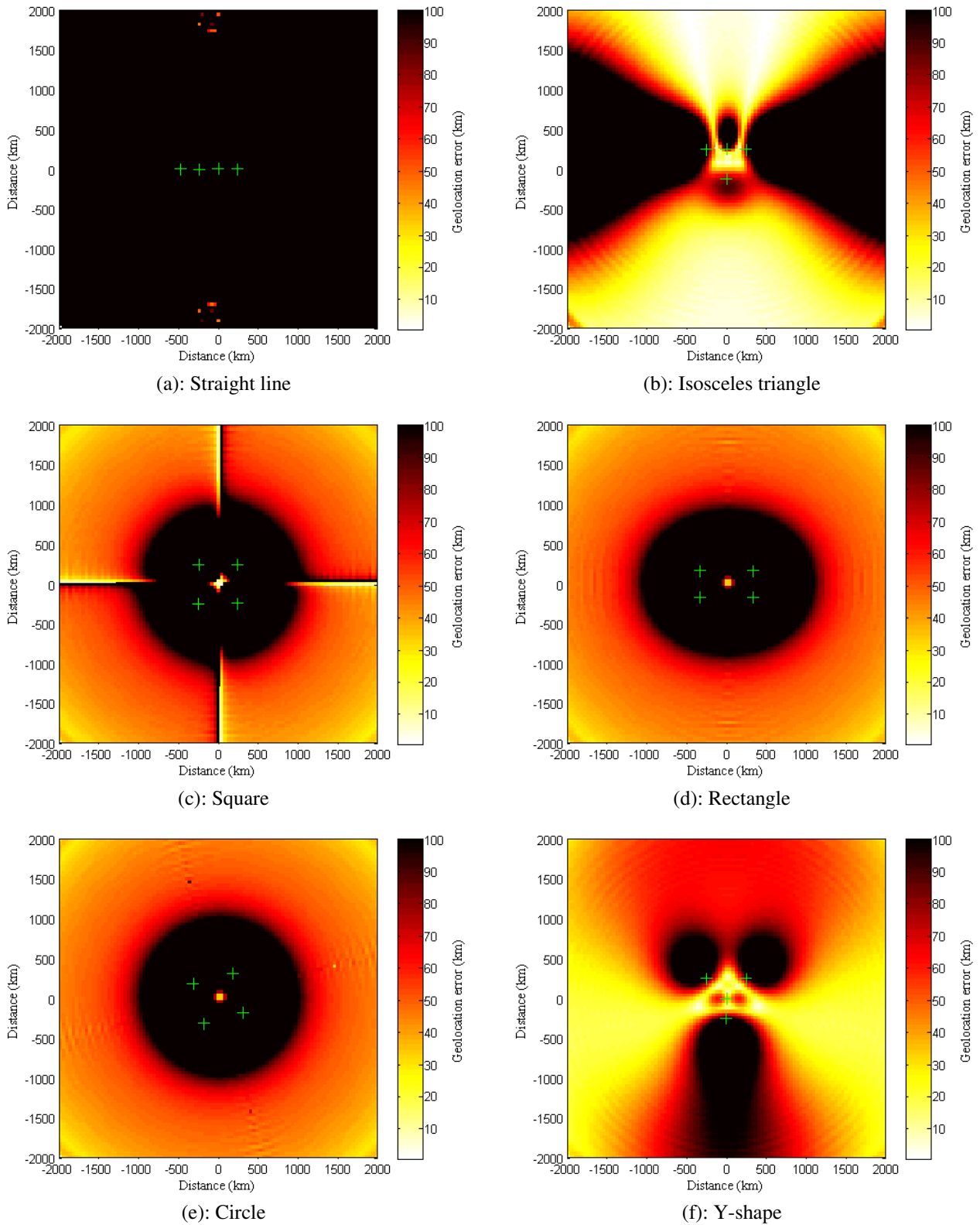


Figure 3.10 Geolocation errors obtained using TDoA method assuming a QP layer for different receiver configurations, receivers configurations resembles approximately a straight line as seen in (a), isosceles triangle in (b), square in (c), rectangle in (d), circle in (e) and y-shape in (f)

The coverage area and the geolocation accuracy are higher when the receivers are placed further away from each other. Thus, the receivers are placed at maximum distance from each other across the square grid for all the following receiver configurations such that the farthest Rx from the farthest Tx (evaluated from the origin) lies within the radio horizon of the Tx. If any one of the Rx lies beyond the radio horizon of the Tx, it cannot receive the signal. In such a case, the Tx location cannot be estimated using the TDoA method.

Case 1: The four receivers are approximately placed in a straight line as seen in (a) of Figure 3.10. If they are placed in an accurate straight line, the Tx location cannot be estimated as the matrix to be solved becomes singular (equation 3.28). The distance between all neighboring receivers is about 235 km. As seen in (a) of Figure 3.10, the observed geolocation error is greater than 100 km almost across the whole grid. The geolocation error is large due to the variation of the equivalent height as a function of the Tx-Rx distance and the geometry of the receivers' w.r.t the Tx location on the grid. For most of the transmitters on the grid, the hyperbolic line of positions (LOP's) generated due to this receiver configuration would be almost parallel when the exact value of TDoA's are known. A slight error in the TDoA's are obtained from the assumption of the QP layer ionosphere whereas the geolocation algorithm assumes a specular reflection from the ionosphere. As a result, the geolocation error is larger across the whole area [106].

Case 2: The four receivers are placed in a way that it represents an isosceles triangle, which can be seen in (b) of Figure 3.10. The length of two sides of the triangle is about 445 km and while the length of the last side is about 495 km. The Tx's located above the receivers at distances in the range of 900-2000 km and at an angle in the range of $\pm 15^\circ$ from the origin could be geo-located with an error of less than 10 km. For the Tx's located below the receivers at distances in the range of 600-2000 km and at an angle in the range of $\pm 45^\circ$ from the origin could be estimated with an error less than 30 km. For Tx's placed on either side of the receivers, the geolocation error was found to be greater than 100 km.

Case 3: In this case, the four receivers are placed such that the receiver configuration looks like a square, as seen in (c) of Figure 3.10. The length of each side of the square formed by the receivers is approximately 490 km. The artifact seen along both axes of the grid in (c) of Figure 3.10 is due to the approximate symmetry formed due to the receiver configuration. The observed geolocation error is greater than 100 km when Tx is located at distances less than 650 km from a Rx station. As explained earlier, this error is mainly due to variation in the equivalent height difference. The Tx located at distances in the range of 1100-2000 km from the origin could be estimated with an error of about 25-50 km. When Tx is far away from the origin, it could be located with a better geolocation accuracy than when it is closer to the origin of the square grid.

Case 4: As seen in (d) of Figure 3.10, the receivers are placed such that it resembles a rectangle. The approximate length and the width of the rectangle are 660 and 330 km respectively. One can observe that the geolocation error along the x axis of the grid is greater than 100 km for distances less than 1200 km from the origin whereas the geolocation error along the y axis of the grid is greater than 100 km for distances less than 800 km from the origin. The transmitter located further away from the origin could be estimated with geolocation error of about 30-70 km.

Case 5: The four receivers are placed at a distance of about 360 km from the origin at angles of about 30° , 120° , 210° and 300° from the origin, respectively. The receiver configuration resembles a circle with a radius of about 360 km as seen in (e) of Figure 3.10. The geolocation errors for the Tx located at distances less than 1000 km from the origin is greater than 100 km. As the Tx location moves further away from the origin, the geolocation error decreases down to 50 km when the Tx is situated at 2000 km from the origin. For Tx located in the range of about 2500 km from the origin, the geolocation error is further reduced down to about 20 km.

Case 6: In this case, the four receivers are placed such that the receiver configuration looks like a y-shape, as seen in (f) of Figure 3.10. This configuration is similar to an isosceles triangle except that one of the receivers is placed within the triangle at the origin of the grid. The length of two sides is approximately equal to 350 km and the length of the other side is about 250 km. As observed in (f) of Figure 3.10, the geolocation error for most of the Tx positions at an angle in the range of $\pm 45^\circ$ from the origin on either sides of the receivers is within 20-60 km. The geolocation errors for the Tx locations at an angle in the range of $\pm 45^\circ$ from the origin and located above the receivers is in the range of 50-80 km except for a few positions located very close to the receivers. The geolocation errors for the Tx positions at an angle in the range of $\pm 15^\circ$ from the origin located below the receivers are higher than 100 km for most cases.

Table 3.2 summarizes the estimated geolocation errors using the TDoA method for different receiver configurations. Using the y-shape receiver distribution, 88% of the geolocation errors across the whole grid are less than 90 km. Square, rectangular and circular receiver distribution provides almost 80% of the geolocation errors less than 90 km. If the Tx to be located is along the north-south direction, the receivers must be distributed as an isosceles triangle whereas if the Tx to be located is along the east-west direction, the receivers must be distributed to resemble a y-shape form. From the geolocation error plots obtained using triangular, rectangular and Y-shape distribution for the TDoA method, it can be said that when the receivers are elongated along the x-direction (horizontal) the geolocation accuracy is better in the y-direction (direction) and vice-versa.

Receiver distribution	Geolocation error ≤ 90 km
\approx Straight line	0.14%
\approx Isosceles triangle	66%
\approx Square	80%
\approx Rectangle	80%
\approx Circle	80%
\approx Y-shape	88%

Table 3.2 Percentage of a given geolocation accuracy evaluated using TDoA method for different receiver configurations

In case the Tx location is unknown, the square distribution is the best as the geolocation accuracy is uniform in all the directions w.r.t the distance from the origin. In square distribution, one can say that the errors are very high when the Tx is very close to the receiver. But in realistic scenario, it is difficult to receive the signals through skywaves via a reflection from the ionosphere when the receiver is located very close to the transmitter. If signals arrive at one of the receiver through ground waves and other receiver through skywaves, the HF geolocation algorithm may fail.

3.3.2 Number of receivers

This section explains the effect of increasing number of receivers on the geolocation accuracy of HF transmitters located far away from all the receivers. The geographic location of the HF transmitter is estimated using the ToA and TDoA method.

3.3.2.1 ToA method

In order to study the effect of more number of receivers on geolocation accuracy, simulations are done using different number of receivers (i.e. 3, 4, 5 and 6) respectively. It is assumed that the electron density profile along the ionosphere is similar to a QP layer model. The QP layer model is defined by the following values $F = 0.8$, $y_m = 100$ km. The propagation durations are obtained as explained earlier in section 3.3.1.1. From the known receiver locations and the obtained propagation duration, the geographic location of the Tx

is estimated using the ToA geolocation algorithm. The value of parameter r_m used to define the height of maximum ionization in the QP layer model is assumed to be fixed or varying as per the Gaussian distribution or varying as a linear gradient along the latitude and longitude of the square grid. This allows the model to render either a uniform ionosphere, or a non-uniform ionosphere with random variation or linear gradient. The obtained geolocation errors for the different cases are explained further.

Case 1: In this case, the height of maximum ionization for the QP layer model is assumed to be fixed at 300 km. Figure 3.11 represents the geolocation error in locating Tx positions all across the square grid of length 4000 km using 4 receivers by the ToA method. The 4 receivers are placed in a manner that it resembles an equilateral triangle with the 3 receivers on the vertices of the triangle and the last receiver at the center of the triangle. The length of each side in the triangle is about 1515 km. The receiver placement also resembles a circular configuration where the radius of the circle is 875 km.

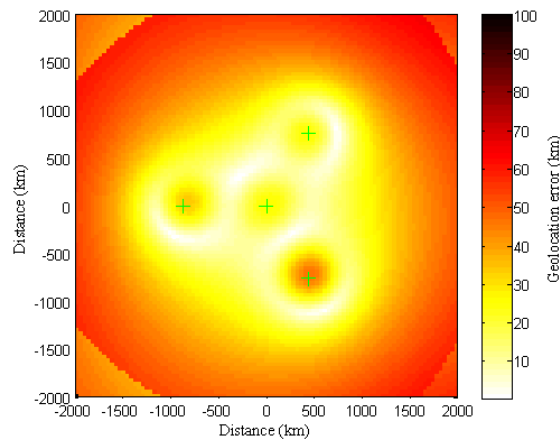


Figure 3.11 Geolocation error obtained using ToA method with 4 receivers assuming a QP layer with a fixed height

The receivers are placed at a maximum distance from the origin of the grid as it results in better geolocation accuracy. Any further increase in the receiver distance from the origin leads to insufficient values of propagation durations required to locate the Tx. This condition arises due to the fact that two receivers are beyond the radio horizon of the Tx located at the farthest distance from the center of the grid. From Figure 3.11, it can be observed that the geolocation error close to the receivers is reduced by a large extent when compared to geolocation done using the minimum number of receivers required by the ToA method. Moreover, all the Tx positions could be located with an error less than about 70 km across the whole grid.

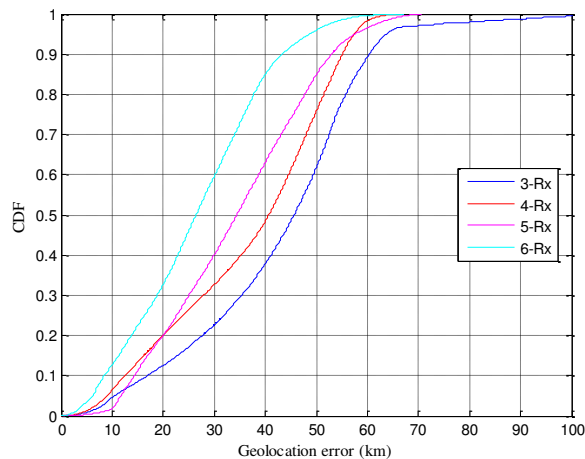


Figure 3.12 CDF of geolocation error obtained using ToA method for different number of receivers assuming a fixed height QP layer

Figure 3.12 presents the CDF of geolocation error in locating Tx positions on a square grid of 4000 km using different number of receivers. The QP layer is defined using a fixed height of 300 km and geolocation is achieved using ToA method. For the 3-Rx curve, the receivers are placed as seen in (e) of Figure 3.9 while for the 4-Rx curve, the four receivers are placed as seen in Figure 3.11. For 5-Rx curve, the five receivers are placed such that the radius of the circle is 1450 km with the 4 receivers placed uniformly at angles of 45° , 135° , 225° and 315° respectively from the center of the circle (also center of the grid) where the last receiver is placed. Again here, this is the maximum distance at which the receivers can be placed from the origin. Finally, for the 6-Rx curve, the six receivers are placed resulting in circle with radius of 1950 km with the 5 receivers placed uniformly at an angle of 72° degree between two neighboring receivers while the sixth receiver is placed at the center of the grid. Here in this case, the distance of the receivers from the origin can be increased further. Larger the number of distributed receivers, larger would be the coverage area. Also, only the receivers which are within the radio horizon (i.e. receives the signal) of the Tx are considered while evaluating the Tx position. From Figure 3.12, it is clear that the geolocation accuracy increases as the number of receivers used for the purpose of geolocation increases. With 3 receivers, 60% of the geolocation errors are less than 50 km whereas with 6 receivers, 60% of the errors are less than 30 km.

Case 2: In this case, the height of maximum ionization to define the QP layer is varied as Gaussian distribution with a mean of 300 km and a variance of 20 km across the square grid. Figure 3.13 shows the geolocation error in locating Tx positions all over the grid using four receivers. The manner in which the receivers are placed is similar to previous case except that the length of each side is about 1470 km. As compared to the case where the QP layer is defined with fixed height, the maximum distance at which the receivers can be placed is reduced due to the varying height of maximum ionization across the grid. As expected, the geolocation accuracy is slightly smaller than compared to the previous case. The geolocation errors for Tx locations distant up to 1200 km from the origin of the grid is in the range of 0-30 km except for a few cases where the Tx locations are very close to the receivers. For Tx locations beyond 1200 km, errors fall in the range of 40-70 km.

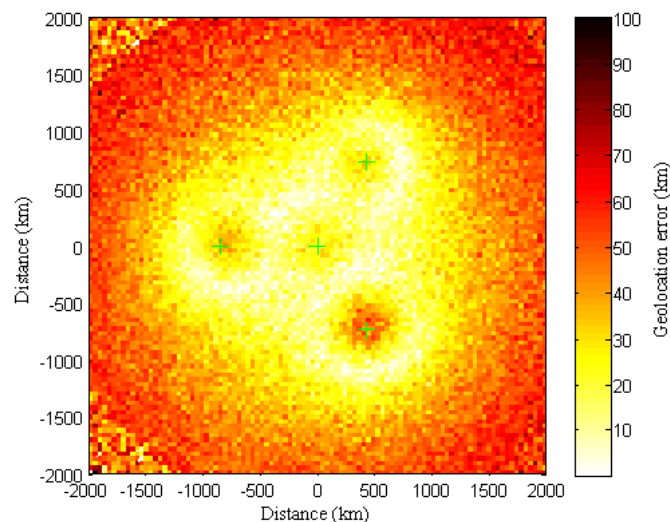


Figure 3.13 Geolocation error obtained using ToA method with 4 receivers assuming a QP layer with variable height following a gaussian distribution

Figure 3.14 presents the CDF of geolocation error in locating Tx positions on a square grid of 4000 km for different number of receivers. The height of maximum ionization is varied as per a Gaussian distribution with mean of 300 km and a variance of 20 km across the grid. Thus, for each HF link (depending on Tx-Rx position), the ionospheric profile is not the same which is the worst possible scenario considering the

coverage area for a one-hop propagation mode. The Tx coordinates are found using the ToA method. For the 3-Rx curve, the receivers are placed in the same manner as seen in (e) of Figure 3.9 but the distance from the origin up to each receiver is 350 km. The decrease again in the maximum distance at which a receiver can be placed is due to the varying height. For the 4-Rx curve, the four receivers are placed as seen in Figure 3.13. For 5-Rx and 6-Rx curves, the receivers are placed as explained in the previous case. From Figure 3.14, it is again clear that the geolocation accuracy increases with the number of receivers.

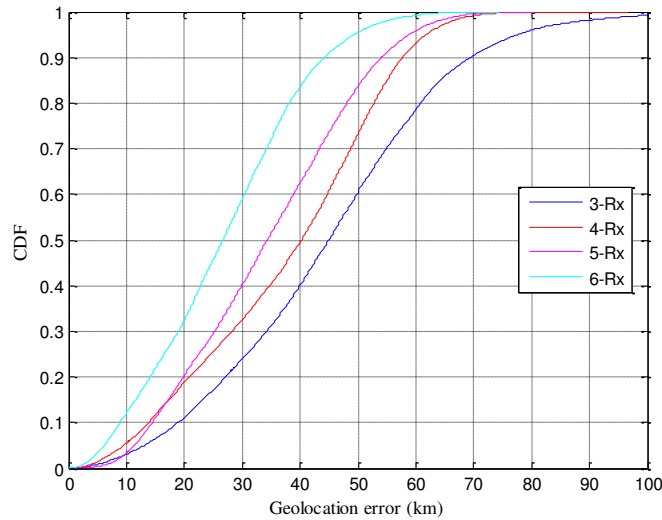


Figure 3.14 CDF of geolocation error obtained using ToA method for different number of receivers assuming a QP layer with variable height following a gaussian distribution

Case 3: The height of maximum ionization to define the QP layer is varied as a linear gradient of 20 km along both the x and the y directions of the grid. Figure 3.15 presents the Tx geolocation error using four receivers. The manner in which the receivers are placed is similar to the first case except that the length of each side is about 1210 km. Any further increase in the receivers distance from the origin, leads to only 2 receivers being able to receive the signals and thus geolocation cannot be achieved. As expected, the geolocation accuracy is slightly smaller than compared to the previous case. The geolocation errors are slightly above to the one's obtained assuming a fixed height QP layer. Almost, all the Tx positions on the grid could be successfully located with an error less than 70 km.

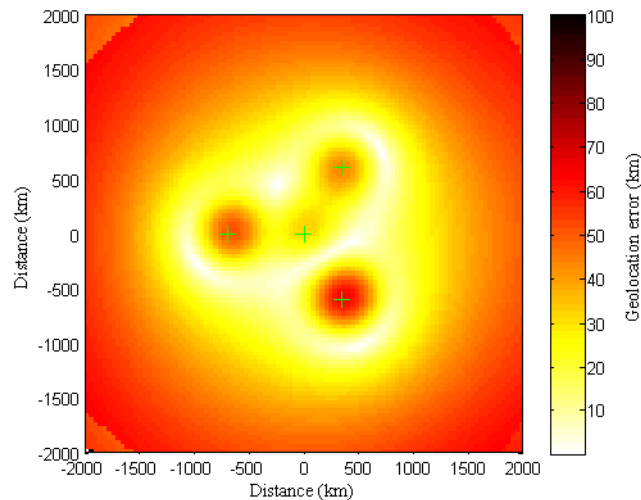


Figure 3.15 Geolocation error obtained using ToA method with 4 receivers assuming a QP layer with variable height following a linear gradient across x and y direction of the square grid

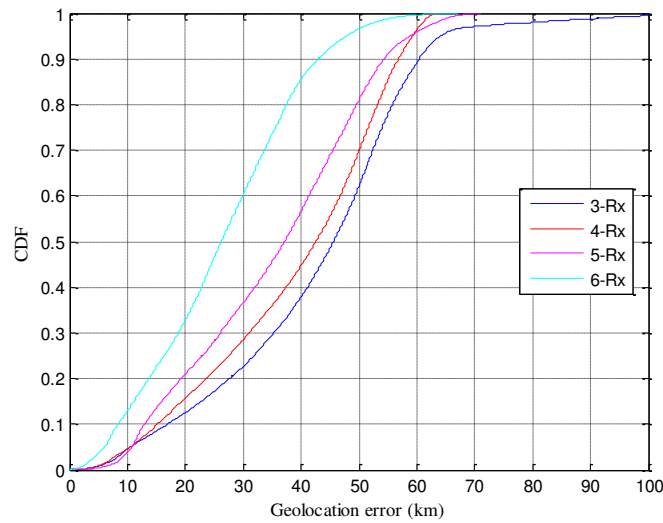


Figure 3.16 CDF of geolocation error obtained using ToA method for different number of receivers assuming a QP layer with variable height following a linear gradient across both x and y direction of the square grid

Figure 3.16 presents the CDF of geolocation error in locating Tx positions on a square grid of 4000 km for minimum and more number of receivers. The height of maximum ionization is varied as linear gradient of 20 km across the x and y direction of the grid, which is a possibility in realistic scenarios. The Tx coordinates are found using the ToA method. For the 3-Rx curve, the receivers are placed in a manner as seen in (e) of Figure 3.9 while for the 4-Rx curve, the four receivers are placed as seen in Figure 3.15. For 5-Rx curve, the receivers are placed as explained in case 1 but the radius of the circle is reduced to 1275 km which is the maximum distance at which the receivers can be placed from the origin. Finally, for the 6-Rx curves, the receivers are placed as explained in case 1 of this section. From Figure 3.16, it can be observed that for a QP layer modelled with a height varying as a linear gradient, the geolocation error decreases as the number of receivers increases. Using 6 receivers, 100% of the geolocation errors are less than 60 km.

Number of receivers	Three	Four	Five	Six
Height of maximum ionization fixed	63%	76%	85%	97%
Height of maximum ionization varying as per gaussian distribution	60%	74%	84%	96%
Height of maximum ionization varying as per linear gradient across latitude and longitude	63%	70%	82%	97%

Table 3.3 Geolocation errors less than 50 km obtained using ToA method for different number of receivers assuming a QP layer with a fixed, gaussian distributed and linear gradient height of maximum ionization

The percentage of geolocation errors less than 50 km obtained using the ToA method with minimum and a larger number of receivers and different assumptions on the height of maximum ionization to model the QP layer are provided in Table 3.3. It is evident that as the number of receivers increases, the geolocation accuracy improves by a large extent. For example, when the height is varied as a Gaussian distribution the geolocation accuracy (error less than 50 km) improves by 36% when the number of receivers is doubled from three to six. From the above table, one can see that the geolocation accuracy does not change by a large extent for the different cases of the height of maximum ionization in the ionosphere.

3.3.2.2 TDoA method

In this section, the geolocation errors obtained using TDoA method for different number of receivers (i.e. 4, 5, 7 and 9) is described. The values used to define the QP model are same as explained in the previous section. The propagation duration differences for the signals received at reference and other receivers are obtained as explained earlier in section 3.3.1.2. From the obtained TDoA's, the geographic location of the transmitter is found using the TDoA geolocation algorithm.

Case 1: In this case, the height of maximum ionization for the QP layer model is assumed to be fixed at 300 km. Figure 3.17 represents geolocation error calculated for each Tx location on the square grid using five receivers by the TDoA method. The 5 receivers are placed in a manner that it resembles a square with the 4 receivers on the vertices of the square and the last receiver at the center of the grid. The 4 receivers are at distance of about 1400 km from the origin of the grid and placed at angles of about 45° , 135° , 225° and 315° respectively. This is the maximum distance at which the receivers can be kept away from the origin considering the square grid of 4000 km. From Figure 3.17, it can be observed that the geolocation error for Tx positions across the whole grid is less than about 40 km. Most of the Tx positions at distances less than about 1800 km from the origin could be geolocated with an error smaller than 20 km. Comparing this result with the geolocation error plot obtained using 4 receivers (Figure 3.10 (c)) shows a significant improvement in the geolocation accuracy. Thus, with the use of an additional receiver and placing it in an optimum position improves the geolocation accuracy significantly.

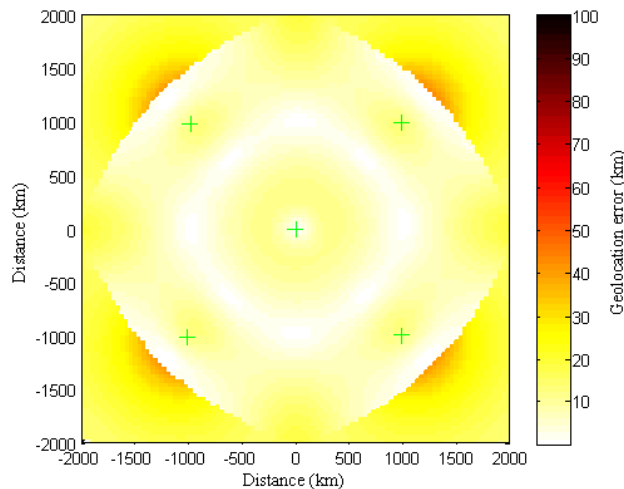


Figure 3.17 Geolocation error obtained using TDoA method with 5 receivers assuming a QP layer with a fixed height

Figure 3.18 presents the CDF of geolocation error in locating Tx positions on a square grid of 4000 km using different number of receivers. The QP layer is defined using a fixed height of maximum ionization. For the 4-Rx curve, the receivers are placed as seen in (c) of Figure 3.10 while for the 5-Rx curve, the five receivers are placed as seen in Figure 3.17. For 7-Rx curve, the five receivers are placed similar to the 5-Rx configuration but at a distance of about 1450 km from the origin whereas the other 2 receivers are placed along the positive and negative x-axis such that all 7 receivers resemble to a square configuration. This represents the maximum distance at which the receivers can be placed from the origin. For the 9-Rx curve, the receivers are placed similar to the seven receiver configuration and the additional 2 receivers are placed along the positive and negative y-axis of the grid. In this configuration, the receivers can be placed further away from the origin. From Figure 3.18, it is evident that about 13% of the geolocation error is less than 40 km using four receivers whereas 100% of the geolocation error is less than 40 km using five receivers. The gain in terms of geolocation accuracy is high at the expense of just an additional receiver. Furthermore, as

the number of receivers is increased, the geolocation accuracy is slightly improved but in a less significant manner.

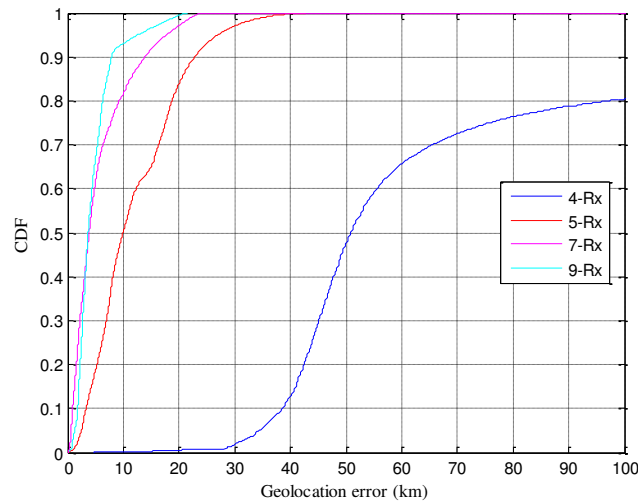


Figure 3.18 CDF of geolocation error obtained using TDoA method for different number of receivers assuming a QP layer with a fixed height

Case 2: The height of maximum ionization of QP layer is varied as Gaussian distribution with a mean of 300 km and a variance of 20 km across the square grid. Figure 3.19 shows the geolocation error in locating Tx positions on the square grid. The manner in which the five receivers are placed is similar to the previous case but the distance of the four receivers from the origin is about 1325 km. This is the maximum distance at which the receivers can be placed from the origin such that the geolocation errors can be calculated across the whole grid. As expected, the geolocation accuracy is slightly smaller than compared to the previous case of uniform ionosphere with 5 receivers. The geolocation errors for Tx positions located far away from the origin of the grid is higher than for those located closer to the origin of the grid.

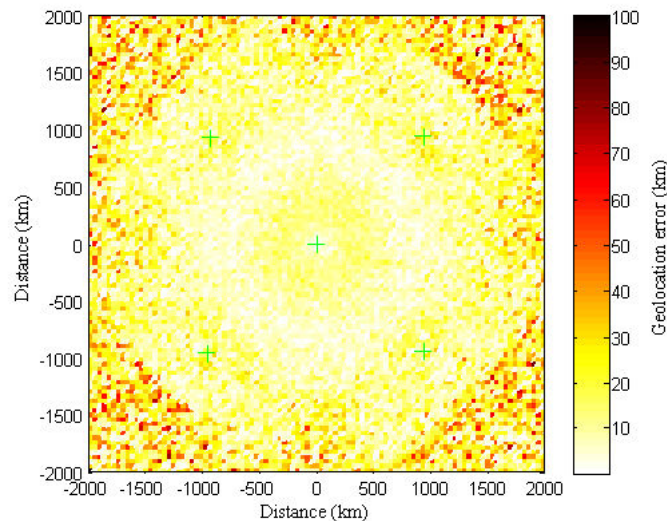


Figure 3.19 Geolocation error obtained using TDoA method with 5 receivers assuming a QP layer with variable height following a gaussian distribution

Figure 3.20 presents the CDF of geolocation error in locating Tx positions on a square grid of 4000 km with different number of receivers. For the 4-Rx curve, the receivers are placed in the same manner as seen in (c) of Figure 3.10 but the distance from the origin up to each receiver is about 325 km. This decrease in the

maximum distance at which the receiver can be placed is due to the varying height. For the 5-Rx curve, the five receivers are placed as seen in Figure 3.19. For 7-Rx and 9-Rx curves, the receivers are placed as explained in the previous case except that the 4 receivers along the vertices of the square are placed at about 1400 km from the origin of the square grid. From Figure 3.20, it is again clear that the geolocation accuracy increases with the number of receivers. Also, the geolocation errors are larger for a similar number of receivers when compared to a QP layer with fixed height of maximum ionization. It can be also seen that about 25% of geolocation error is less than 100 km using four receivers. This is significantly improved using five receivers for which all the geolocation errors are less than about 65 km.

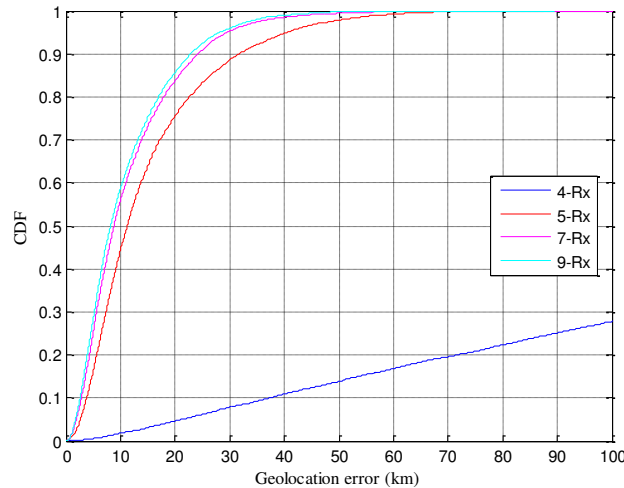


Figure 3.20 CDF of geolocation error obtained using TDoA method for different number of receivers assuming a QP layer with variable height following a gaussian distribution

Case 3: The height of maximum ionization of the QP layer is varied as a linear gradient of 20 km along both the x and the y direction of the grid. Figure 3.21 presents the geolocation error obtained by TDoA method in locating the Tx positions using five receivers. The manner in which the receivers are placed is similar to the first case of this section except that the distance of the receivers from the origin is about 1260 km. It is the maximum distance at which the receivers can be placed to achieve Tx geolocations all across the grid. The geolocation errors are smaller compared to the ones obtained for height varying as Gaussian distribution. The geolocation error for all Tx positions on the grid is less than 30 km.

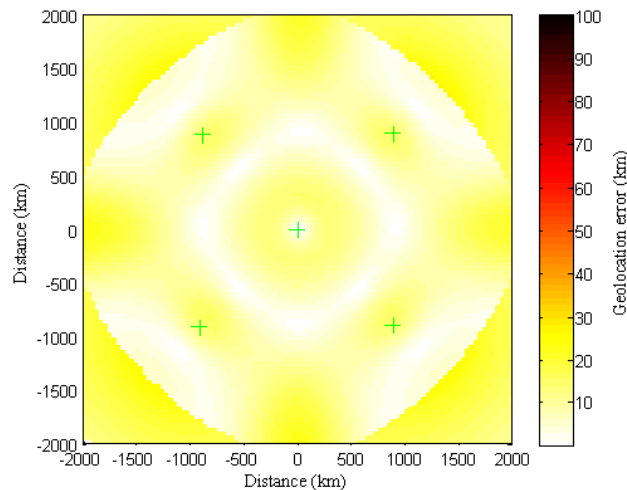


Figure 3.21 Geolocation error obtained using TDoA method with 5 receivers assuming a QP layer with variable height following a linear gradient across both x and y direction of the square grid

Figure 3.22 presents the CDF of geolocation error in locating Tx positions on a square grid of 4000 km for minimum and more number of receivers. The height of maximum ionization is varied as linear gradient of 20 km across the x and y direction of the grid. For the 4-Rx curve, the receivers are placed in the same manner as seen in (c) of Figure 3.10 but the distance from the origin up to each receiver is about 260 km. This decrease in the maximum distance at which the receiver can be placed is due to the varying height. For the 5-Rx curve, the five receivers are placed as seen in Figure 3.21. For 7-Rx and 9-Rx curves, the receivers are placed as explained in the case 1 of this section except that the four receivers along the vertices of the square are placed at about 1280 km from the origin of the square grid. From the CDF curves, it is clear that the geolocation accuracy increases with the number of receivers. About 80% of the geolocation errors are below than 100 km using 4 receivers whereas 100% of the geolocation errors are smaller than 30 km using five receivers. In the case of five receivers, the median geolocation error is reduced by almost 85% compared to the median geolocation error obtained using four receivers. The geolocation accuracy is slightly larger using nine receivers when compared to the accuracy with seven receivers.

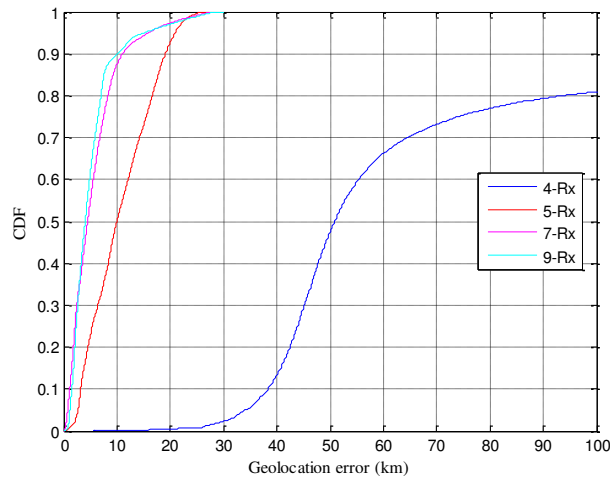


Figure 3.22 CDF of geolocation error obtained using TDoA method for different number of receivers assuming a QP layer with variable height following a linear gradient across both x and y direction of the square grid

Table 3.4 summarizes the percentage of geolocation error less than 20 km obtained using the TDoA method with minimum and larger number of receivers. It can be observed that the improvement in geolocation accuracy is significantly higher with five receivers when compared to that with 4 receivers. It is also important to place the receivers as far away from each other as it results in higher coverage area and the errors due to GDOP are also reduced to a certain extent. Also, with further increase in the number of receivers, the geolocation accuracy is further improved.

Number of receivers	Four	Five	Seven	Nine
Height of maximum ionization fixed	0.5%	84%	97%	99.5%
Height of maximum ionization varying as per gaussian distribution	4.5%	75%	84%	86%
Height of maximum ionization varying as per linear gradient across latitude and longitude	0.5%	93%	97%	97%

Table 3.4 Geolocation errors less than 20 km obtained using TDoA method for different number of receivers assuming a QP layer with a fixed, gaussian distributed and linear gradient height of maximum ionization

From Table 3.3 and Table 3.4, it is also clear that the geolocation accuracy is significantly improved by using one additional receiver in the TDoA method whereas the gain in terms of geolocation accuracy is not that high using one additional receiver in the ToA method.

3.4 Conclusion

This chapter starts with explaining different ionospheric models which are used to model the electron density profile for a single or multi-layer ionosphere. A brief analysis of the QP layer model along with its limitations is explained in detail. The analytical expressions of the QP layer model allow us to obtain ray path parameters which in turn are used to obtain the ToA and TDoA's between different HF links. For the purpose of simulation, the QP model is used to simulate different HF links and obtain the propagation durations. Later, the principle of HF geolocation using ToA and TDoA methods are explained along with its mathematical formulations. The geolocation algorithm assumes a uniform ionosphere with negligible variation of the ray apogee height, a flat earth and one-hop propagation mode. Using the geolocation algorithm, one can locate the position of the transmitter even without the knowledge of the ionospheric profile. Analyses of the geolocation algorithm outputs are provided which can be further used to define whether an estimated location is valid or invalid based on distance physicality and time causality for the case of passive geolocation.

Finally, different simulation studies are presented which shows the effect of receiver positioning and the number of receivers on the geolocation accuracy of a transmitter for both ToA and TDoA methods. For geolocation achieved by the ToA method with minimum number of receivers used, the receivers placed in a circular configuration at maximum distance from each other results in the best geolocation accuracy. For the TDoA method with minimum number of receivers used, the receiver placed in an approximately square distribution leads to higher geolocation accuracy compared to other receiver configurations in the case of passive geolocation. Simulations results also demonstrate that increasing the number of receivers leads to a considerable improvement in the geolocation accuracy using time domain HF geolocation methods.

In order to verify the simulation study of HF geolocation based on TDoA method, multiple receivers were designed and deployed across different cities in France. Chapter 4 explains the complete design of the receiver prototype and the deployed HF receiver network. Using the HF receiver network, experimental measurements are made and analyzed to evaluate the feasibility of broadcast signals in HF geolocation.

Chapter 4 HF Geolocation Receiver

Chapter 3 explained the principle, concepts and mathematical description of time-domain HF geolocation algorithms along with simulation results. In order to study the feasibility of a practical HF geolocation system based on TDoA and validate the simulation results, multiple remotely controllable HF receivers are designed with the ability of synchronously capturing the HF radio signals. First of all, the receiver design is explained in this chapter. In section 4.1, the hardware required to assemble the receiver setup is presented in detail. Then, section 4.2 explains the software development thoroughly. The software part allows us to capture the HF signals synchronously according to the user requirement. Section 4.3 describes an operational country wide TDoA receiver network set up in France to perform measurements and gather experimental data. Different parameters and properties of the captured signals are evaluated using different single processing techniques and then discussed in Section 4.4. These studies are done to verify the potential of the captured broadcast signals in HF geolocation and to find the optimum capture parameters. Simulation results explaining the impact of received SNR on the source geolocation accuracy are also discussed in detail. Part of the work presented in this chapter has been published in [107].

4.1 HF receiver hardware

The primary objective, while designing the receiver, was to make it as compact as possible and to reduce its complexity such that its operation could be handled very easily. The different hardware components used to assemble the receiver setup are explained in detail in the following section.

4.1.1 Software defined radio (SDR)

Communications through data, voice, video etc. is growing exponentially. Thus, modifying radio devices easily and cost-effectively has become a business critical issue. SDR technology brings the flexibility, cost efficiency and power to drive communications forward, with wide-reaching benefits realized by service providers and product developers through to end users. The Wireless Innovation Forum, working in collaboration with the Institute of Electrical and Electronic Engineers (IEEE) P1900.1 group, has worked to establish a definition of SDR that provides consistency and a clear overview of the technology and its associated benefits. It is defined as “Radio in which some or all of the physical layer functions are software defined [108].”

USRP N210 and LFRX daughterboard: Figure 4.1 presents the picture of the USRP N210 SDR module and the LFRX daughterboard used for assembling the receiver setup [109][110]. The Universal Software Radio Peripheral (USRP) is a flexible SDR module which allows normal computers to function as large bandwidth software radios. They are designed and commercialized by Ettus Research (part of the National Instrument group) and widely used by researchers.

The USRP N200/N210 consists of a direct sampling 14-bit analog to digital converter (ADC) capable of sampling up to 100 MHz and is coupled to an FPGA which performs downsampling and frequency conversion. The maximum decimation factor with the USRP N200/N210 is 512, thus the received signal can be downsampled down to 195.3125 kHz. The USRP N200/N210 streaming capability is limited up to 50 MHz to and from the host computer due to the Gigabit Ethernet connection interface. To receive/capture the

radio samples, a RF frontend is fitted in the USRP box as per the needs of the user. In our receiver setup, LFRX daughterboard is used to receive signals from 0 to 30 MHz. The LFRX daughterboard amplifies the received signals while the USRP N200/N210 does the filtering and transposes the signal to baseband. More information about the USRP N200/N210 module and LFRX daughterboard can be found in [109] and [110], respectively.



Figure 4.1 USRP N210 SDR box (left) and LFRX daughterboard (right)

GPS discipline oscillator (GPSDO) and GPS antenna: Figure 4.2 illustrates the picture of the GPSDO kit and GPS antenna for the USRP N-series modules [111][112]. The USRP N200/N210 contains a GPSDO which timestamps the samples with GPS time and synchronizes the clock of both FPGA and ADC. The GPSDO allows multiple USRP's to synchronize their capture with the same clock, irrespective of their locations. The GPSDO is locked to the global GPS standards from the GPS signals are captured by the GPS antenna. It provides time synchronization within 50 ns of the global GPS standards. In order to switch from the external 10 MHz reference clock within the USRP N200/N210 to GPSDO's reference clock, one needs to move the jumper on the USRP's motherboard as explained in [111]. In order to achieve synchronization among multiple USRP's, it is extremely important that all the USRP's are set to GPSDO's reference clock.

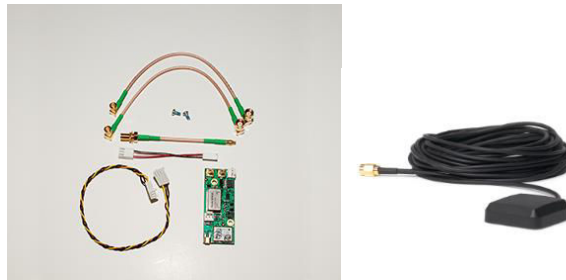


Figure 4.2 GPSDO kit (left) and GPS antenna (right) for USRP N200/N210

More details about the technical specifications of the GPSDO and GPS antenna module can be found in [111] and [112], respectively.

4.1.2 Receiving antenna and filter

The RF frontend of the Ettus USRP N-series is connected to an active receiving antenna via a low-pass filter (LPF) which passes signals from DC to 32 MHz. Unwanted high frequency signals which act as interferers are filtered out. The active receiving antenna setup [113] and the LPF [114] can be seen in Figure 4.3 and Figure 4.4, respectively.

The BCL 1-KA active receiving antenna is mainly suitable for receiving broadcast radio signals within the frequency range of 10 kHz-110 MHz. Furthermore, the antenna consists of a high-capacitance element which is combined with an amplifier and placed in the antenna mount. The antenna is fed with DC-power through the coaxial cable by means of the junction box as seen in Figure 4.3. The junction box isolates the DC and

RF signals and is fed with a 12 V DC power supply. More details about the mechanical and technical specifications about the active receiving antenna are available online [113].

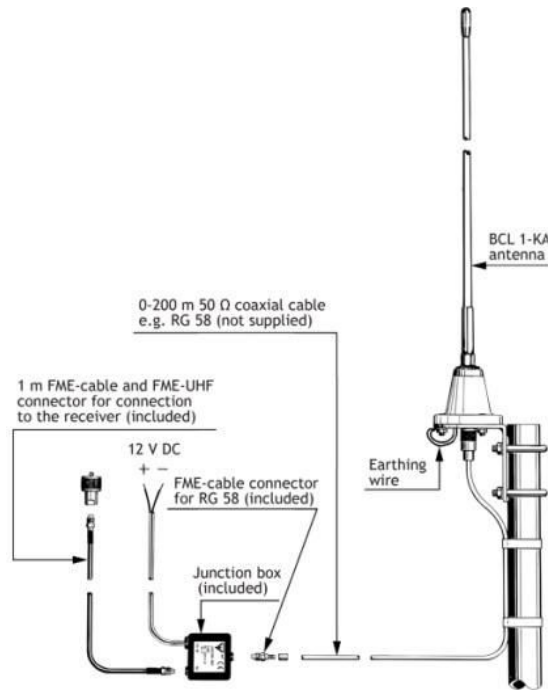


Figure 4.3 Active receiving antenna

The signals received by the active antenna are then passed to the BLP-30+ LPF to filter the undesired captured signals. Moreover, the insertion loss (IL) due to the LPF is 0.1 dB for signals within the HF band. For more specifications, one can refer to the dataset of BLP-30+ LPF [114].



Figure 4.4 Coaxial low-pass filter

4.1.3 Power supply

A single output switch-mode power supply unit from Radiospares (RS) is used to supply 12 V DC to the junction box such that it can receive the radio signals. The power supply unit can be seen in Figure 4.5. The power supply belongs to the EES18B 15W to 18W series. This power supply is selected as it is very compact, lightweight and cost efficient. Moreover, the value of ripple and noise is about 80mV Pk-Pk. The overall specifications of this power supply unit are available online [115].



Figure 4.5 12 V DC power supply

4.1.4 Computer system

As the receiver setups had to be installed in different cities, DEL PowerEdge R230 rack servers were used as it is powerful and efficient. Moreover, this server has 2 ethernet ports which are required to avoid additional external hardware. One ethernet connection is required for the PC to communicate with the USRP module while the other connection is required to obtain remote connectivity of the server at the centralized location. The rack box selected was a 2U panel such that USRP module can be fitted in one panel and the server in another panel, as seen in Figure 4.6. Moreover, this rack box can be closed from both sides which make it portable. Thus, the system can be easily transported from one location to another. On the server, Ubuntu Desktop 14.04 server version was installed as it is a free open-source software.



Figure 4.6 Server and USRP N210 module placed within the box

4.1.5 Assembled hardware schematic and prototype

Figure 4.7 presents the assembled hardware schematic on the left along with its prototype resemblance on the right. The functionality of each hardware component is explained in the previous sections. Considering the receiver designed in terms of hardware, the whole system is quite compact and cost efficient when compared to a large setup of an SSL system. Lastly, the whole receiver setup can be controlled from a remote location and its functionality is explained in section 4.2.1.3.

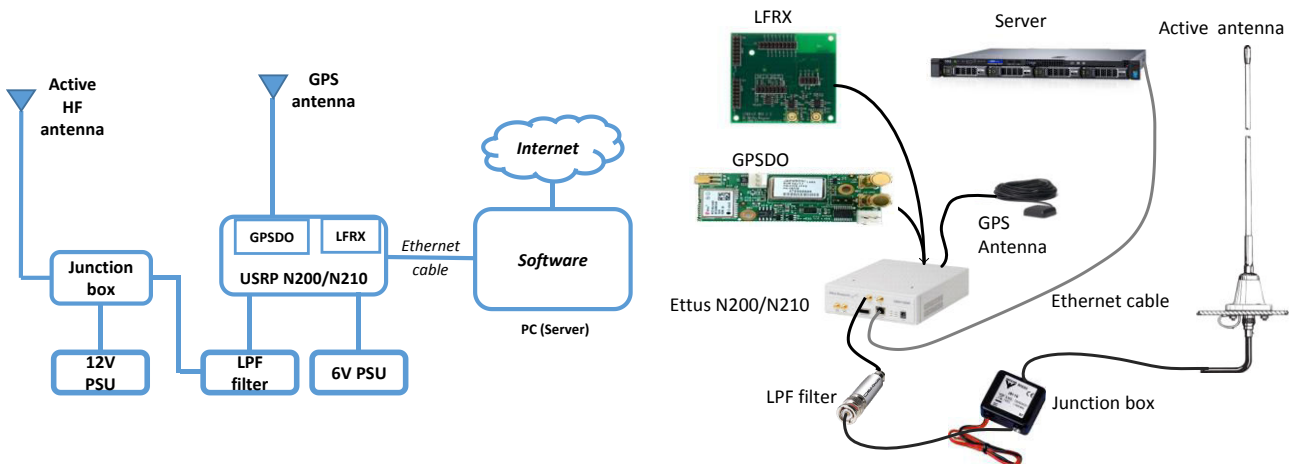


Figure 4.7 Hardware schematic (left) and prototype (right) of the receiver setup

4.2 HF receiver software

This section explains in detail the different programs written to capture the HF radio signals synchronously on all receivers. The parameters to capture the signals are defined by the user. Finally, the tool used to

control the receiver setup remotely is also explained. Part of the receiver software used in the prototype was developed by 2 students at IMT Atlantique as a part of their project studies.

4.2.1 Software development

The host machine (i.e. server in our case) can detect the USRP modules only when the UHD interface (primary driver for all Ettus research products) is installed in the computer. It is freely available in the Ubuntu software center under the GNURadio package and can be installed with ease. Once this installation is done, the host machine and the USRP module are connected and the connection is established through the ethernet port.

GNURadio is a free and open source software development toolkit that provides signal processing blocks to implement software radios. It does all the signal processing and application can be written to transmit or receive data with radio hardware or create simulation based applications. The application can be written in C++ or python programming languages. GNURadio supports all Ettus research USRP modules [116].

The host machine consists of several programs that are used to schedule and capture data as per user requirements. Figure 4.8 illustrates the connections among these programs in the computer.

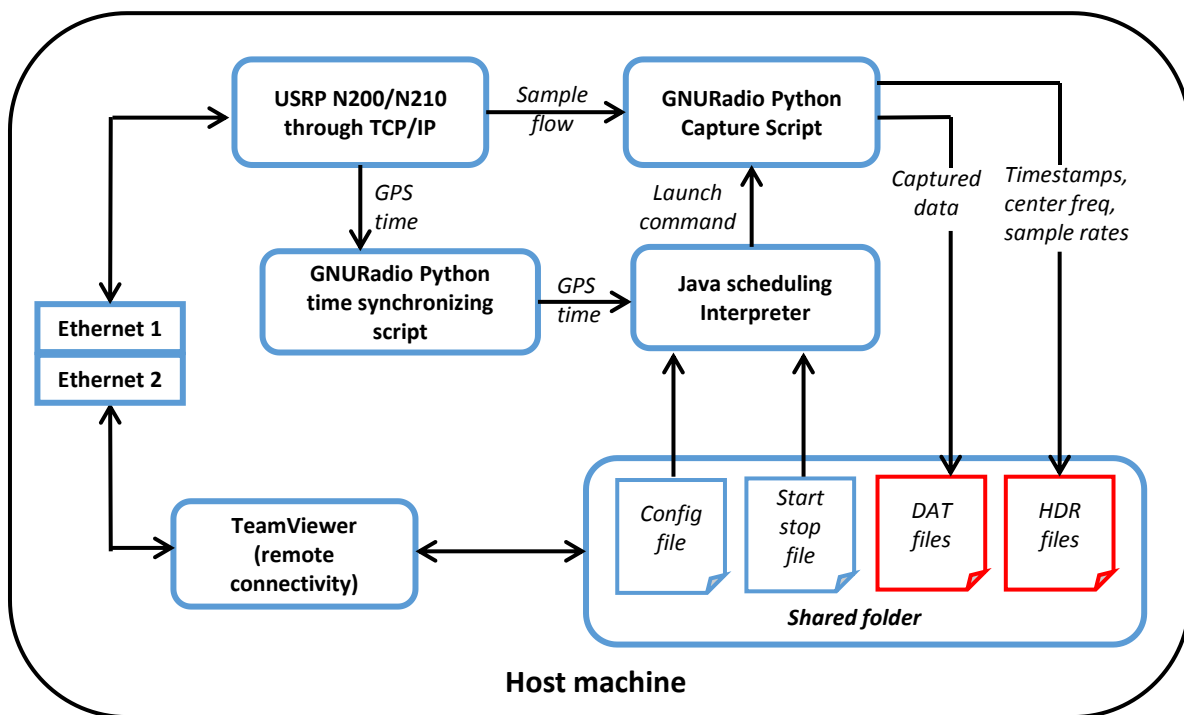


Figure 4.8 Software schematic for capturing signals using the receiver setup

4.2.1.1 Data acquisition parameters

In order to capture the radio signal, the user must specify the parameters of the capture in the “Config file” and “start stop file.” In the “Config file” the following parameters are required:

- Capture start time in GMT0 time zone. Format of the time being in “HH:MM:SS”. For example, a capture time set as “11:10:00” will start a capture at 11:10 AM GMT0 which will be equivalent to a capture at 12:10 PM in France during winter time (Time zone is GMT+1).
- Capture duration in seconds.

- Operational frequency of the HF transmitter in Hz.
- Sampling rate in Hz.

Below is an example of a capture in the config file:

- 10:30:00;10;13665000;200000;

In this example, the radio signal at 13.665 MHz will be captured and sampled at rate of 200 kHz from 10:30:00 AM UT (universal time, GMT0) for duration of 10 seconds.

The “start stop file” allows the user to schedule non-redundant captures. By default, when no “start stop file” is specified, the Java scheduler is programmed in a way that it will load the “config file” in a pile and will schedule every task until everything is done. The config file is reloaded every 24 hours.

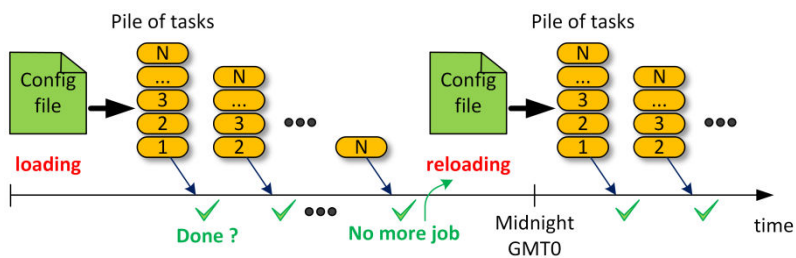


Figure 4.9 24-hour cyclic reloading of the “config file”

Figure 4.9 illustrates how the “config file” is reloaded every time the pile is empty. Note that the program will initiate the first capture at the start time of the first line, move on to the next task until it reaches the last line and perform the last capture. The program will immediately reload the “config file” when the last task is completed and the capture will again start on the next day at the start time of the first task. Thus, it is necessary to write every task in a chronological order, from start to end of the day.

4.2.1.2 Python scripts and Java scheduler

The two Python scripts (i.e. the capture and time synchronizing) acts as interfaces between the hardware and the software. They work with GNURadio objects to perform tasks. As seen in Figure 4.8, the capture script takes the user defined parameters stated in the “Config file” from the Java scheduling interpreter. Later, the script generates two files (one DAT file and another HDR file) which contains data (i.e. samples) generated by the Ettus USRP N200/N210.

The DAT and HDR files created by the program have a structured name. They contain the identification number of the Ettus USRP which can be from 001 to 999, the day and the time of the capture. It is necessary to number the USRP at different locations with a unique number. It provides an easier classification of the captured data from different sites based on the USRP number. Below is an example of a DAT and its corresponding HDR filename:

- 001_12-02-2017_22-30-00.dat
- 001_12-02-2017_22-30-00.dat.hdr

001 represents the Ettus USRP number followed by the capture date and time. The DAT files contain the complex samples (i.e. IQ data) of each capture. The RF samples are arranged in complex 32 bits, leading to a size of 2 x 32 bits = 64 bits per sample. Thus, a 10-second 200 kHz capture will have the following file size:

$$\frac{2 \times 32 \text{ bits/sample} \times 10 \text{ s} \times 200,000 \text{ samples/s}}{8 \text{ bits/byte}} = 16 \text{ MB}$$

The HDR files contain the metadata corresponding to their respective DAT files. Metadata are associated parameters used to operate on the samples, such as the center frequency, sample rate and the absolute timestamp. HDR files can be used with the GNURadio software. More information regarding its usage with GNURadio is available online [117].

Time synchronizing python script: When this script is invoked, it asks for the GPS time from the Ettus USRP module. It then prints out the result in a comprehensible way to the scheduling interpreter. This allows synchronizing the computer time with the GPS time and captures are initiated according to the schedule. In order to ensure that all captures are executed as per the schedule, the synchronization is performed regularly during the run-time of the program.

As mentioned earlier, the capture script takes the start time parameter provided by the user. The script does not wait to run the USRP command by itself. Once it is called, it runs directly and captures the incoming samples from the USRP module. Further when the first sample at the start time of the capture is detected, the script starts saving the samples into the DAT and HDR files. It ensures that all samples from beginning to end are saved. This way of saving captured samples causes some trouble if the script is called too early or after the capture start time. When the time between execution and start time is too long, the script may encounter a buffer overflow while waiting. Also if the start time is found to be in the past when executing the script, it prints an error. All of these issues are resolved by the Java scheduling interpreter. When a task (i.e. a capture) is requested, the scheduler waits until it reaches a time window and then calls the script, as illustrated in Figure 4.10.

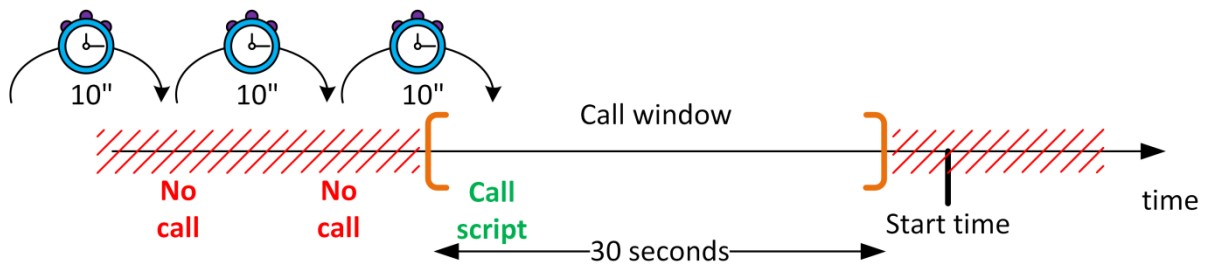


Figure 4.10 Call window before the capture start time

The scheduler calls the script at the right time and prevents the overflow of the incoming samples. In order to ensure that the start time is not in the past, the call window ends a few seconds before the start time. The scheduler waits between each capture to fall into the call window and executes all captures accordingly to the schedule. The wait time of 10-seconds between each check ensures that the program is idle between captures and falls within the available window.

The Java scheduling algorithm flowchart can be seen in Figure 4.11. The whole software is developed in a way that it could be executed with just two commands. One command is to call the python time synchronizing script which synchronizes the computer time with the GPS time and captures are carried out as per the schedule. The other command is to run the java scheduling interpreter which launches the python capture script and data received from the USRP as per the user defined parameters.

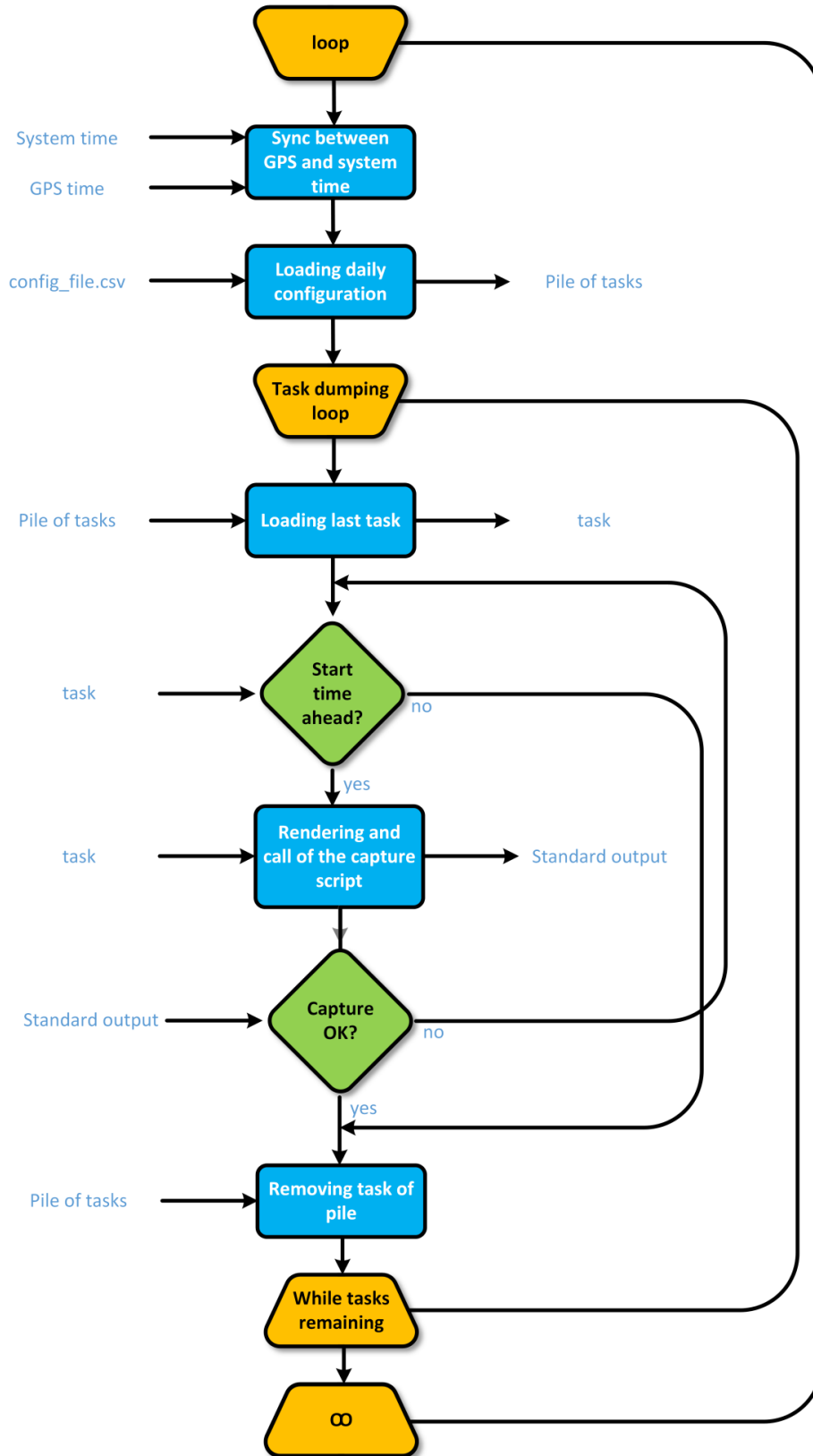


Figure 4.11 Java scheduler algorithm flowchart

4.2.1.3 Remote connectivity

In order to control the whole receiver setup remotely, TeamViewer is installed in all host machines. The TeamViewer is configured in a way that the system at remote location can be accessed with full control from

the centralized location after successfully passing through an authentication process. Files can be uploaded and downloaded from both machines with ease through TeamViewer. The only disadvantage is the time taken for the transfer of large files from a remote location which has a low-rate internet connection.

Remotely controllable HF receiver is designed using different hardware, scripts and software that run together to capture the HF radio signals synchronously as per user requirements. The primary component of the HF receiver setup is the Ettus USRP N210/N220 module which consists of GPSDO. The GPSDO allows multiple USRPs to synchronize their captures irrespective of its location using GPS signals. The whole receiver setup is quite compact, cost-efficient and can be operated with ease. In order to assess the feasibility of a practical HF geolocation system based on TDoA, only four receivers are built and deployed across different sites in France. From simulation results (section 3.3.2), it was seen that the geolocation accuracy is quite high with 5 receivers but only 4 receivers were built. Reasons for this choice are explained in the next paragraph.

At the beginning of thesis, we planned to study the feasibility of HF geolocation using the minimum number of receivers required by the TDoA method (i.e. 4). Considering the time it could take to build 4 receiver prototypes and later deploy them at different locations for experimental validation, the receiver components were ordered very early. It is only later, within the course of the thesis, that simulations were performed to evaluate the impact of the number of receivers on geolocation accuracy and it was observed that with 5 receivers, the geolocation accuracy was far better than with 4 receivers. Therefore, considering the time left in the thesis, building a 5th receiver and deploying was not feasible, due to the delay required to order the receiver components. In addition, finding a 5th location where someone was willing to host our receiver setup was not obvious. Hence, as the objective was to validate the method, it was decided to go ahead with the initial plan of using 4 receivers.

The different locations along with its descriptions at which the receivers are deployed are explained in section 4.3.

4.3 Operational TDoA receiver network

Four remotely controllable receivers capable of synchronously capturing the HF radio signals are developed and deployed in four different cities across France. The different sites at which these receivers are deployed to setup a countrywide operational TDoA receiver network are explained in section 4.3.1. This operational countrywide TDoA receiver network allows a synchronous capture of HF broadcast signals on all receivers from different transmitters located around Europe. The transmitter locations and their distances from each receiver in the network are summarized in section 4.3.2.

4.3.1 Site selection and description

The receiver prototype is deployed in four different cities in France, namely Rx_1 in Brest, Rx_2 in Bordeaux, Rx_3 in Grenoble, and Rx_4 in Lille. The receivers are placed sufficiently far away from each other such that the post-processing of the received signals results in non-zero TDoA values, enabling an estimation of the geographic location of the HF transmitter. The great circle distance between any two receiver's locations is always greater than 490 km. When two receivers are placed too close to each other, the obtained TDoA value would be almost equal to zero. This is due to the fact that the radio signals travel through the skywaves via a reflection from the ionosphere and the distance travelled is almost the same. Thus, the geographic location of the transmitter cannot be accurately estimated.

Receiver in Brest: Figure 4.12 presents the picture of the antenna deployed over the top of a building in the campus of IMT Atlantique. The exact GPS location of the installed antenna is 48.359275° N and 4.568937° W. The other components of the receiver setup are placed in a room which is just below the deployed antenna. As seen in Figure 4.16, this receiver setup in Brest is controlled using a central machine via Internet (TeamViewer).



Figure 4.12 Antenna installed at the measurement location in Brest

Receiver in Bordeaux: Figure 4.13 depicts the picture of the antenna deployed in Bordeaux. The GPS location of the installed antenna is 44.818989° N and 0.587827° W. As seen in Figure 4.16, the receiver setup in Bordeaux is controlled from the central machine located in Brest.



Figure 4.13 Antenna installed in Bordeaux

Receiver in Grenoble: Figure 4.14 shows the picture of the deployed antenna at the IUT1 (Institut Universitaire de Technologie) campus located in Grenoble. We thank the Electrical Engineering department in IUT1 of the University Grenoble Alps for their help in installing the receiver setup and hosting it. The exact GPS location of the installed antenna is 45.198946° N, 5.776244° E. The other components of the receiver setup are placed in a room which is located just below the deployed antenna. Again, this receiver setup is also controlled via the central machine which is located in Brest.



Figure 4.14 Antenna deployed in Grenoble

Receiver in Lille: Figure 4.15 depicts the picture of the antenna deployed at the top of a building in the campus of the University of Lille 1. We thank the Atmospheric Optics Laboratory in University of Lille 1 for their help in installing the receiver setup and hosting it. The exact GPS coordinates of the installed antenna in Lille is 50.611293° N and 3.140469° E. This receiver setup is also controlled from the central machine located in Brest.



Figure 4.15 Antenna installed at the measurement site in Lille

The locations of all receivers are selected such that the effect of noise due to the surrounding environment is minimal on the captured radio signals.

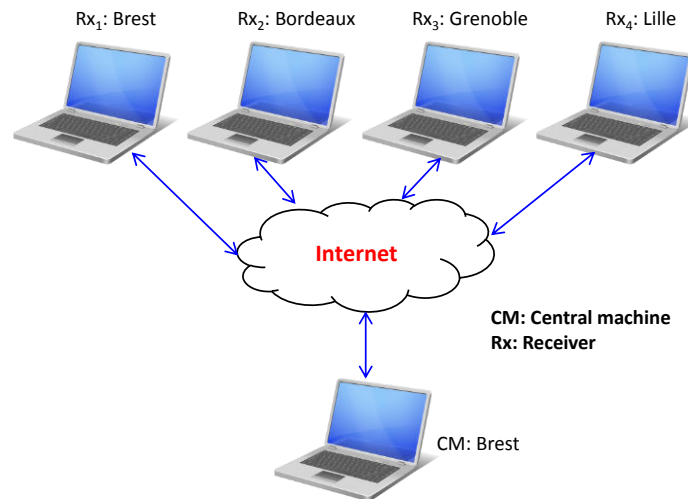


Figure 4.16 Receivers controlled via a centralized machine

4.3.2 HF broadcast transmitters

HF radio broadcast signals are captured simultaneously by all receivers in network from different HF transmitters located around Europe. Details about the transmitting frequency and timings for different HF broadcasters around the globe are available online [118]. To obtain sufficiently high SNR levels, we preferably captured signals from transmitters that emit with very high power (\approx between 50 – 1000 kW). These signals broadcasted with very high power are mainly amplitude modulated audio signals which could be used to verify that the transmitter is operational by listening to the demodulated message signal at the

reception end. No other information of the transmitted broadcast signals are known. Hence, the transmitted broadcasts are similar to unknown HF signals and are a type of signal of opportunity (SOP). These opportunistic HF radio signals can be used to collect the information about the state of the ionosphere and its variation [119]. As the properties of these signals are unknown, they lie within the context of passive HF geolocation.

The geographic location of all HF transmitters and deployed receivers can be seen in Figure 4.17. The ground ranges between the different transmitters and receivers are summarized in Table 4.1 and are within the theoretical range of propagation paths possible using one-hop propagation mode.

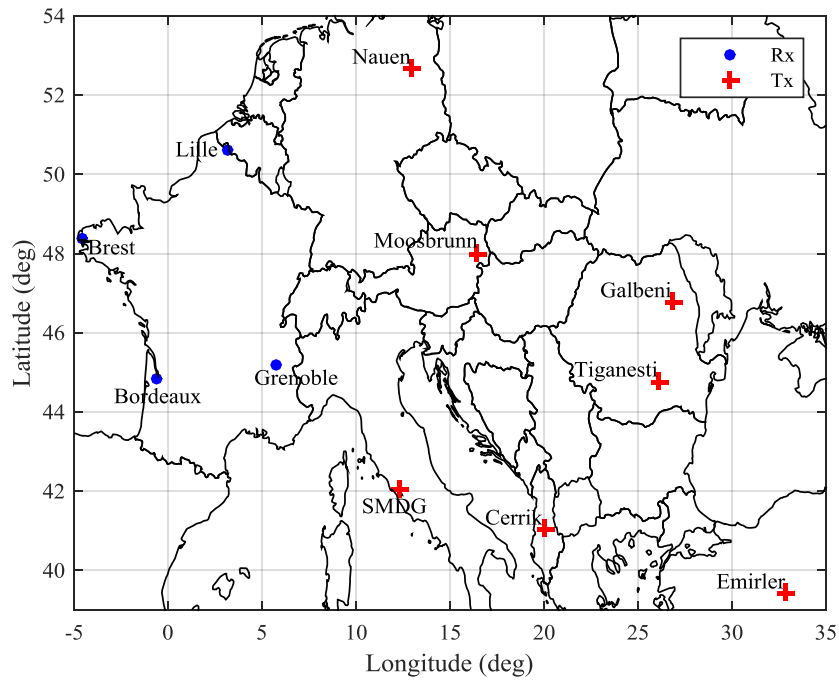


Figure 4.17 GPS coordinates of HF receivers and transmitter sites

Tx site – Country (GPS coordinates)	Tx- Rx ₁ (Brest) (km)	Tx- Rx ₂ (Bordeaux) (km)	Tx- Rx ₃ (Grenoble) (km)	Tx- Rx ₄ (Lille) (km)
Nauen – Germany (52.648°N, 12.908°E)	1321	1314	978	711
Santa Maria di Galeria (SMDG) – Italy (42.04°N, 12.32°E)	1494	1086	633	1183
Cerrik – Albania (41.014°N, 19.993°E)	2095	1724	1242	1680
Galbeni – Romania (46.75°N, 26.86°E)	2348	2128	1633	1785
Moosbrunn – Austria (48°N, 16.46°E)	1555	1351	873	1007
Emirler – Turkey (39.40°N, 32.85°E)	3125	2803	2306	2623
Tiganesti – Romania (44.75°N, 26.11°E)	2364	2098	1596	1830

Table 4.1 Great circle distance for different HF links

TDoA based HF receiver network is setup by deploying HF receivers across different cities in France. The whole receiver network is controlled from a central machine in Brest. HF broadcast signals can be captured synchronously on all receivers from different HF broadcast transmitters located around Europe as per user requirements. The properties of HF broadcast signals captured in Brest are evaluated using different signal processing methods and are discussed in section 4.4

4.4 Signal processing

Before deploying the receivers in different cities across France, several studies were performed with all receiver setups in Brest. As seen in Figure 4.18, the four antennas of the receiver setups capturing the HF broadcast signals were placed very close to each other. The four receivers will be further referred as Rx_1 , Rx_2 , Rx_3 and Rx_4 in this section. The correlation properties of the signals were evaluated by synchronously capturing signals on Rx_1 and Rx_2 . Furthermore, the impact of different capture data lengths on the autocorrelation property of the broadcast signal was studied by capturing signals on the 4 receivers.



Figure 4.18 Antennas deployed in Brest prior to the actual deployment of the receiver setups in different cities

Figure 4.19 represents the captured HF radio broadcast signal at Rx_1 in Brest from the transmitter located in Galbeni on 9th March, 2017 at 15:11 UTC. The signal is captured for a duration of 10 seconds and sampled at a rate of 200 kHz. The data is received in the form of complex samples (IQ data) from the USRP module. The information lies in the magnitude envelope, as the HF broadcast signals are amplitude modulated. When demodulated, it was found that message samples correspond to audio. A significant peak of about 65 dB from the noise floor can be seen at the carrier frequency of the transmitter (15.130 MHz) along with the side lobes on either side of the peak, corresponding to amplitude modulation (Figure 4.19 (b)).

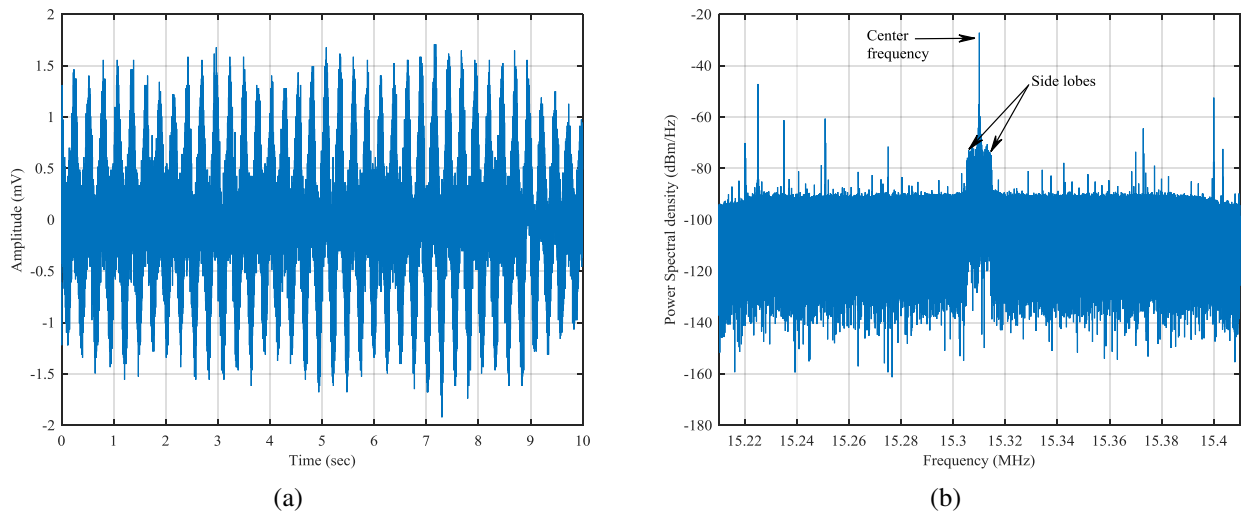


Figure 4.19 Representation of the captured HF radio signal at Brest from Galbeni, Romania in time domain (a) and power spectrum (b)

Apart from the high power signal at the center frequency, several other signals with higher power were also captured, which is evident from the power spectrum shown in Figure 4.19 (b). The capture of these signals is not intended, but is due to simultaneous transmissions at near operating frequencies for a given time during a day. In order to use the captured signal for HF geolocation, it is necessary to filter out the unnecessary part of the signal. The correlation properties of the captured broadcast signals are evaluated to verify its feasibility for the purpose of HF geolocation and are discussed in following subsection.

4.4.1 Correlation properties of the captured signal

In order to measure the TDoA between signals received at distinct receivers, it is imperative that the autocorrelation properties of the transmitted signal are good, i.e. autocorrelation function represents a distinguishable peak with a high SNR. If the peak is not distinguishable, then TDoA cannot be calculated; thus geolocation cannot be performed. A study from the Air Force Institute of Technology in USA analyzed the potential of using AM and FM signals in a TDoA based navigation system by evaluating its correlation properties. Simulation results demonstrated that FM signals exhibits distinct autocorrelation peaks whereas AM signals yielded limited potential for navigation [120].

For evaluating the correlation properties of the broadcast signals, many signals were captured in Brest. As an example, HF radio broadcast signals captured simultaneously by Rx_1 and Rx_2 in Brest on 5th May, 2017 at 08:36 UTC from the transmitter located in Cerrik, Albania is considered. The transmitter in Cerrik was broadcasting at 13.710 MHz during that time. The signal was captured for 10 seconds and sampled at the rate of 200 kHz. The antennas of both receivers (i.e. Rx_1 and Rx_2) were placed about one meter apart from each other as seen in Figure 4.18. The captured broadcasts were speech signals on which the autocorrelation and cross-correlation were calculated. The captured broadcast signals were post-processed and the dataset on which the correlations are computed can be seen in Figure 4.20.

Note: Speech signals corresponds to voice (e.g. news broadcasts) whereas audio signals corresponds to music (e.g. songs)

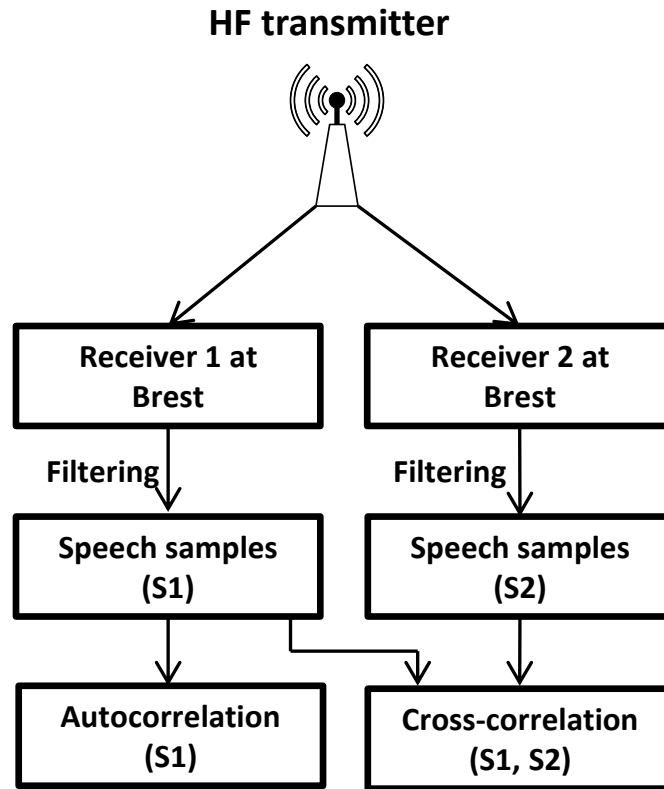


Figure 4.20 Schematic explaining the dataset on which autocorrelation and cross-correlation is evaluated

Autocorrelation is a way to identify the degree of similarity between a signal and its delayed version. It is also referred to as lagged or serial correlation. The autocorrelation ($R_{ss}(t)$) of the received signal ($s(t)$) is calculated as follows:

$$R_{ss}(t) = \int_{-\infty}^{\infty} \bar{s}(\tau)s(t + \tau)d\tau \equiv (s \star s)(t) \quad 4.1$$

where $\bar{}$ denotes the complex conjugate, \star denotes the cross-correlation operator and τ represents the delay.

The received complex samples (IQ data) at the receiver in Brest are filtered in the frequency domain to remove undesired parts of the spectrum. As most of the HF broadcasts are transmitted over a 10 kHz band, only signals within this bandwidth around the carrier frequency of the transmitter are used. The rest is filtered out, i.e. only 5 kHz of the signal on either side of the transmitter frequency is kept and the remaining part of the spectrum is initialized to zero. After filtering, the signal is transformed back to the time domain and demodulated to obtain the message signal samples. Figure 4.21 shows the autocorrelation of captured speech signal which has a peak centered at zero with a signal-to-noise ratio (SNR) of about 10 dB. The message signal samples used to evaluate the autocorrelation was an audible speech signal with negligible level of noise. Thus, it can be assumed that the peak observed in Figure 4.21 is due to speech samples and not noise. However, to assess the autocorrelation properties of the received signal independently from the received noise, two similar signals with different noise must be analyzed. This was performed by cross-correlating the signals received by two separate receivers.

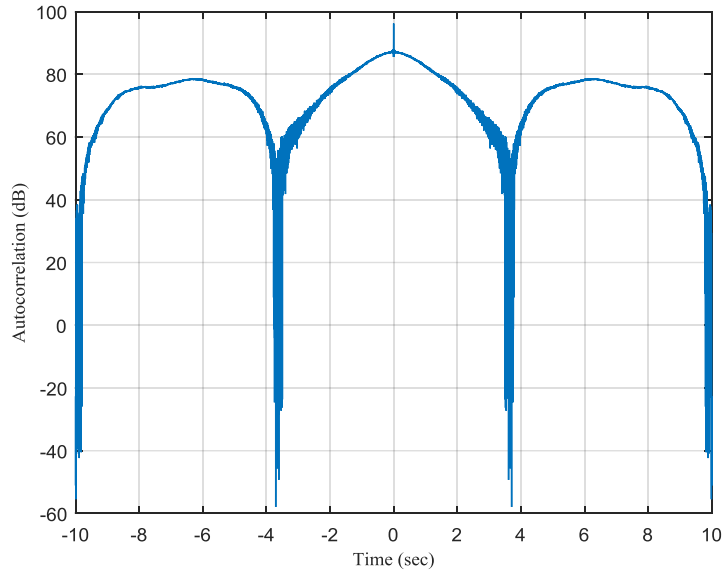


Figure 4.21 Autocorrelation of the captured speech signal in Brest

As seen before, autocorrelation is the cross-correlation of the signal with itself as seen in equation 4.1 and it results in a peak at a lag of zero. On the other hand, cross-correlation is a method of estimating the degree in which two series are correlated as a function of the shift of one relative to the other. The cross-correlation $R_{s_1s_2}(t)$ between two received signals $s_1(t)$ and $s_2(t)$ is given by the following equation:

$$R_{s_1s_2}(t) = \int_{-\infty}^{\infty} \overline{s_1(\tau)} s_2(t + \tau) d\tau \equiv (s_1 \star s_2)(t) \quad 4.2$$

Figure 4.22 presents the cross-correlation between two speech signal samples which are captured at the same time in Brest using two different receivers. The speech signal samples are obtained by filtering and demodulating the captured signals in the same way as described above while evaluating the autocorrelation of a captured signal. The cross-correlation peak is about 6 dB in terms of SNR and is easily distinguishable from the other samples as illustrated in Figure 4.22 (a). As seen in Figure 4.22 (b), there is a cross correlation peak exactly at 0 μ sec (i.e. TDoA is equal to zero). This is due to the fact that both receivers are placed only 1 meter apart from each other. The TDoA resolution is limited to 5 μ sec in our study as all the captured signals are sampled at the rate of 200 kHz. This sampling rate corresponds to a distance resolution of 1.5 km. In order to have a better distance resolution, the sampling rate needs to be increased which further leads to larger data size. If the data is sampled at the rate of 100 MHz, the distance resolution would be equal to 3 m but the data size of a 10 second capture will be 8 GB. Thus, one must note that TDoA based geolocation is performed with a granularity limited by the sampling rate of the signal and the signal bandwidth. At first, the signal of interest itself has a limited bandwidth; when captured the spectrum around the signal is polluted by unwanted jammers (other HF signals). Secondly, one has to distinguish between cases of single and multiple peaks in the correlation plots corresponding to the time delay. If one assumes that there is a single peak, then it is possible to reach a precision in the time-domain that is smaller than the inverse of the signal bandwidth. This is called super-resolution and is feasible by analyzing the phase of the received signal. However, if one assumes that the output signal is composed of several peaks, then the goal is to be able to discriminate among these peaks. In this case, the time-domain resolution is directly linked to the useful signal bandwidth, and it is not possible to increase this resolution by numerically increasing the sampling rate.

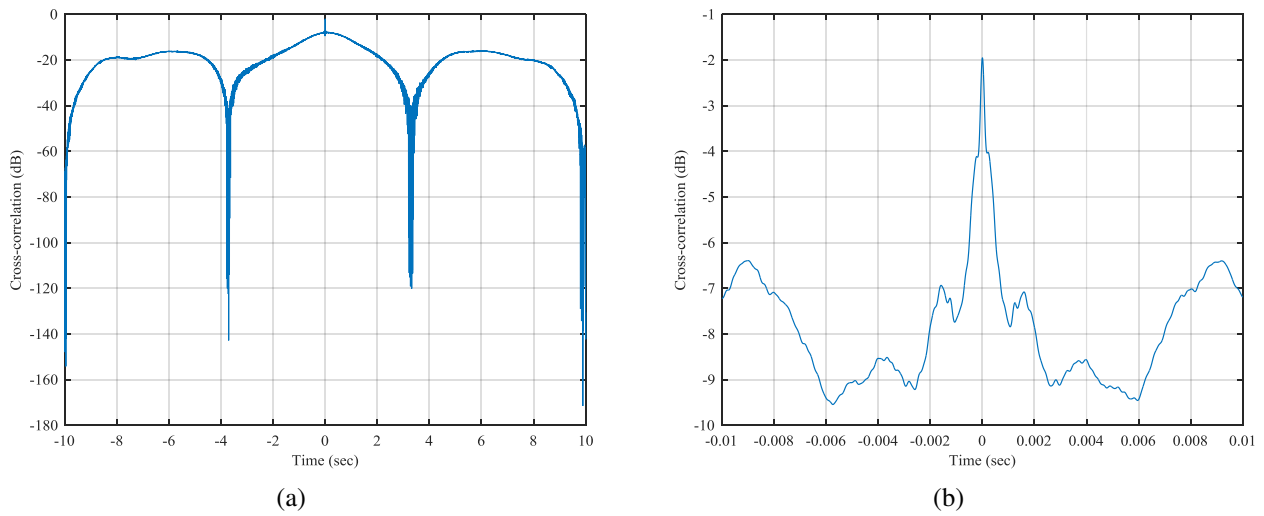


Figure 4.22 Cross-correlation of the captured speech signals in Brest represented over the full time scale in (a) and within a certain time range in (b)

For the example of the captured speech signal, the autocorrelation and cross-correlation resulted in a SNR of about 10 dB and 6 dB, respectively. The peaks obtained in auto and cross-correlation plots are easily distinguishable which shows the feasibility of using AM broadcast signals from HF band for the purpose of HF geolocation. As an example, the correlation properties of an audio broadcast signal captured simultaneously from Galbeni by two different receiver setups in Brest is presented in Appendix C; the autocorrelation and cross-correlation resulted in SNR of about 15 dB. The impact of different data capture durations on the cross-correlation of the captured signals are discussed in section 4.4.2.

4.4.2 Capture data length analysis

In order to understand the effect of different capture data lengths (i.e. different capture durations) on the signal's cross-correlation characteristic, multiple HF broadcast signals were captured simultaneously between 13:38-13:41 UTC on 11th May, 2017 by the 4 receivers in Brest from the transmitter located in Galbeni. The signals were captured for durations of 3, 5, 10 and 15 seconds with a one-minute interval between start times of two captures. The transmitter in Galbeni was broadcasting at a frequency of 15.130 MHz during the capture timings. The cross-correlation between the captured signals at different receivers is evaluated as explained in section 4.4.1.

It must be noted that for any stationary signals, the variance of the estimator decreases as the length of the signal increases. Thus, signals with longer data lengths would lead to better correlation properties. But for signals with longer data lengths, the required computational time is larger. Thus, it is necessary to find an optimum capture duration length which leads to a peak in the correlation function and also the computational time is not very large.

Figure 4.23 represents six cross-correlation plots obtained with a signal captured simultaneously by all four receivers for a duration of 5-second from the transmitter in Galbeni. Each plot represents the cross-correlation for a specific receiver pair. All cross-correlation plots have approximately the same SNR with the peak centered at zero. All the message signal samples used to compute the cross-correlation were audible music signals with negligible amount of noise.

The SNR is calculated using a sliding window method. The length of the sliding window was set equal to 0.1 msec. The minimum value for 1 cycle of windowing was saved in a vector. The total number of cycles for which the windowing is performed is dependent on the length of the cross-correlation output. Finally, the

noise level was selected to be the maximum value obtained from the vector which contained the minimum value obtained from each cycle of windowing. The obtained noise level is represented using a red line in Figure 4.23. The SNR was calculated by subtracting maximum signal value from the obtained noise level.

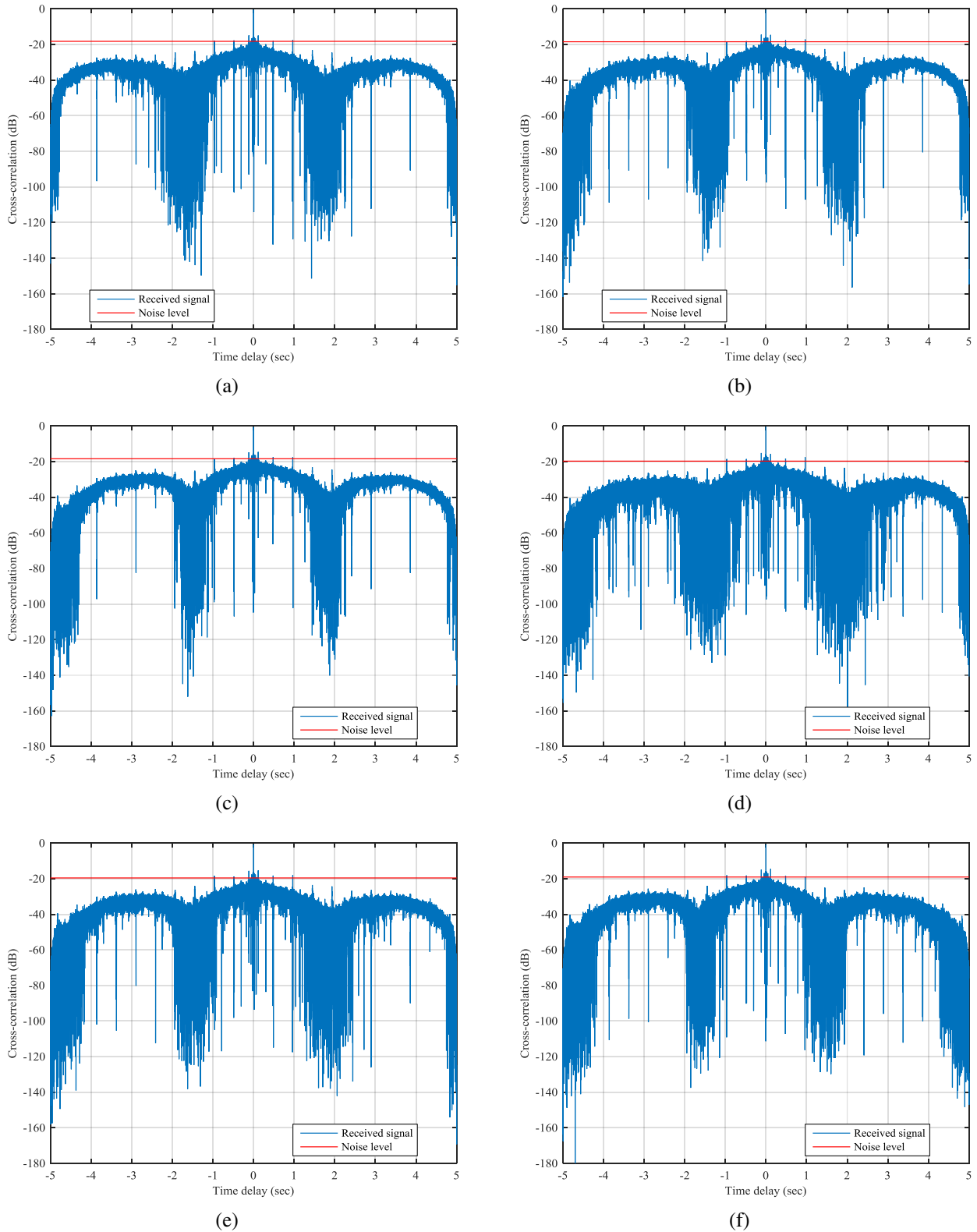


Figure 4.23 Cross-correlation between broadcast signals captured at all receivers in Brest with a duration of 5-second, for RX₁-RX₂ in (a), RX₁-RX₃ in (b), RX₁-RX₄ in (c), RX₂-RX₃ in (d), RX₂-RX₄ in (e) and RX₃-RX₄ in (f)

Table 4.2 presents the summary of the cross-correlation peaks in terms of SNR for captured broadcast signals by 4 receivers in Brest with different capture durations. It can be observed that signals with a capture length of 5 seconds results in the highest SNR. Further, as the capture duration increases, the cross-correlation peak SNR decreases which is contrary to the characteristics of stationary signals. From the obtained SNR values, it is clear that the signals captured for durations of 10 and 15 seconds contains more noise samples compared to the signals captured for 5 seconds. It seems that the signal is apparently not stationary for capture durations greater than 5 seconds.

Capture time and duration Receiver pairs	13:38 (3 sec)	13:39 (5 sec)	13:40 (10 sec)	13:41 (15 sec)
Rx ₁ - Rx ₂	8.2 dB	17.7 dB	14.9 dB	6.8 dB
Rx ₁ - Rx ₃	8.1 dB	17.9 dB	15.8 dB	6.9 dB
Rx ₁ - Rx ₄	8.5 dB	17.8 dB	15.7 dB	13.1 dB
Rx ₂ - Rx ₃	8.3 dB	17.2 dB	15.5 dB	7.9 dB
Rx ₂ - Rx ₄	8.5 dB	18.8 dB	15.5 dB	13.1 dB
Rx ₃ - Rx ₄	8.3 dB	18.3 dB	15.8 dB	7.4 dB

Table 4.2 Cross-correlation in terms of SNR for broadcast signals captured simultaneously by all 4 receivers in Brest with different durations

Despite the fact that signals captured by all receivers in Brest have the same propagation path, the cross-correlation output in terms of SNR is slightly variable for each receiver pair having different capture durations of 3, 5 and 10 seconds. For signals captured with 15-second duration, the variation in the SNR is larger. It is mainly due the different noises captured by the receiver setups.

4.4.3 SNR impact on HF source geolocation accuracy

HF broadcast signals are amplitude modulated and transmitted over long distances through skywaves. In our case, the information content is dependent on the SNR of the captured signals at the receivers. If the SNR of the captured signal is high, the sound quality of the audible broadcast signal is also better. In general, the receptions of HF broadcasts are classified using a standard five grade subjective aural assessment of quality and impairment scale [121]. The sound quality is said to be excellent when the audio/speech is audible to all users and the noise is imperceptible whereas the sound quality is said to be bad when only noise is audible. The required SNR at the receiver for standard minimum acceptable quality for a HF broadcast of 8 kHz bandwidth is 33 dB [122]. As per an ITU report, 30 dB RF SNR is an acceptable value at the receiver for a HF broadcast of 3-kHz bandwidth [123].

In general, localization accuracy mainly depends on the SNR of the captured signal at multiple reception sites. As explained in section 4.4.1, the TDoA's between signals received by multiple synchronized receivers can be estimated by computing the cross-correlation. In order to estimate the TDoA's accurately by cross-correlation, it is imperative that the received signal has a high SNR. If the SNR is low, there will be a shift in the cross-correlation peak due to the noisy data and the obtained time delay will not be accurate, thereby resulting in large geolocation error. In order to evaluate the effect of the received SNR on the geolocation accuracy, simulations are done by emulating realistic scenarios of HF broadcast transmission through one-hop propagation mode.

4.4.3.1 Received signal representation

Let us assume that the transmitted broadcast signal is amplitude modulated; it is represented by $e(t)$. The four receivers are placed at known locations far away from each other. Hence, the signal travels through four different propagation paths and the travel time for the signal to reach the respective receiver are also

different. The signal received on all receivers will contain the original transmitted signal and the noise captured by the respective receivers. This noise mainly comes from the receiver circuitry and different radiated electromagnetic (EM) noise captured by the antenna at the receiver side. Mathematically, the received signal ($s_i(t)$) on each receiver (Rx_i) can be expressed as follows:

$$s_i(t) = e(t - \tau_i) + n_i(t) \quad 4.3$$

where τ_i and $n_i(t)$ is the time taken by the signal to travel from the transmitter to Rx_i and the noise captured on Rx_i , respectively. Since all receivers are synchronized, the TDoA can be estimated by cross-correlating the signal received at the reference receiver with the signals received at other three receivers. From the obtained TDoA's and the known positions of the receivers, the geographic location of the HF transmitter can be estimated using time-domain HF geolocation algorithm explained in section 3.2.3.

4.4.3.2 Received signal modelling

For the purpose of simulation, four receivers are placed in a way that they approximately form a square and the transmitter is placed at a maximum distance of around 1900 km from one of the receivers. The positioning of the receivers and the transmitter in the xy-coordinates can be seen in Figure 4.24. It is assumed that the HF broadcast signals arrive at the receiver through a 1F propagation mode and the corresponding virtual reflection height is 250 km. From the one-hop HF propagation path geometry, the group paths and the corresponding propagation durations for all four Rx's-Tx pairs are computed. The four received signals are modelled using samples of captured audio and speech broadcast signals received in Brest which had an extremely low level of noise.

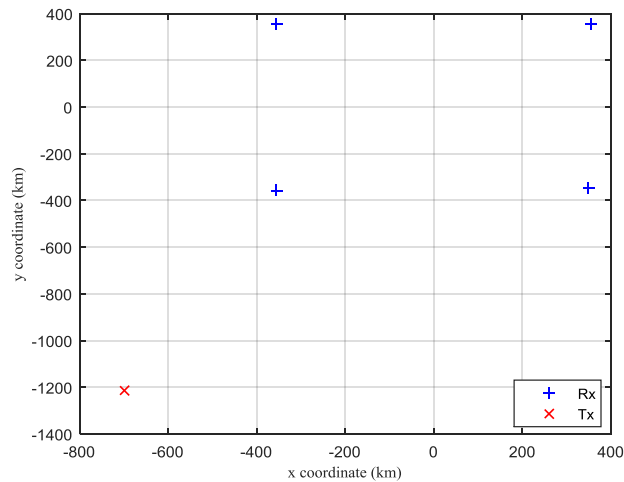


Figure 4.24 Receiver and transmitter placements

The signal received at the reference receiver is modelled using the data set for the audio signal and mixing it with additive white Gaussian noise (AWGN) with a specific SNR. The signals received at the other three receivers consist of the delayed version of the audio samples along with AWGN with the same SNR level as for the reference receiver. The amount of delay on signals received at the other three receivers is equivalent to the evaluated propagation durations from one-hop propagation mode. Furthermore, the modelled received signals with specific values of SNR are cross-correlated to obtain the TDoA and, consequently, the geolocation error is evaluated. If the cross-correlation peak is obtained at exactly the same shift that was used to model the signal, the time delay is assumed equal to the one-hop propagation model to obtain a better resolution in terms of the geolocation error. The geolocation error was also evaluated in the case of a speech

signal. The captured speech signal was also modelled in a similar way as explained above for the audio signal.

4.4.3.3 Simulation results and analysis

Geolocation error for audio datasets of fixed length: Two HF broadcast audio signals of ten seconds captured in Brest are used as dataset. Both the signals are split into ten datasets of one second each resulting in 20 different datasets of audio signals with fixed length. The geolocation error was evaluated for each audio dataset in the same way as explained in section 4.4.3.2. Figure 4.25 (a) presents the geolocation error as a function of the SNR for twenty different audio datasets whereas (b) presents the mean geolocation error of all the different datasets of fixed length. For each dataset, the geolocation error is evaluated several times for each SNR value. Then, the average value of the geolocation error is computed and plotted separately as seen in Figure 4.25 (a). Finally, the mean of the geolocation error is calculated from the average geolocation errors of all datasets. From the simulation results, it is observed that the geolocation error varies largely until the error is zero with respect to the SNR; it is mainly due to the quantization error. The geolocation algorithm is based on TDoA which works on multilateration principle; a wrong estimate of the TDoA results in a large geolocation error. The least geolocation error is achieved at different SNR values for different datasets. As seen in (a) of Figure 4.25, the received SNR which gives the least geolocation error lies in the range of about 6.5 to 8.5 dB. It shows that the variation in the received SNR which gives the least geolocation error depends on the type of received audio signals.

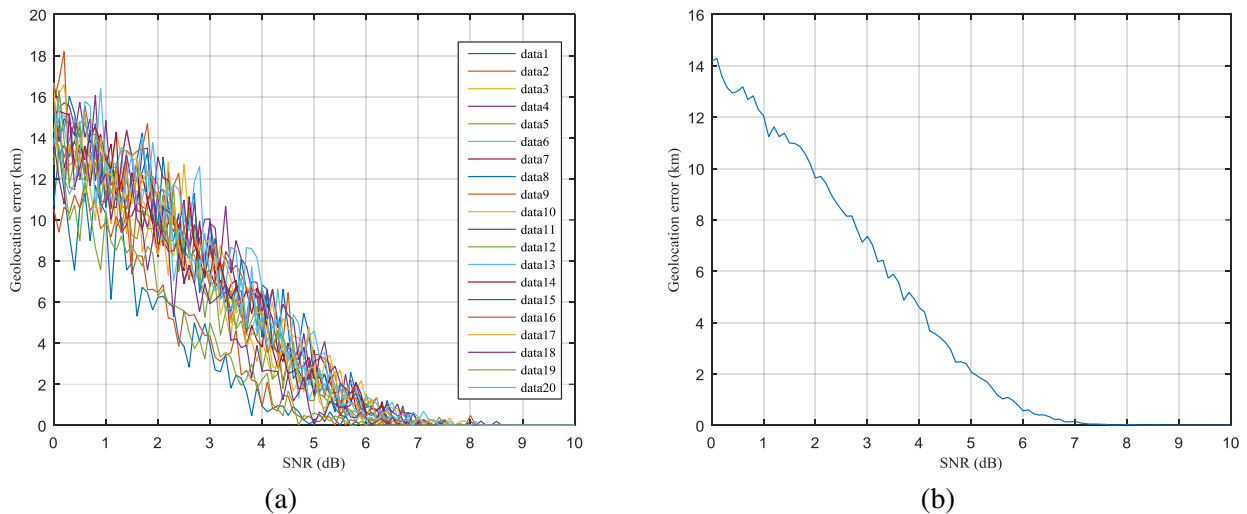


Figure 4.25 Geolocation error as a function of SNR for different audio signals of fixed length plotted in (a) and mean geolocation error of the 20 audio signals plotted in (b)

Geolocation error for audio datasets of varying lengths: In order to see the effect of varying audio data length on geolocation error, one of the audio signals captured in Brest was further divided into five datasets ranging from length of one second to five seconds. Figure 4.26 (a) represents the geolocation error as a function of SNR for audio signals of varying lengths whereas (b) represents the corresponding smoothed data. The smoothed data is obtained by using a moving average filter which replaces the data point by computing the average of neighboring data points defined within the interval. It can be observed that as the length of the datasets is increased, the required SNR to obtain the least geolocation error is also reduced. For audio datasets of 5 seconds, accurate TDoA could be estimated when the SNR of the received signal was about 3.5 dB. This is due to the higher similarity among the data sets from different receivers. Due to higher correlation among the datasets, the cross-correlation outputs yields exact time delays which in turn results in higher geolocation accuracy.

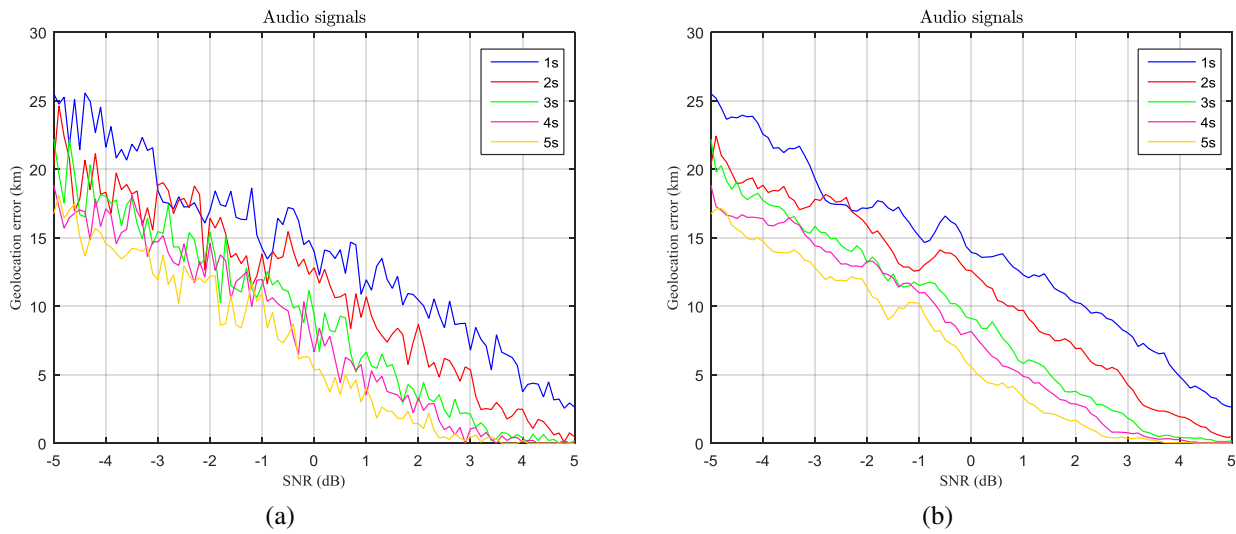


Figure 4.26 Geolocation error as a function of SNR for audio signals of varying lengths, true data plotted in (a) and data plotted after smoothing in (b)

Geolocation error for speech datasets of fixed lengths: In order to model the received signals, two HF broadcast speech signals of 5-second length captured in Brest are used. Both captured speech signals are split into datasets of one second each. The signal modelling and the geolocation error computation are done as explained in section 4.4.3.2. Figure 4.27 (a) represents geolocation error for different speech signals of 1-second length as a function of SNR whereas (b) represents the mean geolocation error of all the 10 different speech datasets. From the simulation results, it can be seen that the least geolocation error is achieved at different SNR values for different speech datasets. The received SNR which gives the least geolocation error for most of the datasets lies within 5.5 dB to 9.5 dB. This variation in the received SNR shows that the geolocation error is dependent on the type of received speech signals, similar to the case of audio signals. In the case of speech signals, the variation in the range of SNR which gives the least geolocation error is high compared to the audio dataset case. This is mainly due to the structure of one second speech data set which consists of several blank samples, thereby affecting the cross-correlation output. It must be noted that the variation in the geolocation error for different speech signals of fixed length is higher compared to the different audio signals of fixed length.

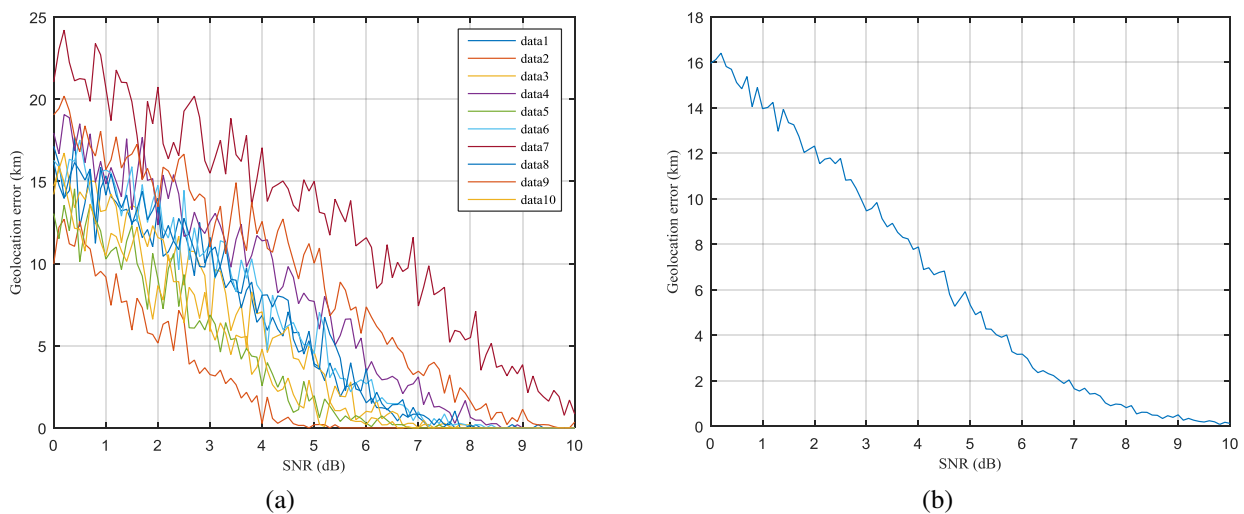


Figure 4.27 Geolocation error as a function of SNR for different speech signals of fixed length plotted in (a) and mean geolocation error of all 10 speech signals plotted in (b)

Geolocation error for speech datasets of varying lengths: To study the effect of varying speech data lengths on geolocation accuracy, a 5-second captured speech signal is split into five datasets with length ranging from one second to five seconds. Figure 4.28 (a) represents the geolocation error as a function of required SNR for speech signal of varying lengths and (b) represents the corresponding smoothed data output. It is clear that as the length of the signal is increased, the required SNR to obtain the least geolocation error is reduced. For speech datasets of 2 seconds or more, it is observed that the geolocation error is the least when the received signal's SNR is about 4 dB. The geolocation error for 5-second speech dataset is equal to zero when the SNR is about 3.5 dB.

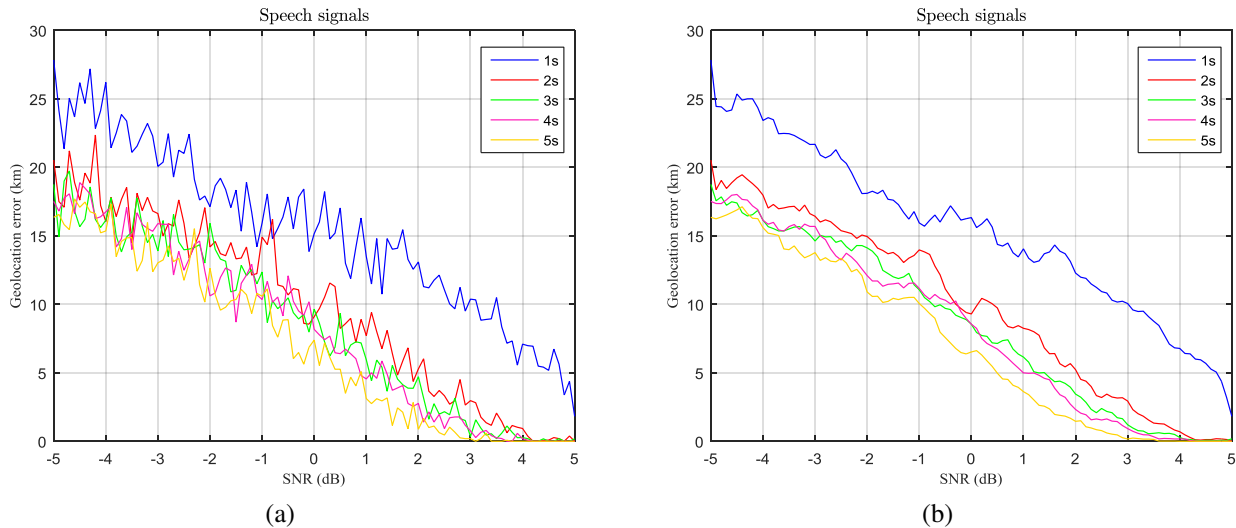


Figure 4.28 Geolocation error as a function of SNR for speech signals of varying lengths, true data plotted in (a) and data plotted after smoothing in (b)

4.5 Conclusion

In this chapter, a programmable and remotely controllable receiver developed to capture HF radio signals is described. This receiver offers multiple configuration possibilities as per the requirements of the user. For example, the user can program the start time of acquisition, capture frequency, sampling frequency and the capture duration. Four receiver prototypes are built and synchronized using the GPSDO kit which can be inserted within the USRP N210/N200 module. Hence, all the receivers are synchronized with the same clock through the GPS signals irrespective of their locations. In order to evaluate the performance of a practical HF TDoA based geolocation system, these receivers are deployed across different cities in France resulting in a countrywide TDoA receiver network. This receiver network is controlled through a central machine in Brest.

The correlation properties of the captured HF broadcast audio/speech signals are evaluated to verify its feasibility in the purpose of HF geolocation. The autocorrelation of the captured analog speech and audio signals in Brest resulted in an SNR of about 10 dB and 15 dB, respectively. The cross-correlation among two speech and audio signals resulted in peaks which were 6 dB and 15 dB, respectively in terms of SNR. Also, the obtained time delays were equal to zero, thereby validating the use of broadcast signals for the purpose of HF geolocation. The impact of data length on the cross-correlation properties of the captured signals in Brest showed that signals captured with 5-second duration resulted in a higher SNR when compared to signals captured with duration of 10 and 15 seconds, which could be due to the stationarity of the signal that degrades for durations larger than 5 seconds.

The impact of received SNR on the accuracy of a HF geolocation system is explained. The received signals are modelled using captured signals and assuming a one-hop propagation mode. The SNR to obtain the best geolocation accuracy varies for audio and speech signals of fixed length of one second. Simulation results demonstrate that the required SNR to achieve the least geolocation error decreases with increase of the data lengths of captured signals. The SNR of the received signal which resulted in the least geolocation error was arbitrarily low for both speech and audio datasets (see (a) of Figure 4.25 and Figure 4.27). Using larger amount of datasets in simulation, a statistical range could be obtained for a considered geolocation accuracy.

As explained, the autocorrelation property of the transmitted signal plays an important role in HF geolocation. Chapter 5 explains the principle and concepts of a new method termed as “cross-channel sounding” which is used to evaluate the time delay of an unknown signal received by multiple synchronized distributed receivers. The mathematical equations for cross-channel sounding show the importance of the nature of the transmitted signals in the estimation of the time delay. Using the TDoA receiver network setup, multiple HF broadcast signals are captured from different transmitters across Europe and the preliminary experimental HF geolocation results are presented.

Chapter 5 Cross-Channel Sounding Concepts and Preliminary Experimental Geolocation Results

Chapter 4 explained the HF receiver prototype design along with its hardware and software descriptions. In addition, characteristics of the captured signals were evaluated using different signal processing techniques and discussed in detail. This chapter explains the principle of a method termed as “cross-channel sounding” along with its concepts. This method is used to evaluate the TDoA of an unknown signal received by two distinct synchronized receivers. Section 5.1 explains the principle and different methods of classical channel sounding. In section 5.2, the principle and concepts of the proposed “cross-channel sounding” method is explained in detail. More importantly, the effect of single and multipath channels on the cross-channel sounding output is explained and illustrated with different figures. In section 5.3, different measurement examples are analyzed to characterize the propagation channel of the signals received at different receiver sites using the cross-channel sounding concepts. The channel characterization (i.e. single, multipath or combination of single and multipath channels) based on the cross-channel sounding output is further validated using the ionospheric profile knowledge along the considered HF propagation path. In section 5.4, some experimental geolocation results for data captured from different HF transmitters during the first series of measurement in July, 2017 are presented and discussed in detail. Part of the work presented in this chapter has been published in [124]-[128].

5.1 Channel sounding

Channel sounding provides information about the propagation channel behavior and different parameters associated with the transmitted and the received signal. The information obtained about the characteristics of the channel helps in improving the overall performance of HF communication systems. Vogler and Hoffmeyer proposed different models for wideband HF ionospheric channels which are explained in [129]-[131]. Experimental results presented in [132] shows distortion in range for HF signals propagating through disturbed ionosphere in polar and equatorial regions. Different HF channel parameters measured at high and mid-latitudes during the last decade of the 20th century are presented in [133]-[135]. More recent channel sounding results obtained in several phases (phase 1: 2006/07, phase 2: 2009/10 and phase 3: 2014) over the ionospheric HF radio link from Antarctica to Spain are explained in [136]-[138]. The distance of the HF link is approximately 12700 km. From the obtained results, the final physical layer was designed for the long-haul HF link, which characterizes the data throughput design as low during the daytime and high during the nighttime. Another study done to evaluate HF radio channels using passive sounding over the Black sea region for distances up to 600 km is explained in [139].

5.1.1 Channel representation

The received signal $s(t)$ is related to the transmitted signal $e(t)$ through the time-variant channel impulse response (CIR) $h(t, \tau)$ by the following filtering operation [140] :

$$s(t) = \int_{-\infty}^{\infty} e(t - \tau)h(t, \tau)d\tau \quad 5.1$$

Note that in the expression $h(t, \tau)$, the variable t is used to represent the variations of the function with time, while the variable τ indicates the delay domain. During the geolocation process, ionospheric variations are negligible. Thus, it is considered that the channel does not vary with time and the CIR can be represented as $h(\tau)$. Equation 5.1 can be rewritten as:

$$s(t) = \int_{-\infty}^{\infty} e(t - \tau)h(\tau)d\tau \equiv (e * h)(t) \quad 5.2$$

where $*$ denotes the convolution operator.

5.1.2 Principle

In the case of time-domain geolocation, one of the main issues is to get access to the CIR between the transmitter and the receiver to estimate the propagation duration of the signal. For instance, in the simple case of single path ideal channel, the CIR $h(\tau)$ is composed of a single Dirac pulse which represents the delay corresponding to the time of flight of the signal (Figure 5.1). The distance travelled between the transmitter and the receiver can be obtained by multiplying the time of flight with the speed of the electromagnetic wave.

The main issue lies in the fact that the CIR cannot be accessed directly, but only by observing a received signal $s(t)$ which is obtained after transmitting a signal $e(t)$ through the channel $h(\tau)$. In other terms, the transmitted signal needs to be wisely selected in order to accommodate for an easy resolution of equation 5.2. Different methods of channel sounding (frequency-domain and time-domain techniques) have been proposed to solve this problem [140] and are explained in section 5.1.3 and 5.1.4, respectively.

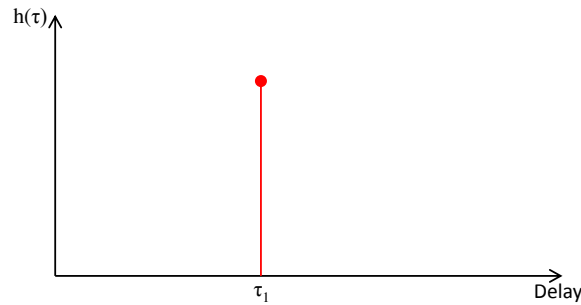


Figure 5.1 Representation of a CIR in the case of a single path ideal channel

5.1.3 Frequency domain channel sounding

In frequency domain channel sounding, the transmitted and the received signals are observed on a wide band of frequencies. It is mainly done using a vector network analyzer (VNA) which is capable of sweeping a very wide frequency band. For measurements, there is a requirement of very good phase synchronization between the transmitter and the receiver which is achieved by connecting cables between the transmitter and the receiver. Thus, it is not applicable for distinct HF links. In addition, the narrow bandwidths of HF signals limit the use of frequency-domain channel sounding techniques.

5.1.4 Time domain channel sounding

In time domain channel sounding techniques, the simplest method consists of using a short pulse $\Pi(t)$ as the transmitted signal $e(t)$. It is referred as the pulsed technique. The received signal $s(t)$ can be expressed as follows:

$$s(t) = (\Pi * h)(t) \quad 5.3$$

The received signal $s(t)$ is an approximation of the CIR $h(\tau)$, provided that the transmitted signal is short enough. The advantage of using short pulses as transmitted signal is its low acquisition duration which can be used to obtain the CIR in real time. However, the disadvantages of this technique are as follows:

- Signal acquisition requires a very fast sampling rate
- SNR is low leading to a strong impact of measurement noise
- Requirement of perfect synchronization between the transmitter and the receiver

A practical way to increase the SNR is to use the technique of correlation sounding. The cross-correlation between the transmitted and the received signal is denoted by $R_{es}(t)$ and is calculated as follows:

$$R_{es}(t) = \int_{-\infty}^{\infty} \bar{e}(\tau)s(t + \tau)d\tau \equiv (e * s)(t) \quad 5.4$$

where $\bar{}$ denotes the complex conjugate, $*$ denotes the cross-correlation operator.

From equation 5.2 and 5.4, the cross-correlation is reduced to the following:

$$R_{es}(t) = (e * (e * h))(t) \quad 5.5$$

As per the definition of cross-correlation theorem [141], equation 5.5 can be expressed as a product of two Fourier transforms:

$$\mathcal{F}[(e * (e * h))] = \overline{[\mathcal{F}(e)]}[\mathcal{F}(e * h)] \quad 5.6$$

where \mathcal{F} represents the Fourier transform. Now, as per the definition of convolution theorem [142], equation 5.6 can be written as follows:

$$\mathcal{F}[(e * (e * h))] = \overline{[\mathcal{F}(e)]}[\mathcal{F}(e)][\mathcal{F}(h)] \quad 5.7$$

After further simplification and taking the inverse Fourier transform of equation 5.7, one obtains the following:

$$[(e * (e * h))] = [((e * e) * h)] \quad 5.8$$

Substituting equation 5.8 in equation 5.5, the cross-correlation can be rewritten as:

$$R_{es}(t) = ((e * e) * h)(t) = (R_{ee} * h)(t) \quad 5.9$$

If the input signal is similar to a white noise, its autocorrelation function tends to a Dirac impulse. In this case, the identification problem is similar to the one occurring in the pulsed technique. In practical implementation, channel sounders use maximum length pseudo-noise (PN) sequences which are also called

m-sequences. It corresponds to a good approximation of colored noise with zero mean and limited bandwidth. The SNR is increased due to the autocorrelation properties of the PN sequences.

5.1.4.1 Correlation sounding example

In order to study the concept of HF geolocation using the ToA method, an experimental campaign was setup by our team in IMT Atlantique before the start of the thesis which involved HF radio transmissions. The receiver and the transmitter were designed using a SDR module (different from the setup developed in this thesis) operating in the HF band. In order to obtain the propagation durations of signals, the transmitter and the receivers were synchronized using GPS disciplined oscillators (GPSDO). The transmitter and the receiver setup were controlled using an ethernet connected laptop.

The experimental campaign involved one transmitter station which was deployed in Brest and 4 receiver stations, which were deployed in Paris, Poitiers, Strasbourg and Toulouse. The ionospheric channels were regularly sounded at 3 different frequencies in the HF band: 6.40 MHz, 8.06 MHz and 9.95 MHz. The transmitted signals consisted of a PN sequence with programmable length and chirp duration. At the receiving end, the signals were correlated with transmitted signals to obtain the CIR. For each HF link, the CIR was computed throughout the day at the rate of 1 measurement every 30 minutes which allowed observing the effect of daily ionospheric variations. Details about the equipment and signal processing are explained briefly in [79]. Different propagation modes and the propagation durations of the signals received at different sites were evaluated from the CIR.

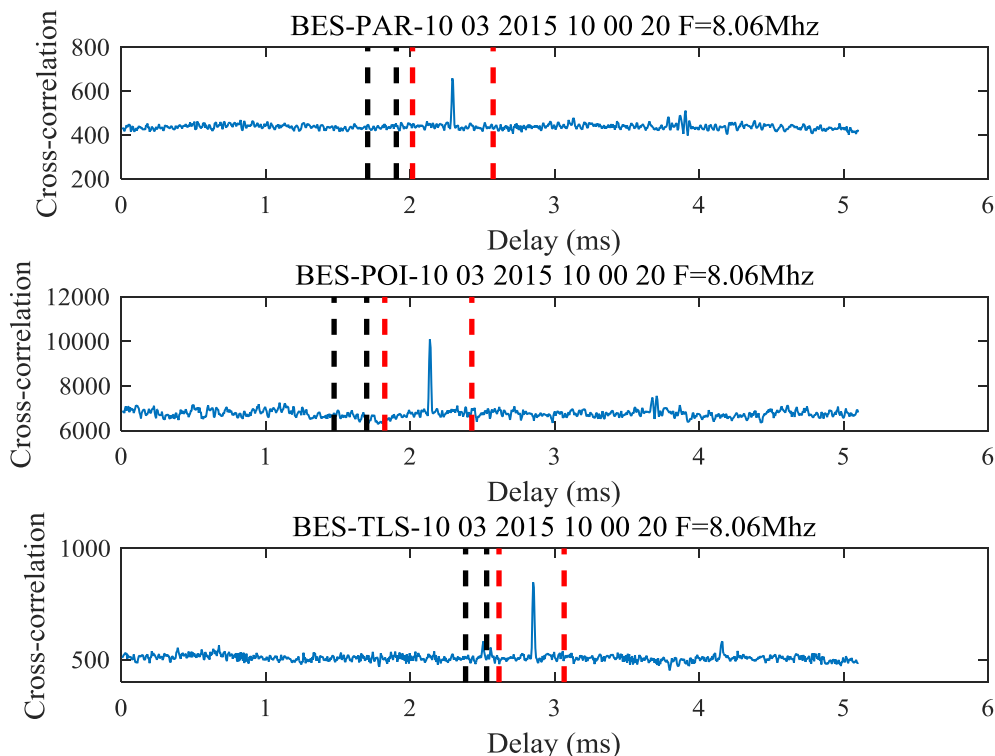


Figure 5.2 Example of CIR measured on different HF links (Brest-Paris, Brest-Poitiers and Brest-Toulouse) using correlation sounding on 10th March, 2015 at 10h00, frequency 8.06 MHz

Figure 5.2 presents a measurement example of the CIR obtained in Paris, Poitiers and Toulouse, respectively, on 10th March, 2015 at 10h00. The channel is sounded at a frequency of 8.06 MHz. According to the principles of ionospheric propagation, the presence of E layer produces signal reflections at a virtual height

in the range of 80-150 km. Similarly, the F layer corresponds to signal reflections at a virtual height in the range of 180-300 km. As the Tx and Rx locations are known, it is possible to compute the range of travel times for each receiver corresponding to one hop modes via the E layer. This range is represented with the black dashed lines on Figure 5.2. Similarly, the range of propagation durations corresponding to one hop mode via the F layer is represented with the red dashed lines. For all the HF links (Brest-Paris, Brest-Poitiers and Brest-Toulouse), a single propagation path via the F layer is observable. It corresponds to one-hop propagation mode.

HF communications through skywaves is a real challenge due to the non-stationary behaviour of the ionosphere. Using HF channel sounding, the propagation channel can be characterized and different parameters (i.e. carrier frequency, signal bandwidth, etc.) can be estimated to overcome channel impairments; thereby ensuring the availability of the HF link. In the case of the passive geolocation, the transmitted signal is unknown. Thus, channel sounding cannot be used. In order to obtain the TDoA between signals received by multiple receivers, a technique named as cross-channel sounding is explained in section 5.2 along with its mathematical description.

5.2 Cross-channel sounding

Cross-channel sounding is a technique used to evaluate the propagation duration differences of an unknown signal received by multiple synchronized distributed receivers.

5.2.1 Principle

In the framework of passive time-domain HF geolocation, the signal transmission time and transmitted signal are unknown. Thus, the duration of propagation cannot be calculated and the classical ToA method cannot be used. The TDoA method can be employed, for which only the time difference between reception instants at any pair of receivers is required.

Let the signals received at receiver 1 (Rx_1) and receiver 2 (Rx_2) be $s_1(t)$ and $s_2(t)$, respectively. These signals share the same origin which is the transmitted signal $e(t)$ but have different propagation channels $h_1(\tau)$ and $h_2(\tau)$ between the Tx- Rx_1 pair and Tx- Rx_2 pair, respectively. Assuming that both the propagation channels do not vary with time, the received signals are expressed as follows:

$$s_1(t) = (e * h_1)(t) \tag{5.10}$$

$$s_2(t) = (e * h_2)(t)$$

In practice, the received signals contain some noises $n_1(t)$ and $n_2(t)$ captured by the Rx_1 and Rx_2 , respectively. These noises are mainly generated from the receiver circuitry and different radiated electromagnetic noise captured by the antenna at the receiver end. In general, these noises will affect the signal detection performance. The received signals at Rx_1 and Rx_2 can be now written as follows:

$$s_1(t) = (e * h_1)(t) + n_1(t) \tag{5.11}$$

$$s_2(t) = (e * h_2)(t) + n_2(t)$$

The duration of propagation of each signal path is captured by the CIRs $h_1(\tau)$ and $h_2(\tau)$. The TDoA method requires a way to retrieve this information in a way similar to what is done in classical channel sounding. In order to find the difference of the propagation durations from the available data which are just the received signals, one can evaluate the cross-correlation between the CIRs $h_1(\tau)$ and $h_2(\tau)$, a technique that is named as “cross-channel sounding.”

5.2.2 Mathematical description

Cross-channel sounding requires to compute the cross-correlation of the received signals $s_1(t)$ and $s_2(t)$ and is denoted by $R_{s_1s_2}(t)$. It is calculated as follows:

$$R_{s_1s_2}(t) = (s_1 \star s_2)(t) = [(e \star h_1) + n_1] \star [(e \star h_2) + n_2](t) \quad 5.12$$

After applying the distributive property of cross-correlation, equation 5.12 is expressed as:

$$R_{s_1s_2}(t) = \{[(e \star h_1) \star (e \star h_2)] + [(e \star h_1) \star n_2] + [n_1 \star (e \star h_2)] + [(n_1 \star n_2)]\}(t) \quad 5.13$$

As per the convolution and cross-correlation theorem, the 1st term of equation 5.13 can be simplified further yielding:

$$R_{s_1s_2}(t) = \{(e \star e) \star (h_1 \star h_2) + [(e \star h_1) \star n_2] + [n_1 \star (e \star h_2)] + [(n_1 \star n_2)]\}(t) \quad 5.14$$

After further simplifications, equation 5.14 is reduced to the following:

$$R_{s_1s_2}(t) = (R_{ee} \star R_{h_1h_2})(t) + R_{s_1n_2}(t) + R_{n_1s_2}(t) + R_{n_1n_2}(t) \quad 5.15$$

where R_{ee} is the autocorrelation of the transmitted signal, $R_{h_1h_2}$ is the cross-correlation between the 2 CIRs ($h_1(\tau)$ and $h_2(\tau)$), $R_{s_1n_2}$ is the cross-correlation between the signal received at Rx₁ without any noise and the noise received at Rx₂, $R_{n_1s_2}$ is the cross-correlation between the noise received at Rx₁ and the signal received at Rx₂ without any noise and $R_{n_1n_2}$ is the cross-correlation between the noises received at Rx₁ and Rx₂, respectively.

The resolution of the cross-correlation peak mainly depends on the SNR of the received signals and the correlation between the different noises and received signals. Assuming that signals and noise received at both receivers are uncorrelated, the cross-correlation of the terms involving noises and received signals (i.e. $R_{s_1n_2}$, $R_{n_1s_2}$, $R_{n_1n_2}$) in equation 5.15 should be small and thus, would reduce the resolution of the cross-correlation peak by a small extent. Therefore, one can neglect the cross-correlation of the terms involving noises and the received signals. Now, the cross-correlation of the received signal is given by the following equation:

$$R_{s_1s_2}(t) = (R_{ee} \star R_{h_1h_2})(t) \quad 5.16$$

A similarity can be observed between equation 5.16 related to cross-channel sounding and equation 5.9 related to correlation based channel sounding. It also explains that the nature of the transmitted signal plays an important role in cross-channel sounding for the estimation of propagation duration differences. More specifically, the cross-correlation output for the received signals will be close to the cross-correlation of the CIRs, provided that the auto correlation of the transmitted signals resembles a narrow, zero-centered peak with a large SNR.

For an optimal signal, such as an m-sequence or any signal with low internal correlation, the autocorrelation will resemble a narrow, zero-centered peak, with a large SNR. In such case, the output cross-correlation $R_{s_1s_2}(t)$ will be close to the cross-correlation of the two CIRs $R_{h_1h_2}(t)$. Practically, for a random signal such as AM modulated radio broadcast signals, longer sequences would lead to better autocorrelation properties. In any case, the transmitted signal being the unknown signal that needs to be located, there will be no way to improve its properties for cross-channel sounding in the framework of passive time-domain geolocation.

Different issues may arise while selecting the cross-correlation peak which corresponds to the time delay between the signals received at two distinct synchronized receivers depending on the nature of both CIRs. These may contain a single peak or multiple peaks depending on the propagation path of the transmitted signals. The effect of the propagation channels on the CIR is briefly explained in section 5.2.3 and 5.2.4.

5.2.3 Single path channels

Let us assume that both channels are single ideal path, where the ionospheric propagation occurs via the F layer of the ionosphere. The output of the CIRs cross-correlation of the received signals having different single path channels is represented in Figure 5.3. In $h_1(\tau)$, τ_1 corresponds to the propagation duration of the signal from the transmitter to Rx₁ via a reflection from the F layer of the ionosphere. Similarly, τ_2 corresponds to the propagation duration of the signal from the transmitter to Rx₂. In the case of single path channels, the time delay between the signals received at different receivers can be obtained with ease provide that the transmitted signal has a higher correlation.

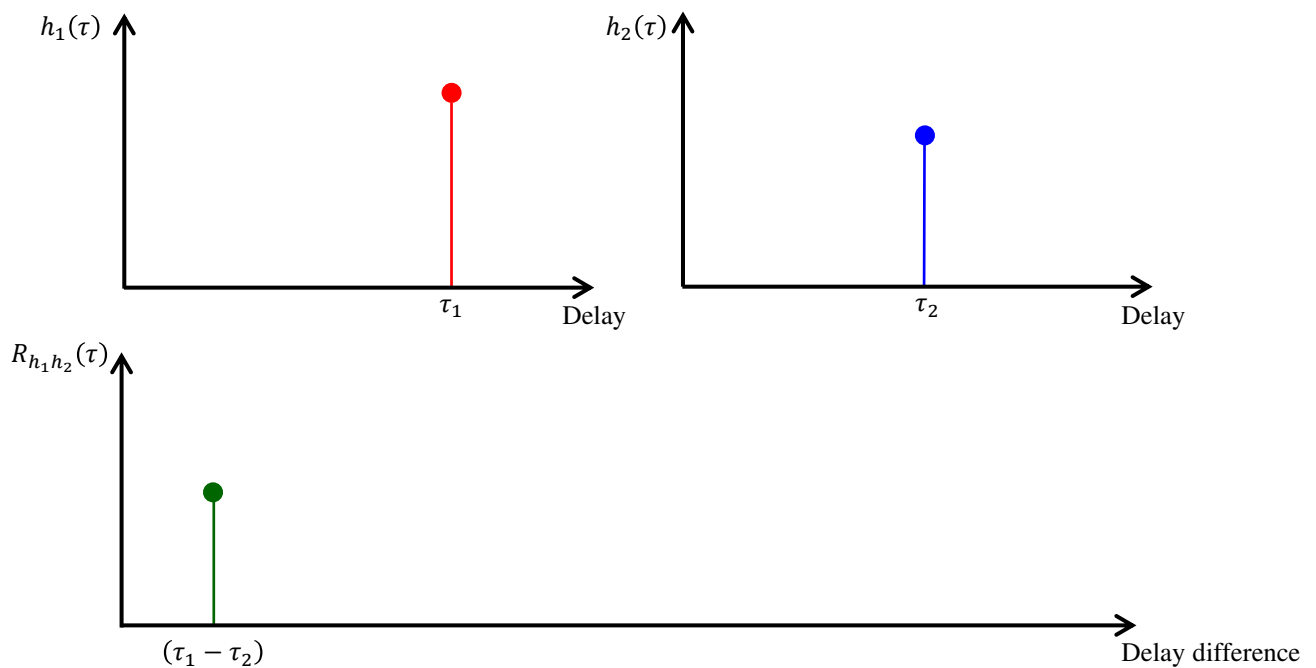


Figure 5.3 Output of the CIRs cross-correlation for single path ideal channels

5.2.4 Multipath channels

Let's assume that both channels are multipath channels where ionospheric propagation occurs via different layers of the ionosphere (e.g. one through the E and the other through F layer). The output of the CIRs cross-correlation of the received signals having different multipath channel is represented in Figure 5.4. In $h_1(\tau)$, τ_1 and τ_2 correspond to the propagation durations of the signal from the transmitter to Rx₁ via a reflection from the E and the F layer, respectively. Similarly, τ_3 and τ_4 correspond to the propagation duration of the signal from the transmitter to Rx₂ via a reflection from the E and F layer, respectively. Due to multipath channels, when the CIRs are cross-correlated, it results in multiple peaks. These peaks have varying intensities depending on the power at which the signals reflected from different layers are received. Different peaks corresponding to different time delays in Figure 5.4 are expressed as follows:

$$\begin{aligned}
 \tau_{14} &= \tau_1 - \tau_4 \\
 \tau_{13} &= \tau_1 - \tau_3 \\
 \tau_{24} &= \tau_2 - \tau_4 \\
 \tau_{23} &= \tau_2 - \tau_3
 \end{aligned}
 \tag{5.17}$$

Due to multiple peaks, it becomes difficult to select the peak which provides the most accurate time delay between the received signals by different receivers. For practical purpose, one can select the peak with the strongest signal level in the cross-correlation output. In the example of Figure 5.4, it corresponds to the time delay (τ_{24}) between the signals reflected via the F layer for both propagation paths.

In the case of multipath channels, TDoA estimation is complex when multiple peaks illustrating different paths with different intensities are very close to each other. Thus, in order to distinguish between multiple peaks which are very close to each other, the system resolution must be very high. It can be achieved by sampling the received signals at a higher rate. However, in the case of multiple propagation paths, the minimum resolution is limited by the useful signal bandwidth.

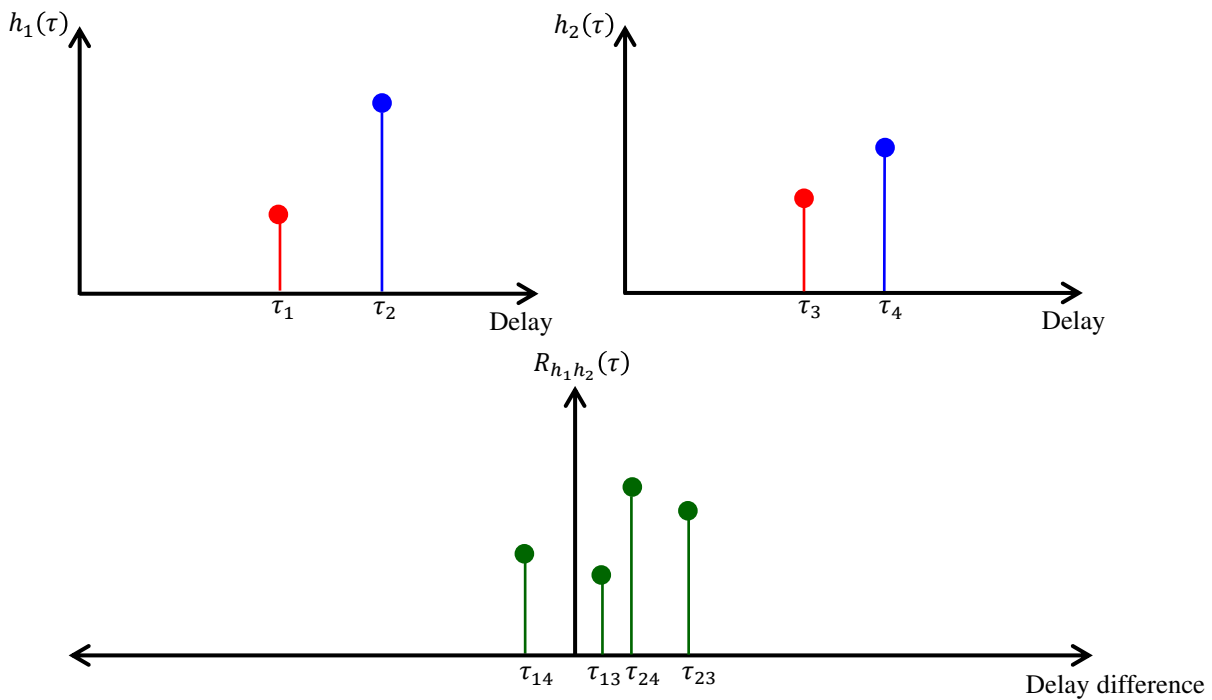


Figure 5.4 Output of the CIRs cross-correlation for multipath channels

Cross-channel sounding method is a way of obtaining the time delay between signals received by distinct synchronized receivers. The time delay is obtained by cross-correlating the received signals as long as the autocorrelation of the transmitted signal is equivalent to a large peak centred at the origin. The time delays estimated for different captures using cross-channel sounding method are explained in section 5.3.

5.3 TDoA estimation and identification of propagation modes

HF radio signals were captured from different HF broadcast transmitters (section 4.3.2) located around Europe using the receiver network explained in section 4.3. All the signals were captured for duration of 5 seconds and sampled at the rate of 200 kHz.

Signal processing: The captured data files were post-processed and data was retrieved in the form of complex samples (IQ data). To eliminate other interfering signals captured with the signal of interest

(intended capture), the captured signal was filtered in the frequency domain. The bandwidth of the captured spectrum was 200 kHz, out of which only 5 kHz of signal on either side of the carrier frequency of the broadcast transmitter was kept and the rest was filtered out. The signal was transformed back to time domain and received signal's average power was calculated. Then, the transformed signal was demodulated to obtain the message signal samples. Finally, the TDoA between the signals received on two distinct distributed synchronized receivers were computed using the cross-channel sounding method (i.e. by cross-correlating two received message signals).

In order to compare the estimated TDoA values obtained from measurements, theoretical TDoA values are computed assuming a one-hop propagation mode for all received signals.

Theoretical TDoA computation: The GPS locations of the HF broadcast transmitters and the receivers were transformed to x and y coordinates using the azimuthal equidistant projection [143] considering the receiver in Brest as the origin of the coordinate system. The virtual reflection height at the midpoint of the one-hop propagation path can be found if the ionospheric profile is known at that location, which is practically not the case. Digital ionograms which gives an estimate of the different ionospheric parameters are recorded every day at different locations around Europe and are available online [16]. At mid-latitudes, the ionospheric variations are not very high. Thus, one can use the ionograms available from the closest location of the midpoint of the one-hop propagation path to calculate the virtual reflection height. The ionogram recorded in Dourbes (Belgium) with respect to the capture times of the radio signal was used. Using the secant's law and the known distance between the transmitter and the receiver, the vertical incidence digital ionogram was converted to an oblique incidence ionogram [5]. An approximate virtual reflection height corresponding to carrier frequency of the transmitter was obtained. From the known transmitter and receiver locations and the estimated approximate virtual reflection height, the group paths were computed using the geometry of one-hop propagation mode. Knowing the speed of a radio wave, the signal travel time was calculated for both propagation paths and the corresponding theoretical TDoA between two receivers was obtained.

Some measurement examples characterizing the different propagation modes based on the TDoA estimate obtained from cross-channel sounding are discussed in the following sections (section 5.3.1 to section 5.3.3).

5.3.1 Case 1: Single path channels

Figure 5.5 represents the TDoA estimate for a HF broadcast signal captured simultaneously in Brest and Bordeaux on 21st of July at 19:13 UTC. The HF broadcast transmitter located in Nauen, Germany was transmitting radio signals at a frequency of 11.790 MHz. As seen in Figure 5.5, there is only a single peak in the cross-correlation output which implies that the radio signals arrived at the different receivers through single path channels (i.e. 1E or 1F mode). This example resembles to the case of two single path channels as explained in section 5.2.3 and illustrated in Figure 5.3. The TDoA corresponding to the cross-correlation peak is equal to 20 μ s.

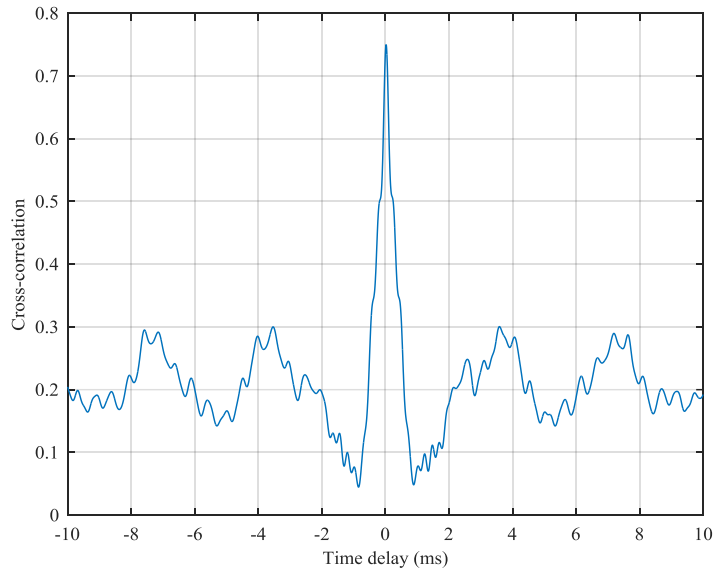


Figure 5.5 Cross-channel sounding output for HF broadcast signals received simultaneously in Brest and Bordeaux from HF transmitter site in Nauen, Germany

In order to verify the propagation modes of the received signals, virtual reflection heights along different HF propagation paths are estimated using data available from ionograms as explained earlier. The estimated virtual reflection heights and the corresponding theoretical TDoA value are listed in Table 5.1. From Table 5.1, one can clearly observe that the radio signals received in Brest and Bordeaux propagated through a single path channel ($1E_s$ propagation mode). The received signals were reflected from E_s layer at a virtual height of about 110 km and the corresponding theoretical TDoA value is equal to 17 μ s.

Ionosonde location	Ionogram capture date & time (UTC)	HF link	Estimated virtual reflection height (km)	Ionospheric reflection layer	Theoretical TDoA (μ s)
Dourbes	21/07/2017 19:15:02	Nauen - Brest	110	E_s	17 (E_s, E_s)
		Nauen - Bordeaux	110	E_s	

Table 5.1 Details of ionospheric conditions and the estimated theoretical TDoA for an example of single path channels

5.3.2 Case 2: Combination of single and multipath channels

Figure 5.6 shows the TDoA estimate for a HF broadcast signal captured synchronously in Brest and Grenoble on 18th of July at 20:13 UTC. The broadcast transmitter is located in Moosbrunn, Austria and was emitting at a frequency of 11.880 MHz. As seen in Figure 5.6, there are 2 peaks with different amplitudes in the cross-correlation output. This implies that the radio signals arrived at one of the receiver through single path channel whereas, on the other receivers, through multipath channel. Table 5.2 provides the estimates of virtual reflection heights for different HF links computed by transforming digital ionograms to oblique ionograms. From Table 5.2, it can be said that the propagation path is a mix of $1E_s$ and $1F_2$ modes for the signal received in Brest whereas it is $1E_s$ mode for the signal received in Grenoble. The TDoA corresponding to the maximum peak is 2.27 ms which is consistent with $1E_s$ propagation mode for signals received on both receivers. The other peak obtained at 2.505 ms corresponds to the signal received in Brest and Grenoble through $1F_2$ and $1E_s$ mode, respectively. The time delays corresponding to these peaks are approximately equivalent to the theoretical TDoA's listed in Table 5.2.

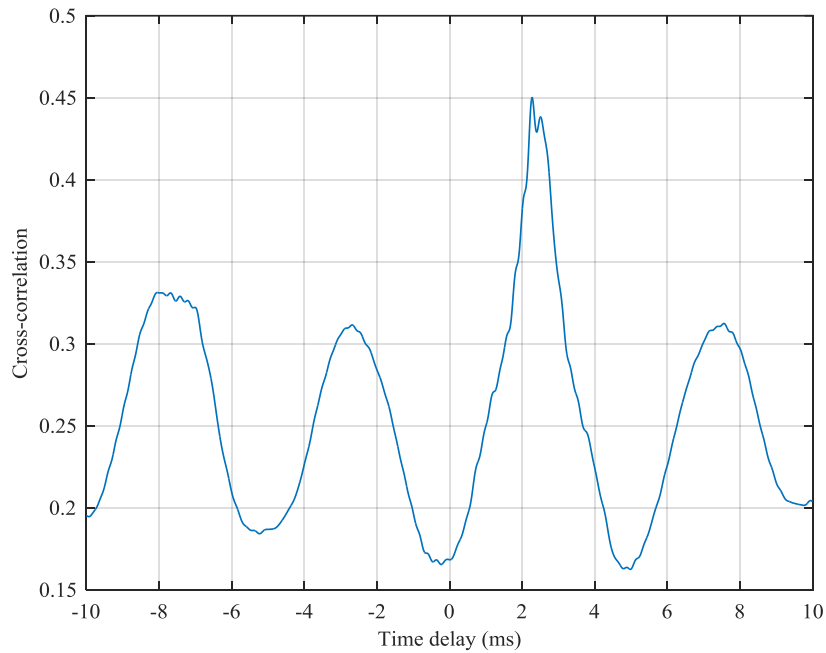


Figure 5.6 Cross-channel sounding output for HF broadcast signals received simultaneously in Brest and Grenoble from HF transmitter site in Moosbrunn, Austria

Ionosonde location	Ionogram capture date & time (UTC)	HF link	Estimated virtual reflection height (km)	Ionospheric reflection layer	Theoretical TDoA (ms)
Dourbes	18/07/2017 20:10:02	Moosbrunn - Brest	105, 260	E_s, F_2	2.2308 (E_s, E_s) 2.4659 (F_2, E_s)
		Moosbrunn - Grenoble	105	E_s	

Table 5.2 Details of ionospheric conditions and the estimated theoretical TDoA values for an example of single and multipath channels

5.3.3 Case 3: Multipath channels

Figure 5.7 shows the TDoA estimate for a HF broadcast signal captured simultaneously in Brest and Lille on 13th of July at 11:46 UTC. The broadcast transmitter is located in Romania and was transmitting at a frequency of 15.130 MHz. As seen in Figure 5.7, there are multiple peaks in the cross-correlation output which implies that the radio signals arrived at both receivers through multipath channels. It can be further interpreted that the received signal at both receivers, consists of signals reflected from E and F layers of the ionosphere. This example resembles the multipath channel case explained in section 5.2.4 and depicted in Figure 5.4. The different amplitudes, with which signals are received for different propagation modes, translate in different amplitudes for the cross-correlation peaks.

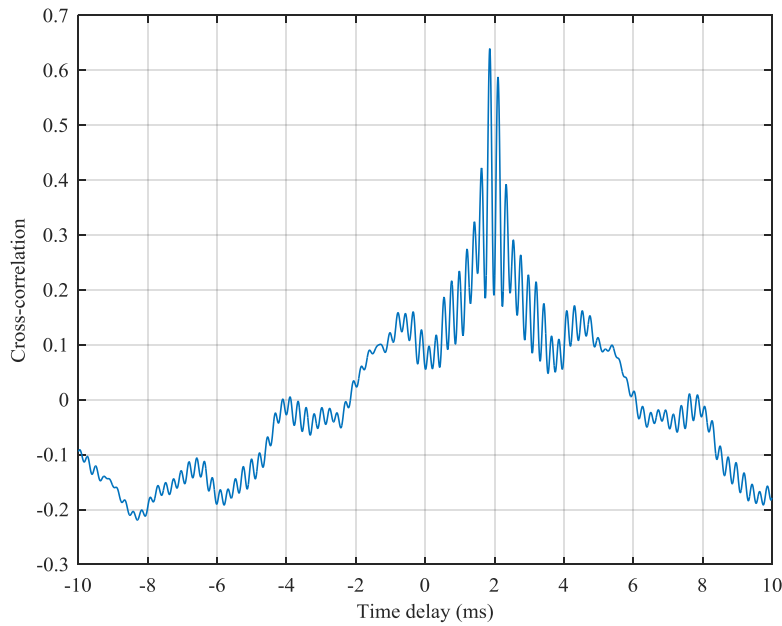


Figure 5.7 Cross-channel sounding output for HF broadcast signals received simultaneously in Brest and Lille from HF transmitter site in Galbeni, Romania

In order to check the validity of multipath channels, data from ionosonde in Dourbes were processed to see the possible propagation paths for the experimental HF links. The estimated virtual reflection heights possible along the two different HF links are summarized in Table 5.3. It can be seen that the propagation path is a mix of 1E and 1F₁ modes for the signal received in Brest and reflected at virtual heights of about 95 and 260 km, respectively. Similarly, the propagation path is a mix of 1E and 1F₁ modes for the signal received in Lille and reflected at virtual heights of about 95 and 210 km, respectively. The maximum peak corresponds to a time delay of 1.86 ms which is approximately equal to the theoretical TDoA obtained from a virtual height of 95 km (i.e. from the E layer) for both propagation paths. It can also be interpreted that signals reflected from the E layer are received with higher amplitudes at both receivers. The other peaks in the cross-correlation outputs correspond to time delays obtained by different combinations of the propagation paths.

Ionosonde location	Ionogram capture date & time (UTC)	HF link	Estimated virtual reflection height (km)	Ionospheric reflection layer	Theoretical TDoA (ms)
Dourbes	13/07/2017 11:45:02	Galbeni - Brest	95, 260	E, F ₁	1.8694 (E, E) 1.9045 (F ₁ , F ₁) 1.7405 (E, F ₁) 2.0334 (F ₁ , E)
		Galbeni - Lille	95, 210	E, F ₁	

Table 5.3 Details of ionospheric conditions and the estimated theoretical TDoA for an example of multipath channels

Table 5.4 provides the summary of the measured TDoA and the corresponding theoretical TDoA values for different cases of HF propagation channels.

HF transmitter site	Capture date	Capture start time (UTC)	Measured TDoA	Theoretical TDoA	TDoA error (μ s)
Nauen	21/07/2017	19:13:00	20 μ s	17 μ s	3
Moosbrunn	18/07/2017	20:13:00	2.27 ms	2.2308 ms	39.2
Galbeni	13/07/2017	11:46 :00	1.86 ms	1.8694 ms	9.4

Table 5.4 Summary of TDoA's obtained from measurements and simulations

It can be concluded that the TDoA estimates can be obtained from cross-channel sounding method (section 5.3.1 – section 5.3.3). In order to find the geographic location of a HF transmitter, a minimum of 3 TDoA estimates are required. Using our receiver network, HF radio signals are captured from different transmitters and processed to obtain the TDoA estimates. Experimental geolocation results of different HF transmitters are presented in section 5.4.

5.4 Preliminary geolocation results

In the first experimental measurement campaign, all HF radio signals were captured for 5-second duration with a one-minute interval between start times of two captures from the same transmitter site. Using azimuthal equidistant projection system, the GPS coordinates of HF transmitters and all receivers in the network were converted into a rectangular coordinate system. Coordinates of the selected reference receiver were used as the origin of the coordinate system. Details of the captures analysed from different HF transmitters over several days are summarized in Table 5.5.

Date	Transmitter site	Capture frequency (MHz)	Capture time (UTC)	Capture count
17-07-17	Galbeni	15.130	13:15-13:18	4
18-07-17	Santa Maria di Galeria (SMDG)	15.570	16:11-16:20	10
21-07-17	Nauen	11.790	19:11-19:20	10
26-07-17	Cerrik	11.885, 13.710	08:16-08:20	5
27-07-17	Moosbrunn	11.880	20:11-20:15	5

Table 5.5 Summary of HF radio signals captured from different transmitters

Reference receiver selection criteria: The geolocation algorithm used to estimate the geographic location of the HF transmitter is dependent on the reference receiver, as explained in section 3.2.3. The received signal average powers were calculated for all receivers and the receiver with the highest signal average power was considered as the reference receiver. Using the cross-channel sounding technique, the message signal samples from the reference receiver were cross-correlated with the message signal samples from the other three receivers to obtain three TDoA estimates. Finally, the transmitter location was estimated using the obtained TDoA values by solving a system based on quadratic equations (section 3.2.3). Some of these captured data from different HF transmitters are analyzed and discussed in section 5.4.1 to section 5.4.4.

5.4.1 Example: Favorable propagation conditions

A HF radio signal which was captured synchronously by the four receivers on 21st July at 19:19 UTC from Nauen is studied. The received signals on all receivers were demodulated and the message signal was extracted as explained earlier. The signal received in Grenoble was considered as the reference signal on account of the received signal power. Figure 5.8 (a) presents the HF radio signal captured in Grenoble from Nauen.

The propagation duration differences calculated using the cross-channel sounding method between the signals received in Brest-Grenoble, Bordeaux-Grenoble and Lille-Grenoble can be seen in (b), (c) and (d) of Figure 5.8, respectively. As seen in the three TDoA plots, there is a single cross-correlation peak which corresponds to one-hop propagation mode for signals received by both receivers. Using the obtained TDoA estimates, the HF transmitter site was located with an error as small as 2.2 km. This corresponds to a relative error of about 0.17% calculated with respect to the maximum ground range among the four possible HF links. Figure 5.12 presents the actual and estimated geographic location of the HF transmitter in Nauen.

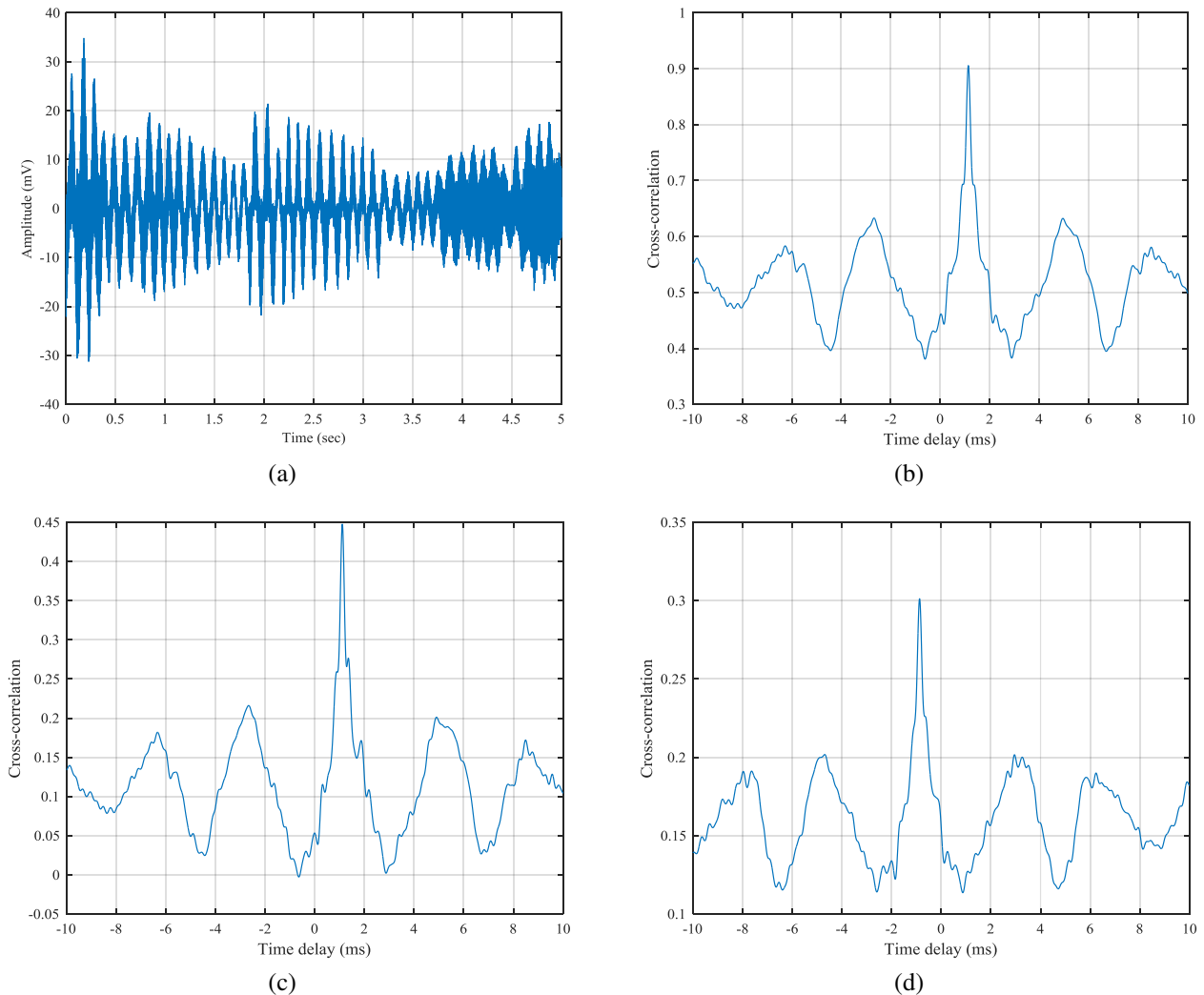


Figure 5.8 HF signal captured in Grenoble from Nauen on 21st July, 2017 at 19:19 UTC (a); TDoA estimates for HF signals captured in Brest-Grenoble (b), Bordeaux-Grenoble (c) and Lille-Grenoble (d)

5.4.2 Example: Moderate propagation conditions

This example provides the analysis of a HF signal captured from the HF transmitter located in SMDG by all receivers in the network on 18th July at 16:12 UTC. Based on the received signal strengths at different receivers, the signal captured in Grenoble was considered as the reference signal. Figure 5.9 (a) represents the power spectrum of the HF signal captured in Grenoble.

The message signal samples extracted after demodulation were cross-correlated and three TDoA estimates were obtained. These estimates corresponding to the cross-correlation peak between the signals captured in Brest-Grenoble, Bordeaux-Grenoble and Lille-Grenoble are presented in Figure 5.9 (b), (c) and (d) respectively. Using the geolocation algorithm, the transmitter coordinates were estimated and the geolocation error was about 81.50 km. This error seems moderate and is equivalent to a relative error of about 5.45%. The actual and estimated transmitter location can be seen in Figure 5.12.

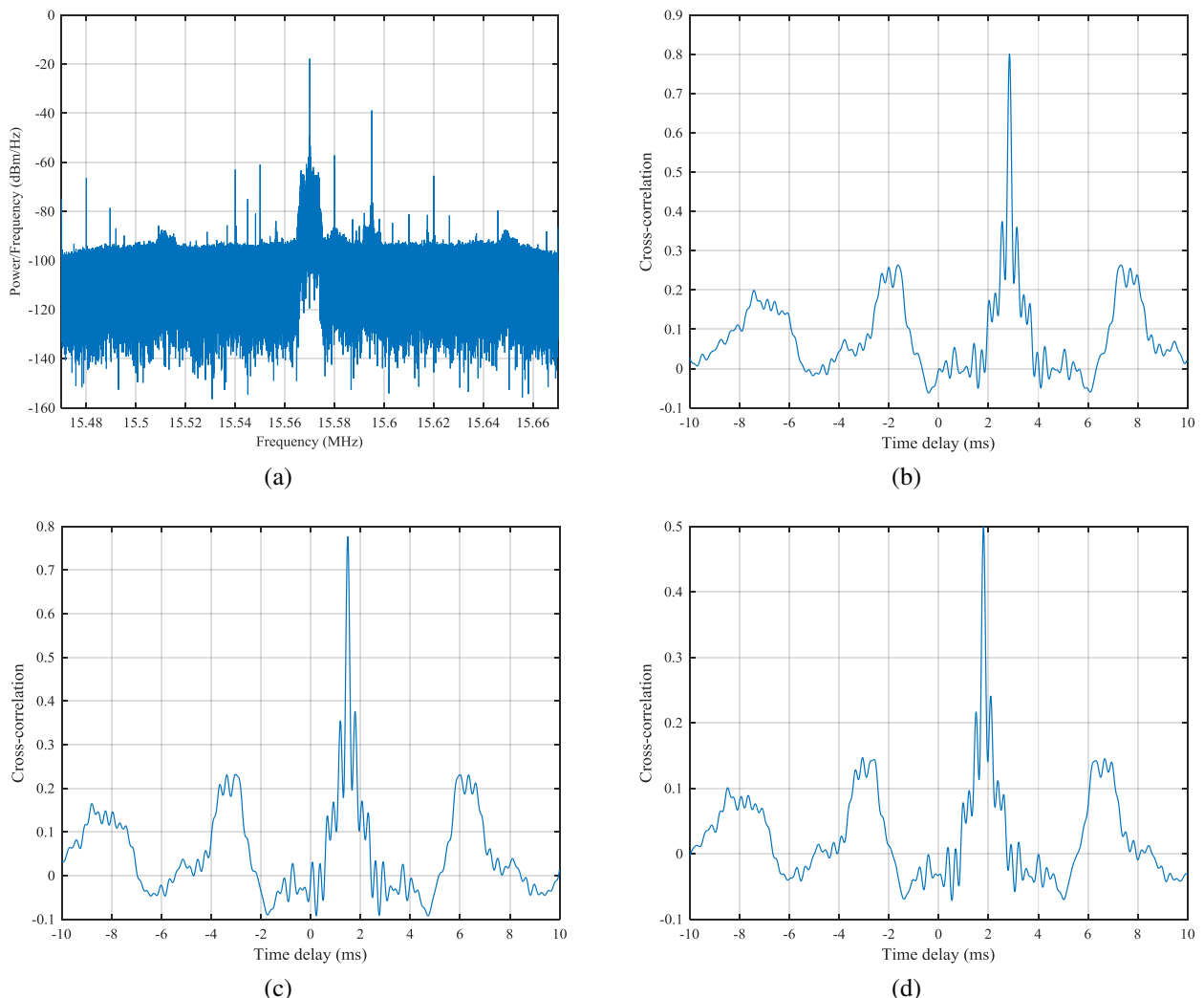


Figure 5.9 Power spectrum of HF signal captured in Grenoble from SMDG on 18th July at 16:12 UTC (a); TDoA estimates for HF signals captured in Brest-Grenoble (b), Bordeaux-Grenoble (c) and Lille-Grenoble (d)

5.4.3 Example: Geometric dilution of precision

In this example, data captured from Moosbrunn on 27th July at 20:12 UTC are analyzed. The signal received in Grenoble was considered as the reference signal based on the received signal intensity. Using the known receiver positions and the TDoA estimates, the geographic location of the transmitter was estimated, and is

presented in Figure 5.12. The geolocation error is large, about 292 km which corresponds to a relative error of 18.8%.

Localization based on TDoA estimations suffers from an error caused by long ranges from the receiver's baseline. The baseline refers to the distance between the receivers. The geometric solution for localization of HF transmitter in Moosbrunn and Galbeni based on TDoA method are illustrated in Figure 5.10 (a) and (b), respectively. TDoA based systems locate the target by using multilateration principle at intersection of hyperbolas in the 2D case (and of hyperboloids in the 3D case). In the following illustrative example, as the receiver and transmitter locations were known, the TDoA estimates were computed assuming the receiver in Brest as the reference. Using the obtained TDoA's, the hyperbolas were plotted using different receiver pairs and considering the locations of the receivers as the foci of the hyperbola. As seen in Figure 5.10 (a) and (b), the hyperbolic line of positions (LOPs) generated from the receiver pair of Brest-Bordeaux and Brest-Grenoble were nearly parallel for the transmitter located in Moosbrunn and Galbeni, respectively. As the TDoA values were exact, the location of the transmitter was found without any error. A small error in TDoA due to noise or small measurement errors will result in shift of the hyperbolic LOPs thereby resulting in large geolocation error. This is referred to as Geometric Dilution of Precision (GDOP). The GDOP gets worse when the transmitters are farther away from receiver baselines [106], which can be seen from the geolocation errors obtained for the HF transmitter in Galbeni. This example explains a case where a slight error in the estimated TDoA's leads to a large geolocation error.

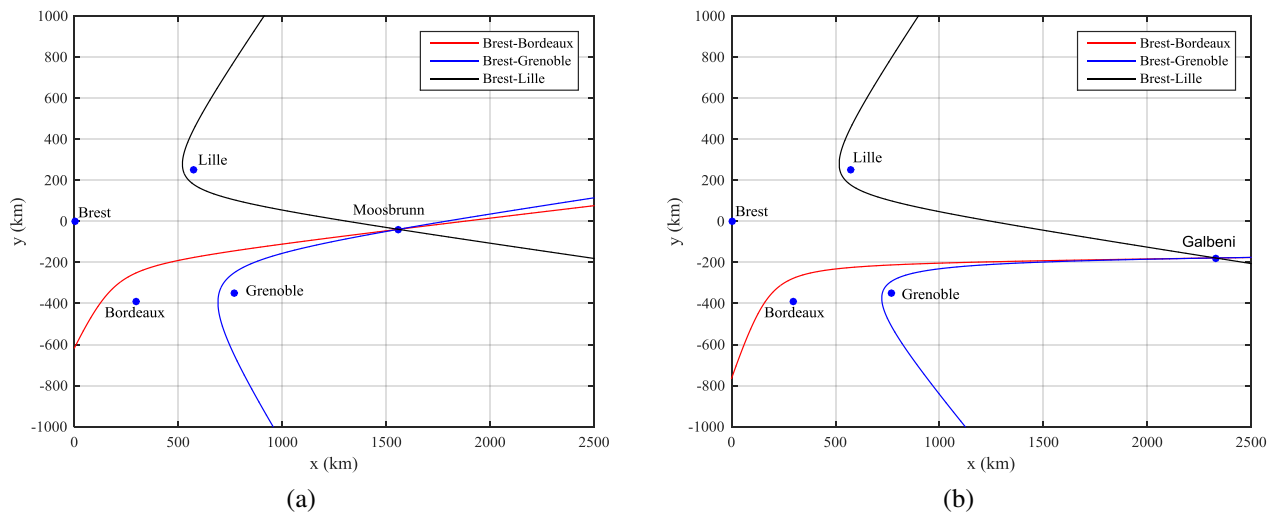


Figure 5.10 Geometric localization for HF transmitter situated in Moosbrunn (a) and Galbeni (b) using the TDoA method

5.4.4 Example: Effect of multipath propagation

This example investigates data captured from the HF transmitter located in Cerrik on 26th July at 08:17 UTC. The signal received in Lille was considered as the reference signal considering the received signal intensity on different receivers. By cross-correlating the reference signal with the signal received by other receivers, estimates of TDoA's were obtained. Figure 5.11 presents the cross-correlation output for the signals captured in Bordeaux and Lille. As seen in Figure 5.11, there are two peaks separated by 265 μ sec in cross-correlation output with different amplitudes. This implies that the signal was received at least at one of the receivers through multipath channels. The time delay corresponding to the maximum power was selected as the TDoA estimate and the transmitter coordinates were estimated using the geolocation algorithm. The geolocation error was about 152 km corresponding to a relative error of about 7.2%. The true and the estimated geographic location of the transmitter can be seen in Figure 5.12.

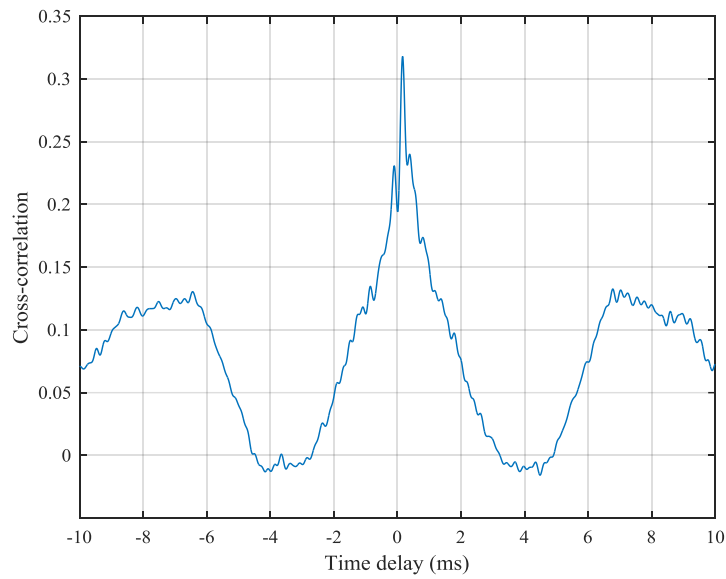


Figure 5.11 TDoA estimate for HF signal captured in Bordeaux and Lille from Cerrik on 26th July at 08:17 UTC

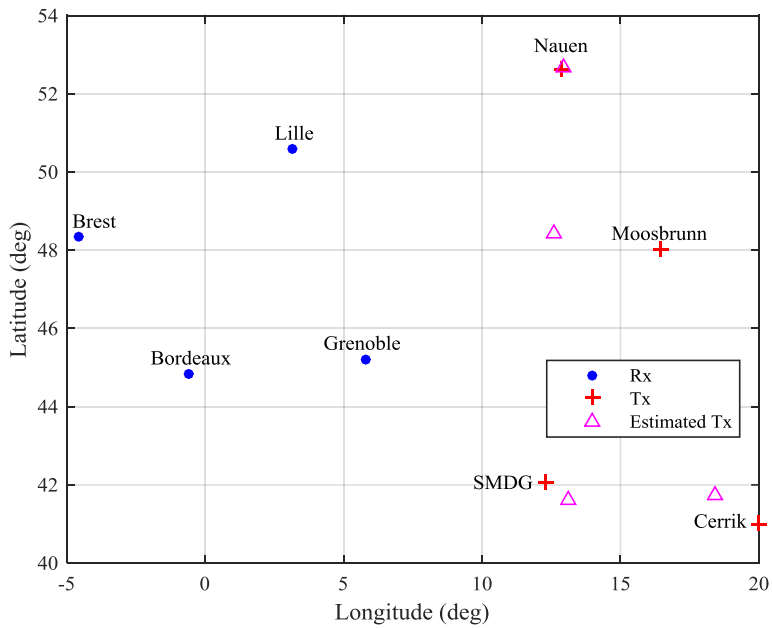


Figure 5.12 Estimated and true geographic location of HF transmitters for different measurement examples

5.4.5 Analysis of azimuthal vs. range error

Table 5.6 provides the summary of the geolocation error for 4 different captured signals from the HF transmitter in Galbeni on 17th July between 13:15-13:18 UTC. The minimum geolocation error of 93.95 km corresponds to a relative error of about 4% computed with respect to the maximum ground range among the four possible HF paths whereas the maximum geolocation error of 1173 km corresponds to a relative error of about 49.9% and it is mainly due to GDOP as explained in section 5.4.3. The obtained azimuth errors for all the captured signals are also listed in Table 5.6. It can be observed that the accuracy of direction of localization in terms of azimuth angle is very high when compared to the geolocation errors.

Data capture time (UTC)	Reference receiver location	Error (km)	Relative error (%)	Azimuth error (°)
13:15	Bordeaux	93.95 (minimum)	3.99	1.34
13:16	Lille	536.13	22.81	3.39
13:17	Lille	1173	49.90	5.30
13:18	Bordeaux	880.59	37.46	-0.63

Table 5.6 Geolocation and azimuth errors for HF radio signals captured from Galbeni, Romania on 17th July, 2017

The summary of geolocation and azimuth errors for 10 different captured signals from the HF transmitter in SMDG on 18th July between 16:11-16:20 UTC is provided in Table 5.7. For all ten captures, the received signal in Grenoble was selected as the reference signal as it was received with the highest SNR. The minimum geolocation error of 43.25 km corresponds to a relative error of about 2.89% whereas the maximum geolocation error of 95.90 km corresponds to a relative error of about 6.42%. The minimum and maximum errors were obtained within an interval of 1 minute. This rapid fluctuation in the geolocation accuracy is due to the fast variations of the ionosphere which leads to variable results in a very short period. In order to reduce this effect, one can consider averaging the obtained results within a certain time interval. From the obtained azimuth errors, it can be said that the direction of localization accuracy in terms of azimuth direction is very high.

Data capture time (UTC)	Reference receiver location	Error (km)	Relative error (%)	Azimuth error (°)
16:11	Grenoble	81.50	5.45	-0.04
16:12	Grenoble	81.50	5.45	-0.04
16:13	Grenoble	81.50	5.45	-0.04
16:14	Grenoble	81.50	5.45	-0.04
16:15	Grenoble	57.38	3.84	0.27
16:16	Grenoble	85.87	5.74	0.17
16:17	Grenoble	57.38	3.84	0.27
16:18	Grenoble	71.23	4.76	0.02
16:19	Grenoble	95.90	6.42	-0.28
16:20	Grenoble	43.25 (minimum)	2.89	0.12

Table 5.7 Geolocation and azimuth errors for HF radio signals captured from SMDG, Italy on 18th July, 2017

Table 5.8 provides the summary of the geolocation and azimuth errors for 10 different captured signals from the HF transmitter in Nauen on 21st July between 19:11-19:20 UTC. For all ten captures, the received signal in Grenoble was selected as the reference receiver on the basis of received signal intensity. The minimum geolocation error of 2.2 km corresponds to a relative error of about 0.17% whereas the maximum geolocation error of 70.64 km corresponds to a relative error of about 5.34%. From the calculated azimuth errors, it can be again said the algorithm output in terms of azimuth direction of localization is very high for HF signals captured from Nauen.

Data capture time (UTC)	Reference receiver location	Error (km)	Relative error (%)	Azimuth error (°)
19:11	Grenoble	70.64	5.34	-1.64
19:12	Grenoble	26.93	2.03	-0.46
19:13	Grenoble	41.03	3.10	-0.86
19:14	Grenoble	64.24	4.85	-1.47
19:15	Grenoble	31.88	2.41	-0.82
19:16	Grenoble	58.67	4.43	-1.54
19:17	Grenoble	2.69	0.20	-0.09
19:18	Grenoble	14.62	1.10	0.30
19:19	Grenoble	2.22 (minimum)	0.17	0.03
19:20	Grenoble	19.69	1.49	0.66

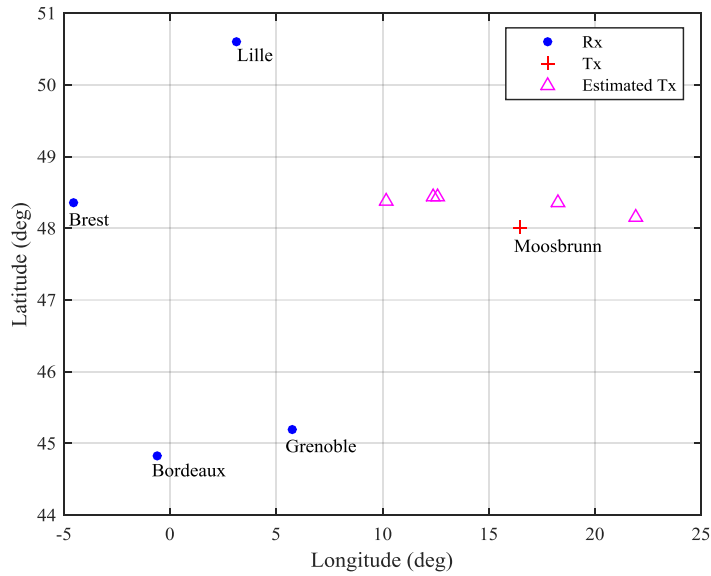
Table 5.8 Geolocation and azimuth errors for HF radio signals captured from Nauen, Germany on 21st July, 2017

The geolocation and azimuth errors for 5 different captured signals from the HF transmitter in Cerrik on 26th July between 08:16-08:20 UTC are listed Table 5.9. The minimum geolocation error of 152.73 km corresponds to a relative error of about 7.28% whereas the maximum geolocation error of 507.53 km corresponds to a relative error of about 24.21%. It is observed that the accuracy in terms of azimuth direction of localization is very high when compared to the geolocation errors.

Data capture time (UTC)	Reference receiver location	Error (km)	Relative error (%)	Azimuth error (°)
08:16	Lille	363.61	17.34	-3.88
08:17	Lille	152.73 (minimum)	7.28	-1.27
08:18	Grenoble	291.37	13.90	0.96
08:19	Lille	507.53	24.21	-5.90
08:20	Grenoble	449.31	21.43	2.29

Table 5.9 Geolocation and azimuth errors for HF radio signals captured from Cerrik, Albania on 26th July, 2017

Table 5.10 provides the summary of the geolocation and azimuth errors for 5 different captured signals from the HF transmitter in Moosbrunn on 27th July between 20:11-20:15 UTC. For all five captures, the received signal in Grenoble was selected as the reference receiver on the basis of received signal intensity. In general, the geolocation errors are large due to the effect of GDOP as explained in section 5.4.3. Figure 5.13 presents the estimated geographic locations for the data captured from Moosbrunn.


 Figure 5.13 Estimated geographic locations for data captured from Moosbrunn on 27th July, 2017

Data capture time (UTC)	Reference receiver location	Error (km)	Relative error (%)	Azimuth error (°)
20:11	Grenoble	305.42	19.63	13.12
20:12	Grenoble	291.96	18.76	12.45
20:13	Grenoble	137.06 (minimum)	8.81	-0.04
20:14	Grenoble	407.48	26.19	-4.05
20:15	Grenoble	466.90	30.01	23.34

 Table 5.10 Geolocation and azimuth errors for HF radio signals captured from Moosbrunn, Austria on 27th July, 2017

5.5 Conclusion

In this chapter, the principle and different methods of classical channel sounding are explained along with its advantages and drawbacks. Correlation sounding technique results in a higher SNR if the transmitted signal has better autocorrelation properties.

A new method termed as cross-channel sounding used to estimate the TDoA between signals received at multiple receivers is proposed and explained. The TDoA estimate can be obtained with a higher accuracy depending on the correlation properties of the transmitted signal. Using different measurement examples, the feasibility of using cross-channel sounding to obtain the TDoA between HF radio signals received at multiple receivers is demonstrated. From the cross-channel sounding output, the propagation channels through which signals arrive at the reception sites can be identified. Further, in order to identify the specific propagation modes along each HF link, one must be aware of the ionospheric profile along the propagation path. In the case of single path channels, the estimation of the TDoA is easier, as there is only a single peak in the cross-channel sounding output. But, for multi-path channels, the multiple peaks in the cross-channel sounding make the estimation of the most accurate TDoA more difficult. In such cases, the TDoA corresponding to the peak with maximum amplitude can be selected. In the future, advanced algorithms taking into account several detected peaks in the cross-correlation output could be devised.

Some of the captured data using the receiver network from different HF stations located around Europe on different days in July, 2017 are analyzed in detail. The TDoA estimates are obtained using the cross-correlation method. From the known receiver positions and estimated TDoA's, the transmitter location is estimated using the geolocation algorithm. Geolocation performance is presented and discussed for the analyzed HF signals captured from different transmitters at different times of different days.

In favorable conditions, the minimum geolocation errors for all the HF transmitters considered are less than 10%. Considering the coverage area for one-hop HF propagation mode in km, these errors are small and acceptable. These geolocation errors can be further reduced by capturing data on more than the minimum number of required receivers in the TDoA method. In most of the cases, the algorithm output in terms of azimuth direction of localization was approximately correct. From the analysis of geolocation results, it can be concluded that HF geolocation is possible using the TDoA method.

After the preliminary measurement presented in this chapter, a large database of measurement was collected in different phases from different HF radio broadcast transmitters located around Europe. The details of the measurement campaign are presented in Chapter 6 along with the statistical analysis done to evaluate the geolocation performance with respect to different system parameters. In particular, the impact of the received SNR, TDoA accuracy, Tx-Rx distance and frequency were investigated, with the aim of improving the geolocation accuracy.

Chapter 6 Large Scale Measurement Campaign: Statistical Analysis

The principle and concepts of cross-channel sounding along with preliminary geolocation results are discussed in detail in Chapter 5. The statistical analysis for all data captured from the HF receiver network is explained in this chapter. Based on the analysis of measurement results, the geolocation performance is evaluated with respect to different parameters. Section 6.1 provides details about the different measurement campaigns conducted during the thesis. In section 6.2, different measurement criteria are discussed with the aim of considering or discarding a measurement. In particular, data reduction is achieved based on the analysis of the estimated TDoA's. Measurements left after data reductions are classified as valid and invalid based on the HF geolocation algorithm output. The geolocation statistics based on the algorithm output for measurements from different transmitters is provided in section 6.3. The analysis of valid measurements with respect to the propagation conditions, estimated reflection heights and the geolocation errors are explained in section 6.4. In section 6.5, the concept of continuous resolution of the TDoA algorithm is explained for which the estimated output represents a region rather than a location estimate.

6.1 Data set details

A total of 22194 HF radio signals were captured for a span of 5 seconds by the 4 receivers in the network from 13 different HF broadcasters located in 3 different continents (Europe: 10, Asia: 2, Africa: 1). Figure 6.1 represents the geographic location of all the receivers and 11 broadcast transmitters (located in Europe and Africa). Most of the transmitters are generally located to the east of the network. Specifically, the transmitters in Moosbrunn, Galbeni and Tiganesti are located at the east, the transmitters in SMDG, Cerril and Emirler are located at the south east; the transmitter in Nauen is located at the north east of the network.

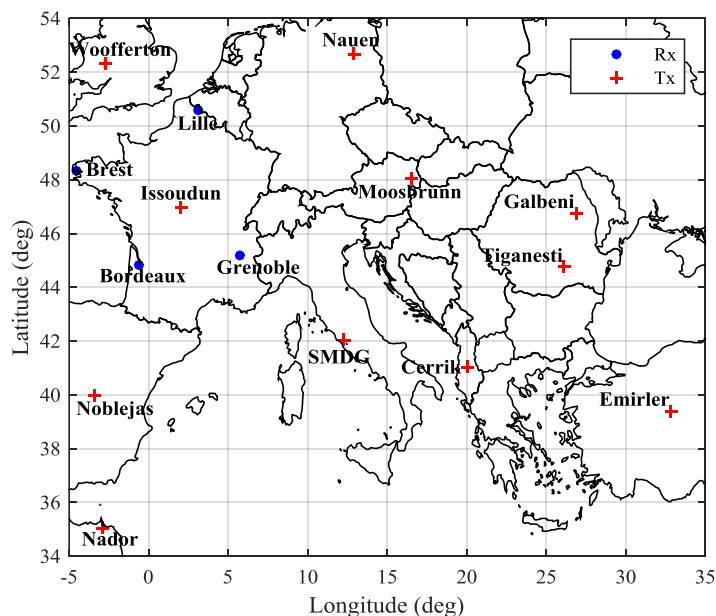


Figure 6.1 Actual geographic location of all receivers and 11 broadcast transmitters

The GPS coordinates of all 13 broadcast transmitters are listed in Table 6.1. All data were captured in 2 different measurement campaigns over a period of about 9 months. Details of the capture from different HF transmitters during measurement campaign 1 and 2 are explained in section 6.1.1 and section 6.1.2, respectively.

Transmitter site	Country	Latitude	Longitude
Nauen (NAU)	Germany	52.65°N	12.91°E
SMDG	Italy	42.04°N	12.32°E
Issoudun (ISN)	France	46.94°N	1.91°E
Nador (NAD)	Morocco	35.04°N	2.91°W
Cerrik (CER)	Albania	41.01°N	19.99°E
Galbeni (GAL)	Romania	46.75°N	26.86°E
Moosbrunn (MOS)	Austria	48°N	16.46°E
Emirler (EMR)	Turkey	39.40°N	32.85°E
Tiganesti (TIG)	Romania	44.75°N	26.11°E
Riyadh (RIY)	Saudi Arabia	24.83°N	46.87°E
Kashi-Saibagh (KAS)	China	39.36°N	75.75°E
Noblejas (NOB)	Spain	39.95°N	3.45°W
Woofferton (WOF)	United Kingdom	52.32°N	2.72°W

Table 6.1 GPS coordinates of HF broadcast transmitters

6.1.1 Measurement campaign 1

During measurement campaign 1, data were captured in 2 different phases. In the first phase, data were captured for some days in July, 2017 whereas during the second phase, data were captured from 19th September, 2017 to 13th November, 2017. The capture details (i.e. capture date, capture timings, capture frequency, HF transmitter site and the number of measurements) for all measurements during the first phase and second phase are summarized in Table 6.2 and in Table 6.5 to Table 6.5, respectively. It must be noted that the measurement schedule is constrained by the HF broadcast schedule, where each transmitter is emitting in a given timeslot and a given frequency on a daily basis. The High Frequency Co-ordination Conference (HFCC) publishes this schedule twice a year (summer and winter) as the whole broadcast is subject to seasonal changes [144]. The broadcasting schedule can also be found on several online resources [118][145]. As the captures were made in different seasons, we needed to adapt the measurement schedule to the forecast broadcast schedule. Also each line in the following tables corresponds to measurements possibly repeated over several days (period indicated in the ‘Date’ column).

Note: While scheduling the captures, the interval between two consecutive captures was 1 minute in most of the cases. Some radio signals were captured at 2 different frequencies from the same HF transmitter and the interval between 2 captures was either 1 minute or 20 seconds. So, captures from the same HF transmitter with 2 different frequencies having an interval of 20 seconds are represented as “20_sec_alt” whereas the captures having an interval of 1 minute are represented as “alt” in tables from Table 6.2 to Table 6.6. () in tables from Table 6.3 and Table 6.6 indicates that data capture were missing on some timings at specific dates within the mentioned date range.*

The missing data captures were mainly due to the improper functioning of the receiver setup at remote sites. Issues were mainly observed with the received GPS timestamps which were incorrect and sometimes the servers were also not responding. To resolve these issues, both server and SDR box were restarted.

Transmitter site	Date	Capture frequency (MHz)	Capture time (UTC)	Capture count
Galbeni	13/07	15.130	11:45-11:47 13:15-13:17	9
		11.950	13:18-13:20	
	17/07	15.130	13:15-13:18	8
		11.950	13:19-13:22	
	18/07	15.130	13:30-13:40	31
		11.950	13:41-13:50 16:41-16:50	
	21/07	11.950	16:41-16:50	10
	25/07 – 27/07	11.650 & 15.400	10:16-10:21 (alt)	18
11.950 & 15130		13:11-13:20 (alt)	30	
11950		16:41-16:45	15	
Cerrick	13/07	13.665	11:48-11:50 12:02-12:04	6
	17/07	13.665	12:40-12:45	6
	18/07	13.710	07:55-07:59	12
		13.665	11:15-11:21	
	25/07 – 27/07	11.855 & 13.710	08:15-08:21 (alt)	21
		13.665	11:21-11:25	15
28/07	11.855 & 13.710	08:15-08:21 (alt)	7	
Emirler	13/07	13.635	11:51-11:53	3
	18/07	13.635	07:50-07:54 10:35-10:39	15
		9.460	17:16-17:20	
	21/07	9.460	17:16-17:20	5
	25/07 – 27/07	15.450 & 9.840	13:04-13:09 (alt)	18
9.460		17:16-17:20	15	
SMDG	13/07	15.570	16:15-16:17 16:20-16:22	6
	17/07	15.570	16:13-16:17	5
	18/07 & 21/07	15.570	16:11-16:20	20
	25/07 – 27/07	15.570	16:11-16:15	15
Nauen	13/07	11.790	19:11-19:13	3
	17/07	11.790	19:13-19:17	5
	18/07 & 21/07	11.790	19:11-19:20	20
	25/07 – 27/07	11.790	19:13-19:18	18
Moosbrunn	13/07	11.880	20:11-20:13	3
	17/07	11.880	20:13-20:17	5
	18/07 & 21/07	11.880	20:11-20:20	20
	25/07 – 27/07	11.880	20:11-20:15	15
Tiganesti	13/07	13.660	17:20-17:22	3
	18/07	15.130	10:30-10:34	5
	18/07 & 21/07	13.660	17:11-17:15	10
	25/07 – 27/07	13.660	17:11-17:15	15
Woofferton	25/07 – 27/07	3.955	20:16-20:21	18
Nador	18/07 & 21/07	9.575	18:16-18:20	10
Issoudun	13/07	15.300	12:12-12:14	8
		13.740	12:15-12:16	
		13.680	14:40-14:42	

Table 6.2 Details of capture schedule from different HF transmitters during first phase of measurement campaign 1

Transmitter site	Date	Capture frequency (MHz)	Capture time (UTC)	Capture count
Emirler	19/09	13.635	08:28-08:30	16
		9.460	17:16-17:20 19:11-19:24 21:21-21:24	
	20/09 – 30/10 (*)	11.980	04:15-04:18 05:15-05:18	1508
		13.635	08:28-08:31 10:28-10:31 11:26-11:29	
		15.450 & 9.840	13:04-13:05:40 (20_sec_alt)	
		9.840	15:04-15:07	
		9.460	17:16-17:20 19:21-19:24 20:41-20:44	
	31/10	11.980	04:15-04:18 05:15-05:18	19
		13.635	08:28-08:31	
		11.815	16:04-16:07	
		6.050	19:41-19:43	
	1/11 – 13/11 (*)	9.700	04:15-04:18 05:15-05:18	432
		15.350	08:28-08:31 09:28-09:31 10:28-10:31 11:26-11:29	
		11.815	15:04-15:07 16:04-16:07	
6.050		19:41-19:43		
Cerrik	19/09	11.855 & 13.710	08:21-08:22:40 (20_sec_alt)	6
	20/09 – 30/10 (*)	11.855 & 13.710	07:15-07:20 (alt) 08:21-08:26 (alt)	899
		13.665	11:21-11:25	
		9.480	18:21-18:23 18:41-18:43	
		5.970	18:44-18:46	
	31/10	11.855 & 13.710	07:15-07:20 (alt) 08:21-08:26 (alt)	22
		7.360	18:41-18:43	
		5.970	18:44-18:46	
		7.285	21:21-21:24	
	1/11 – 13/11 (*)	11.855 & 11.785	07:15-07:20 (alt) 08:21-08:26 (alt)	336
		13.665	11:21-11:25	
		7.360	18:41-18:43	
		5.970	18:44-18:46	
		7.285	21:21-21:24	

Table 6.3 Details of capture schedule from different HF transmitters during second phase of measurement campaign 1

Transmitter site	Date	Capture frequency (MHz)	Capture time (UTC)	Capture count
SMDG	19/09 – 20/09	15.570	16:11-16:15	10
	21/09 – 30/10 (*)	11.625	06:15-06:16 06:45-06:46	807
		13.765	06:17-06:18 06:47-06:48	
		15.570	16:11-16:15 17:06-17:09	
		7.360	20:17-20:18 20:47-20:48	
		9.670	20:19-20:20 20:49-20:50	
	31/10	11.625	06:15-06:16 06:45-06:46 17:16-17:18	28
		13.765	06:17-06:18 06:47-06:48 16:11-16:15 17:06-17:09	
		7.365	20:17-20:18 20:47-20:48	
		9.660	20:19-20:20 20:49-20:50	
	1/11 – 12/11 (*)	13.765	16:11-16:15 17:06-17:09	240
		11.625	17:16-17:18	
		7.365	20:17-20:18 20:47-20:48	
		9.660	20:19-20:20 20:49-20:50	
	Nauen	19/09 – 21/09	11.790	19:13-19:18
22/09 – 30/10 (*)		11.790	19:13-19:18	285
		9.610	20:05-20:07	
31/10		9.535	19:13-19:18	12
		7.205	19:35-19:37	
		9.515	20:05-20:07	
01/11 – 13/11 (*)		11.980	07:35-07:38	248
		15.160	08:05-08:08	
		9.535	19:13-19:18	
	7.205	19:35-19:37		
	9.515	20:05-20:07		
Nador	19/09	9.575	18:21-18:24 18:31-18:34	14
	20/09 – 21/09	9.575	18:21-18:23	
Noblejas	19/09	15.390	18:41-18:43	6
		17.715	18:44-18:46	
	20/09 – 21/09	15.390	18:41-18:42	16
		15.520	18:43-18:44	
		17.715	18:45-18:46	
		17.855	18:47-18:48	

Table 6.4 Details of capture schedule from different HF transmitters during second phase of measurement campaign I (Continued)

Transmitter site	Date	Capture frequency (MHz)	Capture time (UTC)	Capture count
Galbeni	19/09	11.950	16:41-16:43	9
		11.975	17:41-17:43	
		9.500	19:01-19:03	
	20/09 – 30/10 (*)	11.650 & 15.400	10:32-10:32:40 (20_sec_alt)	1215
		11.950 & 15.130	13:11-13:14, 13:21-13:24 (20_sec_alt)	
		11.950	16:41-16:43	
		11.975	17:41-17:43	
	31/10	9.500	19:01-19:03	3
		7.375	19:03-19:05	
	01/11 – 13/11 (*)	7.360	06:15-06:18	280
15.255		11:12-11:15		
11.975		15:14-15:19		
9.810		15:20-15:25		
7.375		19:03-19:05		
Tiganesti	19/09 – 30/10 (*)	9.500	16:31-16:33	245
		11.810	17:11-17:14	
	31/10	7.230	17:11-17:14	8
		7.235	19:21-19:24	
	01/11 – 12/11 (*)	15.430	11:36-11:39	144
		7.230	17:11-17:14	
Riyadh	19/09	7.235	19:21-19:24	18
		17.490	08:24-08:25	
		17.650	08:26-08:27	
		15.380	08:31-08:35	
		15.435	16:44-16:46	
	20/09 – 13/11 (*)	11.820	18:11-18:13 20:11-20:13	1426
		15.380	07:21-07:24	
		15.490	10:21-10:24	
		17.895	14:21-14:22	
		17.705	14:23-14:24	
		15.435	16:44-16:46	
		11.820	18:11-18:13	
		9.555	18:31-18:33 21:11-21:13	
		11.915	19:31-19:33	
11.930	20:31-20:33			
Kashi-Saibagh	20/09 & 21/09	15.410	14:31-14:34	8
	22/09 – 30/10 (*)	13.670	13:31-13:34	256
		15.410	14:31-14:34	
	01/11 – 12/11	15.205	12:15-12:18	96
13.670		13:31-13:34		
Moosbrunn	19/09 – 20/09	11.880	20:11-20:15	10
	21/09 – 30/10 (*)	15.145	08:15-08:18	729
		15.490	12:15-12:18 15:15-15:18	
		11.880	20:11-20:15 21:15-21:19	
	31/10 – 13/11 (*)	15.145	08:15-08:18	186
		9.770	20:11-20:15	
		11.980	21:15-21:19	

Table 6.5 Details of capture schedule from different HF transmitters during second phase of measurement campaign 1 (Continued)

As seen from Table 6.2 to Table 6.5, only a few radio signals were captured from the HF transmitters located in Nador, Issoudun, Noblejas and Woofferton. These captured signals, when demodulated, were found to be noise. Due to the different propagation characteristics, signals were not received at the reception sites. For instance, the transmitter in Issoudun is very close to all receivers in the network; thus, signals could not be received on all receivers through skywaves. For the transmitter in Woofferton, the transmitting frequency is too low for the signals to be propagated via the ionosphere and received, by all receivers. The transmitter in Nador had stopped broadcasting HF radio signals while broadcast signals from Noblejas were not intended to be propagated towards France. Thus, signals captured from these 4 transmitters would not be considered for the HF geolocation study.

6.1.2 Measurement campaign 2

In measurement campaign 2, data were again captured in 2 different phases. During the first phase, data were captured between 14th January, 2018 and 12th February, 2018, whereas in the second phase, data were captured between 19th February, 2018 and 24th March, 2018. Capture details of all measurements during the campaign 2 were identical to the data captured from 1st November to 13th November (see Table 6.5 to Table 6.5) except for a few measurements where capture frequencies were changed and new measurements were added as listed in Table 6.6. Overall, 12191 measurements were made on 4 receivers during the measurement campaign 2.

Transmitter site	Date	Capture frequency (MHz)	Capture time (UTC)
SMDG	14/01 – 12/02 (*)	7.365	20:19-20:20
	19/02 – 24/03 (*)		20:49-20:50
Cerrick	14/01 – 12/02 (*)	7.285	21:25:00
	19/02 – 24/03 (*)		

Table 6.6 Details of changed capture frequency and new capture during measurement campaign 2

Data captured from the transmitter located in Riyadh and Kashi-Saibagh are approximately at a distance of about 5200 and 6200 km, respectively from the receiver setup located in Brest. Due to the ground ranges, signals arrive at receiver network through a multi-hop propagation mode or a mix of different propagation modes. Hence, it does not satisfy our assumption of one-hop propagation mode and, consequently, signals captured from Riyadh and Kashi-Saibagh was not used in the HF geolocation study. However, these signals could be used in the future for the analysis of the ionospheric medium, in particular for analysis of diurnal ionospheric variations.

A large amount of data was captured on 4 receivers in the network from different HF broadcast transmitters located around Europe and Asia. Now, in order to estimate the transmitter location by using the captured data, it needs to be identified whether the captured signals consist of some useful information content or if it is noise. If the captured signal is just noise, the captured data need not be processed further. The identification of the usefulness of the captured signal can be achieved by analyzing them over different measurement qualification metrics which are discussed in the section 6.2.

6.2 Measurement qualification metrics and data reduction

Different means of qualifying a measurement include computing the noise and SNR level of the captured signal. It may happen that the noise and the SNR level are dependent either on the transmitter or on the receiver or on the broadcast frequency or even on a combination of these parameters. Based on the previous outputs, one can qualify a measurement for further processing or exclude it in which case this would result in

data reduction. The measured noise and SNR level for data captured at different receivers from different transmitters are explained in section 6.2.1 and section 6.2.2, respectively.

6.2.1 Noise analysis

In order to compute the noise level of the captured signal, the retrieved complex samples (IQ data) were transformed to the frequency domain. Out of the available 200-kHz bandwidth, data representing only 30 kHz of the spectrum was used to calculate the noise floor level (i.e. 15 kHz on either side of the capture frequency was used); this was mainly done to reduce the processing time required for the calculation of the noise floor. Finally, the noise floor level was calculated using the sliding window method. The sliding window length was equivalent to the number of samples corresponding to 1 kHz of the spectrum. One must note that the capture frequency is the central frequency of the 200-kHz bandwidth.

The obtained noise floor levels for all HF broadcast signals captured during the measurement campaigns in Brest, Bordeaux, Grenoble and Lille as a function of their corresponding capture frequencies can be seen in (a), (b), (c) and (d) of Figure 6.2, respectively. It can be observed that the level of the noise floor generally decreases with the increasing frequency of the different transmitters. In addition, the noise level for all captured signals varies with location of the reception sites. For example, most of the signals captured at around 7.5 MHz in Brest, Bordeaux, Grenoble and Lille has a noise level of about -20 to -5 dBV, -15 to 0 dBV, -5 to 5 dBV and -2 to 2 dBV, respectively.

Table 6.7 provides details of the frequency range of 7 discrete bands out of the available 14 bands for broadcasting over short wave frequency range (2.3 – 26.1 MHz) [145]. The total number of captures corresponding to the different bands is summarized in Table 6.7.

Figure 6.3 represents the CDF's of the noise floor for all the signals captured in Grenoble with regards to different broadcasting frequency bands. From the per-frequency band CDF curves, it can be again observed that the noise floor level decreases with the increase in the broadcast frequency. Unexpectedly, this effect was not observed with the data captured at the other 3 receivers. This observation could be explained by the influence of unbalanced surrounding noise environment considering the different receiver locations. Thus, one can say that the noise level of the received signals depends on the receiver site.

Frequency range (MHz)	Band (m)	Capture count
5.9 - 6.2	49	552
7.2 - 7.45	41	2643
9.4 - 9.9	31	4461
11.6 - 12.1	25	6033
13.57 - 13.87	22	2572
15.1 - 15.8	19	5460
17.48 - 17.9	16	455

Table 6.7 Shortwave broadcasting bands and the number of captures from each frequency band during both measurement campaigns

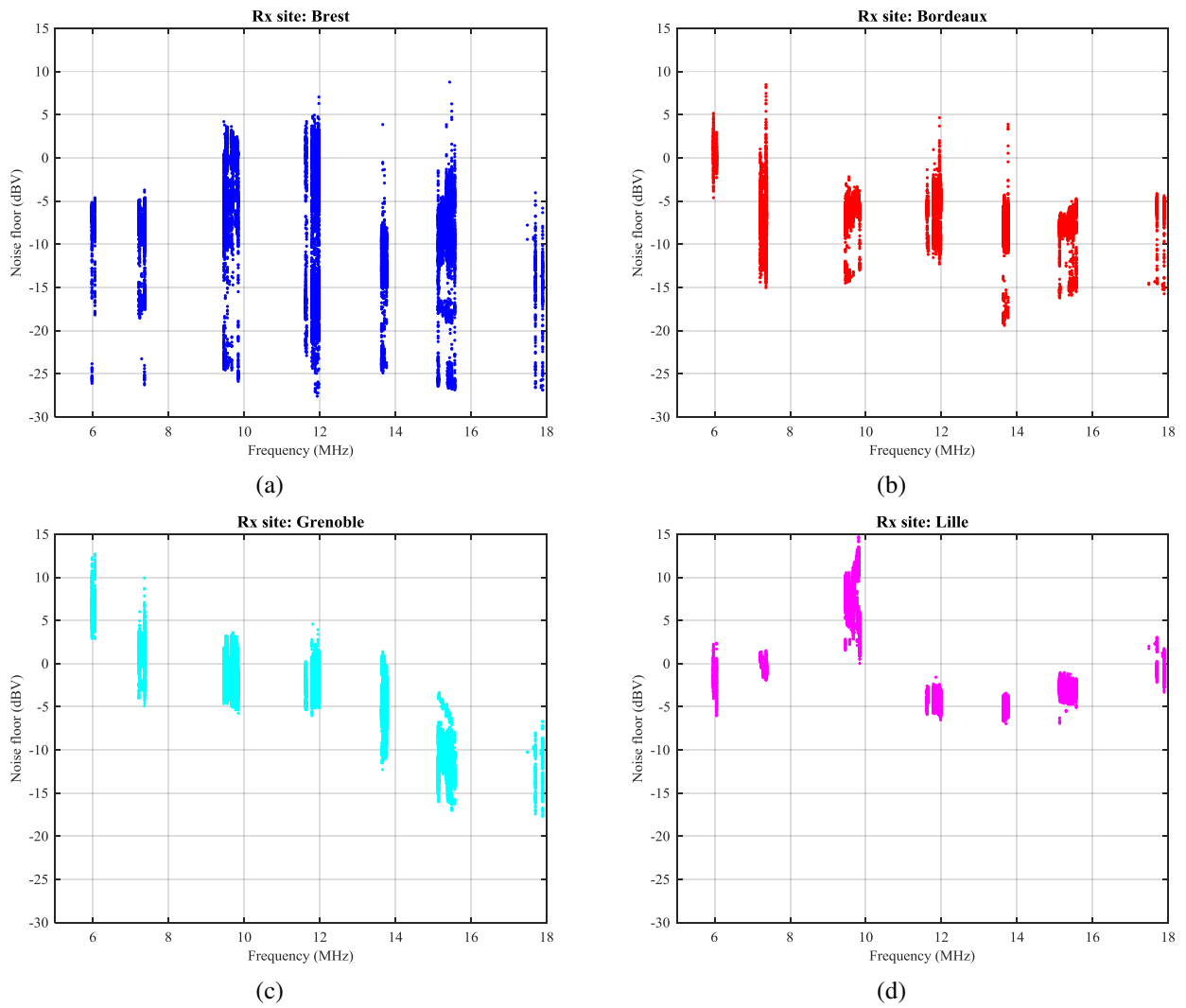


Figure 6.2 Plots representing estimated noise floor as a function of the capture frequency for all signals received in Brest (a), Bordeaux (b), Grenoble (c), Lille (d)

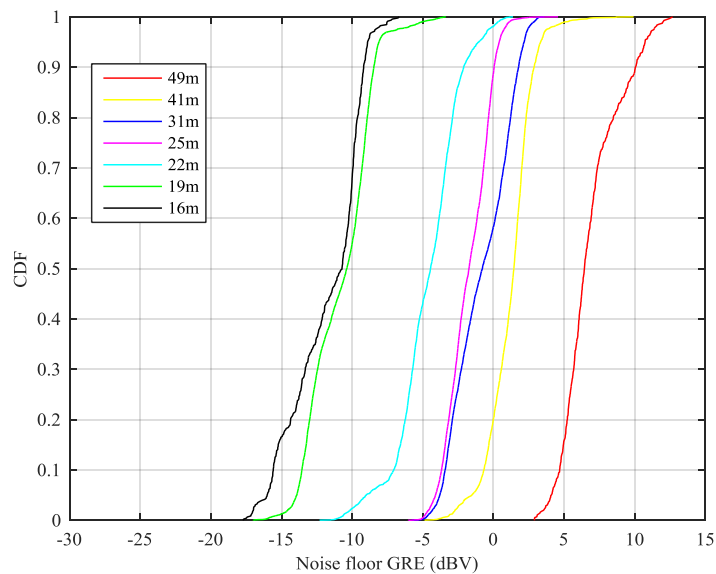


Figure 6.3 Noise floor for all signals captured in Grenoble w.r.t different frequency bands

6.2.2 SNR analysis

The signal level was calculated using the retrieved samples corresponding to the signal of interest in the frequency domain. The captured signals being broadcast signals from different transmitters, the actual signal bandwidth was unknown and different for each transmitter as well. While computing the signal level, it was assumed that the signal was received within the bandwidth of 10 kHz. The data samples corresponding to only 5-kHz band on either side of the center frequency was considered when evaluating the signal level. Finally, the 95 percentile value of the samples in the considered 10-kHz band was assumed to be the signal level and the corresponding SNR was evaluated.

Figure 6.4 (a), (b), (c) and (d) represents the CDF curves of the estimated SNR values for signals captured from different transmitters in Brest, Bordeaux, Grenoble and Lille respectively. It must be noted that the number of captures from each transmitter location is different. The strings in all legend boxes of Figure 6.4 corresponds to the transmitter location (i.e. EMR: Emirler, CER: Cerrik, NAU: Nauen, SMDG: Santa di Maria Galeria, KAS: Kashi-Saibagh, MOS: Moosbrunn, TIG: Tiganesti, GAL: Galbeni and RIY: Riyadh). From Figure 6.4, it can be observed that the estimated SNR at each receiver site is different w.r.t the transmitter site. Also, signals captured from Galbeni, Tiganesti and Cerrik have a higher SNR at all receiver locations except in Lille. It can also be seen that SNR level in general is very low for many captured signals.

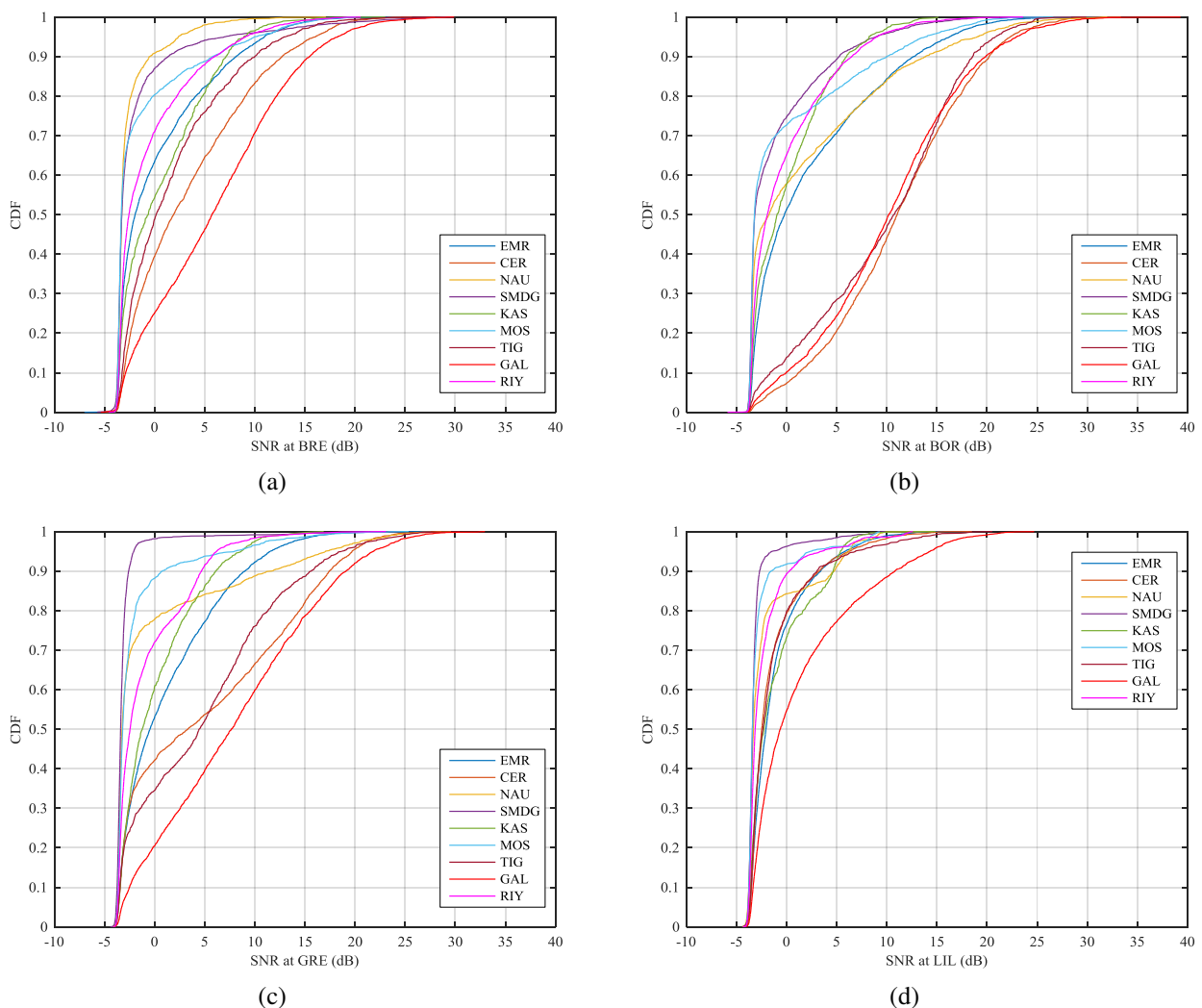


Figure 6.4 Estimated SNR for signals captured in Brest (a), Bordeaux (b), Grenoble (c) and Lille (d) from different HF transmitters assuming a signal bandwidth of 10 kHz

The signal level was computed assuming that signal of interest is present in a 10-kHz band, which may not be true in all cases as different broadcasters use different bandwidths while transmitting the signal. If the signal of interest lies within a smaller bandwidth, the obtained signal level using the method explained above will give incorrect results. Thus, the signal level is also computed assuming that the signal is received in a 5 and 3 kHz band.

The CDF curves of the calculated SNR for 3 different signal bandwidths of 10, 5 and 3 kHz for all signals captured in Bordeaux from Cerrik, Galbeni and Tiganesti can be seen in Figure 6.5. As expected, one can observe that the median SNR increases about 4.5 dB when the assumed signal bandwidth decreases from 10 kHz to 5 kHz and then to 3 kHz.

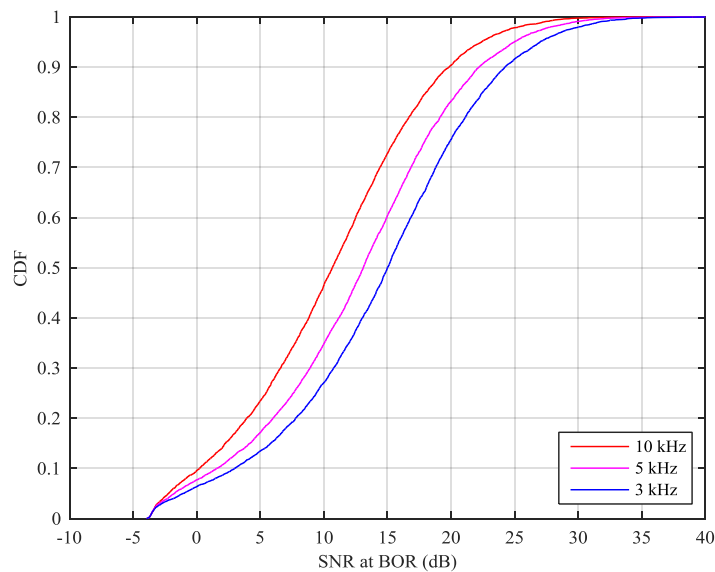


Figure 6.5 CDF curves for estimated SNR at different signal bandwidths of 10, 5 and 3 kHz for of all captured signals in Bordeaux from 3 different HF transmitters (CER, GAL & TIG)

In general from noise and SNR analysis, one cannot decide whether a signal can be considered to estimate the location of the transmitter as many of the captured signals have a low SNR. Moreover, the transmitted signal bandwidth is unknown, which further complicates the calculation of the received SNR at different locations. Another metric that can be used to qualify a measurement could be by analyzing the estimated TDoA's of the collected measurements over the capture time.

The analysis of the estimated TDoA's for signals captured at different receivers from different transmitters are explained briefly in section 6.2.3. Also the TDoA estimates are evaluated assuming that the signal is received with a bandwidth of 10 kHz.

6.2.3 TDoA analysis using statistical likelihood algorithm

Let us assume that there is an unknown transmitter which is static and it is broadcasting HF radio signals. These radio signals propagate through skywaves and are received by multiple distributed synchronized receivers. The TDoA estimates between the signals captured by 2 synchronized receivers would be approximately the same for different signals captured over different times of a day/month/year, provided that the propagation mode is the same (i.e. 1E, 1F ...) and signals are received with low noise levels. For instance, one could look at the distribution of the observed TDoA's over time (over all measurements months), and consider a TDoA output as valid if it is within a given range around the most probable value. It is a kind of validation by repetition of the TDoA estimate over time.

This approach is only valid for fixed targets, but could be refined for moving targets as long as the accurate TDoA variation can be evaluated over time and with sufficient efficiency to separate the actual TDoA from noisy ones.

Using all the estimated TDoA's for a specific receiver pair, the empirical TDoA probability distribution function (PDF) can be computed. The peak of the PDF will represent the most likely TDoA value w.r.t. all measurements. Later, by selecting a time range on either side of the peak, one can decide on the measurement qualification. If the TDoA estimate lies within the specific time range, the measurement can be considered for further processing and if the TDoA estimate lies beyond the specified time range, the measurement can be rejected. If the PDF represents a random curve without any peak, it means that estimated TDoA's are highly scattered, which cannot be true. In such cases, all the measurements have to be rejected.

A time range of ± 0.25 msec on either side of the peak is selected to consider or discard a measurement based on the geometry of the HF receiver network and different ionospheric layers. For transmitters located in one-hop range, the difference between the TDoA's obtained for signals propagating through different propagation modes would lie in the range of ± 0.25 msec in most cases.

The TDoA estimates for all measurements (1860 signals) from Nauen in Bordeaux-Grenoble and Bordeaux-Lille can be seen in (a) and (b) of Figure 6.6, respectively. The blue curves in Figure 6.6 represent their corresponding PDF's. From Figure 6.6 (a), it can be observed that the PDF curve represents a peak for the estimated TDoA's between Bordeaux and Grenoble at about 1.15 msec (i.e. it is the most likely TDoA estimate from all measurements). On the contrary, it can be seen that PDF curve is random for the estimated TDoA's between Bordeaux and Lille as the TDoA values are highly scattered; when compared to the estimated TDoA's between Bordeaux and Grenoble, it implies that the data captured in Lille are likely to be noisy. The measurements were performed using the minimum number of receivers (i.e. 4) required for HF geolocation using the TDoA method; thus, it was imperative that radio signals were captured on all receivers to find the location of the transmitter.

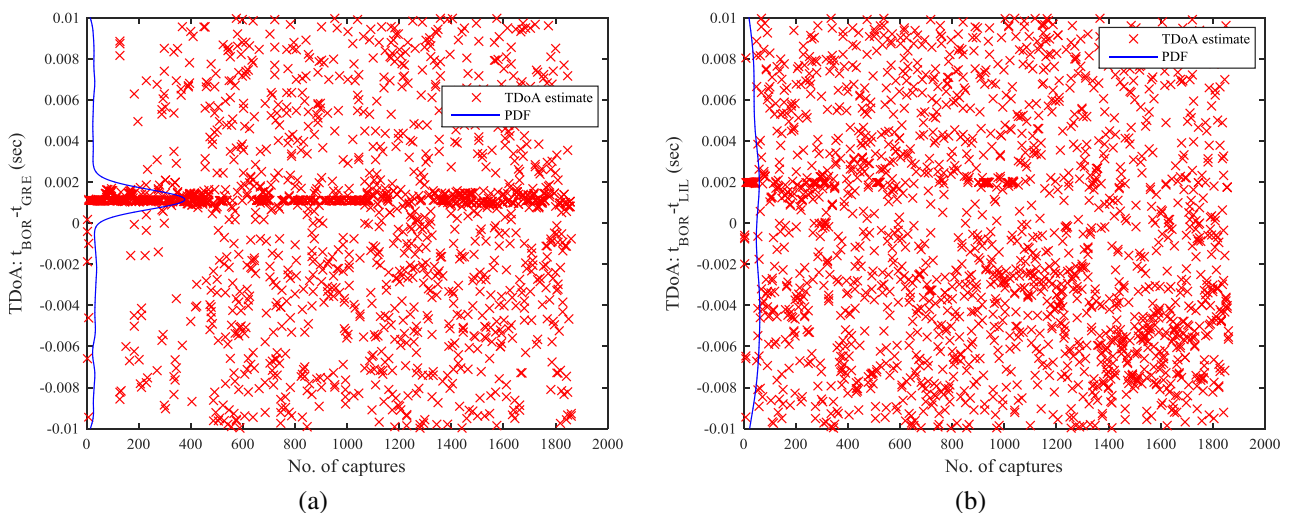


Figure 6.6 Plots representing the TDoA estimates between all signals received at BOR-GRE (a) and BOR-LIL (b) from Nauen along with their corresponding likelihood functions

A similar analysis was done using TDoA estimates obtained from measurements collected from Nauen and classified across different months as per the capture time. It was found that estimated TDoA's from measurements made in July from Nauen had a high degree of similarity and led to measurement

qualification. This can actually be observed on Figure 6.5 (b), as the measurements collected in the month of July corresponds to captures 1 to 46 at the left hand side of the figure. Thus, these measurements were used to perform HF geolocation. Concerning the other months of the measurement campaign, most of the data captured in Lille from Nauen were found to be noisy and, consequently, had to be rejected.

Figure 6.7 (a) and (b) represents the TDoA estimates for all measurements (2641 signals) from SMDG between the signals captured in Brest-Bordeaux and Brest-Lille, respectively. The blue curves in Figure 6.7 represent their corresponding PDF's. It can be seen that the PDF curve for Brest-Bordeaux represent a normal distribution whereas the other PDF curve for Brest-Lille is random which implies that signals captured in Lille are likely to be noisy. Due to the absence of the peak in the PDF plot (Brest-Lille), a selection criterion for considering a measurement could not be applied. Thus, the same analysis was done using the estimated TDoA's by classifying measurements across different months as per the capture schedule from SMDG. It was found that estimated TDoA's which involved signals captured in Grenoble or Lille as receiver were scattered for all months except for July. As a result, measurements performed in July from SMDG only were used for estimating the location of the transmitter. The rest of the data was rejected.

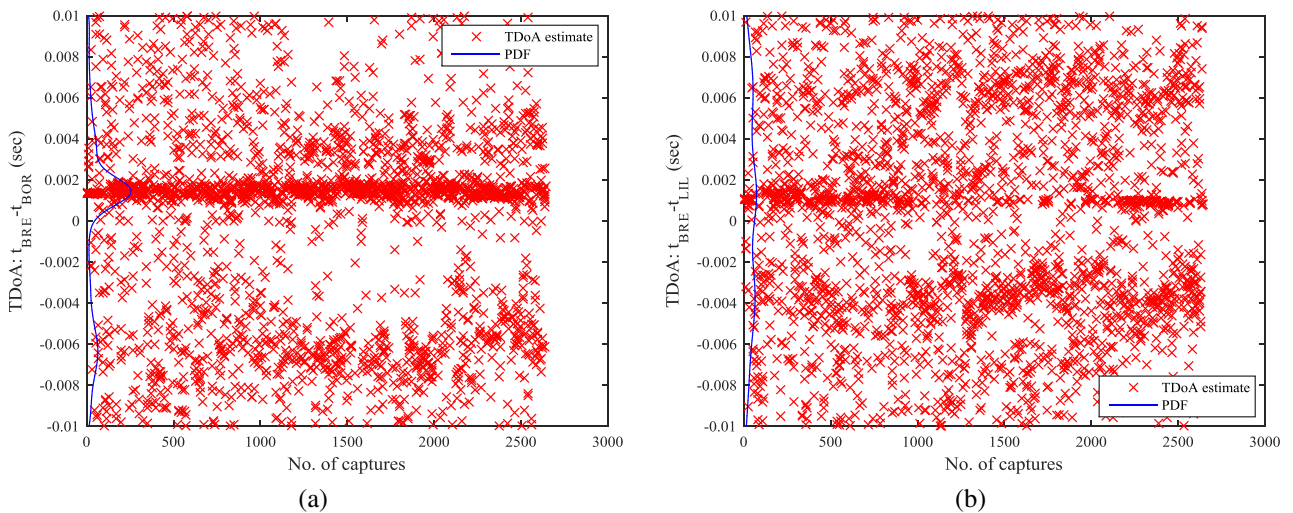


Figure 6.7 Plots representing the TDoA estimates between all signals received at BRE-BOR (a) and BRE-LIL (b) from SMDG along with their corresponding likelihood functions

The estimated TDoA's for all signals (number of measurements: 4228) captured during the measurement campaign in Brest-Bordeaux and Grenoble-Lille from Emirler can be seen in (a) and (b) of Figure 6.8, respectively along with corresponding PDF plot represented by the blue curve. For many measurements, TDoA estimates (Brest-Bordeaux, Grenoble-Lille) looks repetitive with time over a certain range around the PDF peak. The PDF curves over TDoA estimates from both Brest-Bordeaux and Grenoble-Lille data collections represent a normal distribution. One can clearly identify a peak which implies that captured data have a quite high SNR at all receivers. It can also be noticed that the dispersion of the TDoA values around the peak of the PDF seems larger for Emirler's data than for the ones from Nauen and SMDG. Measurements were further rejected if the estimated TDoA was found to be beyond the selected range around the peak of the PDF.

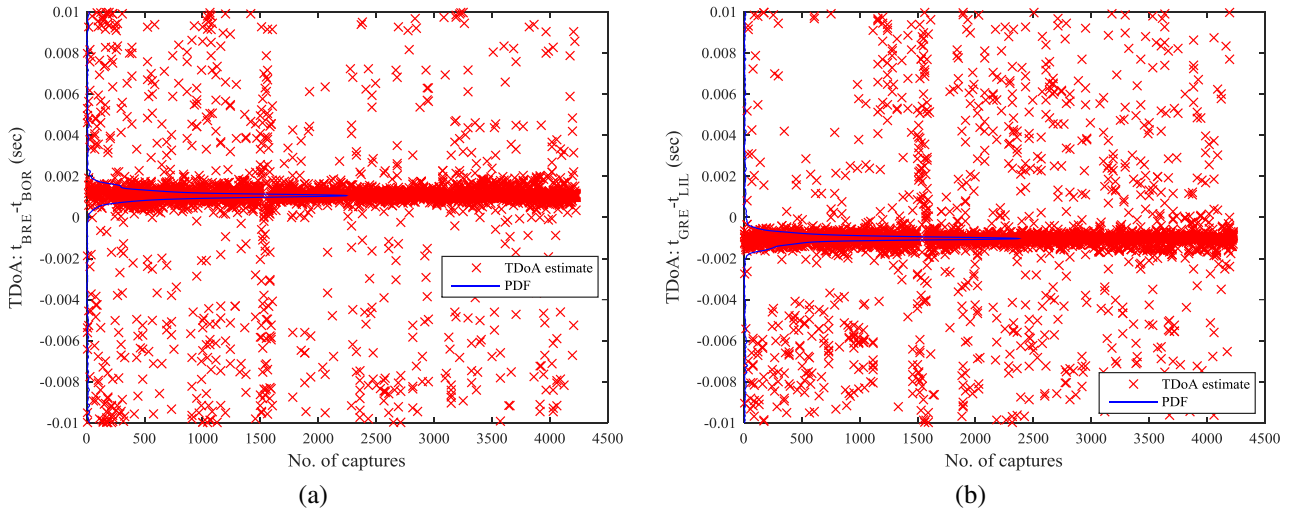


Figure 6.8 Plots representing the TDoA estimates between all signals received at BRE-BOR (a) and GRE-LIL (b) from Emirler along with their corresponding likelihood functions

For all data captured from Emirler, a large PDF peak was obtained through which a selection criterion could be applied very easily for selecting or rejecting any measurement. But, this was not the case for the data captured from Nauen and SMDG during the whole measurement campaign. Thus, TDoA estimates from Nauen and SMDG were analysed by classifying measurements made during different months. One can also classify a measurement over estimated TDoA's from data captured over a course of a day or within an hour or within a span of a few minutes from an unknown transmitter. Then, using the statistical likelihood algorithm, measurements can be accepted or rejected. Statistics related to the number of measurements considered and rejected from different transmitters using the statistical likelihood algorithm are summarized in section 6.3.

6.3 Data reduction statistics

Using four receivers in the network, a maximum of 6 different TDoA combinations can be obtained for a measurement. Using all measurements from a transmitter, the most likely value was computed for each combination of TDoA's as explained in section 6.2.3. TDoA's within the range of 0.25 msec on either side of the most likely value was considered for each of the 6 combinations of the TDoA's and the output for each measurement was stored by setting 6 different flags to different digits (0:TDoA not within the selection range, 1: TDoA within the selection range). Based on the values of these 6 different flags, a measurement was considered as consistent if at least one receiver could be used as a reference with 3 valid TDoA evaluations. Otherwise, the measurement was considered as inconsistent regarding the TDoA measurements and rejected. For example, if the TDoA flags involving Brest and other receivers were set to 1, a measurement was selected for further processing. If all 6 TDoA flags were set to 1 for a measurement, any receiver could be used as reference to estimate the position of the transmitter.

The measurements selected were processed further using the HF geolocation algorithm based on the TDoA method (section 3.2.3). The output of the algorithm was either valid or invalid based on the principles of distance physicality and time causality as explained in section 3.2.3.1. The columns labelled 'Consistent TDoA' (Table 6.8 - Table 6.14) specify the measurements that could be selected w.r.t a reference receiver. Among them, the number of measurements leading to a valid or invalid geolocation is detailed. The corresponding percentages are calculated with regards to the total number of measurements from the transmitter. As a complement, the column 'Inconsistent TDoA' provides the number of measurements rejected due to a lack of coherent TDoA computation.

The number of selected measurements from Emirler by TDoA analysis and their corresponding algorithm output (i.e. valid or invalid) is provided in Table 6.8. It can be observed that around 32% of the measurements from Emirler were selected. Around 11% of all measurements resulted in a valid output.

Reference receiver	Measurement count	Consistent TDoA		Inconsistent TDoA
		Valid geolocation	Invalid geolocation	
Brest	4228	413 (9.77%)	957 (22.63%)	2858 (67.60%)
Bordeaux	4228	480 (11.35%)	898 (21.24%)	2850 (67.41%)
Grenoble	4228	464 (10.97%)	897 (21.22%)	2867 (67.81%)
Lille	4228	466 (11.02%)	910 (21.52%)	2852 (67.46%)

Table 6.8 Statistics for all measurements from Emirler based on the TDoA analysis and algorithm output

Table 6.9 summarizes the statistics of all the measurements from Cerrik based on TDoA analysis and algorithm output. It can be seen that around 55% of measurements were rejected. Considering all measurements, around 33% lead to a valid geolocation output. In addition, the percentage of valid geolocation output from selected measurements with respect to different reference receivers is approximately similar. In general, selected measurements from Cerrik lead to a larger number of valid geolocation cases when compared to selected ones from Emirler.

Reference receiver	Measurement count	Consistent TDoA		Inconsistent TDoA
		Valid geolocation	Invalid geolocation	
Brest	3081	1032 (33.50%)	342 (11.23%)	1707 (55.27%)
Bordeaux	3081	1070 (34.73%)	327(10.61%)	1684 (54.66%)
Grenoble	3081	1027 (33.33%)	233 (7.56%)	1821 (59.11%)
Lille	3081	978 (31.74%)	351 (11.39%)	1752 (56.86%)

Table 6.9 Statistics for all measurements from Cerrik based on the TDoA analysis and algorithm output

Table 6.10 provides statistic details for all measurements from Galbeni in terms of selected measurements and algorithm output (i.e. number of valid and invalid cases). In terms of percentage, the number of measurements selected from Galbeni is around 48% which is the highest when compared to measurements from Emirler and Cerrik. Among all measurements, around 17% lead to valid geolocation output while around 30% lead to an invalid geolocation output.

Reference receiver	Measurement count	Consistent TDoA		Inconsistent TDoA
		Valid geolocation	Invalid geolocation	
Brest	3085	517 (16.76%)	950 (30.79%)	1618 (52.45%)
Bordeaux	3085	518 (16.79%)	983 (31.86%)	1584 (51.35%)
Grenoble	3085	544 (17.63%)	916 (29.69%)	1625 (52.67%)
Lille	3085	540 (17.50%)	881 (28.56%)	1664 (53.94%)

Table 6.10 Statistics for all measurements from Galbeni based on the TDoA analysis and algorithm output

Details about the data reduction statistics for data captured from Tiganesti are provided in Table 6.11. The number of selected measurement is around 25% of overall data captured from Tiganesti and it is the lowest

when compared to measurements from Emirler, Cerrik and Galbeni. Around 11% of all measurements from Tiganesti resulted in a valid geolocation output.

Reference receiver	Measurement count	Consistent TDoA		Inconsistent TDoA
		Valid geolocation	Invalid geolocation	
Brest	1186	132 (11.13%)	175 (14.76%)	879 (74.11%)
Bordeaux	1186	144 (12.14%)	171 (14.42%)	871 (73.44%)
Grenoble	1186	127 (10.71%)	147 (12.39%)	912 (76.90%)
Lille	1186	122 (10.29%)	150 (12.65%)	914 (77.06%)

Table 6.11 Statistics for all measurements from Tiganesti based on the TDoA analysis and algorithm output

When measurements from Nauen were processed using pdf output of all the captures over different months, about 99.5% of them were rejected due to an inconsistent TDoA case. It was mainly due to the noisy signals received in Lille as explained earlier in section 6.2.3. The inconsistent TDoA case decreased down to 95% when the same measurements were processed using the pdf output obtained with the captures specifically made in July. Table 6.12 summarizes the data reduction statistics of all measurements from Nauen based on pdf output of the TDoA analysis done the captures made in July. It can be observed that if only the consistent TDoA cases are considered, around 85% of the measurements lead to a valid geolocation output. When only measurements made in July were processed based on its TDoA analyses, about 18% of them were rejected.

Reference receiver	Measurement count	Consistent TDoA		Inconsistent TDoA
		Valid geolocation	Invalid geolocation	
Brest	1860	78 (4.19%)	13 (0.70%)	1769 (95.11%)
Bordeaux	1860	91 (4.89%)	15 (0.81%)	1754 (94.30%)
Grenoble	1860	89 (4.78%)	5 (0.27%)	1766 (94.95%)
Lille	1860	68 (3.66%)	11 (0.59%)	1781 (95.75 %)

Table 6.12 Statistics for all measurements from Nauen based on the TDoA analysis and algorithm output

All measurements from SMDG when processed using the output of TDoA analysis over all the captures resulted in rejection of about 99.6% of the measurements. Statistics for selected and discarded measurements made from SMDG during both measurement campaigns are provided in Table 6.13; the measurements are filtered based on the pdf output of TDoA analysis done specifically with the captures made in July. Around 98% of all measurements are discarded due to incorrect TDoA values. Out of the selected measurements, around 1.5% of them resulted in a valid geolocation output. Finally, when only measurements made in July are processed using the pdf output, only about 22% of them were rejected.

Reference receiver	Measurement count	Consistent TDoA		Inconsistent TDoA
		Valid geolocation	Invalid geolocation	
Brest	2641	48 (1.82%)	7 (0.26%)	2586 (97.92%)
Bordeaux	2641	46 (1.74%)	22 (0.83%)	2573 (97.43%)
Grenoble	2641	29 (1.10%)	3 (0.11%)	2609 (98.79%)
Lille	2641	28 (1.06%)	3 (0.11%)	2610 (98.83%)

Table 6.13 Statistics for all measurements from SMDG based on the TDoA analysis and algorithm output

Measurements from Moosbrunn are also processed using the pdf output obtained with all captures and it resulted in rejection of about 98.6% of the measurements. The number of selected measurements from Moosbrunn by TDoA analysis and their corresponding algorithm output (i.e. valid or invalid) with respect to different reference receivers are listed in Table 6.14; data reduction is achieved using output of TDoA analysis for the measurements made in July, similar to the Nauen and SMDG case. Around 97% of all measurements are rejected considering Brest, Grenoble and Lille as the reference. Considering Bordeaux as the reference receiver, around 94% of total measurements while around 2% lead to a valid output.

Reference receiver	Measurement count	Consistent TDoA		Inconsistent TDoA
		Valid geolocation	Invalid geolocation	
Brest	1842	3 (0.16%)	35 (1.9%)	1804 (97.94%)
Bordeaux	1842	42 (2.28%)	60 (3.26%)	1740 (94.46%)
Grenoble	1842	7 (0.38%)	51 (2.77%)	1784 (96.85%)
Lille	1842	5 (0.27%)	50 (2.71%)	1787 (97.01%)

Table 6.14 Statistics for all measurements from Moosbrunn based on the TDoA analysis and algorithm output

Geolocation algorithm outputs (i.e. valid or invalid) for all selected measurements from Cerrik and Galbeni over the course of different months are represented in the form of bar charts in (a) and (b) of Figure 6.9, respectively. The geolocation output was evaluated using the receiver in Bordeaux as the reference. From both bar charts, it can be observed that at least one valid algorithm output is obtained in all capture months. Hence, the capture in different months does not affect the algorithm validity.

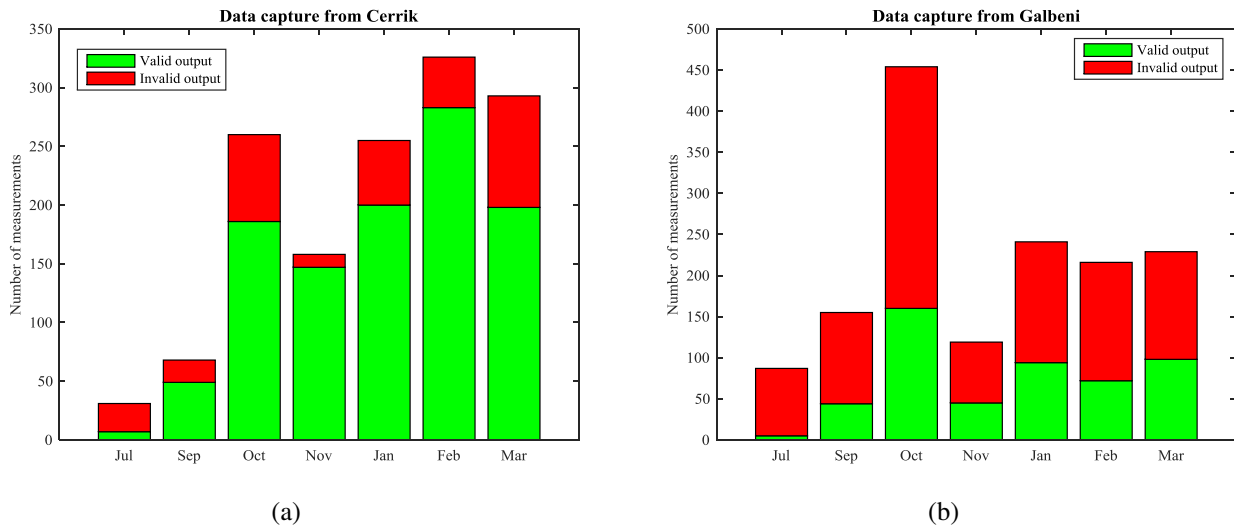


Figure 6.9 Bar chart representing valid and invalid algorithm output for all the signals captured in different months from Cerrik in (a) and Galbeni in (b) assuming the receiver in Bordeaux as the reference

For all measurements (except for the measurements from Woofferton), the geolocation validity output is calculated assuming that the receiver in Bordeaux is the reference. The algorithm output in terms of validity is presented in Figure 6.10 with regards to the different frequency bands stated in Table 6.7. From Figure 6.10, it can be concluded that the frequency band has no impact on the algorithm validity.

Note: Out of 22194 measurements, the capture time of only one single capture was not synchronized on all receivers. This was due to the fluctuation of the GPS signals which yields an accuracy of about ± 50 ns.

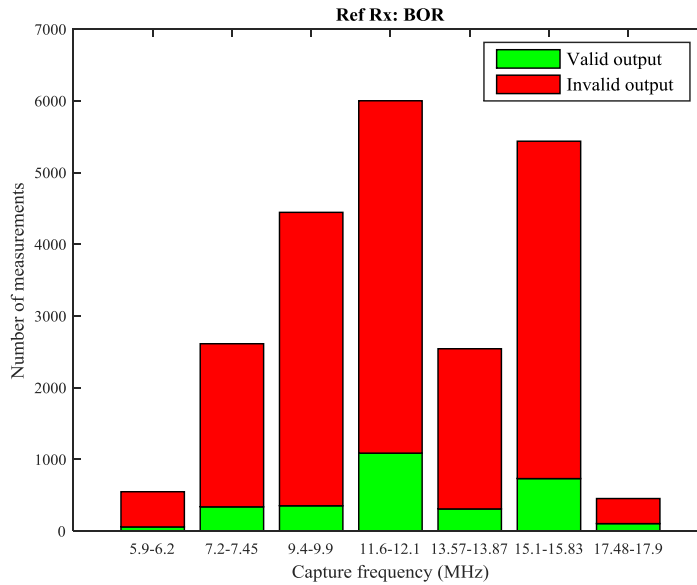


Figure 6.10 Bar chart representing algorithm validity with regards to different capture frequency bands assuming the receiver in Bordeaux as the reference

Table 6.15 provides detail of the unprocessed, selected and discarded measurements. Signals which are too noisy and captured from transmitters located beyond one-hop range are not processed. Data reduction is achieved using TDoA analysis and later measurements are classified as valid and invalid based on the geolocation algorithm output. The analyses of these valid measurements in terms of different parameters are explained in section 6.4.

Total number of measurements	Measurements unprocessed		TDoA analysis		
	Noisy (ISN, NAD, NOB, WOF)	Inadequate distance (RIY, KAS)	Consistent TDoA		Inconsistent TDoA (Discarded measurements)
			Valid (at least 1 Rx)	Invalid	
22194	72 (0.32%)	4198 (18.92%)	3054 (13.76%)	3165 (14.26%)	11705 (52.74%)

Table 6.15 Number of qualified, rejected and unprocessed measurements

6.4 Valid measurements statistical analysis

Valid measurements are analyzed considering the ionospheric conditions for captures from SMDG and Nauen during July, 2017. Further, valid measurements from Emirler, Cerrik, Galbeni and Tiganesti are analyzed in relation to the estimated reflection heights, effect of the received SNR, geolocation errors and the distribution of the estimated geographic location of the transmitters. The number of measurements from Moosbrunn resulting in a valid output (Table 6.14) are too less. It may be due to GDOP effect (section 5.4.3) and a large number of signals captured in Lille are noisy.

6.4.1 Geolocation in the case of sporadic E conditions

Measurements were made over 7 different days in July, 2017 from SMDG using the HF receiver network. For other measurements made over different months, the signal received in Grenoble was mainly noise. It implies that HF propagation through skywaves was not possible over the HF link between SMDG and Grenoble. In order to evaluate this implication, the ground ranges at which communication can occur via a reflection in the F layer ($f_c = 9$ MHz, $h_m = 280$ km, $y_m = 80$ km) is computed using the analytical equation of the QP layer model. Figure 6.11 represents the ground ranges for 2 different HF links (SMDG-

Grenoble, Nauen-Lille) at which communication is possible at the data capture frequencies from SMDG and Nauen in July. It can be observed that the skip distance for HF signals emitting at 15.570 MHz is about 1065 km which is greater than the ground distance between Grenoble and SMDG (≈ 630 km). Thus, HF signals transmitted from SMDG are not received in Grenoble at most times.

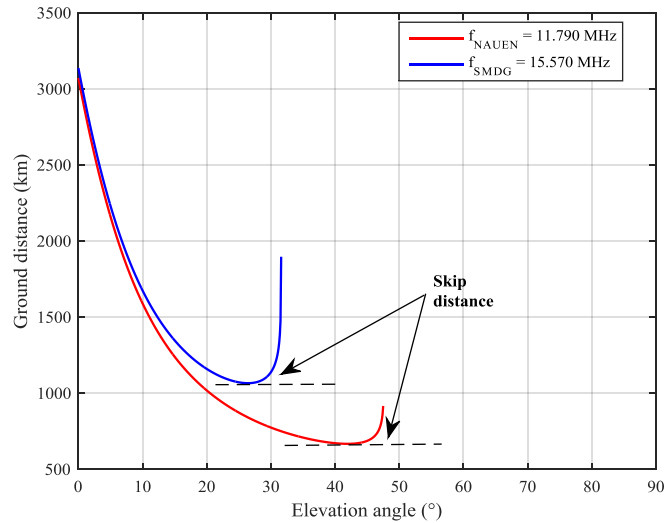


Figure 6.11 Skip distance computed using QP layer model at operational frequencies of the transmitter in SMDG and Nauen

During 3 different days of measurements in July, signals were received on all the receivers. Although the receiver in Grenoble lies within the skip distance, signals were received. Thus, the ionospheric conditions during these particular 3 days were checked from ionograms recorded in Rome specific to the nearest capture start times. An example of the ionogram captured in Rome on 18th July at 16:00 UTC [16] can be seen in Figure 6.12 (a). It can be observed that the E_s layer was present and the critical frequency was 8 MHz. The critical frequencies of the E_s layer obtained from the ionosondes data in Rome for the 3 days are listed in Table 6.16. Due to the presence of E_s layer which is capable of reflecting signals at higher frequencies, the signal was received in Grenoble. The E_s layer was also present on other days of measurements in July from SMDG, but the critical frequency was not high enough to establish a link between Grenoble and SMDG. Figure 6.13 (a) presents the estimated locations obtained assuming Brest as reference location for all 20 measurements made during the 3 days. The maximum geolocation error in terms of distance was about 158 km whereas the minimum geolocation error was about 18 km.

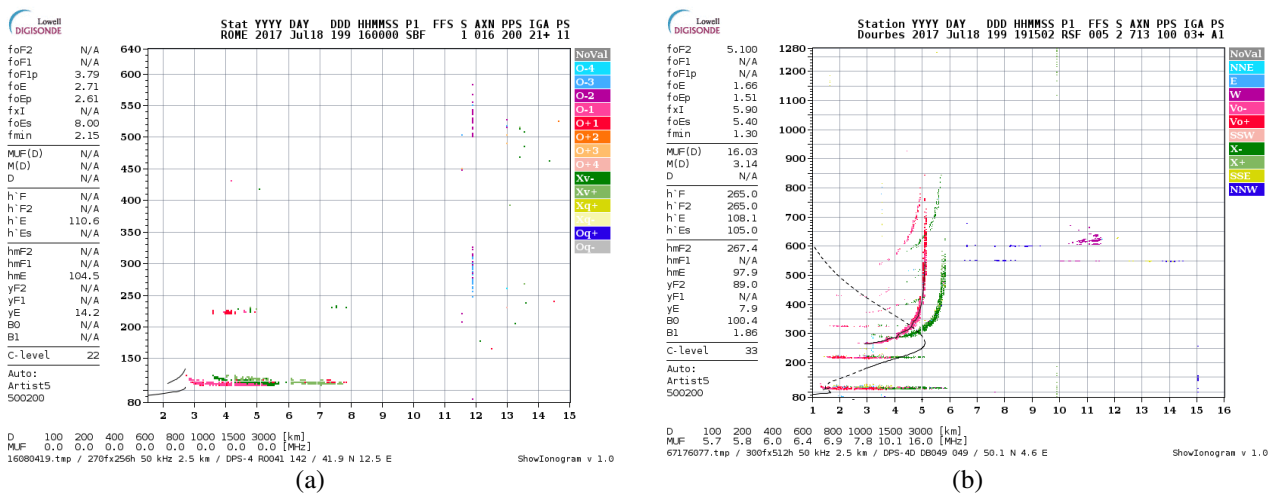


Figure 6.12 Ionograms recorded in Rome (a) and Dourbes (b) on 18th July at 16:00 UTC and 19:15:02 UTC, respectively

Capture date	f_oE_s (MHz)
18/07/2017	8
25/07/2017	5.25
27/07/2017	4.95

Table 6.16 Critical frequency of the sporadic E layer measured by the ionosonde located in Rome at 16:00 hours (UTC) [16]

Measurements made from Nauen only in July are analyzed, as most of the other signals captured in Lille during other measurement months were noisy. From Figure 6.11, it can be seen that the skip distance for HF signals emitting at a frequency of 11.790 MHz is about 665 km which is larger than the ground range between Nauen and Lille (≈ 700 km). As the receiver in Lille lies within the skip range of the transmitter in Nauen, signals are not received in many instances.

Out of the 7 different days over which measurements were made in July, signals were received successfully over 5 different days. For these 5 days, the ionograms in Dourbes were checked respectively to the closest capture start times and presence of E_s layer was confirmed. An example of the ionogram captured in Dourbes at 19:15:02 UTC on 18th July can be seen in Figure 6.12 (b). The critical frequencies of the E_s layer obtained from the ionosondes data in Dourbes for the 5 days are listed in Table 6.17. The signal received in Lille was due to the presence E_s layer and the evaluated TDoA's were valid. Figure 6.13 (b) presents estimated locations obtained assuming Brest as reference location for 36 measurements which resulted in a valid output out of the 38 measurements made during the 5 days (Table 6.17). The maximum geolocation error in terms of distance was about 140 km whereas the minimum geolocation error was about 7 km.

Capture date	f_oE_s (MHz)
18/07/2017	5.40
21/07/2017	3
25/07/2017	3.15
26/07/2017	3.55
27/07/2017	3.90

Table 6.17 Critical frequency of the sporadic E layer measured by the ionosonde located in Dourbes at 19:15:02 (UTC) [16]

The presence of E_s layer facilitated the propagation over 2 different HF links (SMDG-Grenoble, Nauen-Lille), thereby resulting in a measurement which could be used as the signals were successfully received on all 4 sites. In general, the maximum relative geolocation errors were about 10% corresponding to the maximum ground range among the 4 possible HF links.

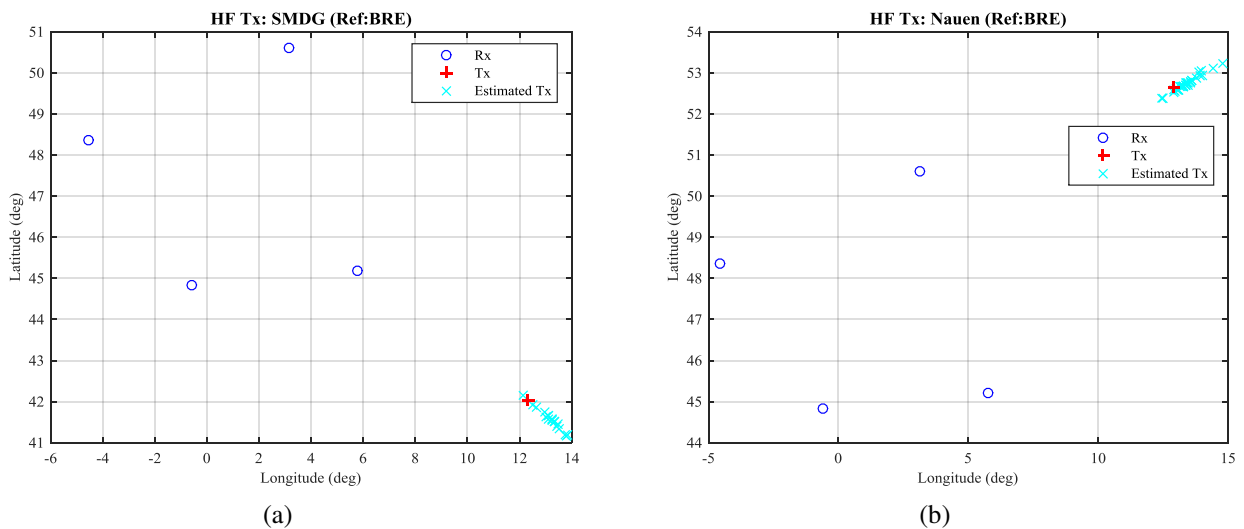


Figure 6.13 Estimated and actual geographic locations for all valid measurements from SMDG (a) and Nauen (b) in July, 2017

6.4.2 PDF of estimated reflection heights

Figure 6.14 (a), (b), (c) and (d) presents the PDF of the estimated reflection heights for all valid algorithm outputs obtained for the signals captured from Emirler, Cerrik, Tiganesti and Galbeni, respectively. The reflection heights are calculated assuming each receiver as reference. For data captured from Emirler, it can be observed that the maximum PDF peak for the estimated reflection heights lies in the range of about 160-190 km for different reference receiver sites. Similarly, for data captured from Cerrik, Tiganesti and Galbeni the maximum peak for estimated reflection heights lies in the range of 190-200 km, 180-220 km and 160-200 km, respectively. From all the PDF plots, it can be seen that a large number of estimated reflection heights lies within the range of 50-400 km which corresponds to the region between the E and F_2 layer of the ionosphere. Some of the estimated reflection heights are too high which might be due to the assumptions made in the HF geolocation algorithm. For instance, it is assumed that the signal is received via a one-hop while in reality it was received through multi-hop modes. The assumption of negligible apogee height variation for different HF links may not hold true in some of the cases. In particular, for valid measurements which resulted in an unrealistic reflection height (i.e. estimated reflection height greater than 400 km), one can discard the geolocation result.

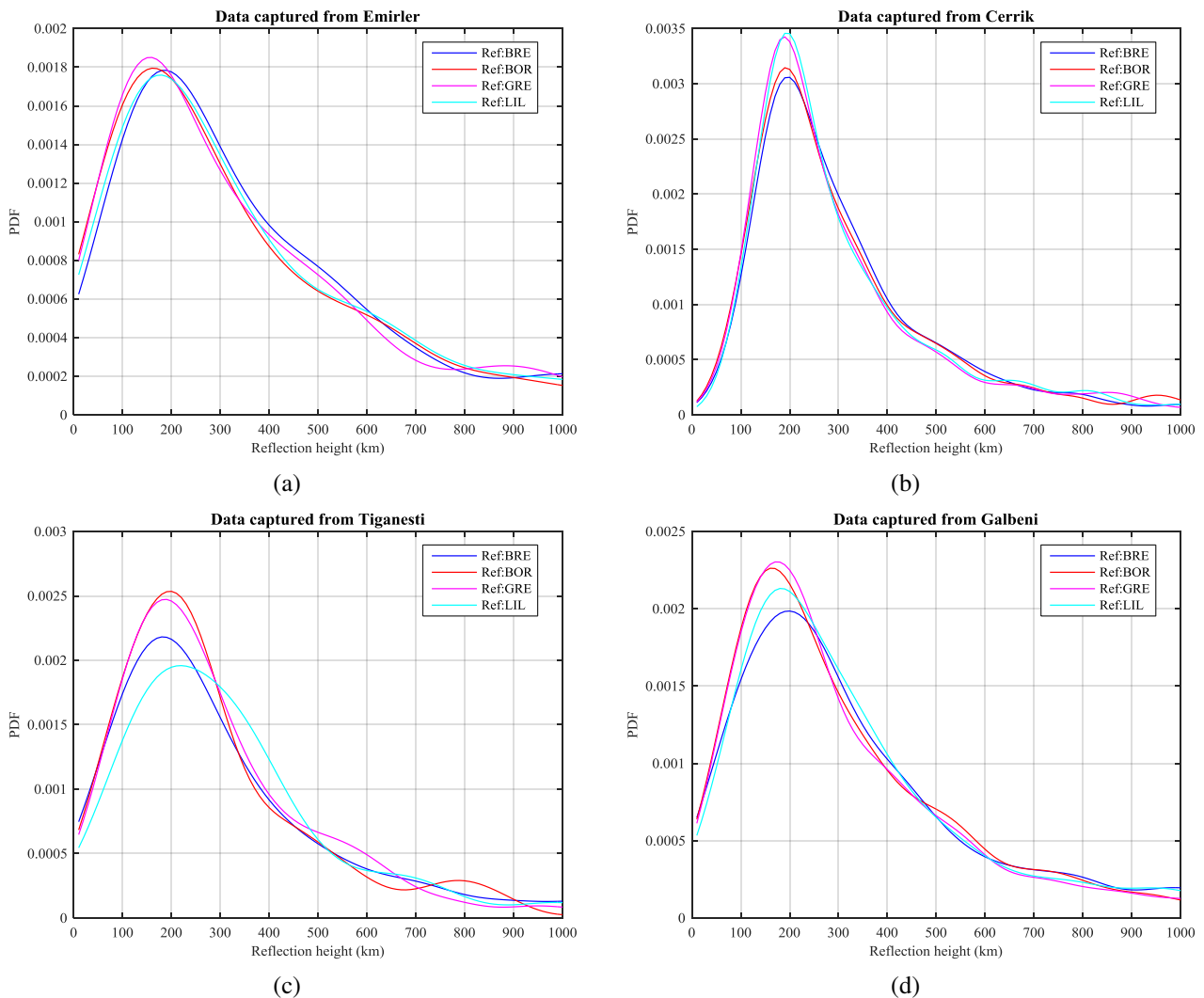


Figure 6.14 PDF curves representing the obtained reflection heights for all valid measurements from Emirler in (a), Cerrik in (b), Tiganesti in (c) and Galbeni in (d), considering each receiver as reference

6.4.3 Geolocation error vs estimated reflection height

Figure 6.15 (a), (b), (c) and (d) represent the scatter plots of the geolocation error in terms of distance with regards to the estimated reflection heights for all valid measurements obtained from Emirler, Cerrik, Tiganesti and Galbeni, respectively. The geolocation output (i.e. geolocation error and reflection height) was calculated assuming the receiver in Bordeaux as the reference. From all scatter plots, a general trend that can be observed is that higher the estimated reflection height, higher is the geolocation error. As explained in section 6.4.2, the geolocation errors obtained with large reflection height could be discarded. In spite of this condition, one can say that some of the geolocation errors are also very large (in the range of 1000 km) when the estimated reflection heights lay within the altitude of the ionospheric layers. A discussion on the possible reasons for large geolocation errors is given in section 6.4.5.

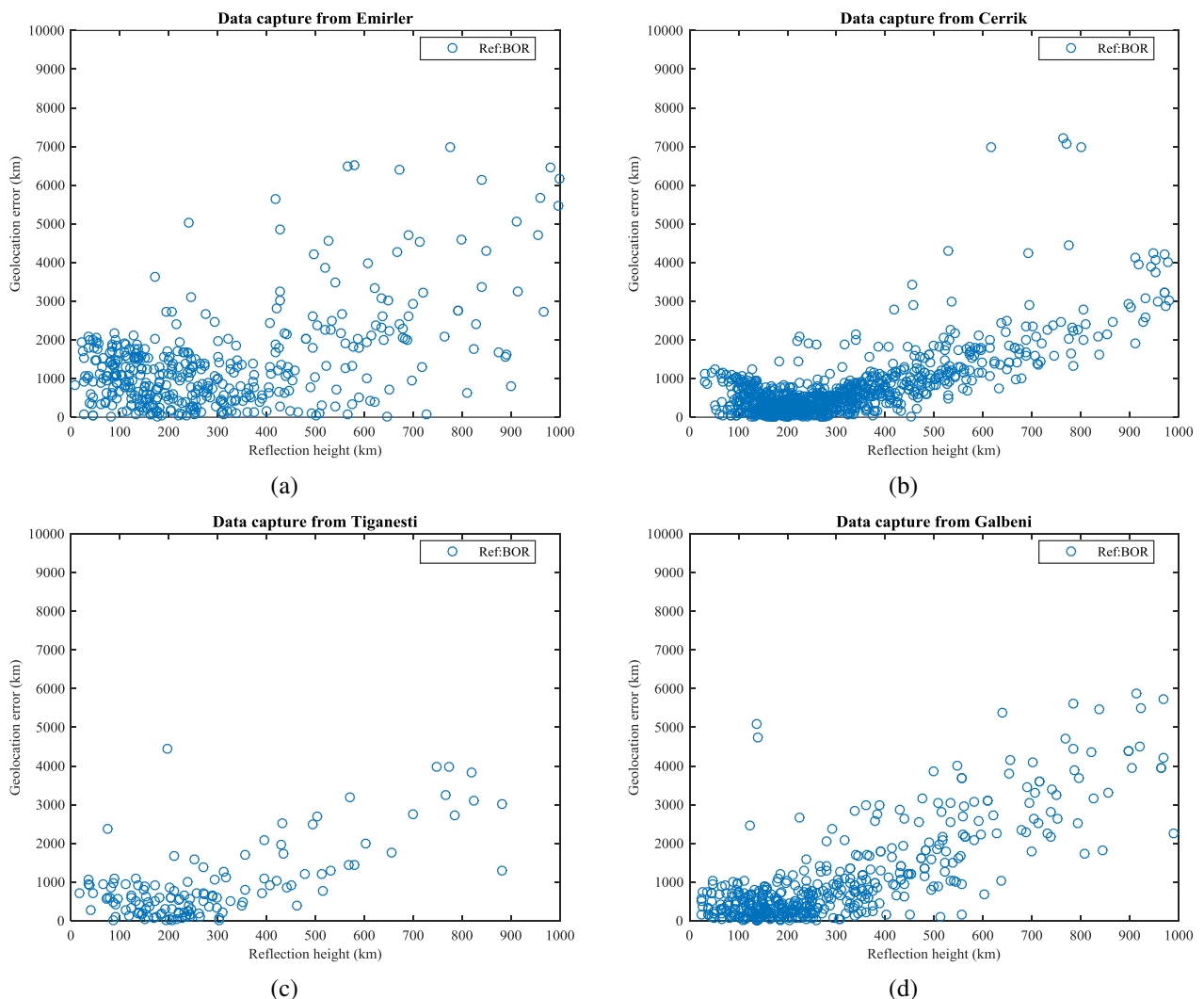


Figure 6.15 Scatter plots of obtained geolocation errors as a function of estimated reflection heights for all valid measurements from Emirler in (a), Cerrik in (b), Tiganesti in (c) and Galbeni in (d), considering the receiver in Bordeaux as the reference

6.4.4 Geolocation error vs received SNR

Figure 6.16 (a), (b), (c) and (d) provide the scatter plots of the geolocation error in terms of distance with regards to the minimum SNR for all valid measurements obtained from Emirler, Cerrik, Tiganesti and Galbeni, respectively. The geolocation error was computed assuming Bordeaux as the reference location. The minimum SNR for a valid measurement corresponds to the least value out of the received SNR at 4

different receiver locations. In general, signals received with higher SNR should result in better geolocation accuracy. But from all scatter plots, it can be seen that signals received with a high or low SNR can lead to both high and low geolocation errors. Thus, it can be concluded that the received SNR cannot be used as a criterion for considering or discarding a geolocation result.

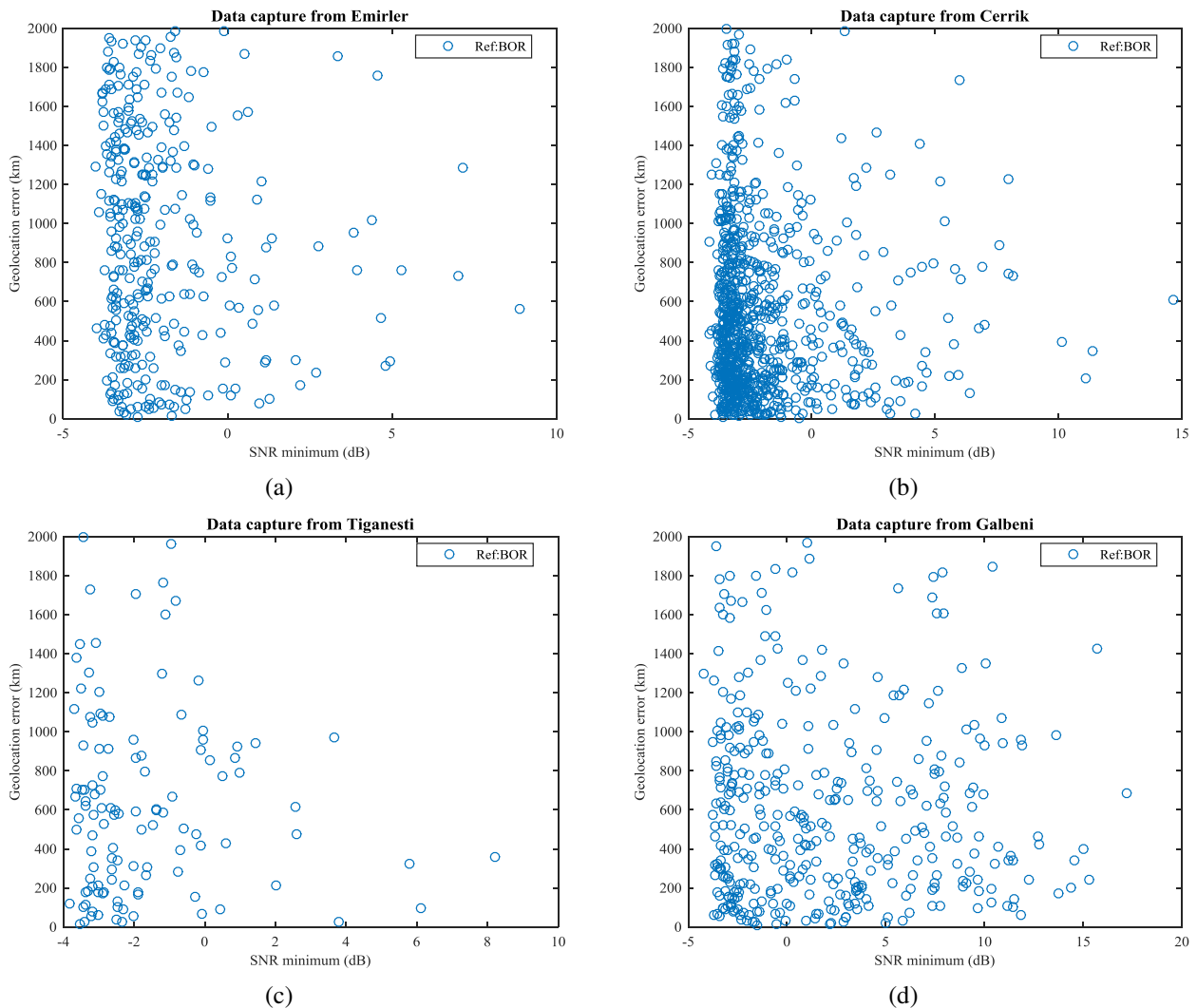


Figure 6.16 Scatter plots of the obtained geolocation errors vs the minimum SNR (least out of the signals received at 4 locations) for all valid measurements from Emirler in (a), Cerrik in (b), Tiganesti in (c) and Galbeni in (d), considering the receiver in Bordeaux as the reference

6.4.5 Estimated transmitters location in terms of GPS coordinates

The actual and estimated geographic location of all the valid measurements resulting in a reflection height between 50 and 350 km from Emirler, Cerrik, Tiganesti and Galbeni are presented in (a), (b), (c) and (d) of Figure 6.17, respectively. The geographic location and reflection height were evaluated considering the receiver in Bordeaux as the reference. The estimated geographic locations are dispersed around the true location in way that it follows a continuous elliptical locus and the actual transmitter location lies within that locus. This elliptical shape arises due to the fact that the location of the transmitter is calculated using the TDoA method.

Geolocation based on TDoA principle is highly sensitive to the time resolution. Higher the time resolution better is the geolocation accuracy. The time resolution used in our measurements was equal to 5 μ sec which provided a low resolution in the distance domain and was one of the reasons for large geolocation errors. In

addition, a small error in a TDoA estimate corresponds to a large distance error. Lastly, the geolocation algorithm assumed that all signals arrive through one-hop propagation mode and a uniform ionosphere which might not be true for all captured signals.

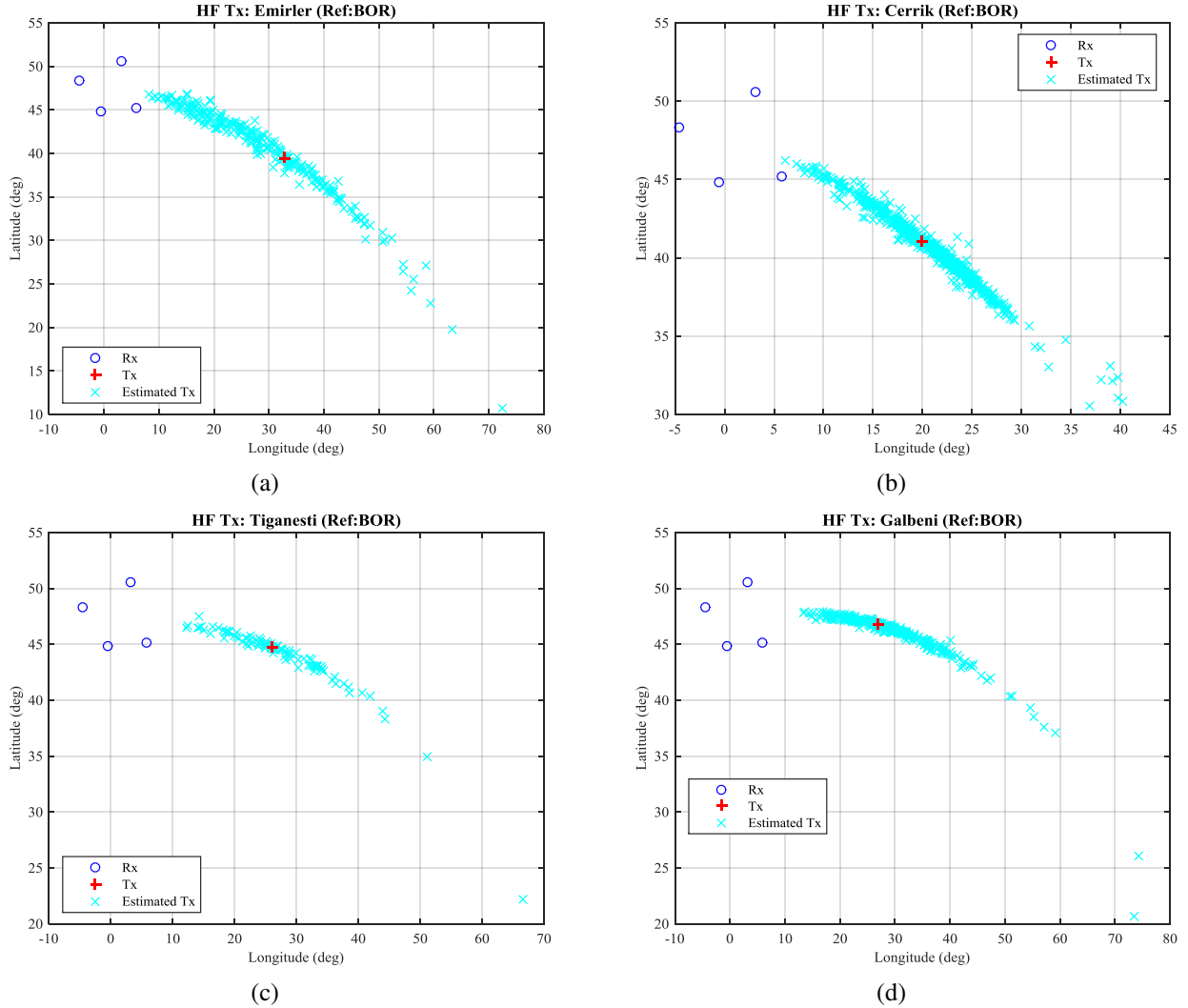


Figure 6.17 Estimated and actual geographic locations for all valid measurements with an estimated reflection height between 50 and 350 km from Emirler (a), Cerrik (b), Tiganesti (c) and Galbeni (d), assuming the receiver in Bordeaux as the reference

6.4.6 Estimated geolocation and azimuth errors

The CDF's of the geolocation error (km) and azimuth error ($^{\circ}$) for all valid measurements from Emirler, Cerrik, Nauen, SMDG, Tiganesti, Galbeni can be seen in (a), (b), (c), (d), (e), (f) of Figure 6.18 and Figure 6.19, respectively. The geolocation and azimuth errors were computed assuming the receiver in Bordeaux as the reference. From Figure 6.18 (a), it can be observed that about 5% of the geolocation errors are less than 100 km for all valid measurements from Emirler. Also, around 65% of the valid measurements from Emirler had an azimuth error less than 5° (Figure 6.19 (a)). It must be noted that the distance between Brest and Emirler is about 3125 km. For the valid measurements from Cerrik, about 10% of the geolocation errors are less than 100 km (Figure 6.18 (b)) whereas about 70% of the azimuth errors are less than 5° (Figure 6.19 (b)). In the case of valid measurements from Nauen, about 85% geolocation errors are less than 100 km as seen in Figure 6.18 (c), while about 95% of the azimuth errors are less than 2° (Figure 6.19 (c)). For the SMDG case, about 65% of the geolocation errors are less than 100 km whereas around 90% of the azimuth errors are less than 5° (Figure 6.19 (d)). From all valid measurements from Tiganesti, around 7.5% of the

geolocation errors less than 100 km and about 80% of the azimuth errors are less than 5° (Figure 6.19 (e)). Finally, out of all the valid measurements from Galbeni, about 7.5% have a geolocation error less than 100 km and about 85% have an azimuth error less than 5° (Figure 6.19 (f)).

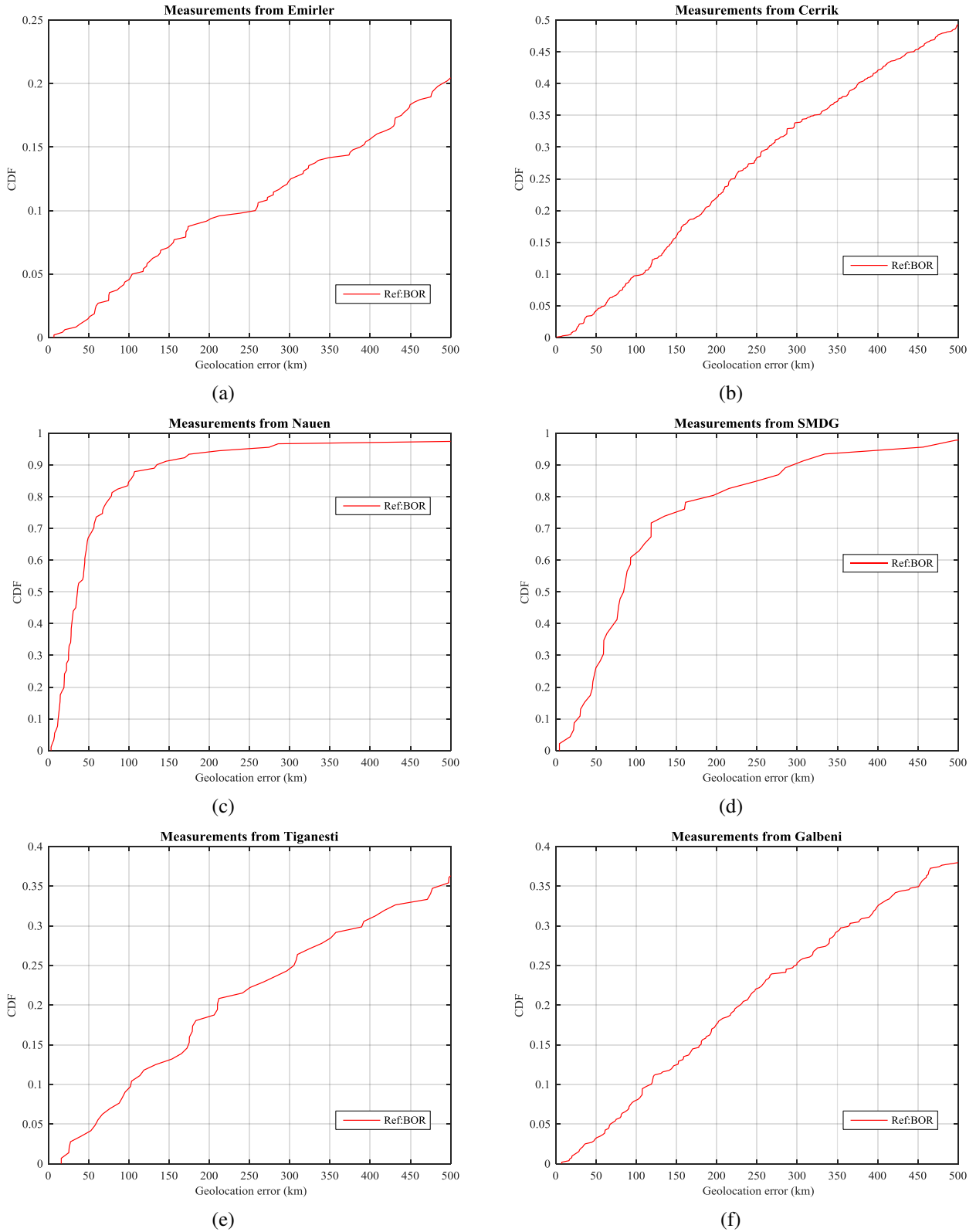


Figure 6.18 CDF's of geolocation errors for all valid measurements from Emirler (a), Cerrik (b), Nauen (c), SMDG (d), Tiganesti (e) and Galbeni (f), considering the receiver in Bordeaux as the reference

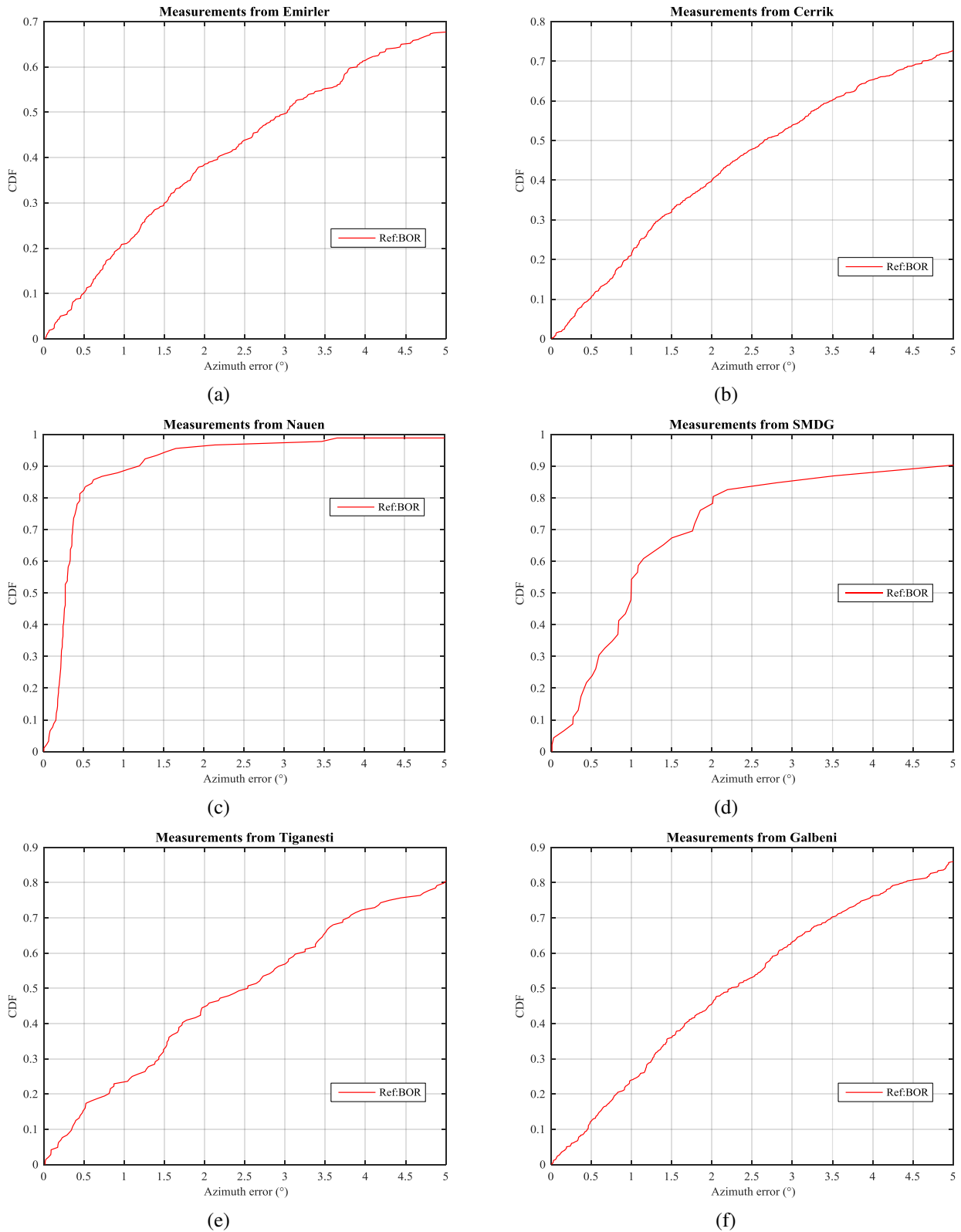


Figure 6.19 CDF's of absolute azimuth errors for all valid measurements from Emirler (a), Cerrik (b), Nauen (c), SMDG (d), Tiganesti (e) and Galbeni (f), considering the receiver in Bordeaux as the reference

The analysis of the geolocation errors based on the captures made from Emirler, Cerrik, Tiganesti and Galbeni over different months and different frequency bands revealed no correlation among them. There was no specific month or frequency band at which the geolocation accuracy was better compared to the others. The measurements made from Nauen and SMDG in July resulted in higher geolocation accuracy when

compared to the measurements made during other months (section 6.4.1). Even though most of the geolocation errors are large, the computed azimuth errors from most of the transmitter estimates provide an approximately accurate direction in which the transmitter lies. The geolocation errors can be drastically reduced by capturing signals on more number of receivers as explained in sections 3.2 and 3.3.2.

A fixed resolution of the TDoA algorithm (i.e. 3 TDoA's for 3 different receiver pairs) generates a single estimate of the transmitter location. The output of the algorithm can be represented in terms of area by switching from a fixed resolution TDoA to a continuous resolution TDoA where time differences lie within a time range for each receiver pairs. The concept of switching from a fixed resolution TDoA to a continuous resolution TDoA is further explained in detail in section 6.5.

6.5 Propagating TDoA uncertainty on geolocation output

TDoA estimates are obtained by evaluating the maximum of the cross-correlation between 2 measured signals on synchronized receivers. If signals arrive at both receivers through multiple modes, the ability to differentiate between the different peaks in the cross-correlation depends on the time resolution of the measurement setup.

Assuming that the transmitted signals has good autocorrelation properties and it resembles a narrow peak which is centered at zero with large amplitude, as illustrated in Figure 6.20 (a). Also, the cross-correlation between 2 different CIR's represents 3 different peaks with varying intensities, as seen in Figure 6.20 (b). The peak corresponding to τ_1 and τ_2 is equal to the time delay of the signals received on both receivers through 1E mode and 1F mode respectively, whereas, the peak corresponding to τ_3 corresponds to the time delay of the signals received through 1E mode on one receiver and 1F mode on the other receiver. Generally, the peaks resembling the combination of E-E and F-F modes lie very close to each other in the range of about 5-50 μsec . The convolution between the autocorrelation of the transmitted signal and cross-correlation between the 2 CIR's is equal to the cross-correlation between signals captured at 2 different receivers. From Figure 6.20 (c), it can be seen that the peak corresponding to τ_1 cannot be identified due to the limited useful signal bandwidth.

Even if one assumes a perfect ionosphere, there would be a certain quantization error in the measurement setup depending upon the location of the receiver and the transmitter. In the case of our measurement setup, the maximum quantization error would be $\pm 2.5 \mu\text{s}$ as the system time resolution is equal to 5 μs .

Due to the above problems, one can consider moving from a fixed resolution of TDoA algorithm (leading to a single output) to a continuous resolution, where the TDoA's lay in a period from t_1 to t_2 for each receiver pair. As a result, the output of the algorithm would represent an area rather than an estimated location. In this way, the error due to quantization and the inability to identify different peaks very close to each other in the cross-correlation output (i.e. error due to resolution in the correlation peak) could be accounted.

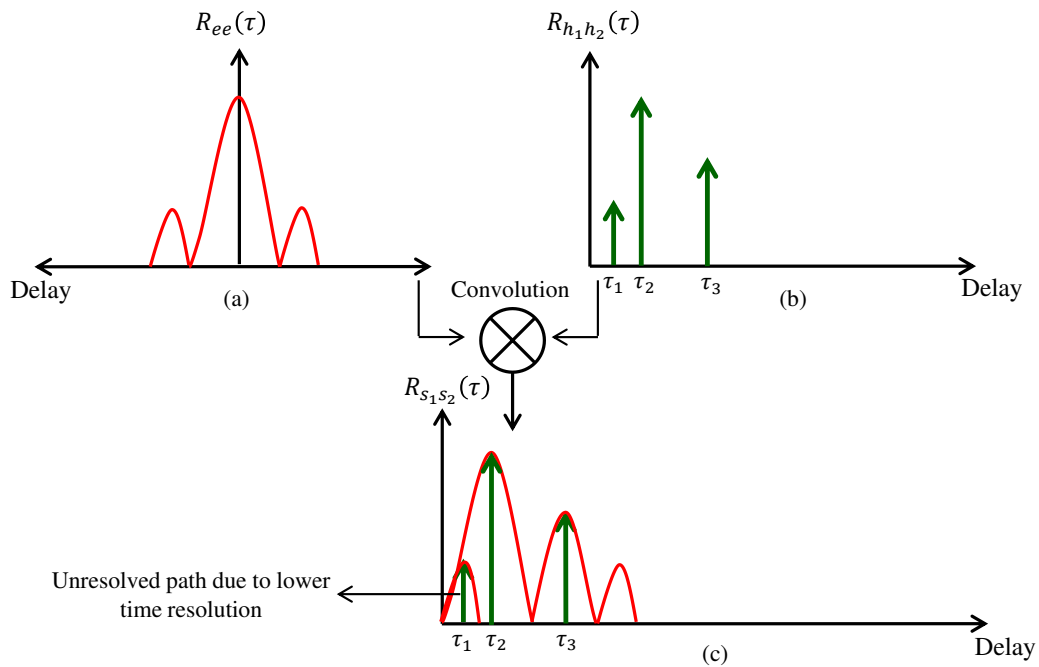


Figure 6.20 Effect of time resolution on the estimation of TDoA

6.5.1 Fixed resolution TDoA and continuous resolution TDoA

Fixed resolution TDoA refers to finding a single estimate of the transmitter location from 3 TDoA estimates whereas continuous resolution TDoA refers to finding a geolocation area by considering a certain range around the TDoA estimates of the different receiver pairs. Figure 6.21 illustrates the geolocation area computed by selecting a time range for the continuous ToA case. In 2D ToA, the location of the transmitter is found at the intersection of the circles. If t is the time required by the signal to travel from the transmitter to the receiver, one can consider a time range from t_1 to t_2 , where $t_1 = t - \Delta t$ and $t_2 = t + \Delta t$. Using these time ranges and the known receiver location, two concentric circles can be computed for each receiver. Later, the intersection between different concentric circles for different receivers results in a region which has a shape similar to a square segment rather than a point, as illustrated in Figure 6.21. This segment when projected on the ground plane will represent an area with the highest and the lowest corners within it. The actual transmitter (Tx) also lies within the area on the ground plane.

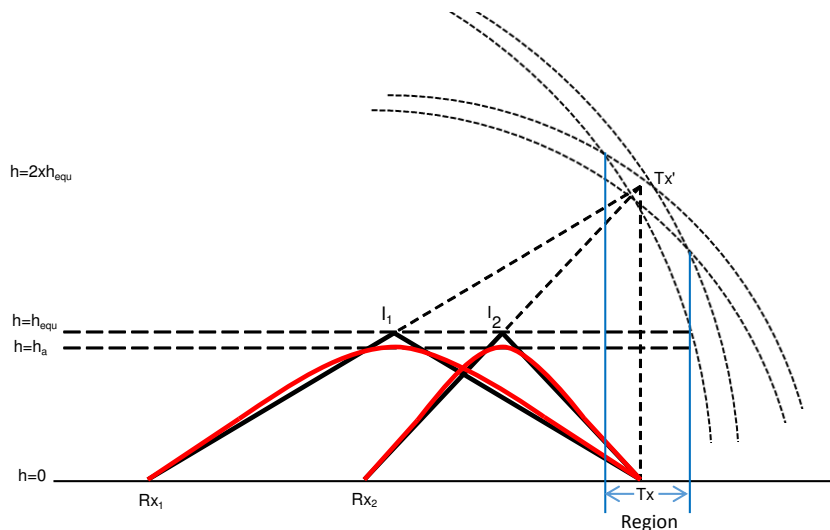


Figure 6.21 Geolocation output in terms of region computed over a certain time range

Similarly for the 3D TDoA case, if t is the time delay corresponding to the maximum peak of the cross-correlation output, one can consider a time range from t_1 to t_2 , where $t_1 = t - \Delta t$ and $t_2 = t + \Delta t$, which would allow for a resolution error in the correlation peak. From the time ranges for each receiver pair, one obtains an output volume which resembles a cube, where each face is a section of a hyperboloid. The 8 corners of the cube correspond to 8 specific solution of the TDoA algorithm, obtained by considering t_1 or t_2 for each of the three receiver pairs.

In order to find the location of the possible transmitter outputs on the ground, one must project the volume of the cube on a plane where $z = 0$. In general, independently of the orientation of the cube in space, the projection on the ground plane will be a hexagon, as illustrated in Figure 6.22. Indeed, from the 8 estimated transmitter locations, the corners with the highest and lowest z values will be projected inside the ground surface. Therefore, they can be discarded when computing the contour of the projected surface. This hexagonal area will be the output of the TDoA algorithm using a set of TDoA ranges as input instead of three fixed TDoA's. This output is generated at the precision of the system resolution.

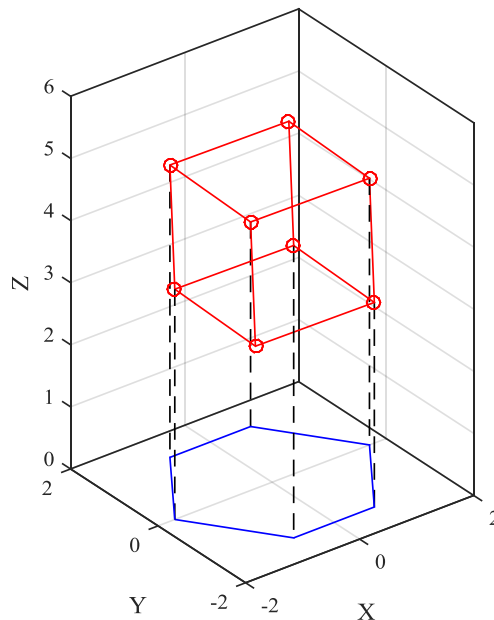


Figure 6.22 Rotated cube and its projection on a ground plane ($z = 0$) forming a hexagon

Figure 6.23 (a), (b), (c) and (d) represents the estimated geolocation area around the transmitters located in Emirler, Galbeni, Cerrik and Tiganesti, respectively. For each transmitter location, the geolocation region is computed by assuming a continuous resolution on the time delays. At first, time delays for different HF links are computed assuming one-hop propagation mode geometry. It is assumed that all the signals are reflected from a virtual height of about 300 km. Then, by setting $\Delta t = 0.25 \mu\text{s}$, the different time ranges for each receiver pair is computed. Finally, different estimates of the transmitter location are found using the HF TDoA geolocation algorithm using Brest as the reference location. Based on the estimated reflection heights, 2 outputs are eliminated and the rest are connected to find a geolocation area. From all plots in Figure 6.23, it can be observed that the geolocation region represents an irregular hexagon (length of sides not equal) and the exact transmitter location lies within the hexagonal region. The hexagon is irregular as the volume obtained from the algorithm output is not delimited by parallel planes, but by section of hyperboloids. Depending on the alignment between the transmitter and the receiver pairs, the output volume can be more or less elongated.

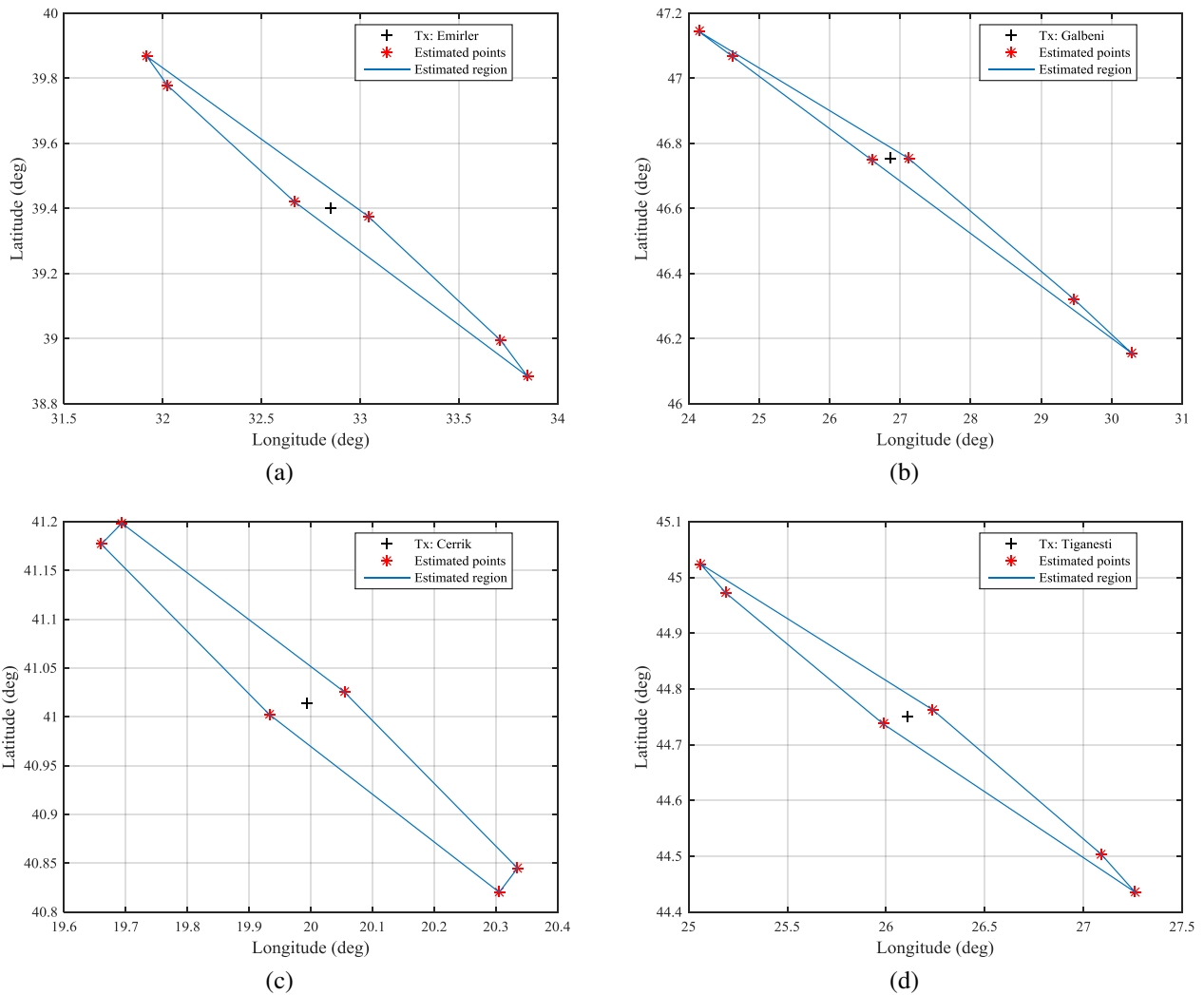


Figure 6.23 Diagrams of estimated regions around different transmitters ((a): Emirler, (b): Galbeni, (c): Cerrik, (d): Tiganesti) obtained from TDoA algorithm assuming a continuous resolution

6.5.2 Measurement examples assuming a continuous resolution TDoA

Figure 6.24 (a) illustrates the estimated geolocation region using the concept of continuous resolution TDoA for a measurement example captured from Galbeni on 6th October, 2017 at 17:43 UTC at a frequency of 11.975 MHz. Based on the received signal strength, the receiver in Bordeaux was selected as the reference. Time ranges were computed for each receiver pair based on the estimated TDoA values. Finally, from the time ranges, the geolocation region was computed. It can be seen that the transmitter lies within the estimated region.

Figure 6.24 (b) presents the estimated geolocation region using computed time ranges for a measurement captured from Cerrik on 10th November, 2017 at 18:41 UTC at a frequency of 7.360 MHz. Based on the received signal strength, the receiver in Bordeaux was selected as the reference. Again in this example, it can be seen that the actual transmitter location lies inside the estimated region which validates the concept of continuous resolution TDoA algorithm output.

In general, from other measurements it was observed that the shapes of estimated regions were elliptical, similar to the estimated transmitter location using a fixed resolution (Figure 6.17). Using continuous resolution TDoA concept, one can say that the transmitter lies within the estimated region or within the

proximity of the estimated region. Also, the percentage at which one can say that the transmitter lies within the estimated region depends on the accuracy at which the TDoA's are estimated.

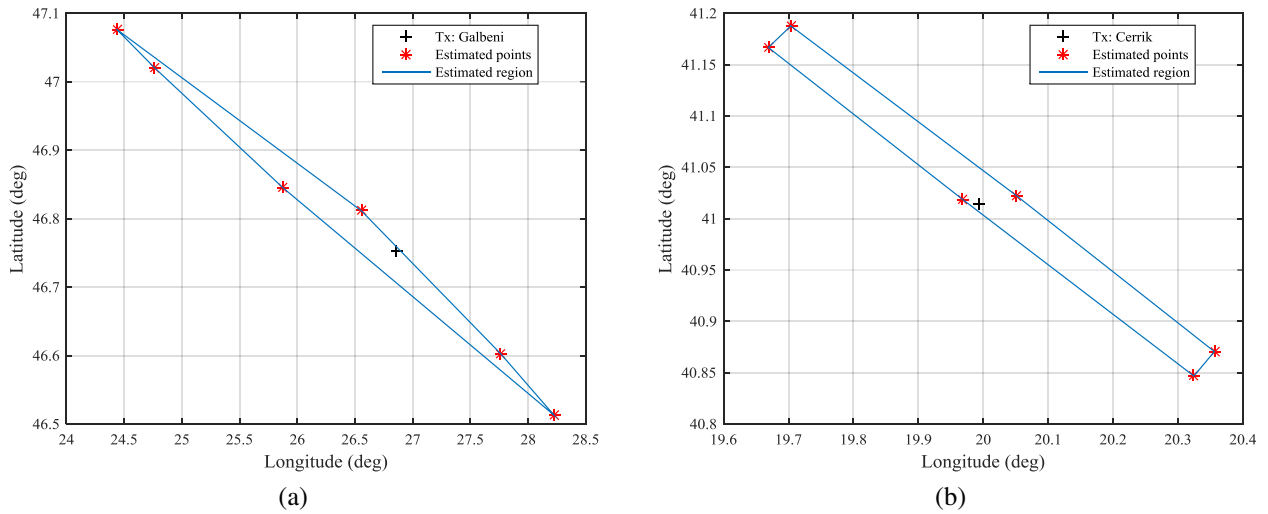
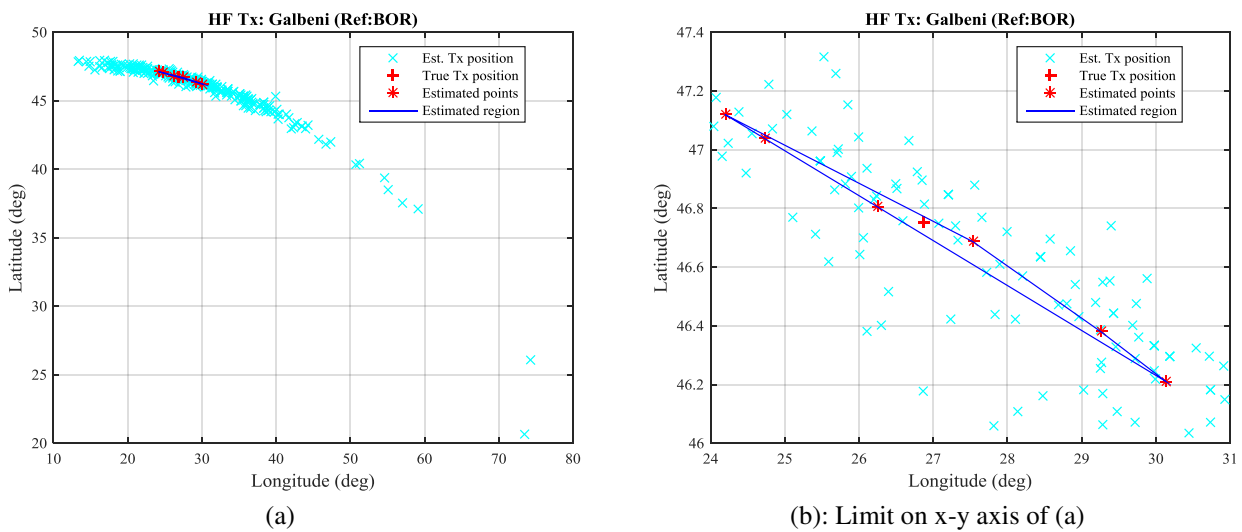
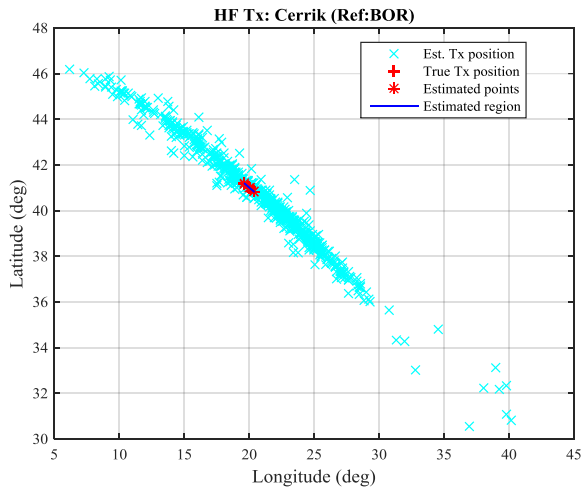


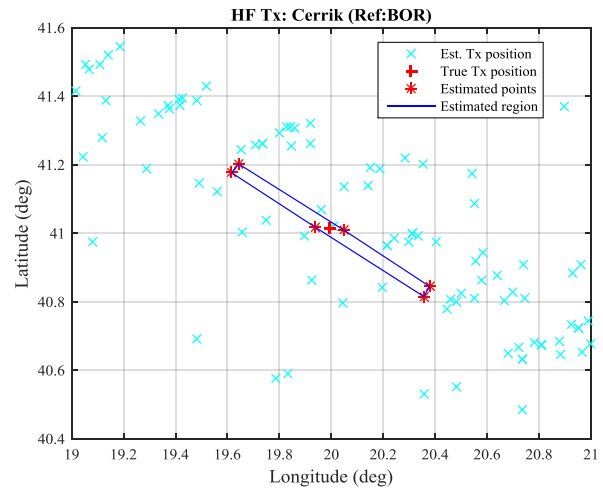
Figure 6.24 Different measurement example from Galbeni and Cerrik representing the estimated region by considering a range around the estimated TDoA's in (a) and (b), respectively

The estimated GPS coordinates of all valid measurements having a reflection height between 50 and 350 km from Galbeni and Cerrik are superimposed on their corresponding theoretical regions evaluated using the continuous resolution TDoA concept and presented in (a) and (c) of Figure 6.25, respectively. The reflection height is assumed to be 350 km and the receiver in Bordeaux is used as the reference while computing the theoretical region. The principle of finding the theoretical region is explained in section 6.5.1. Figure 6.25 (b) and (d) represents the dispersed GPS coordinates which lies within or very close to the estimated region of Galbeni and Cerrik, respectively. It can be observed that some of the estimated GPS coordinates lie within the estimated region and many of them lie in the close proximity of the estimated region. For the estimated coordinates which lies within the hexagonal region, the dispersion is due to the low resolution of the signals. On the other hand, for estimated coordinates which lie around the hexagonal region, the dispersion is due to errors in the estimated TDoA. In order to improve the performance of the system, one can consider applying the algorithm to signals with larger bandwidth or using an additional receiver.





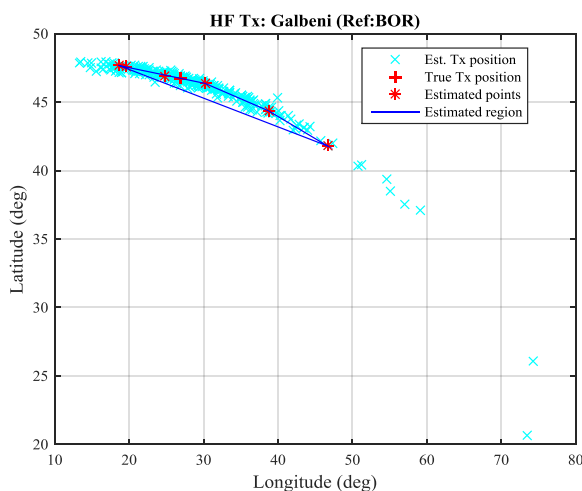
(c)



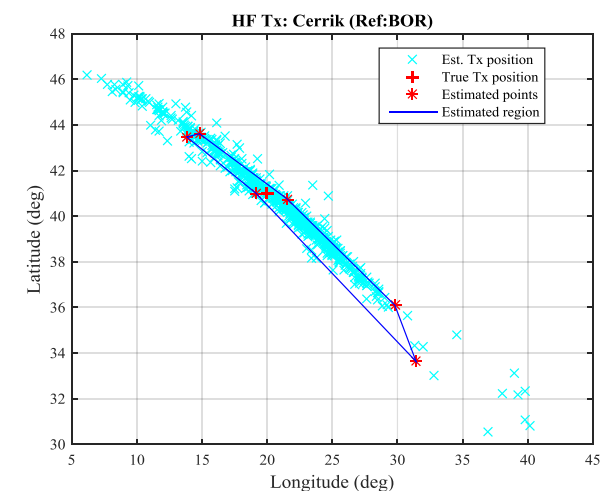
(d): Limit on x-y axis of (c)

Figure 6.25 Estimated geographic locations for all valid measurements with an estimated reflection height between 50 and 350 km from Galbeni (a) and Cerrik (c) superimposed on a theoretical hexagon obtained from a continuous TDoA resolution algorithm

In order to further analyze the largely dispersed GPS coordinates presented in (a) and (c) of Figure 6.25, the theoretical hexagon is computed at values of Δt greater than $0.25 \mu s$. In particular, the estimated region around the transmitter in Galbeni presented in (a) of Figure 6.26 is computed using $\Delta t = 10 \mu s$ whereas the estimated region around the transmitter in Cerrik is computed using $\Delta t = 50 \mu s$ (Figure 6.26 (b)). The values of Δt which will result in a valid geolocation region is dependent on the transmitter position with respect to the receiver network. All the valid measurements from Galbeni and Cerrik having an estimated reflection height between 50 and 350 km are superimposed on their corresponding hexagons, as presented in (a) and (b) of Figure 6.26, respectively. It can be observed that most of the estimated geographic locations for both cases lie within the theoretical estimated region. It allows us to deduce that that the wide spread GPS coordinates of all valid measurements are due to errors in the range of $10\text{-}50 \mu s$ in the computed TDoA's. It must also be noted that the value of Δt selected to compute the theoretical region is not very high, thereby explaining the geolocation estimate sensitivity with respect to the TDoA values.



(a)



(b)

Figure 6.26 Estimated geographic locations for all valid measurements with an estimated reflection height between 50 and 350 km from Galbeni (a) and Cerrik (b) superimposed on a theoretical hexagon obtained using Δt equal to $10 \mu s$ and $50 \mu s$, respectively

6.6 Conclusion

In this chapter, analyses of all data captured during the different measurement campaign are presented. At first, all details (transmitter site, capture start time and duration, capture frequency, capture count) of the measurement campaigns are provided. A large number of signals (22194) were captured by 4 synchronized receivers from different broadcasters located around Europe and Asia. This provided a global database of measurements that can be further post-processed to study the performance of a HF geolocation system and identify different parameters that needs to be considered to improve the overall performance of the system. Overall, the measurement campaign also allowed validating the use of a remotely controlled nation-wide measurement network.

As a first result, data captured on all receivers from different transmitters were analyzed with respect to the received noise level and SNR. It was found that the noise level decreases as the transmitter frequency increases. The calculated noise levels were varying at all the receiver site which was mainly due to the different surrounding external environments at different sites. Thus, it can be concluded that the noise level is highly dependent on the receiver location. Signals captured from Galbeni, Cerrik and Tiganesti were received with a higher SNR on all receiver sites except Lille where most of signals were received with a low SNR. The SNR could not be used as a measurement qualification metric as the transmitted signal bandwidth is unknown. In a second step, data reduction was achieved by exploiting the assumed coherence of collected measurements over time. Using the PDF, the most likely TDoA value was computed over several measurements and then by selecting a range around the most probable value, the measurements were either selected or discarded.

The geolocation statistics based on the geolocation algorithm output for data captured from Cerrik, Galbeni, Tiganesti and Emirler was provided. Out of all selected measurements (after data reduction) from Cerrik, around 80% of the measurements lead to valid algorithm output. It was also seen that the frequency band has no impact on the HF algorithm output validity (i.e. valid or invalid output).

The analysis of valid measurements made from Nauen and SMDG in July, 2017 showed the effect of sporadic E layer in geolocation. Due to the presence of Es layer, signals were successfully received in Lille from Nauen and in Grenoble from SMDG during different days in July, 2017 which otherwise was not possible as the receivers were within the skip range from the transmitters. In favorable propagation conditions, geolocation errors were less than about 10% for all valid measurements from Nauen and SMDG during the month of July, 2017. The analysis for all valid measurements also showed that the geolocation errors are larger when the estimated reflection heights were greater than the real ionospheric reflection height. The geolocation errors for the valid measurements were large even when the estimated SNR was high. Thus, it can be concluded that received SNR cannot be used to decide on the validity of the geolocation estimate.

About 7.5% of the valid measurements from Cerrik, Galbeni, Tiganesti and Emirler resulted in a geolocation error less than 100 km, but the geolocation accuracy in terms of azimuth direction was quite high. About 75% of valid measurements from Cerrik, Galbeni, Tiganesti and Emirler resulted in an azimuth error less than $\pm 5^\circ$. In general, the geolocation error was higher but it could be reduced drastically by deploying additional receivers. In addition, the signals could be sampled at a higher rate which would improve the precision of the estimated TDoA and in turn, improve the accuracy of the geolocation estimate.

The concept of continuous time resolution of the TDoA algorithm is explained and used to find a geolocation area instead of estimating a single location. Using one-hop propagation mode geometry, the geolocation areas around different transmitters are presented. The actual transmitter lies within the estimated region

which is an irregular hexagon. Using 2 different measurement examples from different transmitters, the geolocation area is plotted using the continuous time resolution approach and the transmitter lies within the computed region. Thus to conclude, this approach could resolve the errors due to TDoA uncertainties (i.e. identification of different peaks due to limited time resolution and quantization errors).

Finally, using continuous time resolution TDoA algorithm, the theoretical regions around the actual transmitter location are computed at different values of Δt and it is seen that most of the estimated transmitter coordinates lies within the evaluated region. It allow us to conclude that the dispersed GPS coordinates (around the actual Tx location) leading to large geolocation errors are due to the homogenous random shift in the three computed TDoA's around the exact value

Conclusion

Interest in HF geolocation has been present for decades, particularly in the context of civil and military operations. This is mainly due to the unique characteristic of radio signals from the HF band which can be used to establish communication over long ranges. These radio signals propagate using skywaves with single or multiple reflections within the earth-ionosphere waveguide. The ionosphere and the principles of HF radio propagations are presented in Chapter 2. HF geolocation can be achieved using angular domain and time-domain methods. In angular domain methods, there is a requirement of large antenna arrays at one or multiple sites along with knowledge of the ionospheric profile along the propagation path. On the other hand, with time-domain methods, the location of the HF transmitter can be estimated using distributed single antenna receiver setups. With the specifications of passive HF geolocation (i.e. signal transmission time and propagation channels unknown), the TDoA method is best suited for it as there is only a requirement of synchronization among multiple receivers. The research presented is a complete study involving theoretical aspects, simulation results, signal processing aspects and experimental aspects with the aim of evaluating the performance of a passive HF geolocation system.

As a first step, the HF geolocation algorithm for time-domain methods is presented along with their respective analytical expressions (Chapter 3). The algorithm assumes a one-hop transmission, uniform ionosphere with a negligible variation in the apogee height and a flat Earth. Using the geolocation algorithm, the location of the transmitter could be evaluated without the knowledge of the ionospheric profile. Based on the outputs of the geolocation algorithm, the estimated location of the transmitter could be referred as valid or invalid. In order to evaluate the geolocation accuracy of time-domain methods with respect to the number of receivers and the positioning of receivers, the QP model of the ionosphere is used. This model provides analytical expressions for ray path parameters (i.e. ground range, group path and so on...) for a given HF link. Based on the QP model, the propagation times are evaluated; they serve as inputs to the time domain HF geolocation algorithm. In relation to passive HF geolocation, simulation results show that the receivers placed in an approximately square distribution results in the highest geolocation accuracy. Simulation results also demonstrate that the geolocation error is significantly reduced by increasing the number of receivers.

In order to validate the simulation results and the concept of HF geolocation based on TDoA, four remotely controllable and programmable receivers are designed using USRP N200/N210 to capture HF radio signals synchronously. The receiver design consists of both hardware and software which are explained in detail (Chapter 4). The software part allows the users to capture HF radio signals as per their requirements. All receivers are synchronized using GPSDO kit, thereby capturing the radio signals synchronously independent of the receiver locations. The four receivers are deployed in different cities in France: Brest, Bordeaux, Grenoble and Lille forming a TDoA receiver network. The whole receiver network is controlled through a central machine in Brest. Using measurements made only in Brest, the correlation properties and the impact of capture data length on the correlation properties are evaluated. It is observed that autocorrelation/cross-correlation of the captured analog speech and audio signals resulted in an SNR of about 10 dB and 15 dB, respectively. These estimated values allow us to conclude that HF broadcast signals could be used for geolocation purpose. It is also noticed that signals captured with a 5-second duration results in a higher SNR of the cross-correlation output, compared to signals captured for 10 and 15 seconds, underlying the importance of the signal stationarity on the TDoA evaluation. The effect of the received SNR on the HF geolocation accuracy is also presented in Chapter 4. From simulation results, it can be observed that the geolocation error is arbitrarily low when the received SNR is sufficiently high.

In order to estimate the time delay between signals captured at multiple synchronized receivers, a new method termed as cross-channel sounding is presented in Chapter 5 along with its concepts. Based on the

mathematical description of cross-channel sounding, it is observed that the autocorrelation of the transmitted signal must be equivalent to a large peak centered at zero to obtain the time delay. But, in the case of passive HF geolocation, the transmitted signal is unknown and its properties cannot be altered. From cross-channel sounding output, the signal propagation paths at different receivers can be identified with regards to the different peaks. It is seen that there is a single peak in the cross-channel sounding output when signals arrive at receivers through single path channels; multiple peaks when signals arrive through multi-path channels. However, in the case of multi-path channels, the minimum resolution is limited by the useful signal bandwidth. Analyses of the data captured in July 2017 from different transmitters located around Europe are also presented in Chapter 5. From preliminary measurement results, it is seen that in favorable conditions, the HF transmitters could be located with a relative error in the range of about 0.1 to 10% of the actual ground range. In addition, it is also observed that the geolocation output for most cases in terms of azimuthal direction is highly accurate. The analysis of the preliminary measurements validates the concept of HF geolocation using the TDoA method.

A total of 22194 measurements were made from different HF transmitters located in Europe, Asia and Africa. Details of these measurements made using the HF receiver network and the statistical analysis of these measurements over different parameters are presented in Chapter 6. A first observation is made with the received noise and SNR level of the signal captured at each receiver from different transmitters with the objective of selecting or discarding a measurement. It is noticed that the received noise level decreases as transmitter's broadcast frequency increases. It is also observed that the noise level is also dependent on the receiver location. From the SNR analysis, it is observed that signals from some transmitters (specifically Cerrik, Galbeni and Tiganesti) are received with a higher SNR in Brest, Bordeaux and Grenoble, as compared to Lille. In general, due to the unknown signal bandwidth and the reception of signals with low SNR prevented us to select SNR as a metric for measurement qualification. As a next step, an algorithm to consider or discard a measurement is proposed based on the TDoA analysis. The algorithm exploits the coherence of collected measurements over time (i.e. repetition of the estimated TDoA's over time). The measurements are processed using this algorithm and discarded if it failed to satisfy the requirements of the algorithm. We could select about 35% of the measurements processed using TDoA analysis for further post-processing and evaluating the geolocation performance. For some transmitters with a high signal quality on all HF links, such as Cerrik and Galbeni, this percentage of data selection increased up to 45% and 48%, respectively.

After data selection, the geolocation performance of the TDoA algorithm over the large scale measurement is studied. Out of all the selected measurements, about 49% of the data resulted in a valid geolocation output. About 30% of valid measurements (CER, GAL, TIG, NAU, SMDG and EMR) led to a geolocation error below 100 km. More precisely, about 75% of valid measurements from Nauen and SMDG led to a geolocation error less than 100 km. One must note that the experiment was performed with a minimum number of receivers (i.e. 4) and still about 80% of the valid measurements (CER, GAL, TIG, NAU, SMDG and EMR) resulted in an azimuth error less than 5° . In general, the estimated geolocation errors for all valid measurements from different transmitters are larger than expected from the preliminary results but the distribution of the estimated geographic locations are found to resemble an ellipse around the actual transmitter location. These errors are high due to GDOP and the sensitivity on time delay accuracy for TDoA based geolocation systems. These errors can be reduced to a great extent by using more receivers to capture data (as explained in sections 3.2 and 3.3.2) and increasing the time resolution of geolocation system. Finally, a concept of continuous time resolution of the TDoA algorithm is proposed which can be used to find a geolocation area rather than producing a single location estimate (Chapter 6). In this way, one can have a rough estimate about the region in which the transmitter lies provided the estimated TDoA's are accurate enough.

Overall, the results of our study could serve as a reference for implementing a practical HF geolocation system or even for future studies concerning passive HF geolocation. For instance, the geolocation algorithm could be easily modified to consider HF radio transmissions from ground waves and locate the transmission source. This could be then validated using our HF receiver network and performance of the system could be studied. Similarly, this approach could be used to study geolocation of signals emitted from VLF to MF bands where transmission occurs through lower regions of the ionosphere and ground waves.

Future work

In the continuity of this work, several lines of research have been highlighted.

At first, the proposed geolocation algorithm is based on certain assumptions. The analytical expressions for the geolocation algorithm can be reformulated by taking into account the Earth curvature instead of assuming it to be flat. Even with the assumption of a uniform ionosphere, the difference in the reflection heights for different paths with different elevation angles needs to be investigated and could be accounted for in the algorithm. The proposed modifications would lead to an algorithm which is closer to the realistic scenarios and the obtained results are expected to be more accurate.

The deployed HF receiver network consists of only the minimum number of required receivers (i.e. 4) to perform HF geolocation using the TDoA method. The network could be enlarged by adding more receivers in the network and later evaluate the performance of the geolocation system. From simulation results with minimum and more number of receivers, it can be predicted that the geolocation accuracy would improve. Moreover, the number of qualified measurements would also be higher (i.e. more the number of receivers, higher is the probability of the signal being captured by at least the minimum number of receivers i.e. 4). The time resolution of the geolocation system can be improved further by capturing data with a higher sampling rate and thereby reducing the TDoA errors. It would also improve the geolocation accuracy to some extent.

In this thesis, signals were mainly captured from broadcast HF transmitters. As an extension, HF digital signals could be captured from different beacon locations and their correlations properties could be evaluated to assess the feasibility of using such signals for the purpose of HF geolocation.

The TDoA is evaluated by selecting the peak of the cross-channel sounding output with the highest intensity. The different peaks correspond to different propagation modes and advanced algorithms considering the different peaks can be developed. In general, the geolocation accuracy would be higher if TDoA's correspond to the same propagation modes irrespective of the signals intensities with which they are received. The impact of the received signal SNR on the cross-channel sounding can also be assessed and can be used to define a certain threshold for considering or rejecting a measurement based on the TDoA output.

Lots of data can be captured from several known transmitters (i.e. their signal type are known) located in different directions from the receiver network. The obtained geolocation errors can be classified with regards to different direction from a reference point. If the geolocation errors are coherent over the capture times or frequencies, a correction model can be devised each for a certain direction based on obtained errors. This correction model can be used on a geolocation estimate obtained for an unknown transmitter. In this way, one could refine the results based on the correction model.

The low complexity of each single SDR receiver could allow for the deployment of several tens or hundreds of such receivers in a region of the size of Europe. An estimate of the transmitter could be found with a high accuracy provided the signals are captured by 5 to 6 receivers. In addition, a geolocation area can be found based on the concept of continuous time resolution of the TDoA algorithm. Once a region is established, one can utilize the cooperation with existing open geolocation networks such as KiwiSDR to find another estimate of the transmitter. This estimate of the transmitter might be very close to the actual transmitter location as it is a multi-step process. The optimization and performance of such massive TDoA geolocation network opens a new field of research in cooperative localization.

Appendix A: Minimum number of receivers required for HF geolocation using the TDoA method

In the TDoA case, the transmission time t_0 is unknown. Equation 3.24 in the scalar form for the receiver pair (1-2) is expressed as follows:

$$\begin{aligned} \frac{1}{t_2 - t_1}(x_2^2 - x_1^2) - \frac{2}{t_2 - t_1}(x_2 - x_1)x_0 + \frac{1}{t_2 - t_1}(y_2^2 - y_1^2) - \frac{2}{t_2 - t_1}(y_2 - y_1)y_0 \\ + \frac{1}{t_2 - t_1}(z_2^2 - z_1^2) - \frac{2}{t_2 - t_1}(z_2 - z_1)z_0 = (t_2 + t_1)c^2 - 2t_0c^2 \end{aligned} \quad (1)$$

Similarly, using other 2 possible pairs of receivers (2-3 and 3-1), one obtains a system of three equations. In order to remove the unknown t_0 , one computes the difference of the three equations in a pairwise manner. For instance, using the first and second equation and then using second and third equation, one obtains equation (2) and equation (3), respectively.

$$\begin{aligned} \frac{1}{t_2 - t_1}(x_2^2 - x_1^2) - \frac{1}{t_3 - t_2}(x_3^2 - x_2^2) - \left(\frac{2}{t_2 - t_1}(x_2 - x_1) - \frac{2}{t_3 - t_2}(x_3 - x_2) \right) x_0 \\ + \frac{1}{t_2 - t_1}(y_2^2 - y_1^2) - \frac{1}{t_3 - t_2}(y_3^2 - y_2^2) - \left(\frac{2}{t_2 - t_1}(y_2 - y_1) - \frac{2}{t_3 - t_2}(y_3 - y_2) \right) y_0 \\ + \frac{1}{t_2 - t_1}(z_2^2 - z_1^2) - \frac{1}{t_3 - t_2}(z_3^2 - z_2^2) - \left(\frac{2}{t_2 - t_1}(z_2 - z_1) - \frac{2}{t_3 - t_2}(z_3 - z_2) \right) z_0 \\ = (t_1 - t_3)c^2 \end{aligned} \quad (2)$$

$$\begin{aligned} \frac{1}{t_3 - t_2}(x_3^2 - x_2^2) - \frac{1}{t_1 - t_3}(x_1^2 - x_3^2) - \left(\frac{2}{t_3 - t_2}(x_3 - x_2) - \frac{2}{t_1 - t_3}(x_1 - x_3) \right) x_0 \\ + \frac{1}{t_3 - t_2}(y_3^2 - y_2^2) - \frac{1}{t_1 - t_3}(y_1^2 - y_3^2) - \left(\frac{2}{t_3 - t_2}(y_3 - y_2) - \frac{2}{t_1 - t_3}(y_1 - y_3) \right) y_0 \\ + \frac{1}{t_3 - t_2}(z_3^2 - z_2^2) - \frac{1}{t_1 - t_3}(z_1^2 - z_3^2) - \left(\frac{2}{t_3 - t_2}(z_3 - z_2) - \frac{2}{t_1 - t_3}(z_1 - z_3) \right) z_0 \\ = (t_2 - t_1)c^2 \end{aligned} \quad (3)$$

Since the earth is assumed to be flat, the z-coordinate for all the receivers are equal. Thus, we have 2 linear equations with 2 unknowns (x_0 and y_0), similar to a system of equations with 2 unknowns (Equation 3.20). Comparing equation (2) and (3) with equation 3.20, the different constants are computed and are as follows:

$$\begin{aligned} a_{11} &= \left(\frac{2}{t_2 - t_1}(x_2 - x_1) - \frac{2}{t_3 - t_2}(x_3 - x_2) \right) \\ a_{12} &= \left(\frac{2}{t_2 - t_1}(y_2 - y_1) - \frac{2}{t_3 - t_2}(y_3 - y_2) \right) \\ a_{21} &= \left(\frac{2}{t_3 - t_2}(x_3 - x_2) - \frac{2}{t_1 - t_3}(x_1 - x_3) \right) \\ a_{22} &= \left(\frac{2}{t_3 - t_2}(y_3 - y_2) - \frac{2}{t_1 - t_3}(y_1 - y_3) \right) \end{aligned} \quad (4)$$

$$\begin{aligned}
 b_1 &= \frac{1}{t_2 - t_1} (x_2^2 - x_1^2) - \frac{1}{t_3 - t_2} (x_3^2 - x_2^2) + \frac{1}{t_2 - t_1} (y_2^2 - y_1^2) \\
 &\quad - \frac{1}{t_3 - t_2} (y_3^2 - y_2^2) - (t_1 - t_3)c^2 \\
 b_2 &= \frac{1}{t_3 - t_2} (x_3^2 - x_2^2) - \frac{1}{t_1 - t_3} (x_1^2 - x_3^2) + \frac{1}{t_3 - t_2} (y_3^2 - y_2^2) \\
 &\quad - \frac{1}{t_1 - t_3} (y_1^2 - y_3^2) - (t_2 - t_1)c^2
 \end{aligned}$$

Check: The matrix is of the form $Ax = B$, where x resembles the unknown coordinates of the transmitter. To calculate x vector, A should be a non-singular matrix (i.e. $|A| \neq 0$). However, after calculation, it is found that the determinant of A is equal to zero, which implies that the matrix A is neither non-singular nor full rank.

In addition, if equations (2) and (3) are dependent on each other, then equation (3) can be expressed in terms of equation (2) multiplied by some constant term (α). For a system of 2 unknown equations, the different constants of an equation can be expressed in terms of α with regards to the constants of other equations. These constants can be expressed as follows:

$$\begin{aligned}
 a_{21} &= \alpha a_{11} \\
 a_{22} &= \alpha a_{12} \\
 b_2 &= \alpha b_1 \\
 \alpha &= \frac{a_{21}}{a_{11}} \text{ or } \frac{a_{22}}{a_{12}} \\
 b_2 a_{11} &= b_1 a_{21} \text{ or } b_2 a_{12} = b_1 a_{22}
 \end{aligned} \tag{5}$$

Now, if one can prove that $b_2 a_{11} = b_1 a_{21}$, then equations (2) and (3) would be dependent on each other.

Proof: $b_2 a_{11} = b_1 a_{21}$

The multiplications of constants on the RHS results in the following:

$$\begin{aligned}
 b_1 a_{21} &= \left\{ \left(\frac{1}{t_2 - t_1} (x_2^2 - x_1^2) - \frac{1}{t_3 - t_2} (x_3^2 - x_2^2) + \frac{1}{t_2 - t_1} (y_2^2 - y_1^2) \right. \right. \\
 &\quad \left. \left. - \frac{1}{t_3 - t_2} (y_3^2 - y_2^2) - ((t_1 - t_3)c^2) \right) \left(\frac{2}{t_3 - t_2} (x_3 - x_2) \right. \right. \\
 &\quad \left. \left. - \frac{2}{t_1 - t_3} (x_1 - x_3) \right) \right\}
 \end{aligned} \tag{6}$$

After simplification, equation (6) can be expressed as follows:

$$b_1 a_{21} = \frac{2}{(t_2 - t_1)(t_1 - t_3)(t_3 - t_2)^2} \left\{ \begin{array}{l} (x_1 t_2 - x_1 t_3 + x_2 t_3 - x_2 t_1 + x_3 t_1 - x_3 t_2) \\ \left(\begin{array}{l} x_1^2 t_2 - x_1^2 t_3 + x_2^2 t_3 - x_2^2 t_1 + x_3^2 t_1 - x_3^2 t_2 + \\ y_1^2 t_2 - y_1^2 t_3 + y_2^2 t_3 - y_2^2 t_1 + y_3^2 t_1 - y_3^2 t_2 + \\ t_1 t_2^2 c^2 - t_1 t_3^2 c^2 + t_2 t_3^2 c^2 - t_2 t_1^2 c^2 + \\ t_3 t_1^2 c^2 - t_3 t_2^2 c^2 \end{array} \right) \end{array} \right\} \tag{7}$$

Similar to equation (6), the multiplications of constants on LHS gives the following:

$$\begin{aligned}
 b_2 a_{11} = & \left\{ \left(\frac{1}{t_3 - t_2} (x_3^2 - x_2^2) - \frac{1}{t_1 - t_3} (x_1^2 - x_3^2) + \frac{1}{t_3 - t_2} (y_3^2 - y_2^2) \right. \right. \\
 & \left. \left. - \frac{1}{t_1 - t_3} (y_1^2 - y_3^2) - ((t_2 - t_1)c^2) \right) \left(\frac{2}{t_2 - t_1} (x_2 - x_1) \right. \right. \\
 & \left. \left. - \frac{2}{t_3 - t_2} (x_3 - x_2) \right) \right\} \quad (8)
 \end{aligned}$$

After simplification, equation (8) can be expressed as follows:

$$b_2 a_{11} = \frac{2}{(t_2 - t_1)(t_1 - t_3)(t_3 - t_2)^2} \left\{ \begin{array}{l} (x_1 t_2 - x_1 t_3 + x_2 t_3 - x_2 t_1 + x_3 t_1 - x_3 t_2) \\ \left(x_1^2 t_2 - x_1^2 t_3 + x_2^2 t_3 - x_2^2 t_1 + x_3^2 t_1 - x_3^2 t_2 + \right. \\ \left. y_1^2 t_2 - y_1^2 t_3 + y_2^2 t_3 - y_2^2 t_1 + y_3^2 t_1 - y_3^2 t_2 + \right. \\ \left. t_1 t_2^2 c^2 - t_1 t_3^2 c^2 + t_2 t_3^2 c^2 - t_2 t_1^2 c^2 + \right. \\ \left. t_3 t_1^2 c^2 - t_3 t_2^2 c^2 \right) \end{array} \right\} \quad (9)$$

Since equation (7) is equal to equation (9), it is clear that equation (3) can be expressed in terms of equation (2) multiplied by a constant term (i.e. both equations are dependent on each other). Thus, the coordinates of the unknown transmitter cannot be found by 3 receivers using the TDOA principle. Hence, a minimum of 4 receivers are required to compute the transmitter location using the TDoA method.

Appendix B: Processing of AM signal within SDR module

Amplitude modulation: In amplitude modulation, the amplitude of the carrier wave (i.e. a high frequency wave) is varied in accordance with the message signal while the phase (φ) of the carrier signal is assumed to be zero. The carrier signal $c(t)$ can be seen in Fig. 1 (a) and is represented mathematically as follows:

$$c(t) = A_c \cos(2\pi f_c t) \quad (1)$$

where A_c is the amplitude of the carrier signal, f_c is the frequency of the carrier signal. The message bearing signal (i.e. baseband signal) $m(t)$ can be seen in Fig. 1 (b) and is represented mathematically as follows:

$$m(t) = A_m \sin(2\pi f_m t) \quad (2)$$

where A_m is the amplitude of the message signal, f_m is the modulating frequency of the signal. The message signal is sometimes also referred to as modulation signal. The carrier frequency f_c is much higher than the highest frequency component of the message signal.

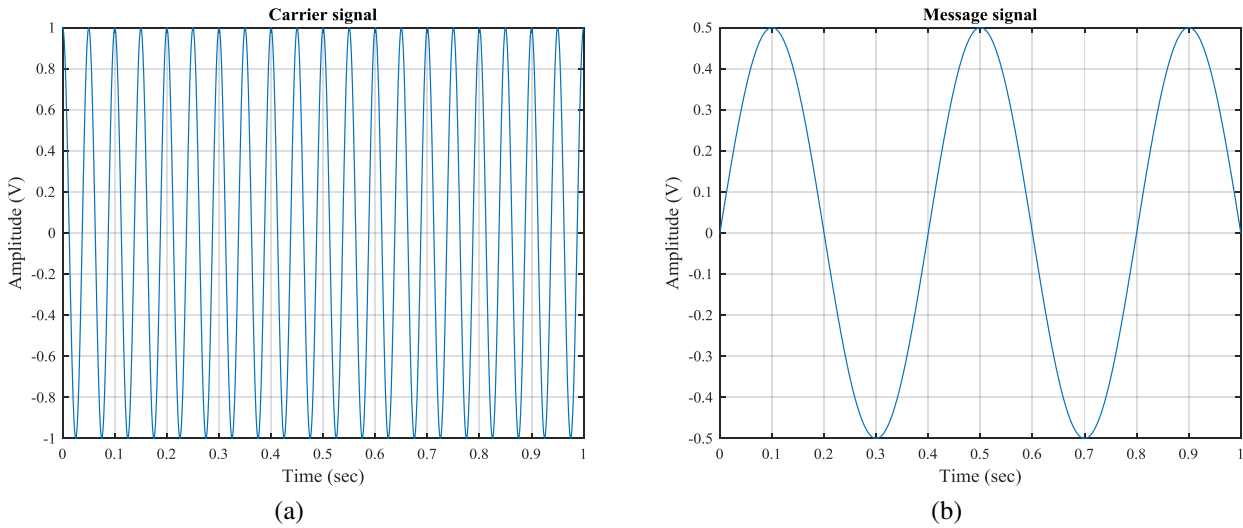


Fig. 1 Representation of carrier signal in (a) and message signal in (b)

Now as per the definition of amplitude modulation, the amplitude of carrier wave will be varied in proportion to the amplitude of the modulating signal that contains information and has to be transmitted. An amplitude modulated signal $e(t)$ when transmitted over the air is given by the following equation:

$$e(t) = A_c(1 + k_a m(t)) \cos(2\pi f_c t) \quad (3)$$

where k_a is the amplitude sensitivity of the modulator and is always positive. As seen in equation (3), a dc component is added to the message signal before multiplying it by the carrier signal. This is done so that the modulated carrier can be easily removed and the message content can be obtained at the reception end using a simple envelope detector. The envelope of the AM signal is given by the following equation:

$$e(t)_{envelope} = A_c |1 + k_a m(t)| \quad (4)$$

Radio broadcasters using AM to transmit voice signals, the envelope has the following form:

$$e(t)_{envelope} = A_c [1 + k_a m(t)] \geq 0 \forall t \quad (5)$$

where \forall denotes ‘for all’. If the envelope is positive for all values of time, then the message signal can be easily recovered from the envelope using an envelope detector which is a non-coherent demodulator. The message signal extracted would be within a scale factor and a constant offset which can be further removed by processing the signal. Equation (3) can be rewritten in the following form:

$$e(t) = A_c(1 + \mu \sin(2\pi f_m t)) \cos(2\pi f_c t) \quad (6)$$

where $\mu = k_a A_m$; known as the modulation index. It is also defined as the ratio of the peak value of double side band term ($k_a A_m A_c$) to the peak of the carrier (A_c). When the value of $\mu = 1$, we have 100% modulation and the signal received at the reception end has a high SNR value. Fig. 2 represents an AM signal with modulation index being equal to 1. When the value of modulation index ($\mu > 1$), we have over modulation and it results in envelope distortion [146].

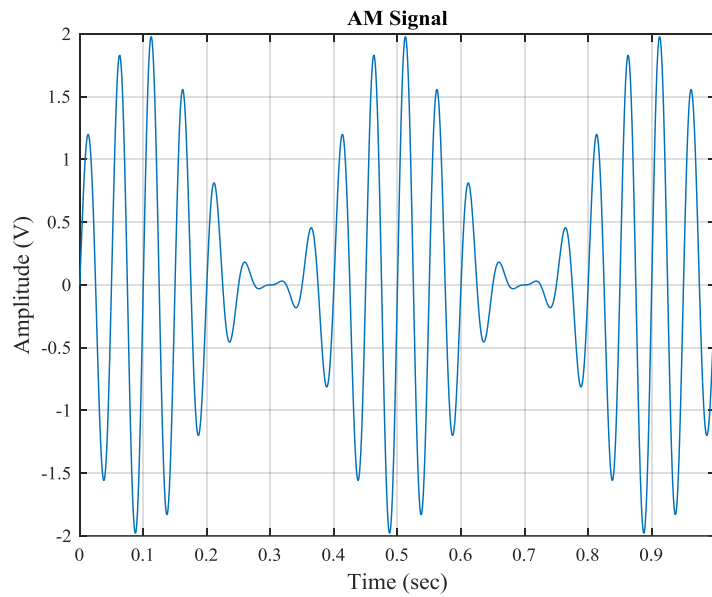


Fig. 2 Representation of AM signal with modulation index being equal to 1

Equation (6) is further simplified and is written as follows:

$$e(t) = A_c \cos(2\pi f_c t) + \left(\left(\frac{\mu A_c}{2} \right) (\sin[2\pi(f_c + f_m)t] + \sin[2\pi(f_c - f_m)t]) \right) \quad (7)$$

As seen in equation (7), the modulated wave transmitted has 3 main components, the carrier signal as it is and two sidebands at $(f_c - f_m)$ and $(f_c + f_m)$ which contains the information content of the message signal.

Complex representation of AM signal: The AM signal could be represented as a real part of the complex signal as follows:

$$e(t) = \text{Re}[a(t)e^{j\varphi} e^{j2\pi f_c t}] = \text{Re}[\tilde{s}(t)e^{j2\pi f_c t}] \quad (8)$$

where $a(t) = A_c(1 + k_a m(t))$ is the baseband amplitude, φ is the initial phase of the carrier wave and can be assumed to zero or constant in case of AM. The complex envelope can be defined as follows:

$$\begin{aligned} \tilde{e}(t) &= a(t)e^{j\varphi} = a(t) \cos \varphi + ja(t) \sin \varphi = I(t) + jQ(t) \\ I(t) &= a(t) \cos \varphi, Q(t) = a(t) \sin \varphi \end{aligned} \quad (9)$$

The $I(t)$ represents the inline phase component whereas $Q(t)$ represents the quadrature phase component of the AM signal. From equation (9), it can also be said that $\tilde{e}(t)$ is a real valued signal when the phase of the carrier wave is zero or constant which is generally the case in AM signals. If the signal is real valued, then the spectrum for the negative frequencies would be a mirrored replica of the spectrum of the positive frequencies. The magnitude of the complex envelope yields $a(t)$, and is not dependent on the phase of the carrier signal and thus not depend on any frequency offset and is given as follows:

$$a(t) = |\tilde{e}(t)| = |I(t) + Q(t)| \quad (10)$$

To conclude, the message signal $m(t)$ could be recovered from $a(t)$ regardless of the phase or any frequency offset in the carrier signal by just taking the magnitude of the complex envelope. In our case, we have the complex samples (i.e. IQ data) available from the USRP.

Signal processing within SDR box: In our experiments, we capture short wave radio broadcasts (AM signals) through an antenna designed for HF reception. The captured signal is fed to the USRP N210/N220 through the RF frontend. The LFRX daughterboard is used which includes hardware for 2 analog RF frontend and provides direct access to the ADC inputs of the USRP. In our application, a single RF frontend is used which receives real mode signals from DC to 30 MHz. The daughterboard has a unit gain operational amplifier configured with a low-pass filter which removes anything which is not from the HF band. If both analog RF frontends are used together, the board is capable of accepting quadrature (IQ) mode signal. The LFRX daughterboard just amplifies the signal and passes it to the ADC. The FPGA consists of the ADC and digital signal processing (DSP) blocks. The real mode signals are now sampled by the ADC at 100 MS/s and the digital samples are passed to the DSP blocks for further processing. The USRP hardware driver (UHD) automatically sets the sub-device specification, if not mentioned by the user, and it is used to establish the routing of ADC samples to the digital signal processing (DSP) blocks within the FPGA [147]. The unused ADC channel is filled with null samples in our case since we just accept real mode signals on one analog RF frontend. The receiver DSP block consists of a digital down converter (DDC) and a decimator. The DDC has two inputs: I and Q; the digital samples from the ADC serves as the input to the DDC. The complex input signal is multiplied with a constant frequency exponential signal (normally the center frequency specified by the user) generated by numerically controlled oscillator (NCO) based on CORDIC algorithm [148]. The resulting signal is the complex baseband signal but centered on zero. Finally, the signal is decimated as per the decimation factor provided by the user (As we specify the sampling frequency to be 200 KHz, the decimation factor is 500). The complex samples are then fed to the PC through the Ethernet port.

DDC: The DDC consists of complex multiplier which results in complex baseband signal. The complex baseband signal is then passed through a cascaded configuration of 4 stage CIC filter and 31 tap half-band filters which results in the down sampling of the baseband signal as per the sampling frequency specified by the user. CIC filters are high performance filters and it uses only adders and delays while the half-band filters are used for spectral shaping and rejection of signals which are out of band [148].

Mathematical description explaining processing within SDR box: The Ettus box in our setup is designed to accept real mode signal and thus the signal received " $s(t)$ " by the RF frontend is similar to equation (8) and is as follows:

$$s(t) = a(t)e^{j\phi}e^{j2\pi f_c t} \quad (11)$$

The received signal passes through the RF frontend and is amplified by the LFRX daughterboard. The amplified signal is then passed to the ADC where it is sampled at 100 MS/s. The digital samples are passed to the DDC where they are multiplied with a complex sinusoid signal to transform the real signal to complex baseband signal. The multiplying term is $e^{-j2\pi f_c t}$ where f_c is the center frequency at which we want to

capture the samples. Thus, the real mode signal is converted to complex baseband signal $x(t)$ and it has the following form:

$$x(t) = s(t)e^{-j2\pi f_c t} = a(t)e^{j\varphi}e^{-j2\pi f_c t}e^{j2\pi f_c t} \quad (12)$$

It can be further simplified and written as:

$$x(t) = a(t)e^{j\varphi} = I(t) + jQ(t) \text{ where } I(t) = a(t) \cos \varphi, Q(t) = a(t) \sin \varphi \quad (13)$$

The complex samples are further decimated according to the decimation factor and then the samples are transferred to the PC through the Ethernet port. The decimator could be treated as a low-pass filter followed by down sampling, since the LPF first removes the unwanted band of the spectrum and the decimator then despreads the samples. The complex baseband spectrum is no more symmetric about zero which was the case for real mode signal $s(t)$. The AM broadcast signal with center frequency (also known as carrier frequency) (f_c) will appear at 0 Hz after the down conversion. Moreover, the complex baseband signal is limited by the sampling frequency. The maximum decimation factor which is possible in USRP N210 is 512. It is also possible to tune other signals by simply multiplying the complex signal ($I(t) + jQ(t)$) by a complex sinusoidal signal having the frequency at which one wants to receive the signal. Correspondingly, that frequency will now appear at 0 Hz.

The output of USRP is always a complex-baseband signal irrespective of the input signal (real mode or quadrature mode signals). In our receiver setup, if one requests to capture a signal with center frequency of 10 MHz and with a sampling rate of 200 kHz, the DDC will down-convert the incoming 10 MHz signal down to the baseband, decimate it (it will appear as 0 Hz) and the complex-baseband signal will then be represented from -100 kHz to +100 kHz (9.9 MHz to 10.1 MHz).

Appendix C: Autocorrelation and cross-correlation of captured audio signal

HF radio broadcast signals captured simultaneously by multiple receivers in Brest on 2nd May, 2017 at 14:45 UTC from the transmitter located in Galbeni, Romania was found to be an audio signal. The transmitter in Galbeni was broadcasting at 15.130 MHz during that time. The signal was captured for 10 seconds at all receivers and sampled at the rate of 200 kHz. The antennas of the receivers were placed about one meter apart from each other. The autocorrelation and cross-correlation of the captured audio signals are calculated as explained in section 4.4.1 and presented in (a) and (b) of Fig. 3, respectively. As seen in Fig. 3 (a) and (b), the autocorrelation and cross-correlation peak is about 15 dB in terms of SNR which again validates the feasibility of using broadcast signals for the purpose of geolocation. Moreover, the estimated time delay obtained from the cross-correlation between the 2 signals is equal to zero and is exact considering the distance between the reception sites.

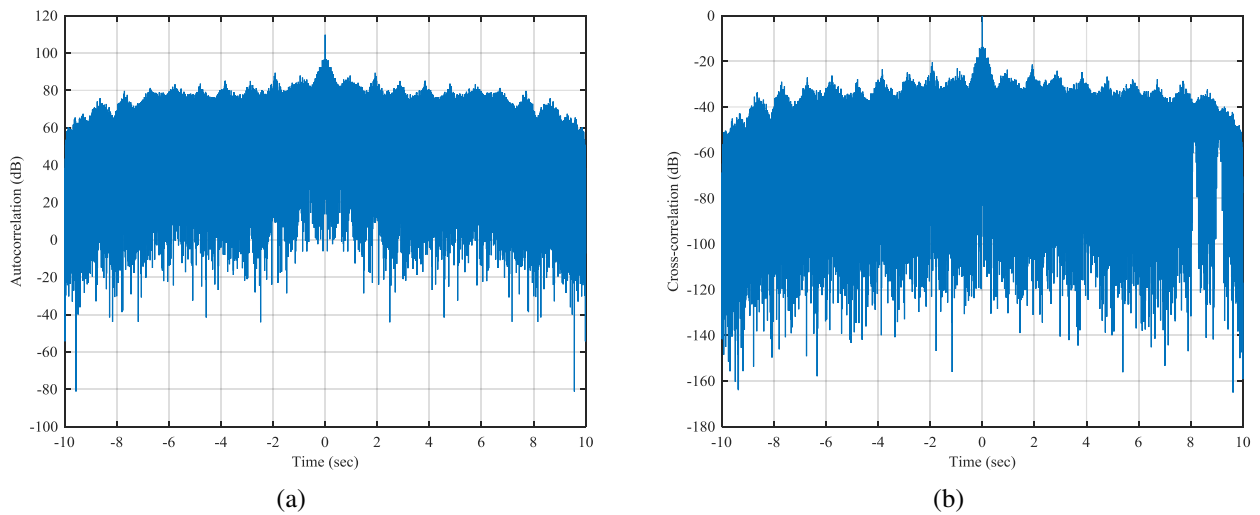


Fig. 3 Autocorrelation and cross-correlation of captured audio signals in Brest from Galbeni represented in (a) and (b), respectively

Appendix D: Study of geolocation error due to flat Earth assumption

The ToA/TDoA geolocation algorithm explained in section 3.2 assumes a flat Earth with a uniform, specular and fixed height ionosphere. It is necessary to compute the error made when considering a uniform, specular and fixed height ionosphere but on a realistic curved Earth, in 2D.

Relationship between ground range D and group path distance P in a uniform, specular and fixed height ionosphere in a curved Earth configuration: Fig. 4 illustrates the geometry of the raypath on a curved Earth in a uniform, specular and fixed height ionosphere. The point R represents the receiver location while the point T represents the transmitter location.

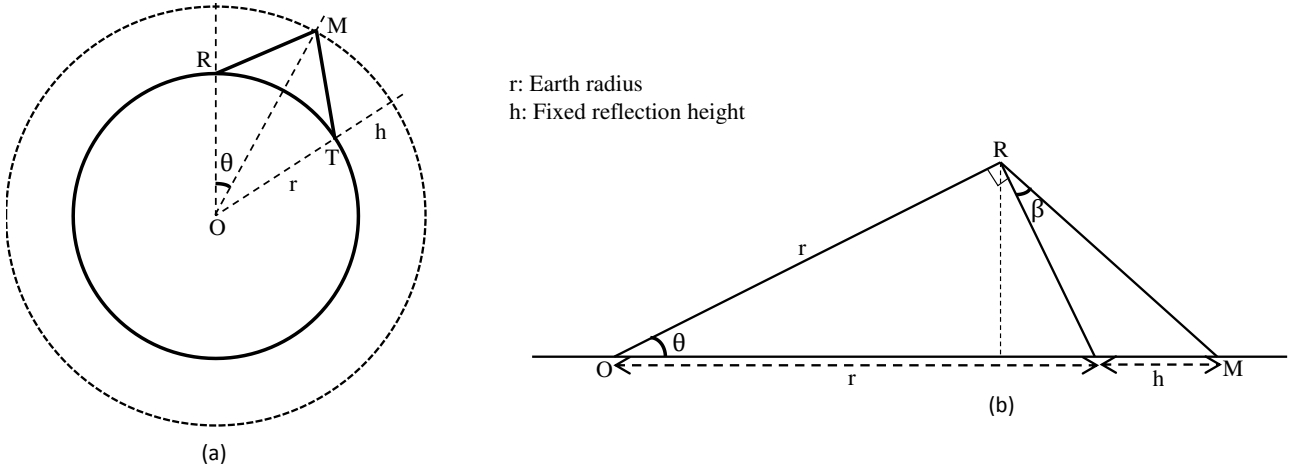


Fig. 4 Geometry of the raypath on a curved Earth for a one-hop HF link

The ground distance D is equal to the curved distance between point R and T. It can be calculated using the following equation:

$$D = 2r \times \theta \quad (1)$$

where θ is in radians. The distance between the raypath RM is half the distance of group path (i.e. $P/2$). Using the law of cosines, one can compute RM as follows:

$$RM^2 = OR^2 + OM^2 - 2 \cos \theta \times OR \times OM \quad (2)$$

Substituting the values of RM and θ , the above equation is reduced to the following:

$$P = 2 \left[r^2 + (r + h)^2 - 2 \cos \left(\frac{D}{2r} \right) r(r + h) \right]^{1/2} \quad (3)$$

Note: Take-off angle $\beta = \widehat{ORM} - \frac{\pi}{2}$. Radio-horizon is defined as $\beta = 0$, thus, $\widehat{ORM} = \frac{\pi}{2}$.

Consequently, at radio horizon $OM^2 = OR^2 + RM^2$. By injecting this expression in equation (2), one obtains the following:

$$\cos \theta_{\max} = \frac{r}{r + h} \quad (4)$$

By substituting equation (4) in equation (1), the maximum ground distance and consequently the maximum group path is given by the following equation:

$$D_{max} = 2r \cos^{-1} \left(\frac{r}{r+h} \right), P_{max} = 2[(r+h)^2 - r^2]^{1/2} \quad (5)$$

Applying the ToA algorithm in the case of a flat Earth (2D case): Fig. 5 represent the raypath geometry for 2 different HF links with a specular reflection from a fixed height ionosphere.

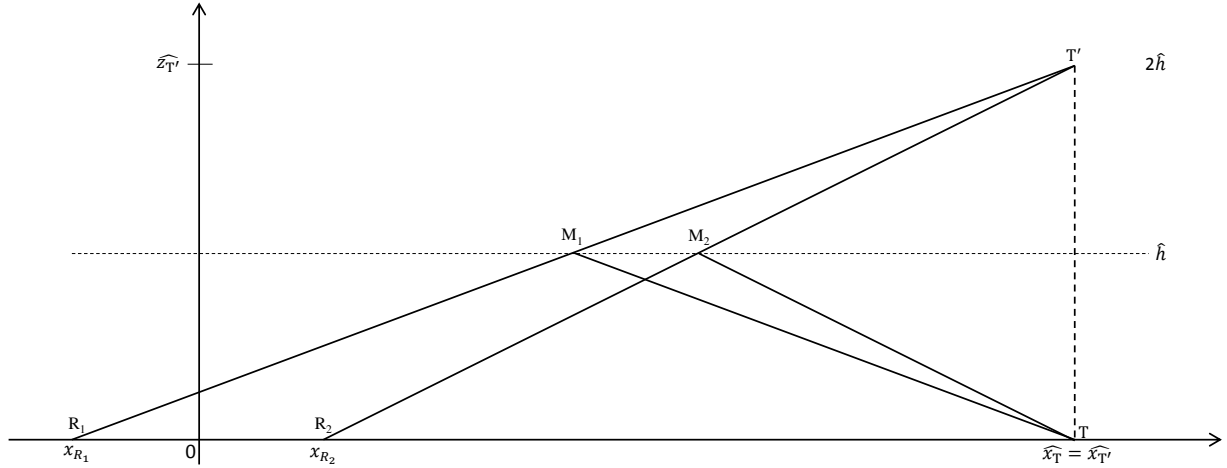


Fig. 5 Raypath geometry for 2 HF links assuming a flat Earth

As seen in Fig. 5, $R_1 T' = P_1$; $R_2 T' = P_2$. T' lies at the intersection of two circles with centers R_1 and R_2 and radii P_1 and P_2 , respectively. $(\widehat{x}_T, \widehat{z}_T)$ is the solution of the following system (equations of circles):

$$(\widehat{x}_T - x_{R_1})^2 + (\widehat{z}_T - z_T)^2 = P_1^2 \quad (6)$$

$$(\widehat{x}_T - x_{R_2})^2 + (\widehat{z}_T - z_T)^2 = P_2^2 \quad (7)$$

Subtracting the above 2 equations (i.e. equation (6) - equation (7)) and after simplification, it leads to the following:

$$\widehat{x}_T - \widehat{x}_T = \frac{x_{R_1} + x_{R_2}}{2} - \frac{1}{2(x_{R_1} - x_{R_2})} (P_1^2 - P_2^2) \quad (8)$$

Replace P_1 and P_2 by their expressions from equation (3), where $D_1 = x_T - x_{R_1}$ and $D_2 = x_T - x_{R_2}$. Note x_T is the actual location on the curved Earth whereas \widehat{x}_T is the estimated location as per the algorithm output.

$$\widehat{x}_T - \frac{x_{R_1} + x_{R_2}}{2} = 4r(r+h) \left[\cos \left(\frac{x_T - x_{R_1}}{2r} \right) - \cos \left(\frac{x_T - x_{R_2}}{2r} \right) \right] \frac{1}{(x_{R_1} - x_{R_2})} \quad (9)$$

Using one of the trigonometric sum to product identities, the above equation after simplification can be expressed as:

$$\widehat{x}_T - \frac{x_{R_1} + x_{R_2}}{2} = 2(r+h) \sin \left(\frac{1}{2r} \left(x_T - \frac{x_{R_1} + x_{R_2}}{2} \right) \right) \operatorname{sinc} \left(\frac{x_{R_1} - x_{R_2}}{4r} \right) \quad (10)$$

where $\widehat{x}_T - \frac{x_{R_1} + x_{R_2}}{2}$ is the estimated distance to the center of the network; $x_T - \frac{x_{R_1} + x_{R_2}}{2}$ is the actual distance to the center of the network. Without the loss of generality, we can set the center of the receiver network at the origin, i.e. $\frac{x_{R_1} + x_{R_2}}{2} = 0$. Equation (10) can be expressed as:

$$\widehat{x}_T = 2(r+h) \sin \left(\frac{x_T}{2r} \right) \operatorname{sinc} \left(\frac{x_{R_1} - x_{R_2}}{4r} \right) \quad (11)$$

Equation (11) allows estimating the relationship between the real distance (to the center of the network) x_T and the estimated distance \widehat{x}_T . The error due to neglecting the earth curvature is the difference between the estimated and the real distance. It can be found for any x_T and realistic values of h and distance $x_{R_1} - x_{R_2}$. Inversely, from the algorithm output \widehat{x}_T and taking an average value of h , a more accurate value of x_T can be computed.

Note: If $x_{R_1} - x_{R_2}$ is small, $\text{sinc}\left(\frac{x_{R_1} - x_{R_2}}{4r}\right) \cong 1$, if $\frac{x_T}{2r}$ is small, $\sin\left(\frac{x_T}{2r}\right) \cong \frac{x_T}{2r}$. If both are small, $\widehat{x}_T \cong \frac{r+h}{r} x_T$.

Study of the output \widehat{z}_T :

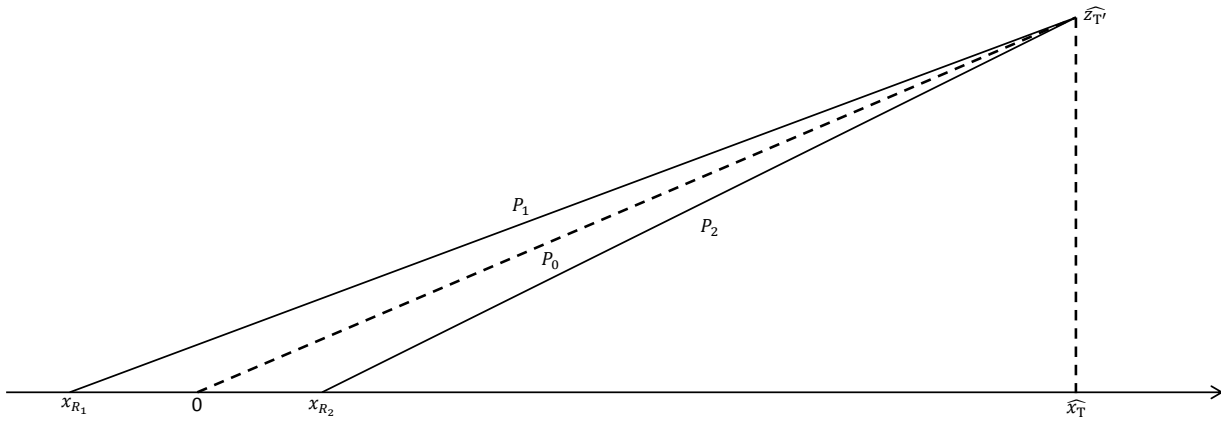


Fig. 6 Principle of estimated reflection height from the geolocation algorithm w.r.t the origin

Using the Pythagoras theorem, the group path P_0 can be expressed as follows:

$$P_0^2 = \frac{1}{2}(P_1^2 + P_2^2) - \left(\frac{x_{R_2} - x_{R_1}}{2}\right)^2 \quad (12)$$

After simplification, the above equation can be rewritten as:

$$P_0^2 = 4(r^2 + (r+h)^2) - 8r(r+h) \cos\left(\frac{x_T - \frac{x_{R_1} + x_{R_2}}{2}}{2r}\right) \cos\left(\frac{x_{R_2} - x_{R_1}}{4r}\right) - \left(\frac{x_{R_2} - x_{R_1}}{2}\right)^2 \quad (13)$$

We selected the origin such that $\frac{x_{R_1} + x_{R_2}}{2} = 0$, hence the above equation can be expressed as:

$$P_0^2 = 4(r^2 + (r+h)^2) - 8r(r+h) \cos\left(\frac{x_T}{2r}\right) \cos\left(\frac{x_{R_2} - x_{R_1}}{4r}\right) - \left(\frac{x_{R_2} - x_{R_1}}{2}\right)^2 \quad (14)$$

Now using Pythagoras theorem,

$$\widehat{z}_T^2 = P_0^2 - \widehat{x}_T^2 \quad (15)$$

Substituting equation (11) and (14) in (15), we get the following:

$$\begin{aligned} \widehat{z}_T'^2 &= 4(r^2 + (r+h)^2) - 8r(r+h) \cos\left(\frac{x_T}{2r}\right) \cos\left(\frac{x_{R_2} - x_{R_1}}{4r}\right) - \left(\frac{x_{R_2} - x_{R_1}}{2}\right)^2 \\ &\quad - 4(r+h)^2 \sin^2\left(\frac{x_T}{2r}\right) \text{sinc}^2\left(\frac{x_{R_1} - x_{R_2}}{4r}\right) \end{aligned} \quad (16)$$

The above equation is the exact expression and the output ionospheric height is computed as: $\hat{h} = \frac{\hat{z}_T'}{2}$. If we assume $x_{R_2} - x_{R_1}$ is small, we have $\cos\left(\frac{x_{R_2} - x_{R_1}}{4r}\right) \cong 1$, $\text{sinc}^2\left(\frac{x_{R_1} - x_{R_2}}{4r}\right) \cong 1$ and $\left(\frac{x_{R_2} - x_{R_1}}{2}\right)^2$ negligible with respect to the other terms, then:

$$\hat{z}_T'^2 = \left((r + h) \cos\left(\frac{x_T}{2r}\right) - r \right)^2 \quad (17)$$

$$\hat{h} = \frac{\hat{z}_T'}{2} = (r + h) \cos\left(\frac{x_T}{2r}\right) - r \quad (18)$$

Note that at radio horizon, $x_T = 2r \cos^{-1}\left(\frac{r}{r+h}\right)$, thus $\hat{h} = 0$. On the contrary, for $x_T = 0$, $\hat{h} = h$. Therefore, depending on transmitter distance, the estimated height \hat{h} decreases from true height h down to zero. In addition, if term $\left(\frac{x_{R_2} - x_{R_1}}{2}\right)^2$ is not negligible, the output value of $\hat{z}_T'^2$ can become negative, especially when x_T increases towards the radio horizon, which can lead to a complex value of \hat{h} .

The error between the estimated (algorithm output) and real transmitter distance by neglecting the Earth curvature for different values of distance between two receivers (0, 100, 200, 300 km) are evaluated using equation (11) and can be seen in (a), (b), (c) and (d) of Fig. 7, respectively. Each curve on a plot corresponds to a specific true reflection height presented with a specific color in the legend box. In all the plots, the real transmitter distance starts at 0 and stops at the corresponding radio horizon which varies with the reflection height and the known distance between the receivers. From all the plots of Fig. 7, it can be observed that the error increases with the distance of the transmitter. There is a steady increase in the error with the increase in the reflection height. Lastly, the effect of distance between the receivers on the error is not significant.

Fig. 8 illustrates the error between the estimated and true reflection heights. The estimated reflection heights are calculated using equation (16) for different true reflection heights ranging from 80 to 300 km with an interval of 20 km between 2 consecutive heights. The plots (a), (b), (c) and (d) of Fig. 8 corresponds to distance between receivers of 0, 100, 200 and 300 km, respectively. When the distance between the receivers is 0, the estimated reflection height varies from true reflection height at a real distance of 0 down to 0 at the radio horizon (Fig. 8 (a)), as explained earlier.

From the estimated distance and height (algorithm outputs), one can obtain the corresponding true height and distance from different plots similar to Fig. 7 and Fig. 8. Specifically, from the known average receiver distance, one can find different value pairs (true distance, true height) which correspond to the estimated distance (Fig. 7). Then, one can find different values pairs (true distance, true height) which correspond to the estimated height (Fig. 8). Two different curves can be plotted from the different value pairs of the estimated height and estimated distance and the point where these two curves intersects would give a new estimate of true height and distance. As these obtained estimates have accounted for the earth curvature, it would have better geolocation accuracy.

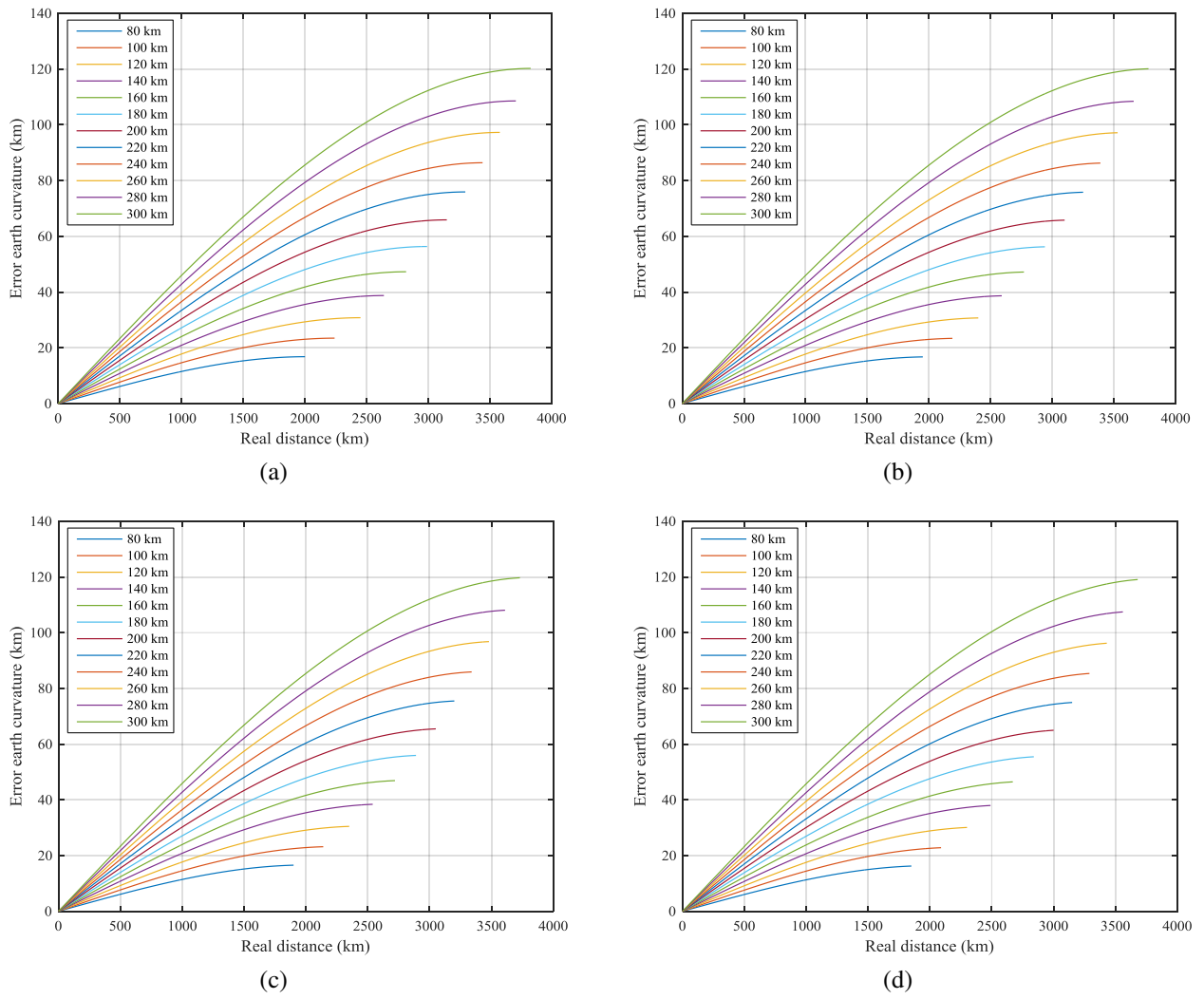
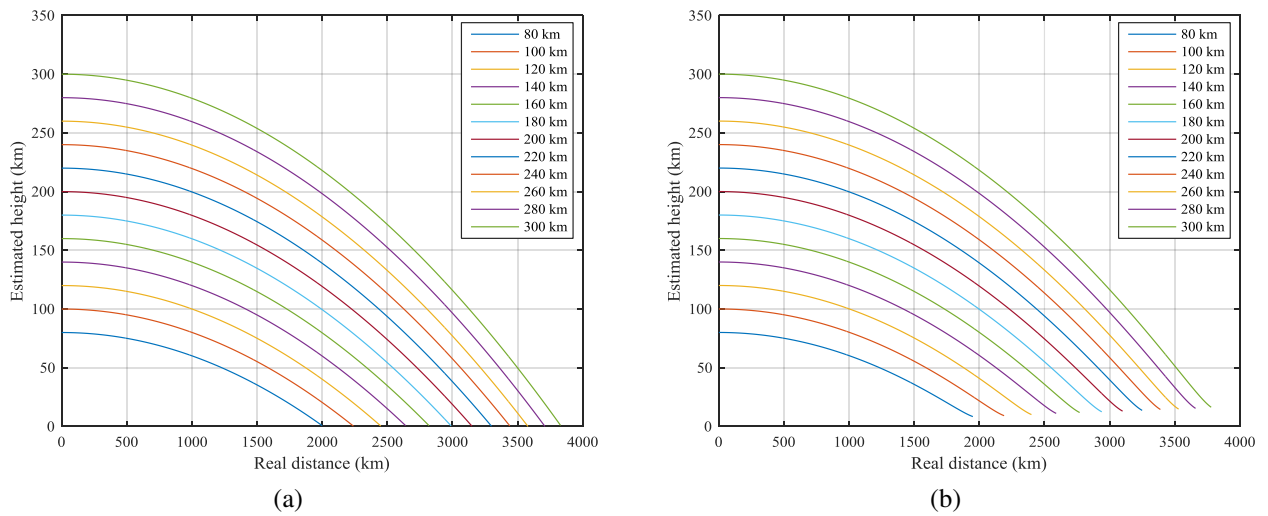
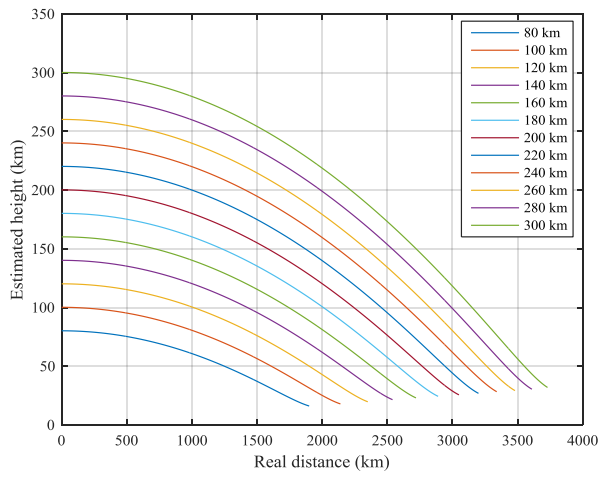
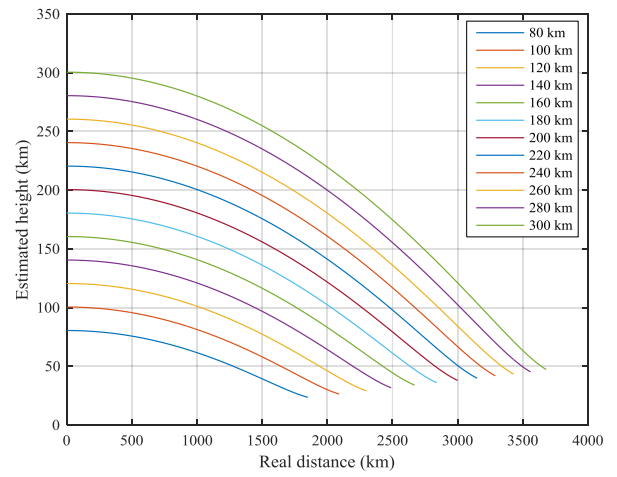


Fig. 7 Error between the estimated and true transmitter distances due to the assumption of flat Earth for different values of distance between 2 receivers





(c)



(d)

Fig. 8 Error between estimated and true heights at different transmitter ranges

Bibliography

- [1] T. D. Carozzi, “Radio waves in ionosphere: Propagation, generation, and detection,” Ph.D. dissertation, Swedish Inst. Space Physics, Uppsala Division, Uppsala, Sweden, Aug. 2000.
- [2] D. Heurguier, “La localisation d’émetteurs de radiocommunication en zone urbaine,” Journées Scientifiques URSI France, Pairs, France, Mar. 2014.
- [3] “Locating Various HF Transmitters and Number Stations with KiwiSDRs,” rtl-sdr.com, 28-Jun-2018. [Online]. Available: <https://www.rtl-sdr.com/locating-various-hf-transmitters-and-number-stations-with-kiwisdrs/>
- [4] “KiwiSDR TDoA Direction Finding Now Freely Available for Public Use,” rtl-sdr.com, 11-Jul-2018. [Online]. Available: <https://www.rtl-sdr.com/kiwisdr-tdoa-direction-finding-now-freely-available-for-public-use/>
- [5] K. Davies, “Ionospheric radio,” IEE Electromagnetic Waves Series 31, Peter Peregrinus Ltd., n° ISBN: 0 86341 186 X, London, 1990.
- [6] “High Altitude Observatory (HAO),” [Online]. Available: <http://www2.hao.ucar.edu>.
- [7] SILSO, World Data Center - Sunspot Number and Long-term Solar Observations, Royal Observatory of Belgium, on-line Sunspot Number catalogue: <http://sidc.oma.be/silso/datafiles>
- [8] “European Digital Upper Atmosphere Server,” DIAS, [Online]. Available: <http://hertz2.space.noa.gr:8080/LatestDias2/loginPage.jsp>
- [9] A. Belehaki et al., “DIAS Project: The establishment of a European digital upper atmosphere server,” *Journal of Atmospheric and Solar-Terrestrial Physics*, vol. 67, no. 12, pp. 1092–1099, Aug. 2005.
- [10] L. F. McNamara, “The Ionosphere: Communications, Surveillance, and Direction Finding,” Krieger Publishing Company, n° ISBN: 0-89464-040-2, Florida, 1991.
- [11] “National Solar Observatory: Global Oscillation Network Group (GONG),” [Online]. Available: <http://gong2.nso.edu/>
- [12] A. Azzarone, “Ionosphere,” INGV Roma2. [Online]. Available: http://roma2.rm.ingv.it/en/research_areas/4/ionosphere.
- [13] D. Bilitza et al., “International reference ionosphere 2016: From ionospheric climate to real-time weather predictions,” *Space Weather*, vol. 15, no. 2, pp. 418–429, Feb. 2017.
- [14] S. Stankov and R. Warnant, “Ionospheric slab thickness: analysis and monitoring applications,” in *12th International Ionospheric Effects Symposium (IES 2008)*, Alexandria, Virginia, May 2008.
- [15] S. S. Kouris, T. D. Xenos, K. V. Polimeris, and D. Stergiou, “TEC and foF2 variations: preliminary results,” *Annals of Geophysics*, 2004.
- [16] “UMass Lowell Center for Atmospheric Research/ DIGISONDE.” [Online]. Available: <http://ulcar.uml.edu/framesd.htm>.
- [17] “ITU-R reference ionospheric characteristics,” ITU-R, *Radiowave propagation* vol. P, no. P.1239-3, Feb. 2012.
- [18] “Space Weather Services homepage,” Space Weather Services, [Online]. Available: <http://www.sws.bom.gov.au/Educational/5/2/2>.
- [19] “Ground-wave propagation curves for frequencies between 10 kHz and 30 MHz,” ITU-R, *Radiowave propagation*, vol. P, no. P.368-9, Feb. 2007.
- [20] B. A. Witvliet, “Near Vertical Incidence Skywave: Interaction of antenna and propagation mechanism,” Ph.D. Thesis, University of Twente, Dec. 2015.
- [21] “Electron density models and data for transionospheric radio propagation,” ITU-R, *Radiowave propagation*, vol. P, no. P.2297-0, 2013.

- [22] B. A. Witvliet, et al., "The importance of circular polarization for diversity reception and MIMO in NVIS propagation," in 8th European Conference on Antennas and Propagation (EuCAP), Hague, Netherlands, pp. 2797–2801, Apr. 2014.
- [23] P. M. Ndao, Y. Erhel, D. Lemur, M. Oger, F. Marie, and J. L. Masson, "Test of HF (3-30 MHz) MIMO communication system based on polarisation diversity," *Electronics Letters*, vol. 48, no. 1, pp. 50–51, Jan. 2012.
- [24] P. M. Ndao, Y. M. Erhel, D. Lemur, M. Oger, and J. L. Masson, "First experiments of a HF MIMO system with polarization diversity," in 12th IET International Conference on Ionospheric Radio Systems and Techniques (IRST 2012), York, United Kingdom, pp. 1–5, May 2012.
- [25] P. M. Ndao, Y. Erhel, D. Lemur, M. Oger, and J. L. Masson, "Implementation of a MIMO solution for ionospheric HF (3–30 MHz) radio links," in 2013 7th European Conference on Antennas and Propagation (EuCAP), Goteborg, Sweden, pp. 510–514, Apr. 2013.
- [26] N. Carrara, M. T. D. Giorgio, and P. F. Pellegrini, "Guided propagation of HF radio waves in the ionosphere," *Space Science Rev*, vol. 11, no. 4, pp. 555–592, Nov. 1970.
- [27] C. C. Watterson, J. R. Juroshek, and W. D. Bensema, "Experimental Confirmation of an HF Channel Model," *IEEE Transactions on Communication Technology*, vol. 18, no. 6, pp. 792–803, Dec. 1970.
- [28] L. E. Vogler and J. A. Hoffmeyer, "A model for wideband HF propagation channels," *Radio Sci.*, vol. 28, no. 6, pp. 1131–1142, Nov. 1993.
- [29] "Radio Noise," ITU-R, Radiowave propagation, vol. P, no. P.372-13, Sep. 2016.
- [30] J. Perkiömäki, "VOACAP Quick Guide: HF Propagation Prediction and Ionospheric Communications Analysis," VOACAP Quick Guide. [Online]. Available: <http://www.voacap.com/>.
- [31] "IONO: logiciels de simulation point à point," [Online]. Available: http://recherche.telecom-bretagne.eu/iono/logiciels_ptp.php
- [32] "Supplement to Report 252-2: Second CCIR Computer-based Interim Method for Estimating Sky-wave Field Strength and Transmission Loss at Frequencies between 2 and 30 MHz," International Radio Consultative Committee (CCIR), Geneva, 1980.
- [33] A. Malaga, "A Characterization and Prediction of Wideband HF Skywave Propagation," in *IEEE Military Communications Conference*, vol. 1, pp. 281–288, Boston, MA, Oct. 1985.
- [34] T. D. Hall, "Radiolocation using AM broadcast signals," PhD Thesis, Massachusetts Institute of Technology, 2002.
- [35] T. D. Hall, C. C. Counselman III, P. N. Misra, "Instantaneous Radiolocation Using AM Broadcast Signals," *Proceedings of the 2001 National Technical Meeting of The Institute of Navigation*, pp. 93–99, Long Beach, CA, Jan. 2001.
- [36] T. D. Hall, C. C. Counselman III, P. N. Misra, "Radiolocation Using AM Broadcast Signals: Positioning Performance," *Proceedings of the 15th International Technical Meeting of the Satellite Division of The Institute of Navigation (ION GPS 2002)*, pp. 921–932, Portland, OR, Sep. 2002.
- [37] J. A. McEllroy, "Navigation Using Signals of Opportunity in the AM Transmission Band," Air Force Institute of Technology, Master Thesis, AFIT/GAE/ENG/06-04, Sep. 2006.
- [38] R. J. Eggert, "Evaluating the Navigation Potential of the National Television System Committee Broadcast Signal," Air Force Institute of Technology, Master Thesis, AFIT/GE/ENG/04-08, Mar. 2004.
- [39] Eggert, Ryan J., Raquet, John F., "Evaluating the Navigation Potential of the NTSC Analog Television Broadcast Signal," *Proceedings of the 17th International Technical Meeting of the Satellite Division of The Institute of Navigation (ION GNSS 2004)*, Long Beach, CA, September 2004, pp. 2436–2446.
- [40] P. J. D. Gething, "High-frequency direction finding," *Proceedings of the Institution of Electrical Engineers*, vol. 113, no. 1, pp. 49–61, 1966.

- [41] R. A. W. Watt and J. F. Herd, "An instantaneous direct-reading radiogoniometer," *Journal of the Institution of Electrical Engineers*, vol. 64, no. 353, pp. 611–617, May 1926.
- [42] I. Pellejero, "EA4FSI-28T1: Adcock/Watson-Watt Radio Direction Finding," EA4FSI-28T1-Technical Articles.
- [43] C. W. Earp and R. M. Godfrey, "Radio direction-finding by the cyclical differential measurement of phase," *Journal of the Institution of Electrical Engineers - Part IIIA: Radiocommunication*, vol. 94, no. 15, pp. 705–721, Mar. 1947.
- [44] P. Denisowski, "A comparison of radio direction-finding technologies," Presentation, Rhode & Schwarz.
- [45] D. Peavey and T. Ogumfunmi, "The single channel interferometer using a pseudo-Doppler direction finding system," in *IEEE International Conference on Acoustics, Speech, and Signal Processing*, vol. 5, Munich, Germany, pp. 4129–4132, Apr. 1997.
- [46] C. W. McLeish and N. Burtnyk, "The application of the interferometer to H.F. direction-finding," *Proceedings of the IEE - Part B: Electronic and Communication Engineering*, vol. 108, no. 41, pp. 495–499, Sep. 1961.
- [47] W. M. Sherrill, "A Survey of HF Interferometry for Ionospheric Propagation Research," *Radio Science*, vol. 6, no. 5, pp. 549–566, May 1971.
- [48] L. Balogh and I. Kollar, "Angle of arrival estimation based on interferometer principle," in *IEEE International Symposium on Intelligent Signal Processing*, Budapest, Hungary, pp. 219–223, Sep. 2003.
- [49] B. D. V. Veen and K. M. Buckley, "Beamforming: a versatile approach to spatial filtering," *IEEE ASSP Magazine*, vol. 5, no. 2, pp. 4–24, Apr. 1988.
- [50] V. Krishnaveni, T. Kesavamurthy, and Aparna. B, "Beamforming for Direction-of-Arrival (DOA) Estimation-A Survey," *International Journal of Computer Applications*, vol. 61, no. 11, pp. 4–11, Jan. 2013.
- [51] Y. Zhang, H. Wu, D. Zhu, and S. Pan, "An optically controlled phased array antenna based on single sideband polarization modulation," *Opt. Express*, vol. 22, no. 4, pp. 3761–3765, Feb. 2014.
- [52] J. Dietrich, "Adaptive Arrays and Diversity Antenna Configurations for Handheld Wireless Communication Terminals," Chapter 3, Doctoral Dissertation, Virginia Tech, Feb. 2000.
- [53] S. M. Razavizadeh, M. Ahn, and I. Lee, "Three-Dimensional Beamforming: A new enabling technology for 5G wireless networks," *IEEE Signal Processing Magazine*, vol. 31, no. 6, pp. 94–101, Nov. 2014.
- [54] F. Marie, L. Bertel, Y. Erhel, D. Lemur, and M. Oger, "Beam-forming techniques operating on HF collocated antennas," *Electronics Letters*, vol. 41, no. 23, pp. 1261–1262, Nov. 2005.
- [55] D. Sadler, "HF Radio Direction Finding," Presentation, Roke Manor Research Ltd., Feb. 2010.
- [56] R. Schmidt, "Multiple emitter location and signal parameter estimation," *IEEE Transactions on Antennas and Propagation*, vol. 34, no. 3, pp. 276–280, Mar. 1986.
- [57] R. Roy and T. Kailath, "ESPRIT-estimation of signal parameters via rotational invariance techniques," *IEEE Transactions on Acoustics, Speech, and Signal Processing*, vol. 37, no. 7, pp. 984–995, Jul. 1989.
- [58] H. K. Hwang, Z. Aliyazicioglu, M. Grice and A. Yakovlev, "Direction of Arrival Estimation using a Root-MUSIC Algorithm," *Proceedings of the International MultiConference of Engineers and Computer Scientists 2008 (IMECS)*, vol. II, Hong Kong, Mar. 2008.
- [59] B. H. Fleury, M. Tschudin, R. Heddergott, D. Dahlhaus, and K. I. Pedersen, "Channel parameter estimation in mobile radio environments using the SAGE algorithm," *IEEE Journal on Selected Areas in Communications*, vol. 17, no. 3, pp. 434–450, Mar. 1999.

- [60] A. Vesa, "Direction of arrival estimation using MUSIC and root-MUSIC algorithm," in 18th Telecommunications Forum, Belgrade, Serbia, pp. 582–585, Nov. 2010.
- [61] T. S. Dhope, "Application of MUSIC, ESPRIT and ROOT MUSIC in DOA Estimation," Faculty of Electrical Engineering and Computing, University of Zagreb, Croatia, 2010.
- [62] Y. Zhang and Z. Ye, "Efficient Method of DOA Estimation for Uncorrelated and Coherent Signals," in IEEE Antennas and Wireless Propagation Letters, vol. 7, pp. 799-802, 2008.
- [63] Y. Erhel, D. Lemur, L. Bertel and F. Marie, "H.F. radio direction finding operating on a heterogeneous array: principles and experimental validation," in Radio-Science, vol. 39, n°1, pp. 1003:1-14, Jan-Feb 2004.
- [64] C. J. Tarran, "Operational HF DF systems employing real time superresolution processing," in Seventh International Conference on HF Radio Systems and Techniques, Nottingham, UK, July 1997, pp. 311–319.
- [65] D. H. Brandwood and D. J. Sadler, "Superresolution direction finding at HF for signals of unknown polarization," in 2000 Eighth International Conference on HF Radio Systems and Techniques, Guildford, UK, July 2000, pp. 133–137.
- [66] G. H. Goldman and C. Reiff, "Localization using ground- and air-based acoustic arrays," in SPIE Defense, Security and Sensing, Orlando, Florida, USA, vol. 8047, May 2011.
- [67] H.H. Jenkins, "Small-Aperture Radio Direction-Finding. Norwood," Norwood, MA, Artech House, 1991.
- [68] E. M. Warrington and T. B. Jones, "Measurements of the direction of arrival of HF sky wave signals and single site location using a seven element wide aperture (294 m) interferometer array," Antennas and Propagation IEE Proceedings H - Microwaves, vol. 138, no. 2, pp. 121–130, Apr. 1991.
- [69] H. C. Horing, "Comparison of the fixing accuracy of single-station locators and triangulation systems assuming ideal shortwave propagation in the ionosphere," IEE Proceedings F - Radar and Signal Processing, vol. 137, no. 3, pp. 173–176, Jun. 1990.
- [70] G. Fabrizio and A. Heitmann, "A multipath-driven approach to HF geolocation," Signal Processing, vol. 93, no. 12, pp. 3487–3503, Dec. 2013.
- [71] G. Fabrizio and A. Heitmann, "Single site geolocation method for a linear array," in 2012 IEEE Radar Conference, Atlanta, USA, pp. 0885–0890, May 2012.
- [72] F. Marie, Y. Erhel, and C. Danion, "An operational HF system for single site localization," in 10th IET International Conference on Ionospheric Radio Systems and Techniques (IRST 2006), Beijing, China, pp. 316–320, July 2006.
- [73] Y. Erhel and F. Marie, "An Operational HF System for Single Site Localization," in IEEE Military Communications Conference, Orlando, USA, pp. 27–31, Oct. 2007.
- [74] R. L. Johnson, Q. R. Black, and A. G. Sonstey, "HF multipath passive single site radio location," IEEE Transactions on Aerospace and Electronic Systems, vol. 30, no. 2, pp. 462–470, Apr. 1994.
- [75] H. J. Strangeways and S. M. Sow, "HF transmitter SSL (single site location) with combined ionospheric update," in Tenth International Conference on Antennas and Propagation (Conf. Publ. No. 436), 1997, vol. 2, pp. 63–66 vol.2.
- [76] A. Bensky, "Wireless positioning technologies and applications," Artech House, n° ISBN-13: 978-1-59693-130-5, Norwood, MA, 2007.
- [77] P. Misra and P. Enge, "Global Positioning Systems," Second Edition, Ganga-Jamuna Press, n° ISBN: 0-9709544-1-7, 2006.
- [78] P. Pagani, R. Fleury, et al., "A study of HF transmitter geolocation through single-hop ionospheric propagation," in 8th European Conference on Antennas and Propagation, Hague, Netherlands, pp. 2689–2693, Apr. 2014.

- [79] P. Pagani et al., "Time domain HF geolocation: Experimental measurements and preliminary results," in 10th European Conference on Antennas and Propagation (EuCAP), Davos, Switzerland, pp. 1–5, Apr. 2016.
- [80] Jansky & Bailey, "The Loran-C System of Navigation." Atlantic Research Corporation, Alexandria VA, 1962.
- [81] E. G. Bakhoun, "Closed-form solution of hyperbolic geolocation equations," IEEE Transactions on Aerospace and Electronic Systems, vol. 42, no. 4, pp. 1396–1404, Oct. 2006.
- [82] R. Stansifer, "Exact solution of a Three Dimensional Hyperbolic Positioning System." [Online]. Available: <https://cs.fit.edu/~ryan/cse4250/projects/multilateration/mult.pdf>.
- [83] E. A. Lewis, R. B. Harvey, and J. E. Rasmussen, "Hyperbolic direction finding with sferics of transatlantic origin," Journal of Geophysical Research, vol. 65, no. 7, pp. 1879–1905, 1960.
- [84] R. W. LaBahn and R. B. Rose, "Time delay variations in HF propagation," Radio Sci., vol. 17, no. 5, pp. 1285–1299, Sep. 1982.
- [85] R. B. Rose, "High resolution HF time of arrival measurements (1981 - 1985)," Radio Science, vol. 23, no. 3, pp. 257–264, 1988.
- [86] R. B. Rose, "HF (High Frequency) absolute time of arrival sensing," Interim Report, Sep. 1981 - May 1985 Naval Ocean Systems Center, San Diego, CA, Feb. 1986.
- [87] N. N. Rao, R. I. Beckwith, and E. W. Ernst, "Prediction of Differential Time-Delay Errors in HF Hyperbolic Position-Fixing Systems," IEEE Transactions on Aerospace and Electronic Systems, vol. AES-10, no. 6, pp. 765–769, Nov. 1974.
- [88] N. N. Rao and R. I. Beckwith, "Reduction of Positional Estimate Errors in HF Hyperbolic Position-Fixing Systems," IEEE Transactions on Aerospace and Electronic Systems, vol. AES-11, no. 1, pp. 113–114, 1975.
- [89] G. Wang, X. Jiang, S. G. Razul, C. M. See, and Z. Lin, "Passive TDOA and DOA based HF geolocation without ionosphere information," in 10th International Conference on Information, Communications and Signal Processing (ICICSP), Singapore, Dec. 2015.
- [90] D. J. Torrieri, "Statistical theory of passive location systems," IEEE Trans. on Aerospace and Electronic Systems, vol. AES-20, no. 2, pp. 183–198, Mar. 1984.
- [91] A. Jain, P. Pagani, R. Fleury, M. M. Ney, and P. Pajusco, "Efficient time domain HF geolocation using multiple distributed receivers," in 11th European Conference on Antennas and Propagation (EuCAP), Paris, France, pp. 1852–1856, Mar. 2017.
- [92] K. Davies and C. M. Rush, "Reflection of high-frequency radio waves in inhomogeneous ionospheric layers," Radio Science, vol. 20, no. 3, pp. 303–309, May 1985.
- [93] S. M. Stankov, N. Jakowski, S. Heise, P. Muhtarov, I. Kutiev, and R. Warnant, "A new method for reconstruction of the vertical electron density distribution in the upper ionosphere and plasmasphere," Journal of Geophysical Research: Space Physics, vol. 108, no. A5, May 2003.
- [94] T. A. Croft and H. Hoogasian, "Exact ray calculations in a quasi-parabolic ionosphere with no magnetic field," Radio Science, vol. 3, no. 1, pp. 69–74, Jan. 1968.
- [95] G.S. Sales, High Frequency (HF) Radiowave Propagation. PL-TR-92-2123, Philips Laboratory, Hanscom AFB, MA, April 1992.
- [96] S. Solous, "Radio Propagation Measurement and Channel Modelling," Wiley Publications, pp. 29–32, n° ISBN: 978-0-470-75184-8, 2013.
- [97] D. E. Westover, "Exact Ray-Path Solutions in a Quasi-Linear Ionosphere," Radio Science, vol. 3, no. 1, pp. 75–79, Jan. 1968.
- [98] D. E. Westover, "Exact Ray-Path Solutions in a Quasi-Linear Ionosphere (Errata)," Radio Science, vol. 3, no. 8, pp. 879–879, Nov. 2015.

- [99] E. Appleton and W. J. G. Beynon, "The application of ionospheric data to radio communication problems: part II," *Proc. Phys. Soc.*, vol. 59, no. 1, p. 58, 1947.
- [100] J. R. Dudeney, "An improved model of the variation of electron concentration with height in the ionosphere," *Journal of Atmospheric and Terrestrial Physics*, vol. 40, no. 2, pp. 195–203, Feb. 1978.
- [101] J. R. Hill, "Exact ray paths in a multisegment quasi-parabolic ionosphere," *Radio Science*, vol. 14, no. 5, pp. 855–861, Sep. 1979.
- [102] R. Badeke, C. Borries, M. M. Hoque, and D. Minkwitz, "Empirical forecast of quiet time ionospheric Total Electron Content maps over Europe," *Advances in Space Research*, vol. 61, no. 12, pp. 2881–2890, Jun. 2018.
- [103] E. V. Dao, L. F. McNamara, and J. J. Colman, "Magnetic field effects on the accuracy of ionospheric mirror models for geolocation," *Radio Science*, vol. 51, no. 4, pp. 284–300, Apr. 2016.
- [104] X. Li, Z. D. Deng, L. T. Rauchenstein, and T. J. Carlson, "Source-localization algorithms and applications using time of arrival and time difference of arrival measurements," *Review of Scientific Instruments*, vol. 87, no. 4, p. 041502, Apr. 2016.
- [105] Y. P. Lei, F. X. Gong, and Y. Q. Ma, "Optimal distribution for four-station TDOA location system," in *3rd International Conference on Biomedical Engineering and Informatics*, Yantai, China, vol. 7, pp. 2858–2862, Oct. 2010.
- [106] R. A. Poisel, "Electronic Warfare Target Location Methods," Second Edition, Artech House, pp. 226–252, n° ISBN 13: 978-1-60807-523-2.
- [107] A. Jain, E. Mejias, M. Prost, P. Pagani, R. Fleury, M. M. Ney, and P. Pajusco, "Récepteur prototype pour l'acquisition à distance de signaux HF," *JNM2017: 20èmes Journées Nationales Microondes*, May 2017, Saint-Malo, France.
- [108] "Introduction to SDR - Wireless Innovation Forum." [Online]. Available: https://www.wirelessinnovation.org/Introduction_to_SDR.
- [109] "USRP N210 Software Defined Radio (SDR) - Ettus Research." [Online]. Available: <https://www.ettus.com/product/details/UN210-KIT>.
- [110] "Ettus Research - Product Detail," [Online]. Available: <https://www.ettus.com/product/details/LFRX>.
- [111] "Ettus Research - Product Detail," [Online]. Available: <https://www.ettus.com/product/details/GPSDO-KIT>.
- [112] "Ettus Research - Product Detail," [Online]. Available: <https://www.ettus.com/product/details/GPS-ANT-3V>.
- [113] "Amphenol Procom's - Products," [Online]. Available: <http://procom.dk/products/518-bcl-1-ka>.
- [114] "Mini-Circuits," [Online]. Available: <https://www.minicircuits.com/WebStore/dashboard.html?model=BLP-30%2B>.
- [115] "Power supply RS Pro, 12V cc, 1.5A, 135 → 370 V c.c., 90 → 264 V c.a., 1 sortie | RS Components," [Online]. Available: <https://fr.rs-online.com/web/p/alimentations-de-bureau/7702817/>.
- [116] "GNU Radio," [Online]. Available: <https://www.gnuradio.org/about/>.
- [117] "GNU Radio Manual and C++ API Reference: Metadata Information," [Online]. Available: https://www.gnuradio.org/doc/doxygen/page_metadata.html.
- [118] "Shortwave schedules around the world with frequencies in kHz and distance calculator." [Online]. Available: <http://www.shortwaveschedule.com/>.
- [119] K. Khoder, R. Fleury, and P. Pagani, "Monitoring of ionosphere propagation conditions using opportunistic HF signals," in *The 8th European Conference on Antennas and Propagation (EuCAP 2014)*, Hague, Netherlands, pp. 2697–2701, Apr. 2014.

- [120] B. S. Kim, "Evaluating the Correlation Characteristics of Arbitrary AM and FM Radio Signals for the Purpose of Navigation," Air Force Institute of Technology, USA, Master Thesis, AFIT/GE/ENG/06-28, Mar. 2006.
- [121] "BS.1284: General methods for the subjective assessment of sound quality," Rec. ITU-R BS.1284-1, Dec. 2003.
- [122] G. Lane, "Required signal-to-interference ratios for shortwave broadcasting," *Radio Science*, vol. 32, no. 5, pp. 2091–2098, Sep. 1997.
- [123] CCIR, "Minimum AF and RF Signal-to-Noise Ratio Required for Broadcasting in Band 7 (HF)," Report 1058, X-I, 62-66, ITU, Geneva, 1986.
- [124] A. Jain, P. Pagani, R. Fleury, M. M. Ney, and P. Pajusco, "Cross-Channel Sounding for HF Geolocation: Concepts and Experimental Results," in 12th European Conference on Antennas and Propagation (EuCAP), London, UK, Apr. 2018.
- [125] A. Jain, P. Pagani, R. Fleury, M. M. Ney, and P. Pajusco, "Accurate time difference of arrival estimation for HF radio broadcast signals," *Microwave and Optical Technology Letters*, vol. 60, no. 6, pp. 1406–1410, Jun. 2018.
- [126] A. Jain, P. Pagani, R. Fleury, M. M. Ney, and P. Pajusco, "HF Source Geolocation Using an Operational TDoA Receiver Network: Experimental Results," *IEEE Antennas and Wireless Propagation Letters*, vol. 17, no. 9, pp. 1643–1647, Sep. 2018.
- [127] A. Jain, P. Pagani, R. Fleury, M. M. Ney, and P. Pajusco, "Passive HF Geolocation Using TDoA Based receiver Network," URSI-France 2018 Workshop (Journée Scientifiques), Paris, France, Mar. 2018.
- [128] A. Jain, P. Pagani, R. Fleury, M. M. Ney, and P. Pajusco, "Passive HF Geolocation Using TDoA Based receiver Network: Principle and Measurement Results," *Revue de l'électricité et de l'électronique (REE)*, accepted for publication.
- [129] L. E. Vogler and J. A. Hoffmeyer, "A New Approach to HF Channel Modeling and Simulation, Part 1: Deterministic Model," NTIA Technical Report TR-88-240, December 1988.
- [130] L. E. Vogler and J. A. Hoffmeyer, "A New Approach to HF Channel Modeling and Simulation. Part 2: Stochastic Model," NTIA Technical Report TR-90-255, February 1990.
- [131] L. E. Vogler and J. A. Hoffmeyer, "A new approach to HF channel Modeling and Simulation. Part 3: Transfer function," NTIA Technical Report TR-92-284, March 1992.
- [132] R. P. Basler, G. H. Price, R. T. Tsunoda, and T. L. Wong, "Ionospheric distortion of HF signals," *Radio Science*, vol. 23, no. 4, pp. 569–579, July 1988.
- [133] L. S. Wagner, J. A. Goldstein, W. D. Meyers, and P. A. Bello, "The HF Skywave Channel: Measured Scattering Functions for Midlatitude and Auroral Channels and Estimates for Short-Term Wideband HF Rake Modem Performance," *IEEE Military Communications Conference*, Boston, 1989.
- [134] L. S. Wagner and J. A. Goldstein, "Response of the High Latitude HF Skywave to an Isolated Magnetic Disturbance," *Fifth International Conference on HF Radio Systems and Techniques*, pp. 233-237, Edinburgh, 1991.
- [135] C. A. Nissen and P. A. Bello, "Measured channel parameters for the disturbed wide-bandwidth HF channel," *Radio Science*, vol. 38, no. 2, pp. 6-1-6-7, Apr. 2003.
- [136] C. Vilella, D. Miralles, and J. L. Pijoan, "An Antarctica-to-Spain HF ionospheric radio link: Sounding results," *Radio Science*, vol. 43, no. 4, Aug. 2008.
- [137] A. G. Ads et al., "A comprehensive sounding of the ionospheric HF radio link from Antarctica to Spain," *Radio Science*, vol. 48, no. 1, pp. 1–12, Jan. 2013.
- [138] M. Hervás et al., "Narrowband and Wideband Channel Sounding of an Antarctica to Spain Ionospheric Radio Link," *Remote Sensing*, vol. 7, no. 9, pp. 11712–11730, Sep. 2015.

- [139] R. Mitran and P. Bechet, “HF radio channels evaluation using passive sounding in the Black Sea area,” *Journal of Electromagnetic Waves and Applications*, vol. 31, no. 5, pp. 532–543, Mar. 2017.
- [140] P. Pagani, F. Tchoffo Talom, P. Pajusco and B. Uguen, “Ultra-Wideband Radio Propagation Channels: A Practical Approach,” ISTE / Wiley, London/New Jersey, 2008.
- [141] E. W. Weisstein, “Cross-Correlation Theorem.” [Online]. Available: <http://mathworld.wolfram.com/Cross-CorrelationTheorem.html>.
- [142] E. W. Weisstein, “Convolution Theorem.” [Online]. Available: <http://mathworld.wolfram.com/ConvolutionTheorem.html>.
- [143] J. P. Snyder, “Map projections: A working manual,” U.S. Government Printing Office, Washington, D.C., Series 1395, pp. 191–202, 1987.
- [144] “HFCC - International Broadcasting Delivery.” [Online]. Available: http://www.hfcc.org/about/HFCC-IBD_Basic_Information.phtml
- [145] “Short-wave frequencies and bands used for radio broadcasting.” [Online]. Available: <https://www.short-wave.info/index.php?feature=frequencies>.
- [146] S. Haykin, “Communication Systems,” Fourth Edition, USA: John Wiley & Sons, Inc., n° ISBN- 978-0-471-17869-9, May 2000.
- [147] “Application_note_frontends_subdevices_antenna_ports.” Available: https://www.ettus.com/content/files/kb/application_note_frontends_subdevices_antenna_ports.pdf.
- [148] F. A. Hamza, “The USRP under 1.5 x magnifying lens.” Available: http://gnuradio.org/redmine/attachments/129/USRP_Documentation.pdf

List of Publications

Peer-reviewed International Journal Papers

A. Jain, P. Pagani, R. Fleury, M. M. Ney, and P. Pajusco, “HF Source Geolocation Using an Operational TDoA Receiver Network: Experimental Results,” *IEEE Antennas and Wireless Propagation Letters*, vol. 17, no. 9, pp. 1643–1647, Sep. 2018.

A. Jain, P. Pagani, R. Fleury, M. M. Ney, and P. Pajusco, “Accurate time difference of arrival estimation for HF radio broadcast signals,” *Microwave and Optical Technology Letters*, vol. 60, no. 6, pp. 1406–1410, Jun. 2018.

A. Jain, P. Pagani, R. Fleury, M. M. Ney, and P. Pajusco, “Passive HF Geolocation Using TDoA Based receiver Network: Principle and Measurement Results,” *Revue de l’électricité et de l’électronique (REE)*, accepted for publication.

International Conference Papers

A. Jain, P. Pagani, R. Fleury, M. M. Ney, and P. Pajusco, “Cross-Channel Sounding for HF Geolocation: Concepts and Experimental Results,” in *12th European Conference on Antennas and Propagation (EuCAP)*, London, UK, Apr. 2018.

A. Jain, P. Pagani, R. Fleury, M. M. Ney, and P. Pajusco, “Efficient time domain HF geolocation using multiple distributed receivers,” in *11th European Conference on Antennas and Propagation (EuCAP)*, Paris, France, pp. 1852–1856, Mar. 2017.

A. Jain, P. Pagani, R. Fleury, M. M. Ney, and P. Pajusco, “Measurement Qualification Metrics for Passive HF Geolocation,” in *13th European Conference on Antennas and Propagation (EuCAP 2019)*, accepted for publication.

National Conference Papers

A. Jain, P. Pagani, R. Fleury, M. M. Ney, and P. Pajusco, “Passive HF Geolocation Using TDoA Based receiver Network,” *URSI-France 2018 (Journée Scientifiques)*, Paris, France, Mar. 2018.

A. Jain, E. Mejias, M. Prost, P. Pagani, R. Fleury, M. M. Ney, and P. Pajusco, “Récepteur prototype pour l’acquisition à distance de signaux HF,” *JNM2017: 20èmes Journées Nationales Microondes*, May 2017, Saint-Malo, France.

Titre : Détection d'émetteurs radio HF par des techniques de géolocalisation passive

Mots clés : Géolocalisation HF, Ionosphère, Différence de temps d'arrivée, mesures HF

Résumé : La transmission radioélectrique à longue distance dans la bande HF permet de couvrir de vastes zones géographiques à l'aide d'infrastructures légères et mobiles. Elle est donc bien adaptée pour établir des communications lors d'opérations militaires ou pour le déploiement rapide d'un réseau de communication agile lors d'opérations humanitaires. Dans ce contexte, il est important de pouvoir localiser les émetteurs inconnus par l'analyse des signaux électromagnétiques de communication. L'objectif de la thèse est de développer une technique de géolocalisation alternative et complémentaire, intitulée Time Difference of Arrival (TDoA), qui a rarement été étudiée dans le cas de la propagation ionosphérique. Dans un premier temps, l'algorithme de géolocalisation HF basé sur la technique TDoA est adapté et optimisé par des simulations paramétriques. Les résultats de simulation montrent que l'augmentation du nombre de récepteurs entraîne une amélioration significative de la précision de géolocalisation. Afin d'étudier la faisabilité de mise en œuvre d'un système de géolocalisation HF basé sur la technique TDoA, plusieurs récepteurs HF pilotable à distance ont été développés à partir de modules de radio logicielle, et un réseau national de récepteurs a été déployé en France. Un concept original de sondage de canal croisé est proposé et décrit mathématiquement. Il permet d'évaluer les différences de durée de propagation entre les signaux reçus sur deux récepteurs synchronisés distincts. Les résultats expérimentaux collectés montrent qu'il est possible de localiser les émetteurs HF dans des conditions favorables avec une erreur de géolocalisation relative comprise entre 0,1 et 10% de la distance réelle au sol. Les données collectées lors de la campagne de mesure sont analysées de manière statistique afin d'évaluer la performance de l'algorithme de géolocalisation et de définir les paramètres les plus pertinents à prendre en compte pour déployer cette technique dans une approche opérationnelle.

Title : Detection of HF radio transmitters using passive geolocation techniques

Keywords : HF geolocation, Ionosphere, Time Difference of Arrival, HF measurements

Abstract : Long-range radio transmission in the HF band can cover large geographical areas using light and mobile equipment. It is therefore well suited for communications during military operations or for the rapid deployment of an agile communication network during humanitarian operations. In this context, it is important to determine the geographic location of the transmitters by analyzing the electromagnetic communication signals. The aim of the thesis is to develop an alternative, complementary geolocation technique, entitled Time Difference of Arrival (TDoA) that has rarely been studied in the case of ionospheric propagation. As a first step, HF geolocation algorithm based on TDoA is setup and analyzed by parametric software simulations. Simulation results demonstrate that increasing the number of receivers leads to a significant improvement in the geolocation accuracy. In order to study the feasibility of a practical HF geolocation system based on TDoA, multiple remotely controllable HF receivers are designed using software defined radio (SDR) modules and a country wide operational receiver network is deployed in France. A concept of cross-channel sounding along with its mathematical description is proposed to evaluate the propagation duration differences between the signals captured by two distinct receivers. Preliminary experimental results show that it is possible to locate the HF transmitters under favorable conditions with a relative geolocation error ranging from about 0.1 to 10% of the actual ground distance. Data captured during the large scale measurement campaign are analyzed statistically to evaluate the performance of the geolocation algorithm and define parameters that could be considered in an operational approach.